AFFDL-TR-73-146-VOL. III

METHODS FOR PREDICTING THE AERODYNAMIC AND STABILITY AND CONTROL CHARACTERISTICS OF STOL AIRCRAFT

VOLUME III ★ ENGINEERING METHODS

M. I. Goldhammer
M. L. Lopez

Douglas Aircraft Company
McDonnell Douglas Corporation

and other Datcom contributors, is also appreciated.

This report contains no classified information.

This technical report has been reviewed and is approved.

C. B. Westbrook
Chief, Control Criteria Branch
Flight Control Division
Air Force Flight Dynamics Laboratory

ABSTRACT

This volume describes analytical engineering methods for the prediction of the aerodynamic and stability and control characteristics of STOL aircraft employing internally ducted jet flaps, externally blown jet flaps, and mechanical flap systems with vectored thrust. These methods are intended to be used in conjunction with the theoretical methods and the associated computer program (STOL Aerodynamic Methods Program) discussed in Volumes I and II, respectively. These engineering methods are intended to provide a rational approach for the aerodynamic analysis of complete STOL aircraft configurations and to provide semi-empirical methods to account for those effects not treated by the theoretical methods.

For the three selected powered high-lift systems, a common set of analytical engineering methods has been presented, and these methods have been divided into three major sections:

- Static Coefficients and Derivatives
- Dynamic Stability Derivatives
- Control Derivatives

The methods presented include brief discussions of the importance of each coefficient and derivative and the impact of each term on the overall stability and control characteristics of the aircraft.

Finally, these methods have been applied to configurations representative of each of the powered high-lift concepts, and the results of these analyses have been presented along with available experimental data to indicate the validity and range of applicability of the methods.

CONTENTS

LIST OF ILLUSTRATIONS

NOMENCLATURE

A	Fuselage cross-sectional area
A_o	1. Fuselage cross-section area at x_o where flow ceases to be potential 2. Freestream capture area of each engine
AR	Aspect ratio
b	Wing span
C_D	Total drag coefficient
C_{D_u}	Drag coefficient due to variation of forward speed
C_{D_i}	Total induced drag coefficient
$C_{D_{\delta_e}}$	Drag coefficient due to elevator deflection
$C_{D_{\delta_r}}$	Drag coefficient due to rudder deflection
C_{D_o}	Drag coefficient at zero angle of attack
$C_{D_{base}}$	Base drag coefficient
C_{D_R}	Ram drag coefficient
CI	Circular intercept
C_J	Total jet momentum coefficient
C_L	Total lift coefficient
C_{L_J}	Jet reaction coefficient
C_{L_q}	Lift coefficient derivative due to pitching
C_{L_α}	Lift-curve slope
$C_{L_{\dot{\alpha}}}$	Lift coefficient derivative due to $\dot{\alpha}$
C_{L_Γ}	Circulation lift coefficient
C_{L_o}	Lift coefficient at zero angle of attack
$C_{L_{\delta_f}}$	Lift coefficient due to flap deflection
$C_{L_{\delta_s}}$	Lift coefficient due to slat deflection
$C_{L_{\delta_J}}$	Lift coefficient due to jet deflection

$C_{L_{\delta_{sp}}}$	Lift coefficient due to spoiler deflection
C_l	Total rolling moment coefficient
C_{l_J}	Jet reaction rolling moment coefficient
C_{l_p}	Rolling moment coefficient derivative due to roll
C_{l_r}	Rolling moment coefficient derivative due to yaw
C_{l_Γ}	Circulation rolling moment
$C_{l_{\delta_a}}$	Rolling moment coefficient due to aileron deflection
$C_{l_{\delta_r}}$	Rolling moment coefficient due to rudder deflection
C_m	Total pitching moment coefficient
$C_{m_{i_H}}$	Pitching moment coefficient due to stabilizer incidence
C_{m_J}	Pitching moment coefficient due to the vertical component of jet reaction
C_{m_q}	Pitching moment coefficient derivative due to pitching
C_{m_T}	Pitching moment coefficient due to the horizontal component of jet reaction
$C_{m_{\dot{\alpha}}}$	Pitching moment coefficient derivative due to $\dot{\alpha}$
C_{m_Γ}	Circulation pitching moment
$C_{m_{\delta_e}}$	Pitching moment coefficient due to elevator deflection
C_n	Total yawing moment coefficient
C_{n_J}	Jet reaction yawing moment coefficient
C_{n_p}	Yawing moment coefficient derivative due to roll
C_{n_r}	Yawing moment coefficient derivative due to yaw
C_{n_Γ}	Circulation yawing moment
$C_{n_{\delta_a}}$	Yawing moment coefficient due to aileron deflection
$C_{n_{\delta_r}}$	Yawing moment due to rudder deflection
C_T	Total thrust coefficient
C_Y	Total side force coefficient

C_{Y_J}	Jet reaction side force coefficient
C_{Y_p}	Side force coefficient derivative due to roll
C_{Y_r}	Side force coefficient derivative due to yaw
C_{Y_Γ}	Circulation side force
$C_{Y_{\delta_a}}$	Side force coefficient due to aileron deflection
$C_{Y_{\delta_r}}$	Side force coefficient due to rudder deflection
c	Chord
$\bar{c}$	Mean aerodynamic chord
$\tilde{c}$	Wing reference chord
c_a	Distance from section leading edge to slot lip (Figure 3.5)
c'_a	Extended wing chord due to forward flap deflection (Figure 3.5)
c_1	Forward flap chord
c_2	Aft flap chord
c'	Extended wing chord
c_d	Sectional drag coefficient
c_{d_c}	Cross-flow drag coefficient infinite cylinder
c_{d_i}	Sectional induced drag coefficient
$\Delta c_{d_{flap}}$	Incremental sectional drag due to flap deflection
c_f	1. Skin friction coefficient
	2. Flap chord
c_ℓ	Sectional lift coefficient
c_m	Sectional pitching moment coefficient
c_{mac}	Mean aerodynamic chord
c_p	Pressure coefficient
Δc_p	Difference in pressure coefficient between lower and upper surfaces (pressure jump coefficient)

c_r	Root chord
c_t	Tip chord
c_μ	Sectional jet momentum coefficient
d	Fuselage cross-section diameter
e	Oswald's span efficiency factor
F	Fuselage (subscript)
F_g	Gross thrust
F_R	Ram drag
F_T	Thrust force
F_x, F_y, F_z	Forces in the (x,y,z) directions
g	Gravitational acceleration constant (32.2 ft/sec^2)
H	Horizontal tail (subscript)
h	Height of wing above ground
h_x, h_y, h_z	Components of momentum in (x,y,z) directions
I_x, I_y, I_z	Moments of inertia in the (x,y,z) directions
I_{xz}	Product of inertia
K	Empirical factor (several uses, defined in text)
K_b	Empirical factor to account for the profile drag of partial span flaps
K_F	Empirical fuselage length effect factor
K_{WB}	Empirical wing-body interference factor
K_1	Ratio of theoretical c_{ℓ_α} of a thick section to that of a flat plate
K_2	Empirical factor to account for the development of the boundary layer near the airfoil trailing edge
K_3	Ratio of theoretical c_{ℓ_δ} of a thick flapped section to that of a thin airfoil with flap
K_4, K_5, K_6	Empirical correction factors to account for boundary layer effects on flapped sections
K_M	Munk's apparent mass factor

L	1. Total lift or total rolling moment 2. Empirical airfoil thickness factor for profile drag
ℓ	1. Sectional lift 2. Length of body
ℓ_F	Length of fuselage
ℓ_H	Horizontal distance between the wing 1/4 MAC and the horizontal tail 1/4 MAC
ℓ_V	Horizontal distance between the wing 1/4 MAC and the vertical tail 1/4 MAC
ℓ/K	Admissible roughness
M	1. Total pitching moment 2. Mach number
MAC	mean aerodynamic chord
m	Sectional pitching moment
N	1. Total yawing moment 2. Number of engines
P_{T_J}	Jet total pressure
P_a	Ambient pressure
p	Rate of roll
Q_i	Intake mass flow of engine
q	Rate of pitch
R_ℓ	Reynolds number based on length
$R_{\ell_{fus}}$	Reynolds number based on fuselage length
$R_{L.S.}$	Empirical correction factor to account for the spanwise flow on a finite lifting surface.
R_{WB}	Empirical wing-body interference factor for drag
r	Fuselage cross-section radius
S	Wing planform reference area
S_B	Blown wing area

S_{wet}	Wetted area
T	Total thrust
t	Sectional thrust
t/c	Thickness-chord ratio
t_2	Spiral mode time constant
U, V, W	Freestream velocity in (x,y,z) directions. (NOTE: in a wind axis system V and W are zero.)
V	Vertical tail (subscript)
x,y,z	Cartesian coordinate system
x_o	Fuselage station where flow ceases to be potential
x_1	Fuselage station where the cross-section area gradient, dA/dx, first reaches its maximum negative value
x_{cg}	x - coordinate of aircraft center of gravity
$\bar{y}_{flap}$	Mean spanwise position of the flap
z_w	Height of wing relative to fuselage centerline
Δz_H	Height of horizontal tail MAC above wing plane
Δz_v	Height of vertical tail MAC above wing plane
α	Angle of attack
α_t	Twist angle of a wing section
β	Sideslip angle
Γ	1. Circulation (subscript) 2. Dihedral angle
δ_f	Flap deflection angle
δ_J	Jet deflection angle
δ_s	Slat deflection angle
δ_{sp}	Spoiler deflection angle
ϵ	Tailplane downwash angle

ε_{mean}	Mean tailplane downwash
δ_f	Flap deflection angle (degrees)
δ_J	Jet deflection angle (degrees)
δ_s	Slat deflection angle (degrees)
δ_{sp}	Spoiler deflection angle
ζ_{sp}	Damping constant for short period oscillation
ζ_p	Damping constant for Phugoid oscillation
ζ_D	Damping constant for Dutch Roll oscillation
η	Ratio of drag on a finite cylinder to drag on an infinite cylinder
θ	Jet deflection angle relative to freestream
θ_J	Vectored jet deflection angle
$\Lambda_{c/4}$	Wing sweepback angle (1/4 - chord line)
$\Lambda_{L.E.}$	Wing sweepback angle (Leading edge)
ν	Static jet turning angle = $\tan^{-1}(F_Z/F_X)$
ρ	Density of freestream flow
σ	Sidewash angle
τ	Static jet turning efficiency = $\frac{F_X^2 + F_Z^2}{F_T}$
τ_R	Roll mode time constant
$\omega_{n_{sp}}$	Frequency of short period oscillation
ω_{n_p}	Frequency of Phugoid oscillation
ω_{n_D}	Frequency of Dutch Roll oscillation

1.0 INTRODUCTION

A collection of theoretical methods for the prediction of the aerodynamic and stability and control characteristics of a STOL aircraft employing either jet-flap high-lift systems or mechanical flaps with vectored thrust systems is presented in Volume I of this report. These methods are based on an idealized representation of such aircraft and their implementation requires a supplementary set of analytical engineering methods to account for those effects not treated by the methods of Volume I. In addition, it is appropriate to describe how the theoretical methods can be applied most effectively to practical aircraft configurations. Although the use of the computer program developed for the theoretical methods is discussed in Volume II, Volume III is, in part, intended to provide a rational approach for treating complicated aircraft goemetries so that the many capabilities of the computer program can be effectively and efficiently used.

The analytical engineering methods presented herein are divided into three basic categories: static coefficients and derivatives, dynamic stability derivatives, and control derivatives. In addition, general empirical methods are presented to account for those effects not amenable to theoretical treatments. The primary objective of this work is to establish prediction methods for the aerodynamic and stability and control coefficients and derivatives. It is necessary, however, to examine briefly the aircraft dynamics problem insofar as the impact of the coefficients and derivatives calculated is concerned for the purpose of establishing accuracy requirements in the calculation of stability and control parameters.

In order to assess the validity of the methods developed in this work, they have been applied to a variety of STOL transport aircraft configurations for which experimental data are available. In this respect, methods correlations are presented throughout, and in addition, analyses for complete aircraft for configurations employing internally ducted jet flaps, externally blown jet flaps, and mechanical flaps with vectored thrust are presented.

This volume, in conjunction with the computer program, is intended to provide aerodynamic and stability and control prediction methods for STOL aircraft suitable for use by design personnel. However, it is recommended that

Volume I of this report be read to gain an understanding of the theoretical methods, including their assumptions and limitations, before any attempt to use these methods and the associated computer program is made.

2.0 AIRCRAFT GEOMETRY DEFINITION

Before a detailed description concerning prediction methods for each of the aerodynamic and stability and control coefficients and derivatives can be presented, certain aspects of aircraft geometry definition, which should clarify and simplify application of the methods presented, will be discussed. The basis for application of the analytical prediction methods developed in this work is the STOL Aerodynamic Methods Program (STAMP), described in detail in Volume II. Effective implementation of STAMP requires that the aircraft geometry be suitably defined for input into the program. The details of actually translating an aircraft geometry into a set of numerical data suitable for program use is extensively discussed in Volume II, including such topics as methods limitations and element spacing criteria. In this section, some of the more fundamental aspects of geometry preparation are discussed, primarily to aid the design engineer to effectively and efficiently utilize the program.

The logical starting point in defining aircraft geometry is the wing planform. Although the actual mode of input described in Volume II is straightforward and quite simple, confusion may arise for complex planforms, particularly when extended chord devices (e.g., Fowler flaps) are employed. First of all, for wing-body configurations the wing planform should be extrapolated to the plane of symmetry (the x-z plane) to represent the fuselage carryover lift. Secondly, consider a trapezoidal planform with a Fowler-type flap whose extension is a function of the deflection angle $[c_f/c = F(\delta_f)]$. To consider a range of deflection angles, it would actually be necessary to define a new planform for each chord extension and run the program for each particular flap deflection. However, it is not an unreasonable engineering approximation to choose a single planform shape representative of the mean over the range of flap deflections considered and make use of the fundamental/composite case feature of the EVD segment of the program to efficiently treat the variations in flap deflection if the chord variation is not too large. The ratio of the wing area with chord extension to the reference wing area should provide a reasonable estimate of the importance of the variation in chord extension. Of course, if the specific purpose of a parametric study is to determine the effectiveness of a flap system, then clearly the mean planform concept is not

a good approximation and the program must be fully rerun for each chord extension.

There are several other areas where confusion may arise in planform definition. First, the program cannot consider the geometric aspects of wing dihedral with the exception of evaluating the effect of sideslipping, so the projection of the planform in the x-y plane should be used instead. In addition, the program can only consider straight wing tips that are parallel to the freestream. Since the wing loading is not significantly affected by tip shape, no attempt to carefully define a rounded wing tip should be made unless the rounding is faired over a large part of the wing span. Rather, the rounded wing tip should be represented by a trapezoidal segment of equivalent surface area. Skew wing tips should be similarly treated. Finally, engineering judgment must be applied to insure that all planform characteristics that will affect the aerodynamic characteristics of the wing are included in the geometry definition and that all unimportant aspects of the planform are neglected.

In general, definition of the chordwise geometries is not as simple a task as planform definition, but effective use of the fundamental case concept can reduce the labor involved. In particular, separation of the wing incidences into camber, twist, and control deflections can simplify the input preparation task. Camber is actually the parameter that presents the most confusion to a user of the program because the equivalent camber line is often subject to user judgment. Ideally, the basic camber distribution of a wing section would be fixed, and variations in camber due to device deflections would be superimposed on it [see figure (2.1)]. However, high-lift devices involving Fowler action do not deflect by simple rotation, but rather the motion is a combination of surface rotation and translation. Therefore, the section camber must either be explicitly defined for each device deflection as a separate fundamental case, or some mean basic camber line which approximates the surface camber over the full range of device deflections must be defined and then simple surface rotations added to it using the composite case feature of the program. The latter option offers the most versatility and requires the least user effort, but the former option can provide a more accurate representation of the section camber. A considerable amount of user

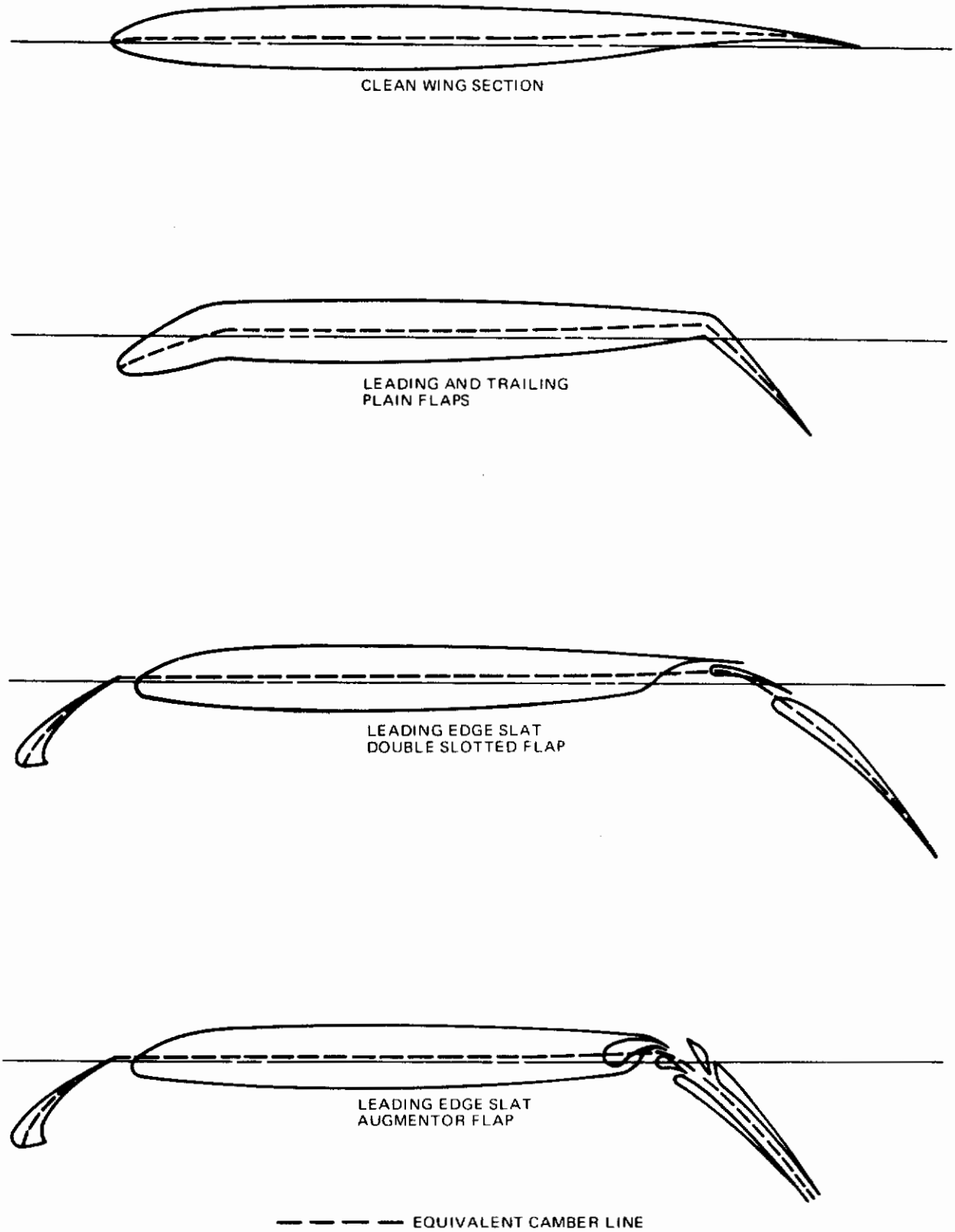

Figure (2.1). Representation of Wing Sections by Equivalent Camber

judgment may be required to fair a mean section camber line and then to determine a distribution of camber angles from the fairing. Figure (2.1) illustrates a typical section geometry and the procedure used to represent the mean camber line.

Specification of jet sheet parameters, including the sectional distribution of jet momentum $c_\mu(y)$ and the sectional distribution of jet deflection relative to the trailing edge $\delta_J(y)$, often presents considerable difficulty to the user. The distribution of trailing edge jet momentum for internally-ducted systems (IDF) can usually be determined from a knowledge of the geometry of the duct exit along the wing span and the gross thrust available. If the internally ducted jet is blown over a flap surface, however, losses in momentum due to scrubbing of the jet over the flap surface must be considered, and the jet turning ability of the flap must be determined. Unfortunately, there are no general analytical methods developed to predict the friction and turning losses over blown flaps, and usually available experimental results must be applied. For externally blown flap (EBF) systems, not only must the friction and turning losses in the jet be known, but a knowledge of the spreading of the jet by the mechanical flap system is required. Again, experimental data will provide the best estimate of jet parameters. A more complete discussion of the jet turning and spreading is presented in Section 7.1, including some basic experimental data which may aid in selecting jet sheet input data. There should be little confusion concerning the specification of vectored jets. However, it should be mentioned that if the exit duct of the vectored jet is not circular, a circular exit of area equivalent to the actual duct must be used.

The preceding discussion has attemped to provide some helpful suggestions for representing a wing with a jet sheet or vectored jets to aid in effective use of the program. There are also several comments which can be made concerning definition of the fuselage and empennage. As discussed in Volume I, the fuselage analysis in STAMP is approximate in nature and is intended primarily to calculate the pitching moment and yawing moment contributions of the fuselage rather than to provide a detailed fuselage surface pressure distribution. Thus, it is not recommended to use this method to determine the

fuselage shape required for an optimum pressure distribution, for example. Therefore, some of the less important aspects of the fuselage geometry (e.g., windshield shape) may be neglected, simplifying the input task. Geometry definition for the empennage analysis in STAMP generally is subject to the same set of guidelines as for the wing. However, in order to simplify input, the program allows only trapezoidal planform inputs. Therefore, such details as dorsal fins and other tail planform irregularities must be neglected.

The preceding discussion is intended to provide a set of general guidelines to be used in conjunction with the program usage instructions which are fully discussed in Volume II. Additional suggestions for program use and further engineering approximations are presented throughout the remainder of this volume, discussed in conjunction with the particular aerodynamic or stability and control coefficient or derivative to which they apply.

3.0 STATIC COEFFICIENTS AND DERIVATIVES

The aerodynamic forces and moments acting on an aircraft in steady flight must be accurately calculated before the performance, the static stability, and the dynamic stability and control characteristics of the aircraft can be predicted. The methods provided herein to calculate the three static force components (lift, drag, and side force) and the three static moment components (pitching, rolling, and yawing moments) are applicable to each of the STOL concepts under consideration; namely,

a. Internally ducted jet flap (IDF)

b. Externally blown jet flap (EBF)

c. Mechanical flap with vectored thrust (MFVT)

These methods are applicable for angles of attack where the flow is essentially attached to the wing such that potential flow theory can be applied. If the wing is stalled or partially stalled these methods are no longer adequate, and experimental data and/or empirical methods must be used. In addition, these analytical methods are applicable only for flight speeds where compressibility effects are negligible ($M_\infty < 0.5$) and must be modified if higher subsonic Mach numbers are desired.

The coordinate system in which the static aerodynamic forces and moments are calculated is shown in figure (3.1). The x-axis is aligned with the free-stream flow, and lift, drag, and side force are defined to be positive in the positive z, x, and y directions, respectively. Pitching moment is taken about the y-axis and is positive for a nose up moment; rolling moment is taken about the x-axis, positive for a right wing down moment; and yawing moment is taken about the z-axis, positive for a nose right moment.

In the following sections each of the static coefficients is discussed in detail, including the contribution of each aircraft component. Variations with angle of attack, flap angle, leading edge device angle, etc. are discussed, in and out of ground effect, for each of the STOL concepts under consideration.

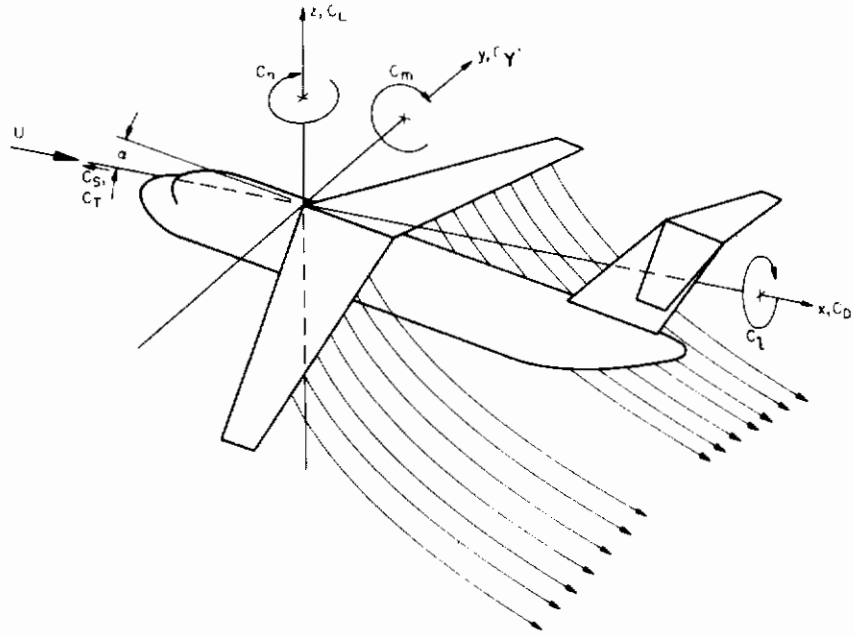

Figure (3.1). Reference Coordinate System for Aerodynamic Coefficients

3.1 Longitudinal Static Coefficients and Derivatives

3.1.1 Lift

For STOL aircraft lift is derived both from aerodynamic forces on the airframe and directly from the component of the propulsion system reaction force normal to the flight path, and can be expressed as

$$C_L = C_{L_\Gamma} + C_{L_J} \tag{3.1}$$

where C_{L_Γ} is the aerodynamic lift due to wing circulation and C_{L_J} is the jet reaction lift. Both terms in equation (3.1) are calculated directly by the program within the context of linear theory, but modification of the

predicted C_{L_Γ} contribution is necessary in order to account for wing thickness and viscous effects.

It is necessary to discuss first the sectional wing lift characteristics in order to account for those effects not considered by the program, and then to discuss the total lift contribution of the wing, the jet sheet or vectored jets, the fuselage, and the empennage in order to arrive at the total aircraft lift.

3.1.1.1 Sectional Wing Lift

The program calculates the sectional wing circulation lift (c_{ℓ_Γ}) and, for jet-wings, the sectional wing reaction lift (c_{ℓ_μ}) for a zero thickness wing in inviscid flow. For conventional wings or jet-wings, the program prints the sectional lift variation with angle of attack for each composite case in the form

$$c_{\ell_\Gamma}(y) = c_{\ell_{\Gamma_o}}(y) + c_{\ell_{\Gamma_\alpha}}(y)\alpha \qquad \text{(Free Air)} \qquad (3.2a)$$

$$c_{\ell_\Gamma}(y) = c_{\ell_{\Gamma_o}}(y) + c_{\ell_{\Gamma_\alpha}}(y)\alpha + c_{\ell_{\Gamma_{\alpha^2}}}(y)\alpha^2 \qquad \text{(Ground Effect)} \qquad (3.2b)$$

$$c_{\ell_\mu}(y) = c_{\ell_{\mu_o}}(y) + c_{\ell_{\mu_\alpha}}(y)\alpha \qquad \text{(Free Air or Ground Effect)} \qquad (3.2c)$$

For wings with vectored jets these equations are not applicable because the interference between the wing and vectored jets is a nonlinear function of angle of attack. For this case the program explicitly calculates the sectional circulation lift at specific angles of attack, in the form

$$c_{\ell_\Gamma}(y) = c_{\ell_\Gamma}(y)\Big|_\alpha \qquad (\alpha = 0,\ 5,\ 10,\ 15,\ 20 \text{ degrees}) \qquad (3.2d)$$

Approximate theoretical methods and empiricism must be used to modify equations (3.2) to account for those effects not considered in the EVD lifting surface theory. The effects considered of primary importance are section thickness, the effects of the viscous boundary layer, and the effects of separation

of this boundary layer forward of the airfoil trailing edge. First, unblown wing sections will be considered, relying primarily on the semi-empirical methods presented in Datcom (reference 3). Then blown wing sections will be considered.

Unblown Wing Sections

Lift Curve Slope. The lift curve slope c_{ℓ_α} calculated by the computer program [equation (3.2a)] can be corrected approximately for thickness and viscous effects using the equation

$$c_{\ell_\alpha} = 1.05\ K_1 K_2\ c_{\ell_\alpha}\Big|_{EVD} \tag{3.3}$$

where

K_1 is the ratio of the theoretical c_{ℓ_α} of a thick section to that of a flat plate ($c_{\ell_\alpha} = 2\pi$ per radian) calculated by the Joukowski transformation and presented in figure (3.2a).

K_2 is an empirical correction factor to account for the development of the boundary layer near the airfoil trailing edge. It is related to the Reynolds number with transition fixed at the airfoil leading edge, and the trailing edge angle ϕ_{TE} is defined as the angle between straight lines passing through points at 90 and 99 percent of the chord on the upper and lower airfoil surfaces. K_2 is presented in figure (3.2b).

$c_{\ell_\alpha}\Big|_{EVD}$ is the program output result.

The factor 1.05 of equation (3.3) is an empirical correction factor based on a large body of test data (reference Datcom, section 4.1.1.2).

Thin airfoil theory shows that the lift curve slope does not change with camber or flap deflection. Experiment verifies that this is true for angles of attack and flap deflections where the flow remains attached to the airfoil. Even for high flap angles where some flow separation is unavoidable, there are not appreciable losses in c_{ℓ_α}. However, as stall is approached, the lift

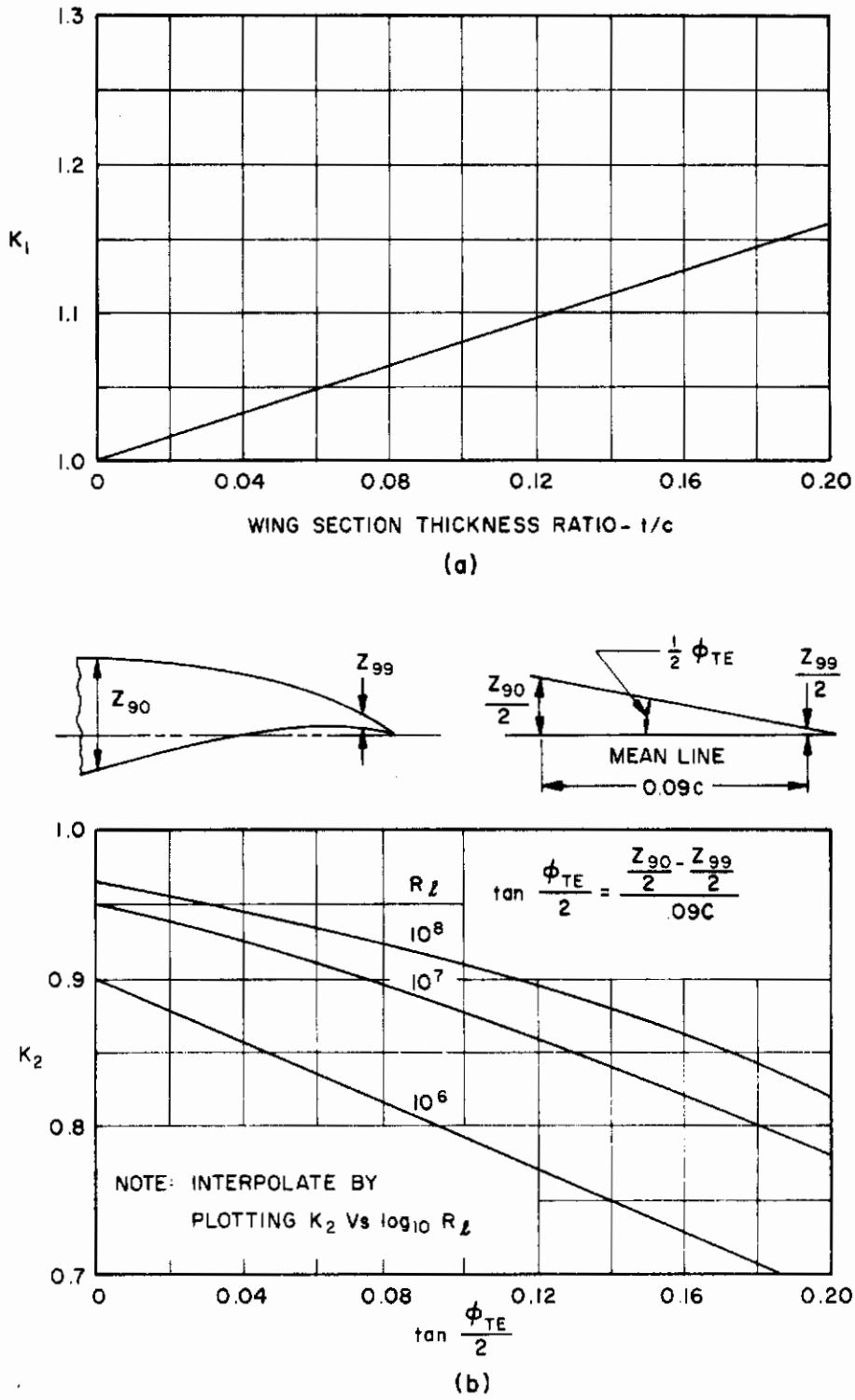

Figure (3.2). (a) Thickness Correction to c_{ℓ_α} for Section Thickness;
(b) Empirical Correction to c_{ℓ_α} for Boundary Layer Effects.

curve slope will become smaller. Near stall experimental data is required to determine c_{ℓ_α}.

Lift at Zero Angle of Attack. The lift at zero angle of attack, c_{ℓ_0}, calculated by the program [equations (3.2a)] is more difficult to modify for thickness and viscous effects because of the different type of empirical relations that are required for different types of flap geometries. For unflapped sections, Datcom offers only tabulated airfoil experimental data for standard section shapes. Hence the most accurate way to correct the program result would be to know both the experimental value of the two-dimensional thick airfoil c_{ℓ_0} and the thin airfoil theory c_{ℓ_0}, and then calculate the corrected sectional lift from

$$c_{\ell_0} = \left(\frac{c_{\ell_0}\Big|_{\text{experiment}}}{c_{\ell_0}\Big|_{\text{thin}}} \right) c_{\ell_0}\Big|_{\text{EVD}} \tag{3.4}$$

In lieu of experimental data, a correction that is often applied to c_{ℓ_0} is

$$c_{\ell_0} = (1 + 0.8t/c)\, c_{\ell_0}\Big|_{\text{EVD}} \tag{3.5}$$

where t/c is the average thickness-chord ratio based on the extended chord and for some section types a constant other than 0.8 may be applicable.

Datcom does present several empirical methods to calculate the change in sectional c_{ℓ_0} due to flap deflection. These methods have been modified here so that they can be used to correct program calculated sectional lift.

Plain Flaps. For plain flaps the program calculated c_{ℓ_0} can be corrected for thickness and viscous effects using the empirical relation

$$c_{\ell_0} = K_3 K_4 K_5\, c_{\ell_0}\Big|_{\text{EVD}} \tag{3.6}$$

where

K_3 is the ratio of the theoretical c_{ℓ_0} of a thick flapped section to that of a thin airfoil with flap, presented in figure (3.3a).

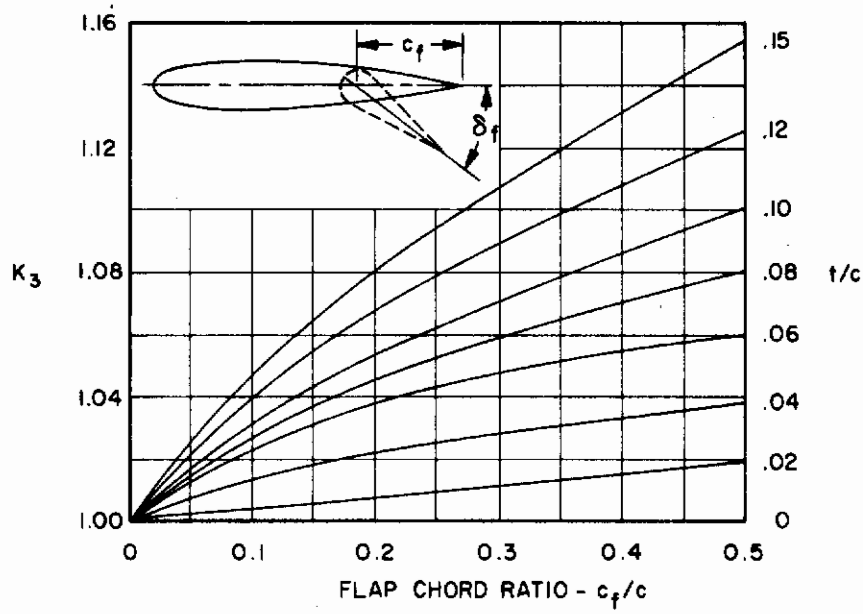

(a)

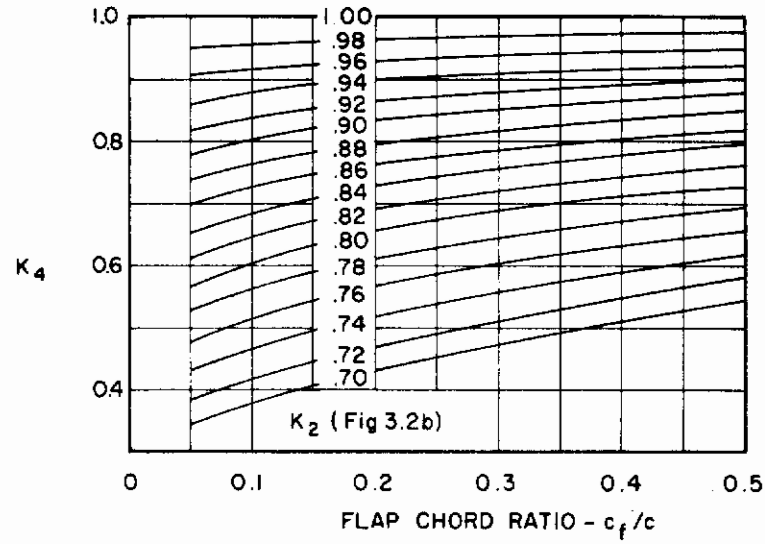

(b)

Figure (3.3). (a) Theoretical Correction to c_{ℓ_0} for Plain Flaps for Section Thickness; (b) Empirical Correction to c_{ℓ_0} for Plain Flaps for Boundary Layer Effects.

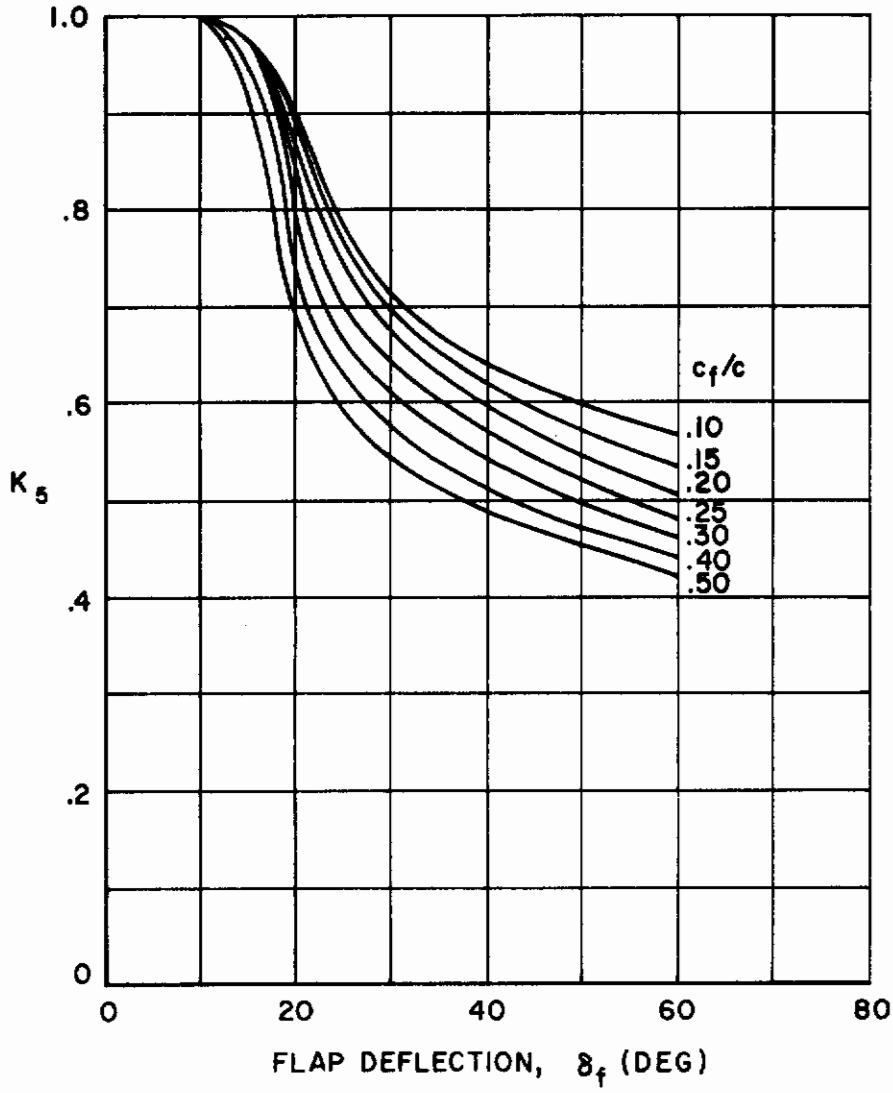

Figure (3.3c). Empirical Correction Factor for Plain Flap Effectiveness

K_4 is an empirical correction factor to account for viscous effects and is a function of the sectional lift curve slope factor K_2 in figure (3.2b). K_4 is plotted in figure (3.3b).

K_5 is an empirical correction factor for plain flap lift effectiveness. K_5 is plotted in figure (3.2c).

$c_{\ell_o}\Big|_{EVD}$ is the program output result.

Single-Slotted Flaps. For single-slotted type flaps the program calculated c_{ℓ_o} can be corrected for thickness and viscous effects using the empirical relation

$$c_{\ell_o} = K_6 K_3 \, c_{\ell_o}\Big|_{EVD} \tag{3.7}$$

where

K_6 is an empirical correction factor to account for viscous effects and is a function of the flap deflection and flap chord ratio and is plotted in figure (3.4).

K_3 is the ratio of the theoretical c_{ℓ_o} of a thick flapped section to that of a thin airfoil with flap, plotted in figure (3.3a).

$c_{\ell_o}\Big|_{EVD}$ is the program output result.

Double-Slotted Flaps. For double-slotted flaps the program calculated c_{ℓ_o} can be corrected for thickness and viscous effects using the empirical relation

$$c_{\ell_o} = \left[(K_6 K_3)_{FWD} + 0.72(K_6 K_3)_{AFT}\right] c_{\ell_o}\Big|_{EVD} \tag{3.8}$$

where the K_6 and K_3 correction factors are the same as those described above for the single-slotted flap, the constant 0.72 is an empirically determined factor which accounts for the presence of the forward flap, and

$(K_6 K_3)_{FWD}$ indicates that these quantities are to be taken from figures (3.3a) and(3.4) using c_1/c'_a and δ_{f_1} .

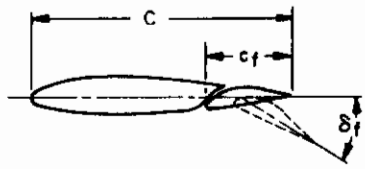

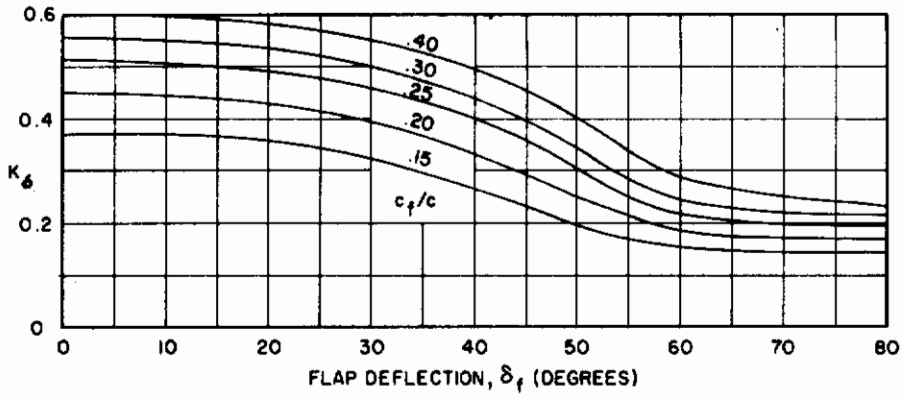

Figure (3.4). Empirical Correction to c_{ℓ_0} for Single-Slotted Flaps for Boundary Layer Effects

$(K_6K_3)_{AFT}$ indicates that these quantities are to be taken from figure (3.3a) and (3.4) using c_2/c' and δ_{f_2} where these geometric quantities are defined in figure (3.5).

Leading-Edge Devices. The empirical methods in Datcom for treating leading-edge flaps and slats are considered to be inadequate for correcting program calculated lift due to leading-edge device deflection, and it is recommended that the program result be used directly.

Blown Wing Sections

The empirical methods described above are based largely on extensive test data and simple two-dimensional airfoil theory for unblown sections. Clearly, they are not applicable to jet-wings because of the boundary-layer control effect of the jet flap which prevents separation over a wide range of angle of attack and flap deflection. In addition, boundary-layer growth over the aft portion of the airfoil is prevented by the favorable pressure gradient due to the jet flap, and in fact the boundary-layer thickness can actually

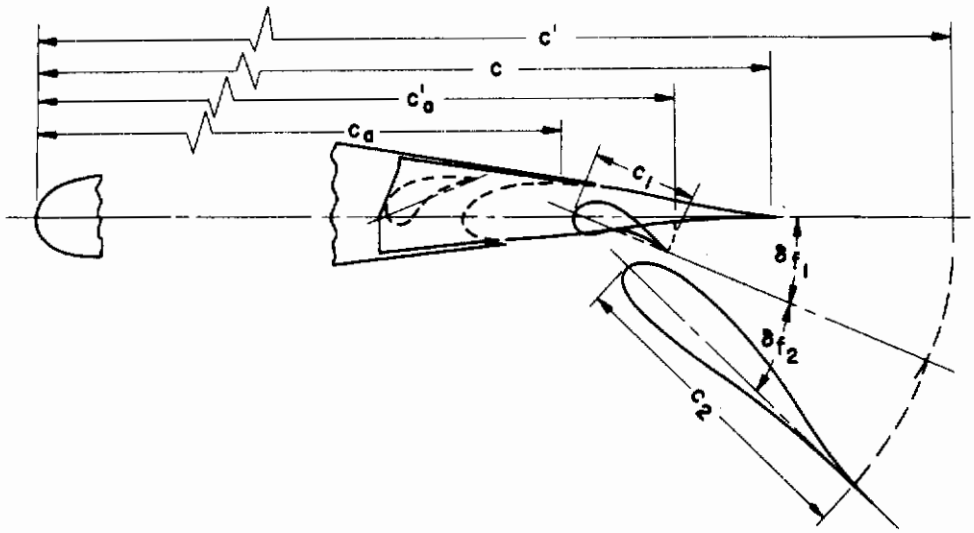

c wing chord (flap in neutral position).

c_a distance from section leading edge to slot lip.

c'_a extended wing chord due to forward-flap extension. In measuring c'_a, first rotate the forward flap from its deflected position about the point of intersection of the forward-flap chord and the chord of the airfoil section, until the two chords coincide.

c' extended wing chord due to the double-slotted flaps. In measuring c', the aft flap is first rotated from its deflected position about the point of intersection of the aft-flap chord and the chord of the forward flap, until the two chords coincide. Then both flaps are rotated from the deflection of the forward flap about the point of intersection of the forward-flap chord with the wing chord, until these two coincide.

δ_{f_1} optimum flap deflection of the forward flap.

δ_{f_2} optimum flap deflection of the aft flap.

c_1 forward-flap chord.

c_2 aft-flap chord.

Figure (3.5). Notation Applied to Double-Slotted Flaps

decrease near the trailing edge due to the presence of the jet. Hence for blown wing sections, the primary effect not considered by the program that should be applied to the calculated result is due to airfoil thickness. Spence (reference 9) has assumed that airfoil thickness for blown sections can be treated in a manner analogous to that used for conventional sections, increasing the circulation component of the lift by

$$c_{\ell_\Gamma} = [1 + (K)t/c]\, c_{\ell_\Gamma}\Big|_{EVD} \tag{3.9}$$

where equation (3.9) applies to both $c_{\ell_{\Gamma_0}}$ and $c_{\ell_{\Gamma_\alpha}}$ in equation (3.2a). Here t/c is the section thickness-chord ratio, $c_{\ell_\Gamma}|_{EVD}$ is the program calculated circulation lift, and K is a factor which depends on the section thickness distribution. For an elliptic section K is 1.0, while for sections with sharp trailing edges the value of 0.8 is a better approximation (Kuchemann, reference 10). Spence has compared his well-known linearized two-dimensional theory with the experimental data of Dimmock (reference 11) for a 12.5-percent-thick elliptical section jet-flap airfoil by removing thickness effects from the experimental data using equation (3.9) with K equal to 1.0. His results, presented in figure (3.6), indicate that the thickness correction alone is quite reasonable for blown sections.

Another comparison of the validity of equation (3.9) is presented in table (3.1). Tabulated is the lift for a NACA 0012 section calculated by the Douglas Two-Dimensional Non-Linear Jet-Flap Potential Flow Method (reference 12) and the lift for a flat plate airfoil calculated by a linearized theory, multiplied by the $(1 + 0.8t/c)$ correction factor.

Table (3.1). Thickness Correction for NACA 0012 Airfoil

α(deg)	$c_{\ell_{thick\ nonlinear}}$	$c_{\ell_{thin\ linear}}$	$(1 + 0.8t/c)c_{\ell_{thin}}$	Δ%
0	0.59813	0.54357	0.59575	-0.4
5	1.19148	1.08714	1.19151	0
10	1.77447	1.63070	1.78725	+0.7

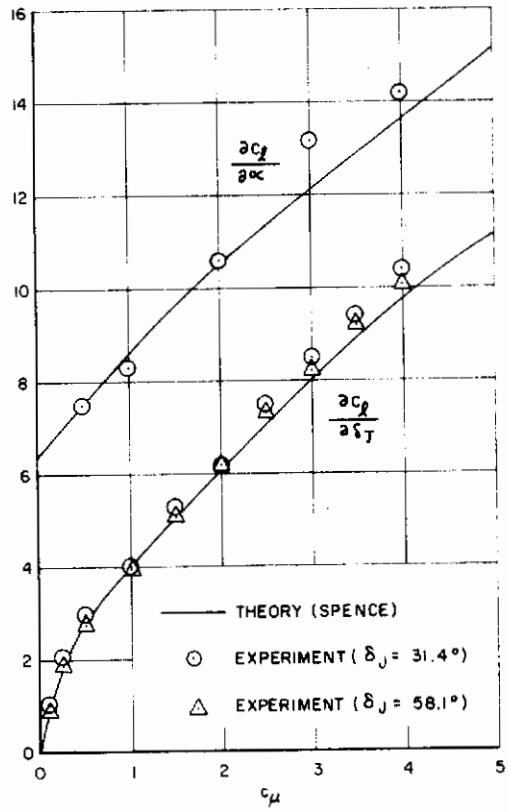

Figure (3.6). Comparison Between the Two-Dimensional Theoretical Results of Spence and the Experimental Data of Dimmock Corrected for Thickness Effects.

Since these data are for a fully-attached flow, which is essentially what is obtained for blown sections, they are indicative of the validity of equation (3.9). The displacement effects of the viscous boundary layer are not included in this correction for blown sections, but, as previously mentioned, this effect should be small.

Ground Effect

To this point modification of the program calculated sectional lift has been concerned only with the terms in equation (3.2a), the free-air case. These modifications cannot be arbitrarily applied to the sectional lift in ground effect, however. First of all, in severe cases ground effect can appreciably alter the section pressure distribution to the extent that

premature flow separation might occur. Secondly, while thickness has been shown to increase sectional lift in inviscid flow in free air relative to the thin airfoil, in ground effect thickness has just the opposite effect. Therefore, it is clear that the theoretical and empirical corrections presented are not applicable to lift in ground effect.

Corrections to the ground effect solution are considered to be beyond the scope of this work. As discussed in Volume I, considerable work is required to more adequately solve the ground-effect problem. The method developed in Volume I, however, is considered to be a first step in such a solution and is intended primarily to provide the relative magnitude of the ground effect compared to the free-air solution. Within this context, the magnitude of the change of lift due to ground effect should be expressed as

$$\frac{\Delta c_{\ell_{ground}}}{c_{\ell_{free\ air}}} = \frac{c_{\ell_{ground}} - c_{\ell_{free\ air}}}{c_{\ell_{free\ air}}} \tag{3.10}$$

where only uncorrected program results are used in equation (3.10).

Mechanical Flaps with Vectored Thrust

Corrections should be applied to the program calculated sectional lifts for mechanical flap systems with vectored thrust [equation (3.2c)] in the same manner as for unblown sections because there is no boundary-layer control effect for this type of system as there is for jet-flap airfoils.

3.1.1.2 Total Wing Lift

The EVD segment of STAMP integrates the sectional lift coefficients, equations (3.2), along the span of the wing to calculate total wing lift by approximating the integral

$$C_L = \frac{1}{S}\int_{-b/2}^{b/2} c(y)\, c_{\ell_\Gamma}(y)dy + C_{L_J} \tag{3.11}$$

by a finite summation, treating $c_{\ell_\Gamma}(y)$ and $c(y)$ as constant over each spanwise division. In order to correct the total wing lift calculated by the program for thickness and viscous effects, the corrected sectional values

obtained in Section 3.1.1.1 must be reintegrated using the equation

$$C_L = \frac{1}{S} \sum c(y) c_{\ell_\Gamma}(y) \Big|_{\text{corrected}} \Delta y + C_{L_J} \tag{3.12}$$

where the summation is taken over the span of the wing.

A considerable simplification to the thickness and viscous corrections to total wing lift, which has proven valuable for preliminary design purposes, involves applying a single correction factor to the program calculated total wing lift. The approximation employed is to assume that for unblown wing sections the thickness correction is cancelled by the viscous correction, leaving the program-calculated c_{ℓ_0} and c_{ℓ_α} values; and that for blown wing sections the thickness correction of $[1 + (K)t/c]$ is applied to $c_{\ell_{\Gamma_0}}$ and $c_{\ell_{\Gamma_\alpha}}$. Finally, it is assumed that the portion of circulation lift due to blown sections is directly proportional to the wing area of the blown sections, so that the total corrected wing lift can be expressed as

$$C_{L_\Gamma} = \left[1 + (K)\left(\frac{S_B}{S}\right)t/c\right] C_{L_\Gamma}\Big|_{EVD} \tag{3.13}$$

where S_B is the blown wing area, illustrated in figure (3.7). It should be noted that the average values of K and t/c (see page 19) for the blown section of the wing should be used in equation (3.13). Obviously, this approximation will break down as angle of attack or flap deflection is increased and viscous effects including boundary-layer separation become significant.

The information presented to this point in this section has been concerned with correction of program calculated total lift data. With a working knowledge of program use (Volume II) and the empirical corrections presented here, the reader has the capability to accurately calculate the total wing lift for a STOL aircraft employing the high-lift concepts being considered. In addition, for zero jet momentum these methods reduce to conventional aircraft (CTOL) analysis methods. In the following paragraphs techniques for increasing program flexibility are discussed, primarily to indicate methods of program use that will provide the most useful assortment of wing lift data.

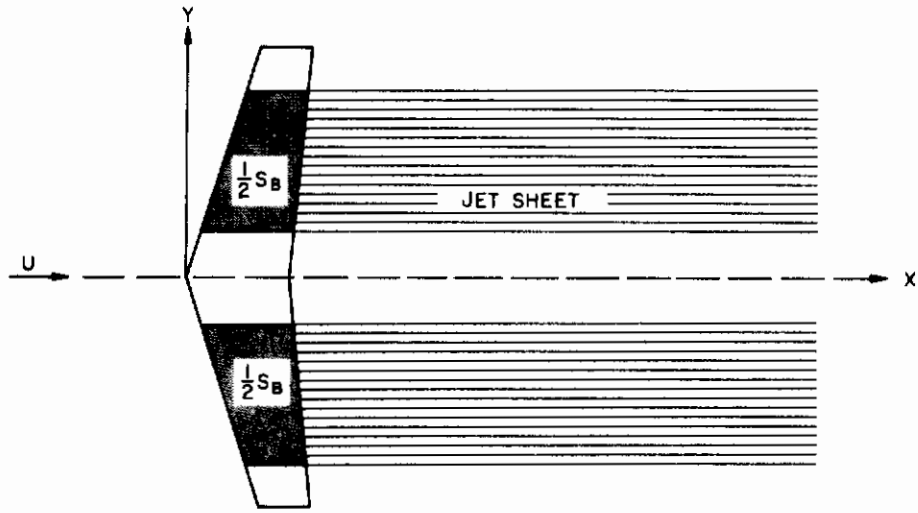

Figure (3.7). Illustration of Blown Wing Area

Calculation of Wing Lift from Fundamental Case Derivatives

It is often desirable and convenient to express the total wing lift in terms of derivatives which explicitly show the effects of angle of attack, flap deflection, slat deflection, jet sheet deflection, etc. This is particularly easy to do using the EVD method because of the linear nature of the approach and the fundamental case structure of the program. For mechanical flap systems with vectored thrust it is not possible to calculate such derivatives because of the nonlinear interference between the vectored jets and wing. In addition, for jet-wings it is not possible to explicitly calculate derivatives for the change in lift due to a change in jet momentum because of the nonlinear behavior of the solution with C_J.

For a wing or jet-wing in free air, the lift can be expressed within the context of linear theory as

$$C_L = C_{L_o} + \frac{\partial C_L}{\partial \alpha}\alpha + \frac{\partial C_L}{\partial \delta_f}\delta_f + \frac{\partial C_L}{\partial \delta_s}\delta_s + \frac{\partial C_L}{\partial \delta_J}\delta_J + \frac{\partial C_L}{\partial \delta_{sp}}\delta_{sp} \qquad (3.14)$$

These terms, all functions of C_J, represent the basic lift, the lift curve slope, and the change in lift due to deflection of flap, slat, jet sheet, and spoiler, respectively. Each of these terms can be directly calculated from the program except the spoiler term, for which resort to empiricism is required. The procedure for calculating each one of these terms is presented below.

An expression similar to equation (3.14) for a wing or jet-wing in ground effect could be formulated based on the results of the EVD method, but because of the important influence of the image jet-wing employed in the solution (see Volume I), second-order derivatives (e.g., $\partial^2 C_L/\partial\alpha^2$, $\partial^2 C_L/\partial\alpha\partial\delta_f$, $\partial^2 C_L/\partial\delta_f^2$, etc.) would be required. The complexity of the resulting expression precludes its usefulness, and hence only the free air case is considered here.

Basic Lift — C_{L_o}

The basic wing lift due to camber and twist can be calculated by combining the inputs for these parameters into a single fundamental case with all other deflections set to zero. Or, if desired, camber and twist effects can be separated by specifying one fundamental case for camber alone and one for twist alone. The program calculated C_{L_o} should be corrected for thickness and viscous effects using equation (3.12) or (3.13).

Lift Curve Slope — $(\partial C_L/\partial\alpha) \equiv C_{L_\alpha}$

The slope of the lift curve versus angle of attack is fundamentally important and is automatically calculated by the program for any wing configuration (except antisymmetric wings). The program output is the lift curve slope per degree of angle of attack and should be corrected for thickness and viscous effects using either equation (3.12) or (3.13).

Lift Due to Flap Deflection — $(\partial C_L/\partial\delta_f) \equiv C_{L_{\delta_f}}$

The change in wing lift due to a unit deflection of a trailing edge flap can be easily calculated by defining a fundamental case with all surface deflections zero except for the flap surface, which should be input with a deflection angle of one degree. The resulting program output for that fundamental case is simply $\partial C_L/\partial\delta_f$ per degree of flap deflection, which

should be corrected for wing thickness and viscous effects using equation (3.12) or (3.13). If there is more than one flap, then each can be treated in this fashion by defining a new fundamental case for each flap. For multi-segmented flaps, deflection of each segment can be treated as a separate fundamental case, or the composite deflection can be input corresponding to the relative deflection of each segment. Various methods of treating flap deflections as fundamental cases are illustrated in figure (3.8).

Lift Due to Slat Deflection - $(\partial C_L/\partial \delta_S) \equiv C_{L_{\delta_S}}$

Changes in lift due to the deflection of a leading-edge slat or leading-edge flap are treated in a manner analogous to that for a trailing-edge flap. It should be noted that gaps or surface overlap cannot be strictly considered in this method. This is not a serious restriction for trailing-edge flaps, but it can impose serious restrictions on the geometric representation of a slat because of the important mutual interference effects of the slat and main wing. In addition, representation of a slat by a mean camber line in thin airfoil theory is an approximation which cannot be expected to predict accurately the loading distribution at the leading edge. However, the proposed treatment of a slat by the EVD method is expected to give a qualitative prediction of the lift due to slat deflection for attached flow.

Lift Due to Jet Deflection - $(\partial C_L/\partial \delta_J) \equiv C_{L_{\delta_J}}$

The effect on lift of jet sheet deflection relative to the wing trailing edge is calculated by defining a fundamental case with all wing surface deflections zero and the jet sheet deflected downward one degree. Even though all wing surface deflections are zero, the jet sheet will induce a loading on the wing (C_{L_I}), and this value should be corrected for wing thickness and viscous effects using either equation (3.12) or (3.13). Multiple jet sheets are treated in a manner similar to multiple flaps.

Change in Lift with Jet Momentum - $(\partial C_L/\partial C_J)$

The term $\partial C_L/\partial C_J$ does not appear in equation (3.14) because the effect of a change in jet momentum coefficient cannot be separated from the surface deflections. Each of the coefficients and derivatives discussed to this point

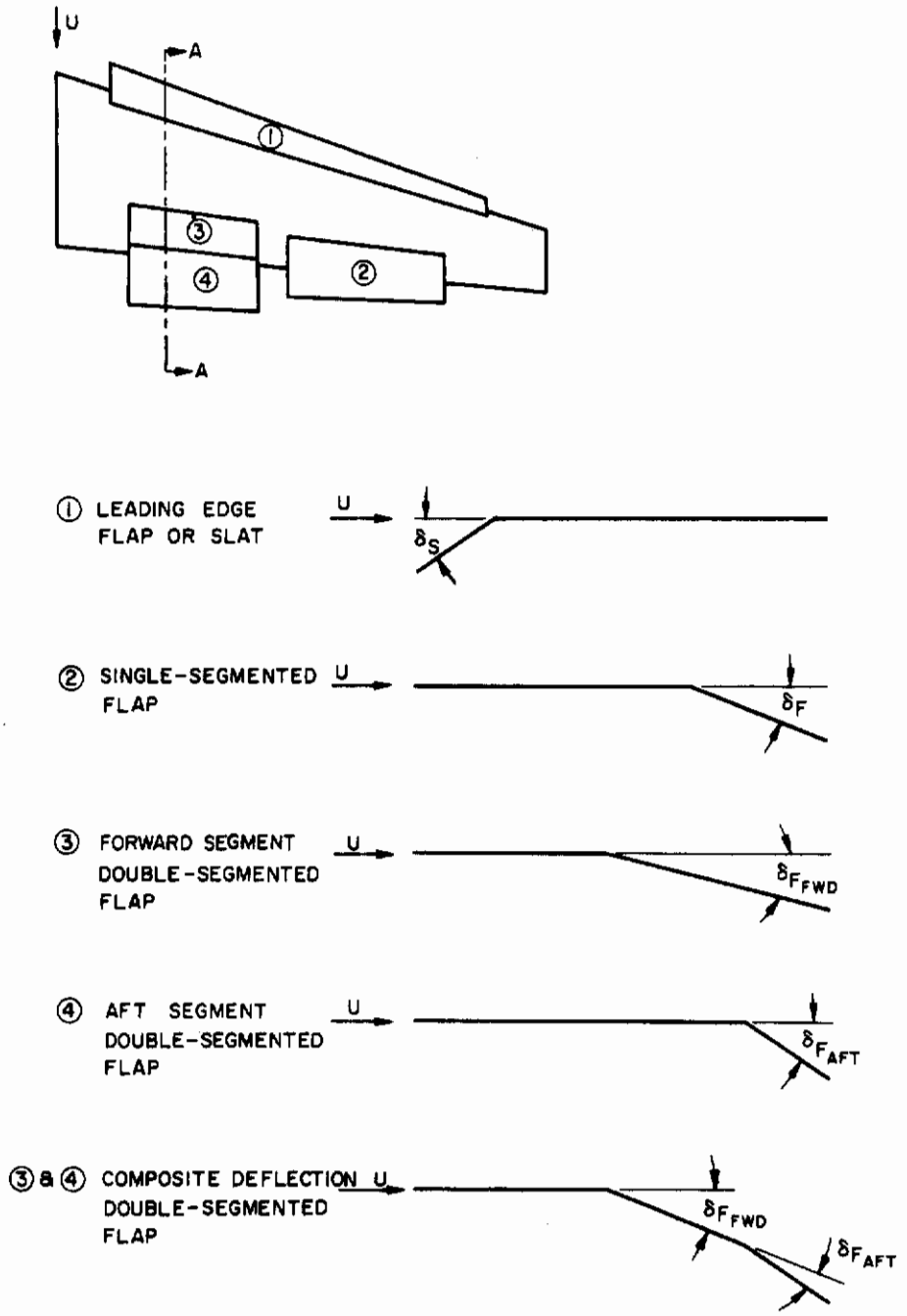

Figure (3.8). Various Methods of Treating Flap Deflections as Fundamental Cases

vary nonlinearly with C_J. Hence, each of the terms must be expressed as a function of C_J, as

$$\begin{aligned} C_{L_o} &= C_{L_o}(C_J) \\ C_{L_\alpha} &= C_{L_\alpha}(C_J) \\ C_{L_{\delta_f}} &= C_{L_{\delta_f}}(C_J) \\ C_{L_{\delta_s}} &= C_{L_{\delta_s}}(C_J) \\ C_{L_{\delta_J}} &= C_{L_{\delta_J}}(C_J) \end{aligned} \tag{3.15}$$

There is no simple means of determining this functional relationship, except for special cases such as the Maskell and Spence (reference 13) solution for an elliptically loaded jet-wing. To determine the functional relationships in equations (3.15) for an arbitrary jet-wing, it is necessary to run the EVD segment of the program over a range of jet momentum coefficients and then either graphically or numerically curve fit the data.

Change in Lift Due to Spoiler Deflection — $\partial C_L/\partial \delta_{sp}$

Deflection of a spoiler causes severe flow separation aft of the device, and consequently viscous effects become quite important, rendering the EVD method not applicable. Various empirical methods to estimate the effect of spoiler deflection on sectional lift are presented in Datcom (reference 3, Section 6.1), but these methods are based on limited experimental data and do not in general apply to arbitrary sections, particularly where blowing is present. At this point only experiment can provide a reasonable estimate of spoiler effectiveness.

Calculation of Wing Lift Using Composite Cases

The fundamental case derivative concept previously discussed can be useful as a preliminary design method to examine the relative merits of various high-lift configurations rapidly. However, for the analysis of complete wing configurations, it will usually be more convenient to use the composite case capability of the program to calculate the total wing lift. The composite case capability of the program evaluates equation (3.14) for

the input values of δ_f, δ_s, δ_J, and C_J. For each composite case input, the program prints the total wing lift as a function of angle of attack, in the form:

$$C_L = C_{L_o} + \frac{\partial C_L}{\partial \alpha}\alpha \qquad \text{(Free Air)} \qquad \left.\begin{matrix} \\ \\ \end{matrix}\right\} \text{(Jet-Wing)} \qquad (3.16a)$$

$$C_L = C_{L_o} + \frac{\partial C_L}{\partial \alpha}\alpha + \frac{\partial^2 C_L}{\partial \alpha^2}\alpha^2 \qquad \text{(Ground Effect)} \qquad (3.16b)$$

$$C_L = C_L(\alpha) \qquad (\alpha = 0, 5, 10, 15, 20 \text{ degrees}) \qquad \text{(MFVT)} \qquad (3.16c)$$

The circulation component of each term in equations (3.16) should be corrected for wing thickness effects using the methods described in Section 3.1.1.1. By using composite cases as such, it is not necessary to explicitly know the value of the lift derivatives in equation (3.14).

3.1.1.3 Empennage Lift — Tailplane Downwash

The lift contribution of the horizontal tail depends not only on the geometric characteristics of the tail but also on the downwash field induced on the tail by the jet-wing high-lift system. Tail lift is calculated by the program both for the tail by itself (isolated tail analysis) and for the tail in the induced flow field of the jet-wing (interference tail analysis). For the isolated tail analysis, the program calculated horizontal tail lift can be expressed in the form

$$\left(C_{L_H}\right)_{Isol} = C_{L_{o_H}} + \frac{\partial C_{L_H}}{\partial \alpha}\alpha \qquad (3.17)$$

where the first term is the basic lift level of the horizontal tail and includes the effects of any input surface deflections, such as tail camber, elevator deflection, and tail incidence (other than angle of attack); and the second term is the lift curve slope of the horizontal tail. Equation (3.17) should not be confused with the actual lift curve of the installed horizontal tail given by equation (3.18). The installed tail lift curve is non-linear and is calculated in the interference tail analysis. However, the term $(\partial C_{L_H}/\partial \alpha)_{ISOL}$ could be used, for example, to modify the actual lift curve for, say, a change in horizontal tail incidence.

For the interference tail analysis, the program calculated horizontal tail lift is expressed as

$$\left(C_{L_H}\right)_{\text{Installed}} = C_{L_H}(\alpha) \quad (\alpha = 0,\ 5,\ 10,\ 15,\ 20 \text{ degrees}) \qquad (3.18)$$

For other angles of attack within this range, either graphical or numerical interpolation of equation (3.18) should be used. As fully discussed in Volume I, tail lift as expressed in equation (3.18) is calculated by determining the induced flow field due to the wing and jet sheet or vectored jets and treating these perturbations as induced camber. Since the flow field velocities induced on the tail by the wing are a nonlinear function of the wing lift, it is necessary to modify the wing circulation lift to account for thickness and viscous effects before the flow field velocities are calculated. Hence, there is a provision in the program to input the mean wing t/c to approximately account for these effects.

The program output includes a summary of the induced flow field velocities on the horizontal tail, but it is often desirable in an aircraft aerodynamic analysis to know the mean tailplane downwash as a function of wing angle of attack. This can be calculated from equations (3.17) and (3.18) to be

$$\varepsilon_{\text{mean}}(\alpha) = \alpha - \frac{C_{L_H}(\alpha) - C_{L_{O_H}}}{\partial C_{L_H}/\partial\alpha} \qquad (3.20)$$

This quantity is of great importance in both static and dynamic stability and control work and will be more fully discussed in later sections.

3.1.1.4 Fuselage Lift

For the type of configurations typical of STOL transport aircraft, characterized by large wing span to body diameter ratios, the fuselage lift can be essentially regarded as arising from two separate effects. One is the carryover of lift from the wing onto the fuselage. This effect is accounted for in the present method by extending the wing planform to the aircraft plane of symmetry. Hence this portion of the fuselage contribution to lift is an integral part of the total wing lift calculated in equation (3.11). Lift on the fuselage also arises from nonpotential flow effects which generally occur on the fuselage afterbody in the form of boundary-layer separation and

vortex shedding. Flow visualization studies for typical upswept transport aircraft fuselages (references 14 and 15) indicate that severe vortex shedding often can occur, even for angles of attack as small as 10 degrees. A typical vortex shedding pattern for such a fuselage is presented in figure (3.9).

No account for boundary-layer separation or vortex shedding from the fuselage afterbody is included in the analytical methods presented here or in the computer programs. Approximate methods to calculate the lift due to these effects are presented in Datcom (Section 4.2.1.2), based primarily on the work of Munk and Allen and Perkins. This method is restricted to bodies of revolution. The expression for fuselage lift given is

$$C_{L_F} = \frac{2(K_M)A_o}{(57.3)S}\alpha + \frac{2}{(57.3)^2 S}\alpha^2 \int_{x_o}^{x_E} \eta r c_{d_c} dx \quad (\alpha \text{ in degrees}) \quad (3.21)$$

where

S is the reference area

K_M is the familiar apparent mass factor for spheroids from exact potential flow theory, plotted in figure (3.10a).

A_o is the body cross-sectional area at x_o.

x_o is the body station where the flow ceases to be potential. This is a function of x_1, the body station where the cross-sectional area gradient, $dA(x)/dx$, first reaches its maximum negative value. A plot relating x_o and x_1 is presented in figure (3.10b).

c_{d_c} is the experimental steady-state cross-flow drag of a circular cylinder of infinite length given in figure (3.10c) and equal to 1.20 in incompressible flow.

η is the ratio of drag on a finite cylinder to the drag of an infinite cylinder, plotted in figure (3.10d).

r is the local body radius.

x_E is the body tail station.

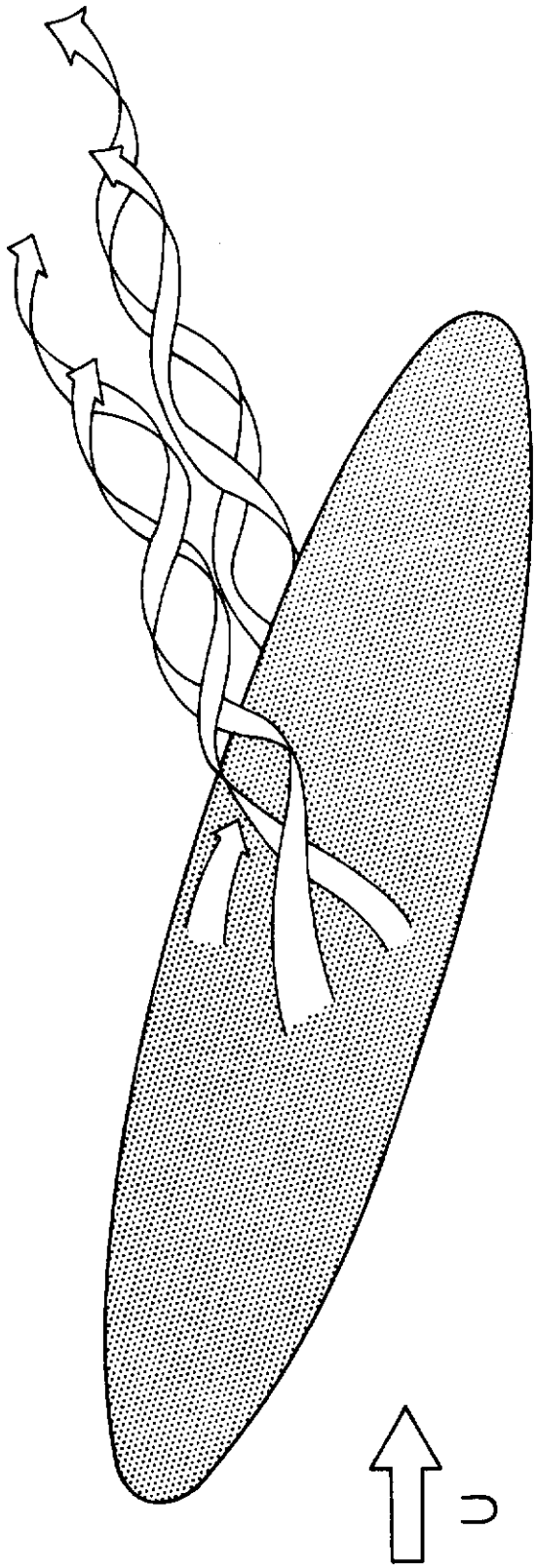

Figure (3.9). Illustration of Typical Vortex Shedding Pattern from Fuselage Afterbody

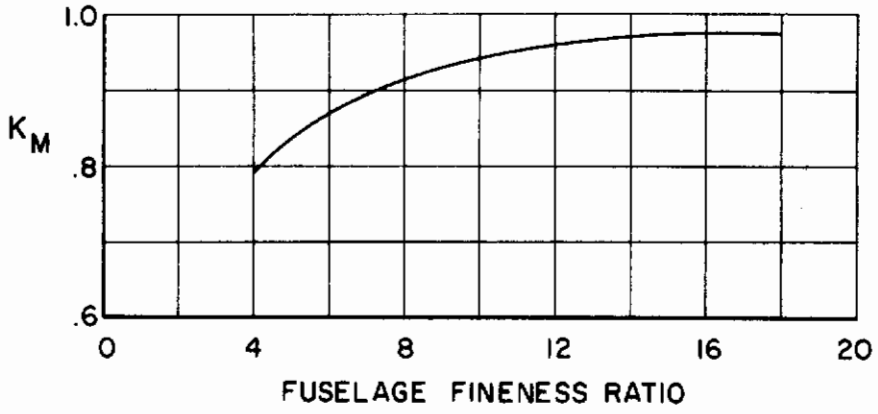

(a)

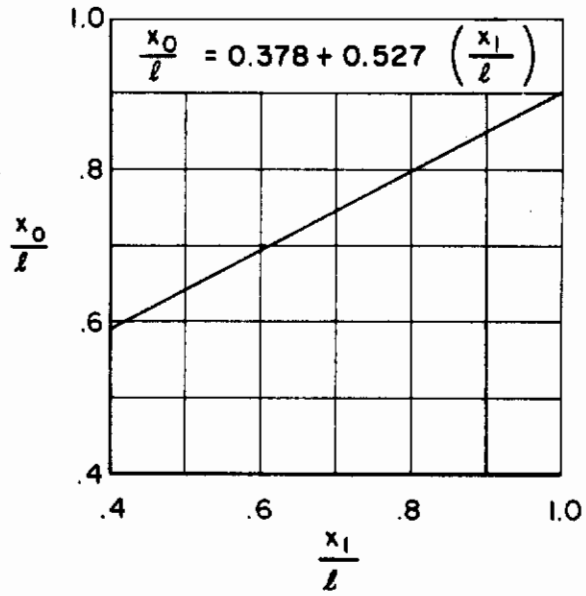

(b)

Figure (3.10). (a) Apparent Mass Factor for Spheroids;
(b) Body Station Where Flow Becomes Non-Potential.

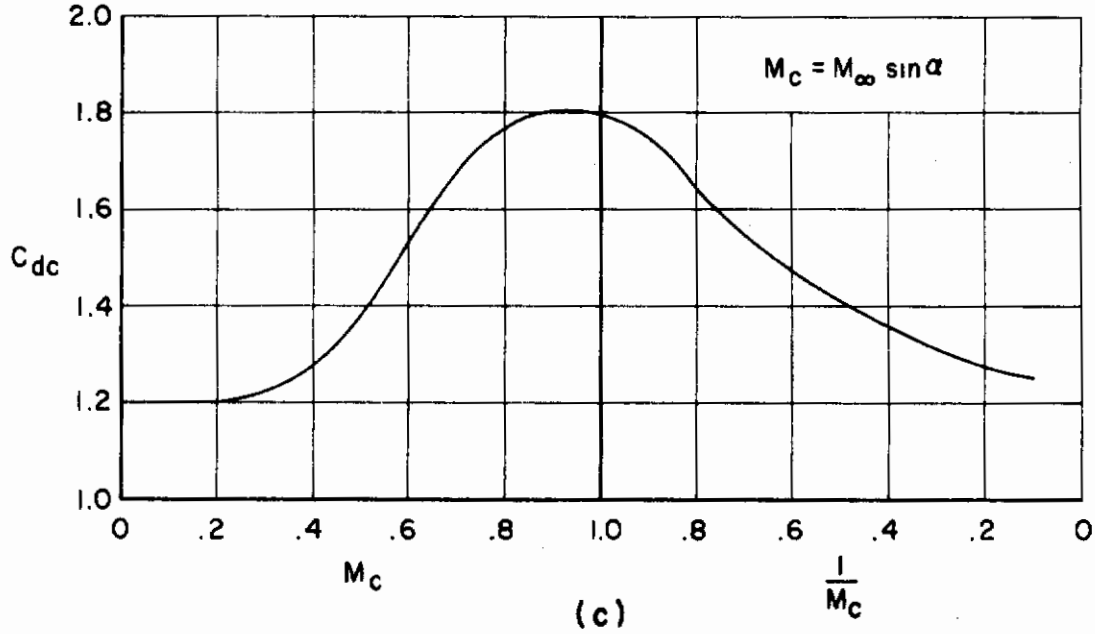

(c)

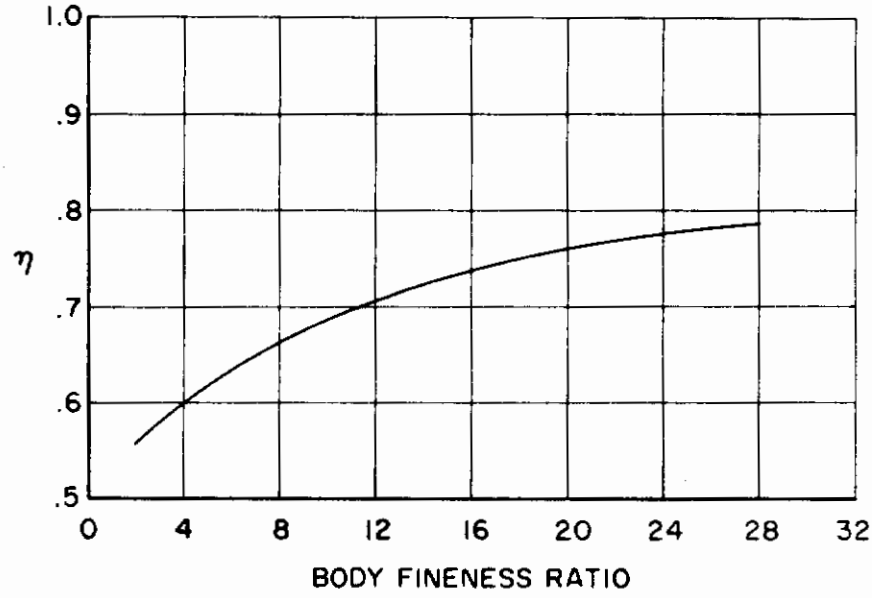

(d)

Figure (3.10) (c) Steady-State Cross-Flow Drag on a Circular Cylinder of Infinite Length;
(d) Ratio of Drag on a Finite Cylinder to the Drag on an Infinite Cylinder.

The integral in equation (3.21) would, in practice, be evaluated using a finite summation approximation; and, for small angles of attack, the second term in equation (3.21) could be neglected. In addition, for preliminary design purposes it would be expected that the nonpotential lift on the fuselage could be entirely neglected.

3.1.2 Drag

For STOL aircraft employing powered lift systems, drag is usually defined as the difference between the ideal thrust, C_J, and the actual thrust, C_T, expressed as

$$C_D = C_J - C_T \tag{3.22}$$

The drag force is composed of contributions due to skin-friction drag, pressure drag, engine ram drag, and drag due to lift (induced drag). Only the induced drag, C_{D_i}, is calculated directly by the program. Semi-empirical methods, taken from Datcom (reference 3) and WINSTAN (reference 4) and modified for use here, are the basis for calculating the other effects. Application of some of these semi-empirical results, which were developed for conventional aircraft, to STOL aircraft employing powered lift cannot be justified at this time because of a lack of systematic experimental data for these aircraft concepts. However, some uncertainty in the profile drag estimate can be tolerated since, from a stability and control standpoint, profile drag does not significantly affect the longitudinal static or dynamic stability characteristics of an aircraft (see Section 4.0).

The structure of the EVD segment of STAMP requires that the induced drag coefficient, C_{D_i}, be expressed as a function of angle of attack rather than lift, as is used in most conventional aircraft methods, such as those in Datcom. Hence, because of this, it is most convenient to express the total drag coefficient as a function of angle of attack as well, in the form

$$C_D = C_{D_o} + \frac{\partial C_D}{\partial \alpha}\alpha + \frac{\partial^2 C_D}{\partial \alpha^2}\alpha^2 \tag{3.23}$$

The task is then to calculate the three terms in equation (3.23). First the contribution of the jet-wing system to C_D will be fully discussed, followed by the contributions of the fuselage and empennage, including interference effects.

3.1.2.1 Total Wing Drag

The total wing drag is composed of skin-friction drag, pressure drag, and induced drag. Skin-friction drag is caused by shearing stresses within the boundary layer on the surface of the body. The boundary layer arises from the resistance of the viscous fluid to the motion of the body passing through it. Three types of boundary-layer flow are possible: laminar, turbulent, and transitional. For aircraft in flight, transition usually occurs very close to the leading edge of wings and to the nose of bodies; and, consequently, it is common engineering practice to consider the flow to be fully turbulent.

While skin-friction drag is actually a function of the surface pressure distribution, it is the standard engineering approximation to assume that flat-plate boundary-layer flow will provide sufficient accuracy in the estimation of skin-friction drag. The skin-friction coefficient (c_f) is evaluated using the method due to Eckert, and the result is plotted in figure (3.11) as a function of Reynolds number based on length for several Mach numbers. The data plotted in figure (3.11) are for a fully turbulent boundary layer. The effect of surface roughness is such that above a critical Reynolds number based on the roughness height parameter, ℓ/K, the mean skin friction is essentially constant. Therefore, the concept of admissible roughness is introduced. Figure (3.12) presents the critical Reynolds number as a function of admissible roughness. If the Reynolds number based on the reference length ℓ is below the critical Reynolds number obtained from figure (3.12), then the value of c_f is read directly from the curves of figure (3.11). However, if the computed Reynolds number is greater than the critical Reynolds number, the value of c_f is read from figure (3.11) at the critical Reynolds number. Typical values of the surface roughness height for normal aircraft surface finishes are listed in table (3.2) below.

The pressure drag contribution is due to boundary-layer displacement thickness effects and flow separation forward of the trailing edge. No accurate analytical solution exists for analyzing the pressure drag on general shapes in subsonic flow, and consequently empirical prediction methods must be employed. The pressure drag effects are in general small for the low-speed regime under consideration and can be estimated by applying empirical correction factors to the skin-friction drag, c_f. The empirical method presented

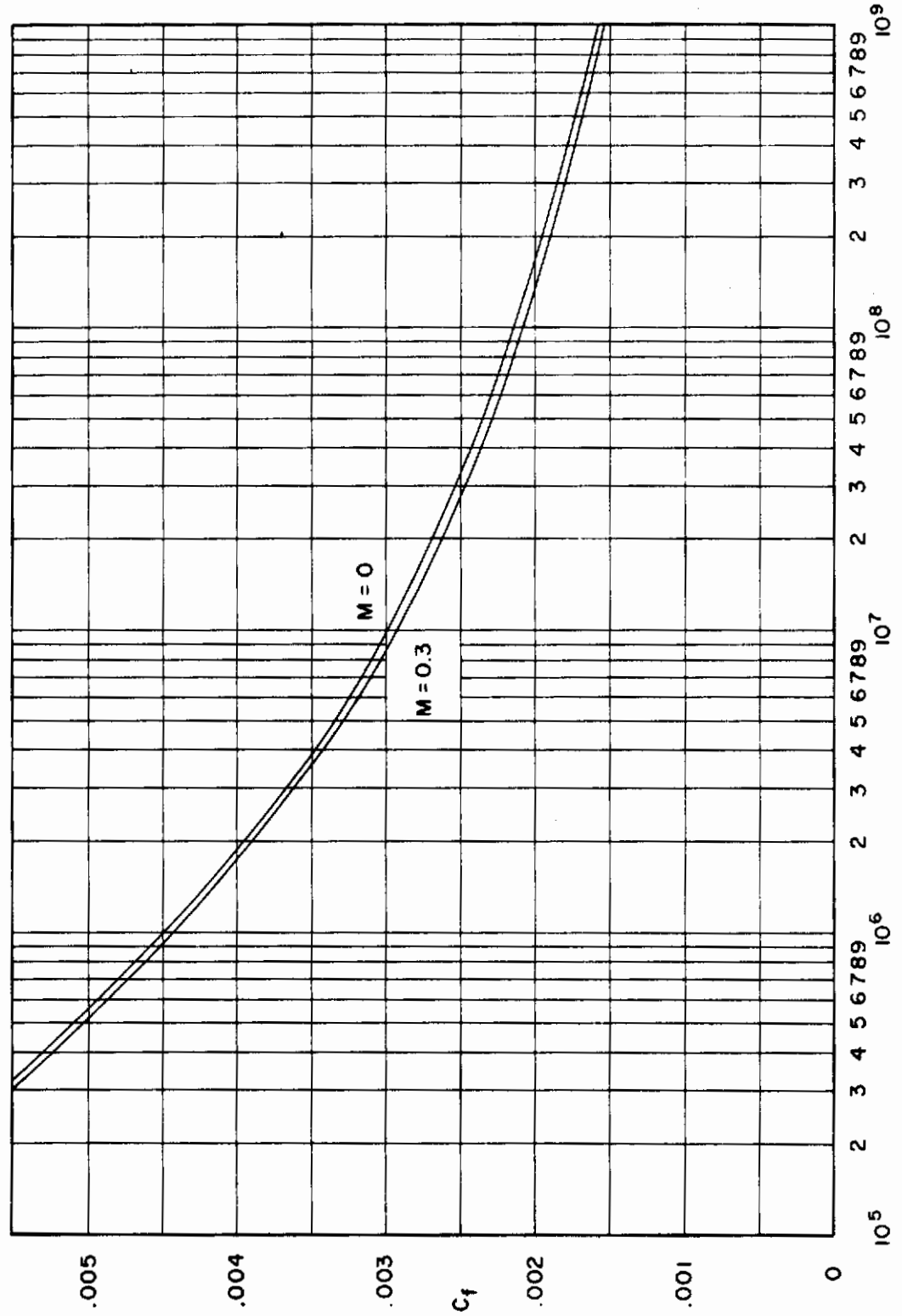

Figure (3.11). Flat Plate Skin Friction Coefficient.

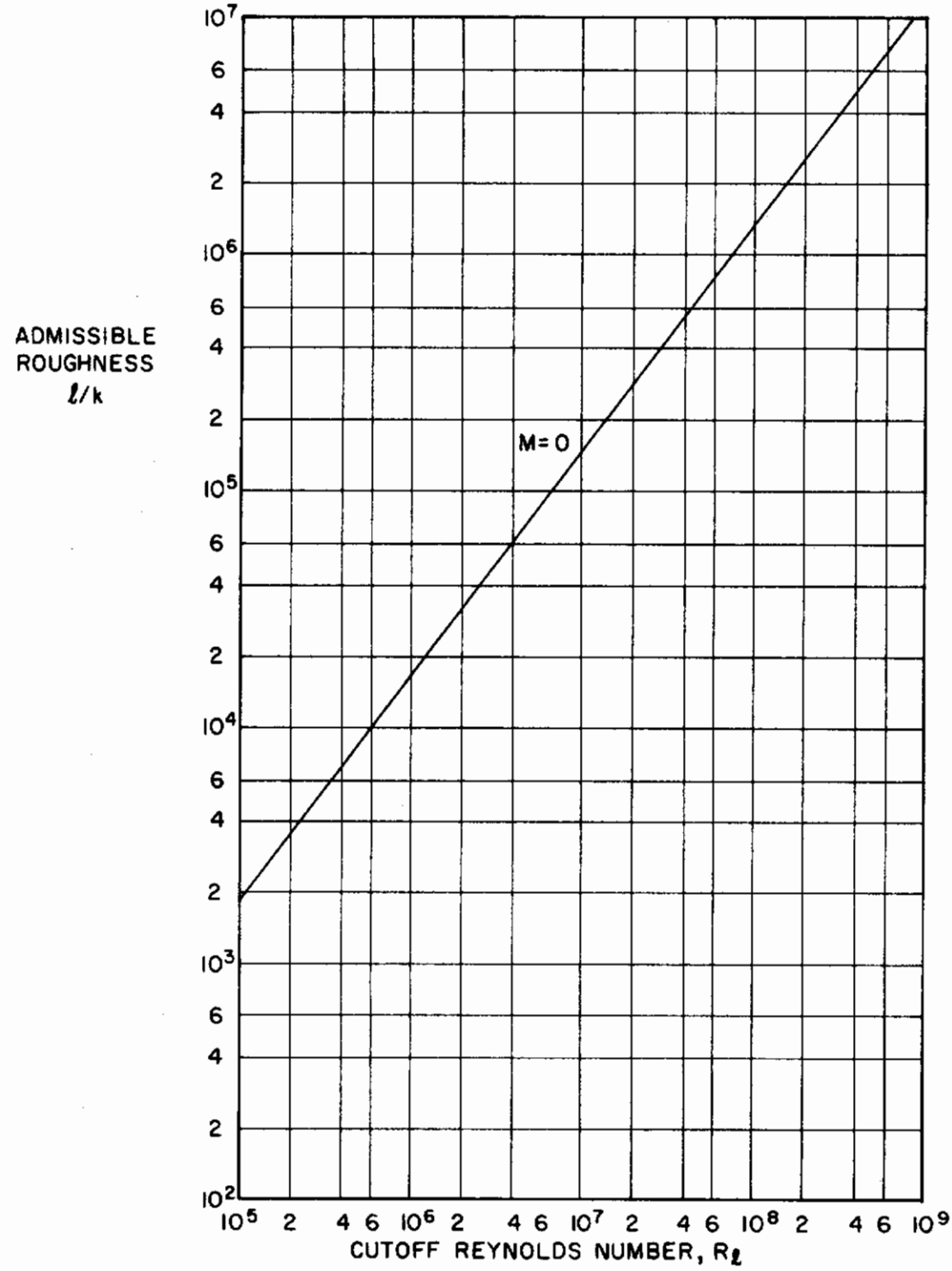

Figure (3.12). Cutoff Reynolds Number as a Function of Admissible Roughness.

Table (3.2). Typical Values of Surface Roughness Height

Type of Surface	Equivalent Sand Roughness K (inches)
Aerodynamically smooth	0
Polished metal or wood	$0.02 - 0.08 \times 10^{-3}$
Natural sheet metal	0.16×10^{-3}
Smooth matte paint, carefully applied	0.25×10^{-3}
Standard camouflage paint, average application	0.40×10^{-3}
Camouflage paint, mass production spray	1.20×10^{-3}
Dip-galvanized metal surface	6×10^{-3}
Natural surface of cast iron	10×10^{-3}

here is that used in Datcom with some modification. The method is based on a correlation of experimental data with planform shape and the chordwise location of the maximum section thickness. Although the correlations used to establish the empirical corrections are for conventional wings only, they will also be applied to jet-wings, primarily because there is not sufficient data available to establish jet-wing correction factors. Some of the available jet-wing data indicate that the profile drag is a function of the jet momentum coefficient (C_J), but other data contradict this result. Further work in this area for jet-wings is obviously required. The applicable empirical relation for wing friction plus pressure drag is

$$C_{D_{o_w}}\Big|_{profile} = \left\{ C_f \left[1 + L\left(\frac{t}{c}\right) + 100\left(\frac{t}{c}\right)^4 \right] R_{L.S.} \right\} \frac{S_{wet}}{S} + \Delta c_{d_{flap}} K_b \qquad (3.24)$$

where

C_f is the flat-plate turbulent skin-friction coefficient obtained from figures (3.11) and (3.12), with the Reynolds number based on the mean aerodynamic chord (c_{mac}).

t/c is the average streamwise thickness ratio of the wing

L is an empirical parameter to account for the chordwise location of the maximum airfoil thickness and
= 1.2 for $(t/c)_{max}$ located at $x/c \geq 0.3$
= 2.0 for $(t/c)_{max}$ located at $x/c < 0.3$.

The quantity $[1 + L(t/c) + 100(t/c)^4]$ is plotted in figure (3.13) as a function of (t/c).

$R_{L.S.}$ is an empirical correction factor to account for the spanwise flow on a finite lifting surface and is plotted in figure (3.14).

S_{wet} is the total wetted area of the wing.

S is the reference area.

$\Delta c_{d_{flap}}$ is the incremental sectional profile drag coefficient due to flap deflection, plotted in figures (3.15a) and (3.15b) for plain and single-slotted flaps, respectively. For flaps with jets, these corrections are not applicable because of the boundary-layer-control effects of the jet. No empirical $\Delta c_{d_{flap}}$ data are available for jet-wings, and it is recommended that the additional profile drag due to flap deflection for blown flaps be neglected.

K_b is a factor to account for partial span flaps, plotted in figure (3.16). For wings with multiple flaps, several $\Delta c_{d_{flap}} K_b$ terms will be required.

Equation (3.24) is only part of the $C_{D_{ow}}$ term, however, the remaining contribution being that due to induced drag and other lift-dependent drag. Wing-induced drag is calculated directly by the program in the form

$$C_{D_{i_w}} = C_{D_{i_o}} + \frac{\partial C_{Di}}{\partial \alpha} \alpha + \frac{\partial^2 C_{Di}}{\partial \alpha^2} \alpha^2 \qquad (3.25)$$

for a composite case. Since induced drag is a nonlinear function of angle of attack and the other deflection angles, it is not worthwhile to look at the separate induced drag contributions of each fundamental case, as was done for lift (Section 3.1.1.2), since the separate induced drag contributions cannot be added directly. Hence, the discussion here deals only with composite wing cases.

It is necessary to provide some modification to the program calculated induced drag to account for thickness and viscous effects not yet considered. Empirical work done over the years to provide such modifications to potential

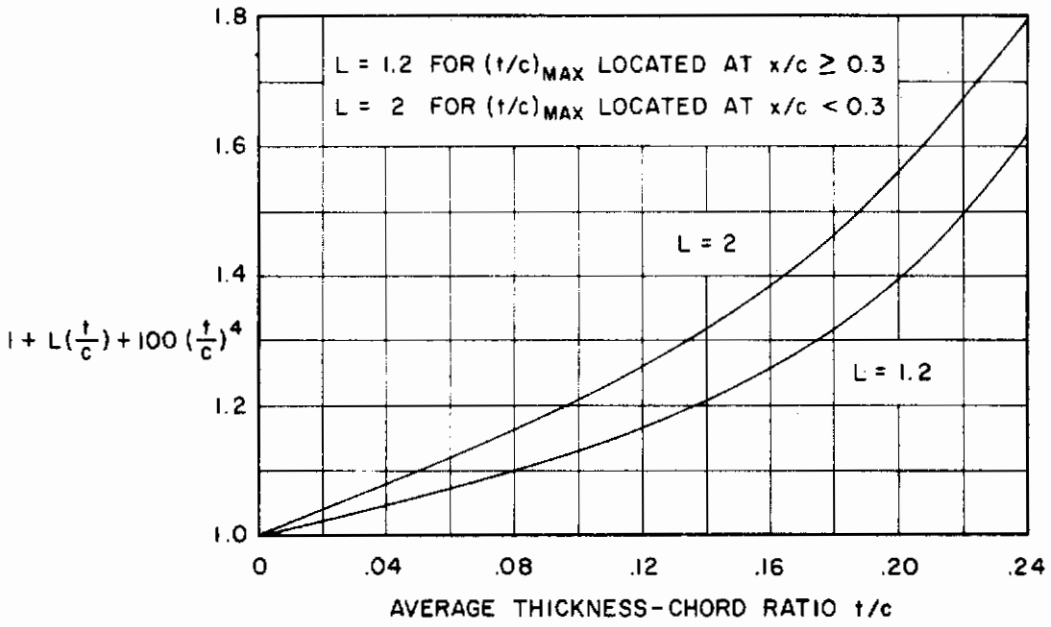

Figure (3.13). Empirical Factor to Account for Wing Profile Drag.

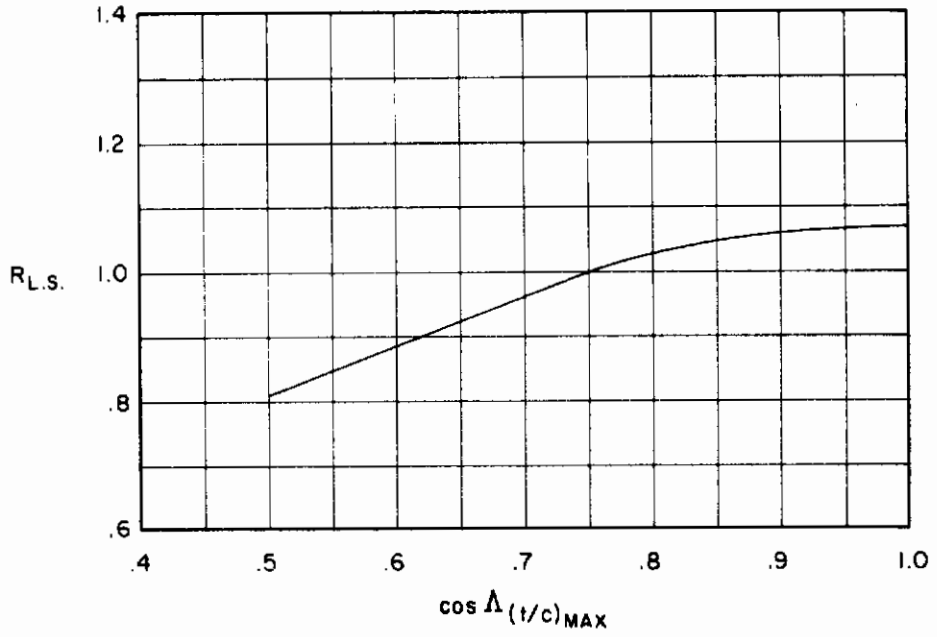

Figure (3.14). Empirical Factor to Account for Finite Lifting Surface.

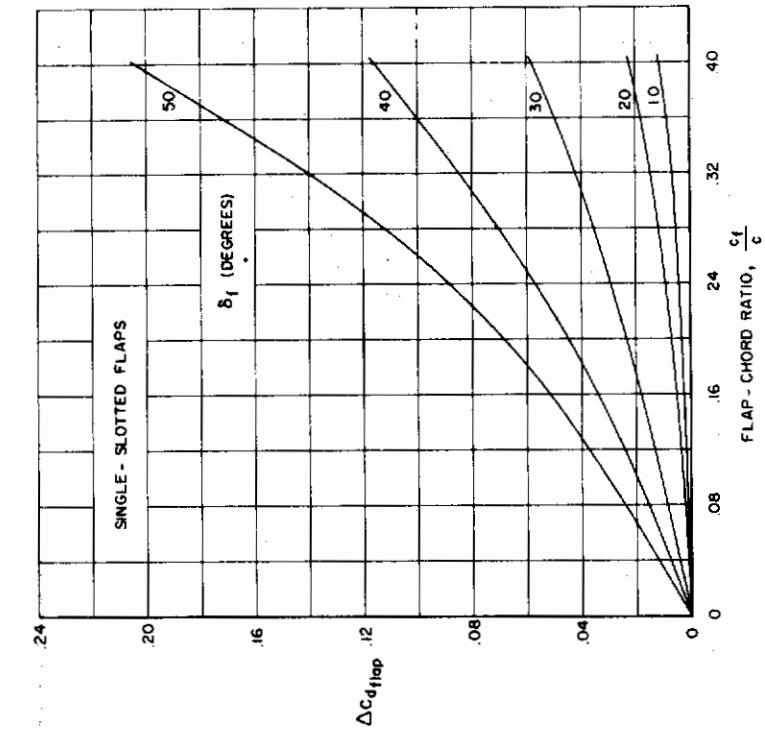

(b)

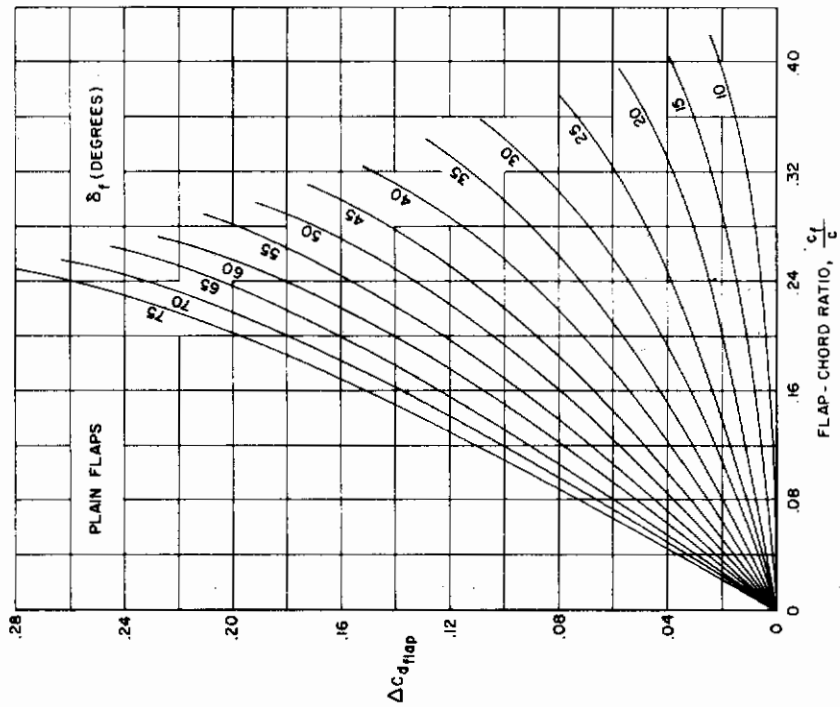

(a)

Figure (3.15). Incremental Sectional Profile Drag Coefficient Due to Flap Deflection

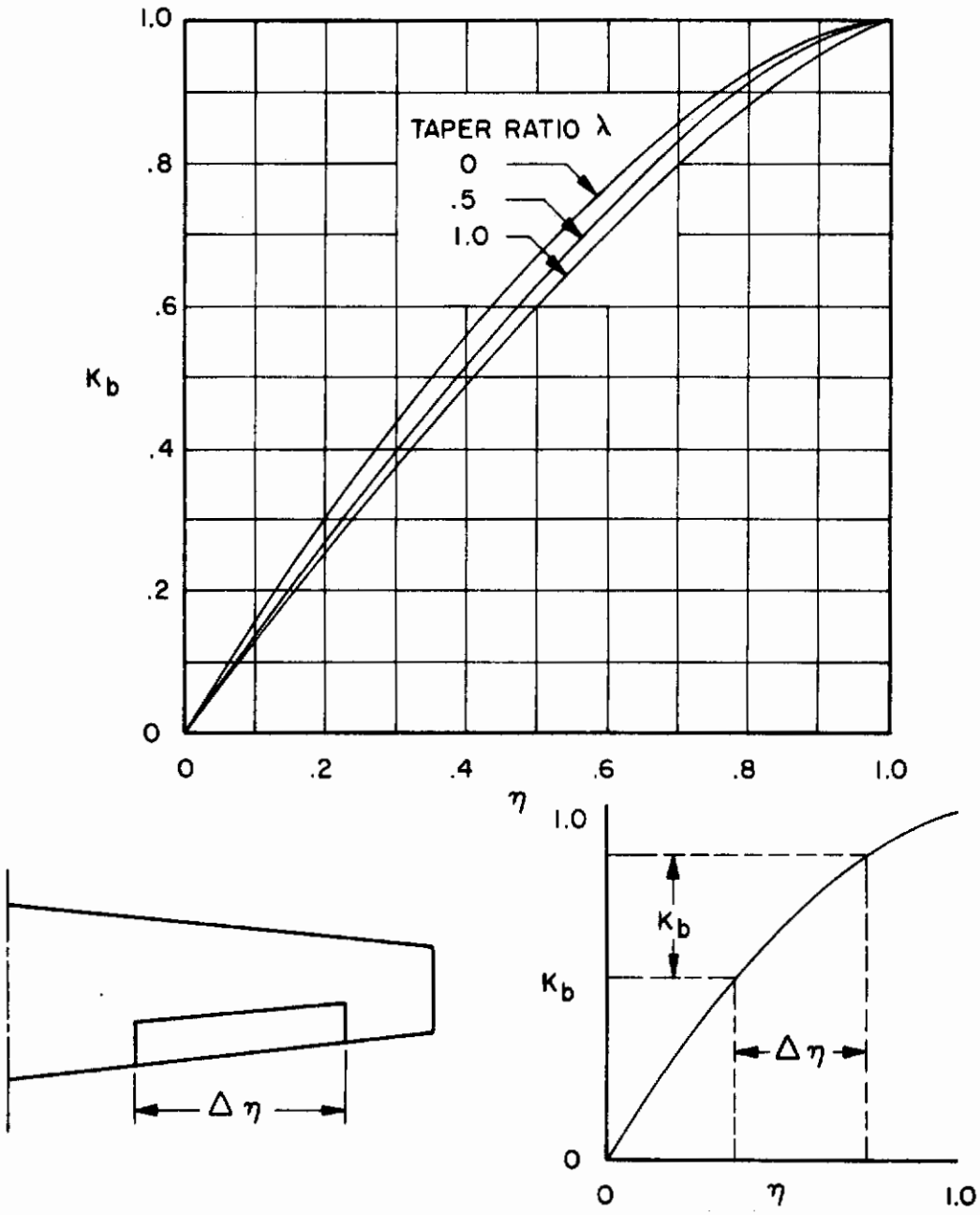

Figure (3.16). Factor to Account for Partial Span Flaps

drag of an isolated body is composed of lift-independent terms and lift-dependent terms.

The lift independent drag of smooth slender bodies is primarily skin friction. Just as for the wing, the boundary layer is assumed to be fully turbulent and is affected by the roughness of the surface. The expression for lift independent drag given by Datcom (Section 4.2.3.1) is

$$C_{D_{oF}} = C_f \left[1 + \frac{60}{(\ell/d)^3} + 0.0025 \left(\frac{\ell}{d}\right)\right] \frac{S_{wet}}{S} + C_{D_{base}} \tag{3.28}$$

where

C_f is the turbulent flat-plate skin-friction coefficient obtained from figures (3.11) and (3.12), with the Reynolds number based on body length, ℓ.

ℓ/d is the body fineness ratio, where ℓ is the body length and d is the maximum diameter of an equivalent body of revolution.

S_{wet} is the wetted area of the body.

S is the reference area.

$C_{D_{base}}$ is the base drag coefficient based on reference area and is required only for bodies with blunt aft ends (see Datcom Section 4.2.3.1).

The method for calculating the variation of fuselage drag with angle of attack is based on the fuselage lift calculated by equation (3.21) and is expressed in the form

$$C_{D_F}(\alpha) = \frac{2(K_M)A_o}{(57.3)^2 S}\alpha^2 + \frac{2}{(57.3)^3 S}\alpha^3 \int_{x_o}^{x_E} \pi r c_{d_c} dx \tag{3.29}$$

It is again expected that the second term could be neglected for small angles of attack.

The total wing drag is now established from equations (3.24) and (3.27), and the total fuselage drag from equations (3.28) and (3.29). It is now necessary to calculate the effect of the mutual interference between the wing and body. For the lift-independent wing-body drag,

flow methods predictions of induced drag have not been as successful as for lift because of the nonlinear behavior of drag and because of the overwhelming importance of the viscous boundary layer. The method provided in Datcom for calculating the lift dependent portion of drag (C_{D_L}) combines the induced drag and viscous drag effects into one term, the Oswald span-efficiency factor (e), and expresses this in the form

$$C_{D_L} = \frac{C_L^2}{\pi ARe} + C_L f[\alpha_t(y)] \tag{3.26}$$

where $f[\alpha_t(y)]$ indicates a functional dependence with twist. However, the Datcom method is limited in its range of applicability because it can only approximately treat irregular planform shapes, and its empirical factors are based on quite limited data correlations. For jet-wings these correlations cannot be assumed to apply, however, because the boundary-layer-control effects of the jet sheet will alter the variation of viscous drag with lift. Hence, the Datcom corrections cannot be applied in this work. Because of the lack of a consistent set of experimental data for jet-wing configurations, it is not possible at this time to present any general empirical relations to correct program-calculated induced drag. Simple corrections to approximately account for airfoil thickness can be applied, however, in the form

$$C_{D_{i_w}} = \left[C_{D_{i_o}}\Big|_{EVD} + \left(\frac{\partial C_{Di}}{\partial \alpha}\right)_{EVD}\alpha\right]\left(\frac{C_L}{C_L\Big|_{EVD}}\right) + \left(\frac{\partial^2 C_{Di}}{\partial \alpha^2}\right)_{EVD}\left(\frac{C_L}{C_L\Big|_{EVD}}\right)^2 \alpha^2 \tag{3.27}$$

where $(C_L/C_L|_{EVD})$ is the ratio of the total corrected lift to the total program-calculated lift, from Section 3.1.1.2, and the C_{D_i} terms are calculated by the momentum-induced-drag method (see Volume I). Although additional corrections to account for variation of viscous drag with lift are not presented herein, this is not considered to be a serious restriction since the dominant variation of drag with lift is the induced drag, which has been shown to be accurately predicted by the program.

3.1.2.2 Fuselage Drag

The drag of wing-body combinations will be treated by separately calculating the contributions of the wing (Section 3.1.2.2) and the fuselage and then applying correction factors to account for the mutual interferences. The

$$(C_{D_o})_{WB} = \left[C_{D_{ow}}\Big|_{Profile} + C_{D_{oF}}\right] R_{WB} \tag{3.30}$$

where R_{WB} is an empirical wing-body interference factor, plotted in figure (3.17), and $C_{D_{ow}}|_{profile}$ and $C_{D_{oF}}$ are from equations (3.24) and (3.28), respectively.

Little is known concerning the mutual interferences that affect the lift-dependent portion of wing-body drag. The usual procedure is to add directly the wing contribution, which is calculated in equation (3.27) from program results, and the fuselage contribution, which is calculated in equation (3.29). Thus,

$$[C_D(\alpha)]_{WB} = C_{D_{i_w}} + C_{D_F}(\alpha) \tag{3.31}$$

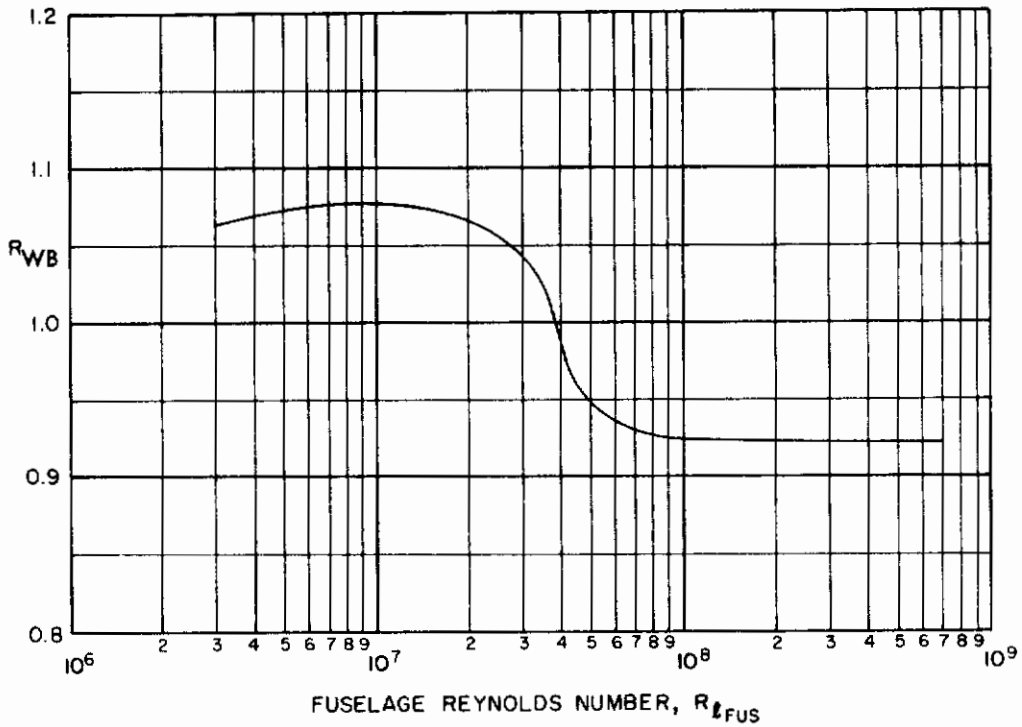

Figure (3.17). Empirical Wing-Body Interference Factor

3.1.2.3 Empennage Drag

The drag contribution of the empennage is calculated in a manner similar to that for the wing, separating the effects into those which can be calculated by potential-flow methods (induced drag) and those for which empirical methods are required (friction and pressure drag). Interference effects due to the jet-wing are calculated by the program, as discussed in Section 3.1.1.3 for the empennage lift coefficient. Interference effects due to the fuselage are considered only so far as to treat the vertical tail as endplated by the fuselage.

The procedure for calculating skin-friction drag and pressure drag is identical to that for the wing, equation (3.24), and can be expressed in the form

$$C_{D_o}\Big|_{H\&V} = \left\{ C_{f_H} \left[1 + L_H \left(\frac{t}{c}\right)_H + 100 \left(\frac{t}{c}\right)_H^4 \right] R_{L.S._H} \right\} \frac{S_{wet_H}}{S} + \Delta c_{d_{elevator}} K_b$$
$$+ \left\{ C_{f_V} \left[1 + L_V \left(\frac{t}{c}\right)_V + 100 \left(\frac{t}{c}\right)_V^4 \right] R_{L.S._V} \right\} \frac{S_{wet_V}}{S} + \Delta c_{d_{rudder}} K_b \qquad (3.32)$$

where all terms are defined following equation (3.24) and the subscripts H and V refer to the horizontal and vertical tails, respectively. The elevator and rudder terms, of course, should only be used when these devices are deflected.

The induced drag contribution of the empennage is calculated directly by the program, both for the isolated tail solution and the interference tail solution. The latter solution is actually the only one of interest, however, and it is calculated explicitly at five angles of attack because of the nonlinear interference of the jet-wing. The empennage induced drag, as calculated by the program, is expressed as

$$C_{D_{i_{H\&V}}} = C_{D_{i_H}}(\alpha) + C_{D_{i_V}}(\alpha) \qquad (\alpha = 0, 5, 10, 15, 20 \text{ degrees}) \qquad (3.33)$$

For other angles of attack within this range, either graphical or numerical interpolation of equation (3.33) should be used.

The total empennage contribution to aircraft drag is then simply

$$C_{D_{H\&V}} = C_{D_{o_H}} + C_{D_{o_V}} + C_{D_{i_H}} + C_{D_{i_V}} \qquad (3.34)$$

3.1.2.4 Ram Drag

Ram drag is defined as the loss in freestream momentum of the streamtube of air entering the engine inlet. The ram drag coefficient (C_{D_R}) can be calculated from

$$C_{D_R} = 2\frac{NA_o}{S} = 2\frac{NQ_i}{\rho U S g} \qquad (3.35)$$

where

N is the number of engines.

A_o is the freestream capture area of each engine.

Q_i is the intake mass flow of each engine (lb/sec)

g gravitational constant (32.2 ft/sec^2).

Note that ram drag should not be included in these calculations if the net engine thrust is given, although gross engine thrust must be known for the calculation of other aerodynamic characteristics.

3.1.2.5 Total Aircraft Drag

Total aircraft drag is calculated from equation (3.22) by summing the contribution due to each aircraft component. However, in practice the C_J term in equation (3.22) has been absorbed into the induced drag term calculated by the program. Hence the total aircraft drag can be expressed as

$$C_D = \underbrace{[C_{D_{o_W\ \text{profile}}} + C_{D_{o_F}}]R_{WB}}_{(3.30)} + \underbrace{C_{D_{i_W}}}_{(3.27)} + \underbrace{C_{D_F(\alpha)}}_{(3.29)} + \underbrace{C_{D_{o_{H\&V}}}}_{(3.32)} + \underbrace{C_{D_{i_{H\&V}}}}_{(3.33)} + \underbrace{C_{D_R}}_{(3.35)} \tag{3.36}$$

3.1.3 Pitching Moment

For STOL aircraft there are contributions to the overall aircraft pitching moment from the aerodynamic loading on the airframe and from both the lift and thrust components of the propulsion system reaction force, which can be expressed as

$$C_m = C_{m_\Gamma} + C_{m_J} + C_{m_T} \tag{3.37}$$

where

C_{m_Γ} is the circulation component of pitching moment

C_{m_J} is the reaction lift component of pitching moment

C_{m_T} is the reaction thrust component of pitching moment

Each of the terms in equation (3.37) is calculated directly by the program, including contributions of the wing, jet sheet or vectored jets, fuselage, and empennage. Modification of the program calculated results is required, however, to account for wing thickness and viscous effects, which are not considered by the program.

The approach used in this section is similar to that in Section 3.1.1 for lift, and many of the corrections applied here are formulated in the same manner as those for lift. Hence, the sectional pitching moment characteristics of the wing are discussed first, followed by discussions of the total contributions of the wing, jet sheet or vectored jets, the fuselage, and the empennage.

3.1.3.1 Sectional Wing Pitching Moment

The program calculates the sectional wing circulation pitching moment (c_{m_Γ}) and, for jet-wings, the sectional pitching moment due to jet reaction (c_{m_μ} and c_{m_t}) for a zero thickness wing in inviscid flow. For conventional wings or jet-wings the program prints the sectional moment variation with angle of attack for each composite case in the form

$$c_{m_\Gamma}(y) = c_{m_{\Gamma_o}}(y) + c_{m_{\Gamma_\alpha}}(y)\alpha \qquad \text{(Free Air)} \qquad (3.38a)$$

$$c_{m_\Gamma}(y) = c_{m_{\Gamma_o}}(y) + c_{m_{\Gamma_\alpha}}(y)\alpha + c_{m_{\Gamma_{\alpha^2}}}(y)\alpha^2 \qquad \text{(Ground Effect)} \qquad (3.38b)$$

$$c_{m_\mu}(y) = c_{m_{\mu_o}}(y) + c_{m_{\mu_\alpha}}(y)\alpha \qquad (3.38c)$$

$$c_{m_t}(y) = c_{m_{t_o}}(y) + c_{m_{t_\alpha}}(y)\alpha \qquad \text{(Free Air or Ground Effect)} \qquad (3.38d)$$

For wings with vectored jets these equations are not applicable because the interference between the wing and vectored jets is a nonlinear function of angle of attack. For this case

$$c_{m_\Gamma}(y) = c_{m_\Gamma}(y)\Big|_\alpha \qquad (\alpha = 0,\ 5,\ 10,\ 15,\ 20 \text{ degrees}) \qquad (3.38e)$$

As for sectional lift, the effects of section thickness, viscous effects, and boundary-layer separation will be discussed, first for unblown wing sections and then for blown sections.

Unblown Wing Sections

Pitching Moment Curve Slope.— The slope of the pitching moment curve c_{m_α} calculated by the program [equation (3.38a)] can be readily corrected for thickness and viscous effects using the equation

$$c_{m_\alpha} = K\left(\frac{c_{\ell_\alpha}}{c_{\ell_\alpha}\Big|_{EVD}}\right) c_{m_\alpha}\Big|_{EVD} \qquad (3.40)$$

where

K is the ratio of the theoretical aerodynamic center location for a thick section to that for a thin section, plotted in figure (3.18).

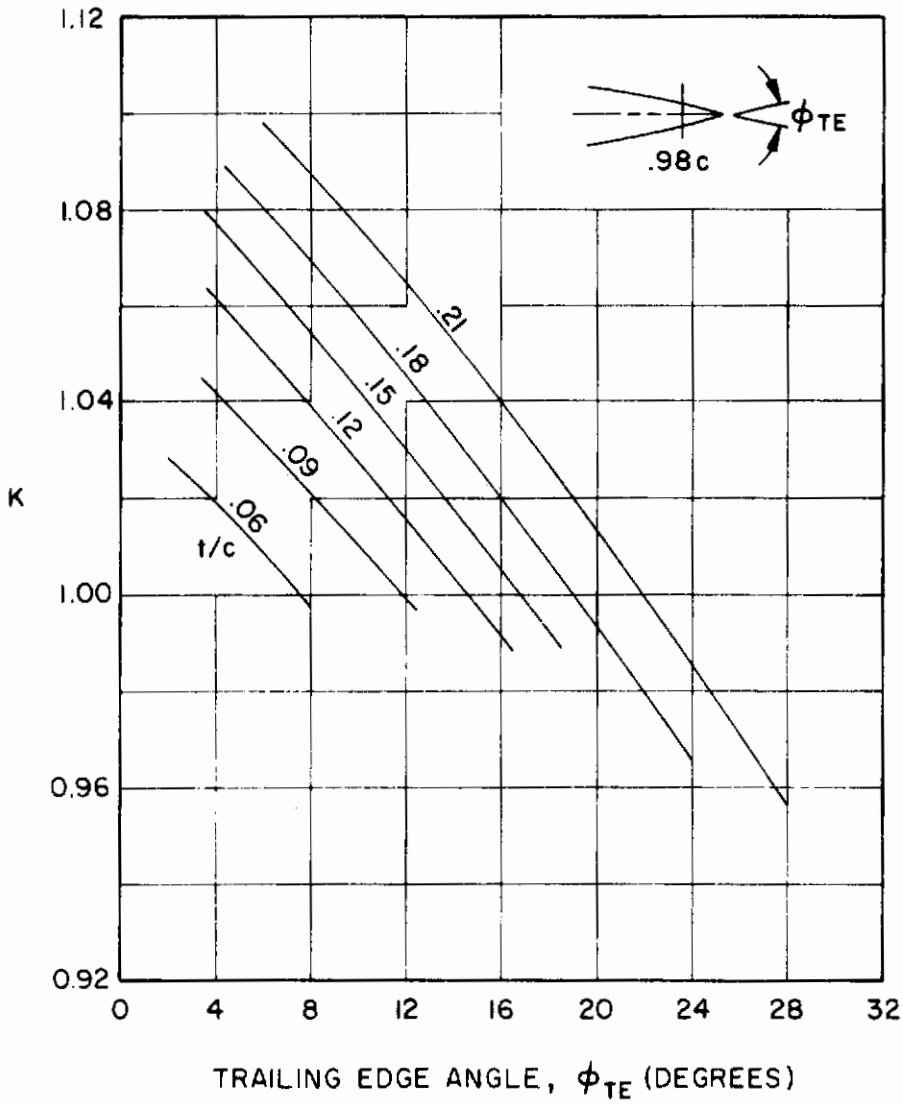

Figure (3.18). Theoretical Correction to Pitching Moment Curve Slope for Section Thickness

$\left(\frac{c_{\ell_\alpha}}{c_{\ell_\alpha}\big|_{EVD}}\right)$ is the ratio of the corrected lift curve slope to the program calculated lift curve slope, from equation (3.3).

$c_{m_\alpha}\big|_{EVD}$ is the program output result.

Thin airfoil theory shows that c_{m_α} does not change with camber or flap deflection. Experiment verifies this to be true for angles of attack and flap deflections where the flow remains essentially attached to the airfoil. When separation begins some of the aft flap loading is lost and the pitching moment becomes more nose up, although the changes are small. No methods are currently available to predict this phenomenon and correlation with experiment is required.

Pitching Moment at Zero Angle of Attack. It is more difficult to modify the sectional c_{m_0} calculated by the program because of the importance of viscous effects, particularly boundary-layer separation. Various flap types exhibit markedly different c_{m_0} characteristics because of their varying ability to maintain attached flow. Also, c_{m_0} is particularly difficult to estimate because it is a function of the pressure distribution which depends, of course, on the detailed flap geometry (i.e., the shape of slots, vanes, etc.) and on the point of flow separation from the flap.

For unflapped wing sections Datcom presents only tabulated airfoil data for standard sections. As for lift, the most accurate way to correct the program result would be to know both the experimental value of c_{m_0} for a two-dimensional thick airfoil and the thin airfoil theory c_{m_0}, and then calculate the corrected c_{m_0} from

$$c_{m_0} = \left(\frac{c_{m_0}\big|_{experiment}}{c_{m_0}\big|_{thin}}\right) c_{m_0}\big|_{EVD} \tag{3.41}$$

In lieu of experimental data, the same correction as was applied to c_{ℓ_0} is often used for c_{m_0}, that is

$$c_{m_0} = [1 + (K)t/c]\, c_{m_0}\big|_{EVD} \tag{3.42}$$

where K is usually 0.8.

For flapped sections Datcom does present empirical data for the change in sectional pitching moment with flap deflection, $\partial c_m/\partial \delta_f$, which is a part of c_{m_0}. This empirical data, some of which is presented here, should be regarded as only a guideline for correcting program calculated c_{m_0}, since the agreement between these data and experiment is not consistently good. For plain and single-slotted flapped sections, the correction to the program calculated c_{m_0} is calculated from

$$\frac{\partial c_m}{\partial \delta_f} = K \left.\frac{\partial c_m}{\partial \delta_f}\right|_{EVD} \tag{3.43}$$

where

K is an empirical factor for the ratio of c_{m_0} to the thin airfoil theory result, plotted in figure (3.19) for plain and single-slotted sections.

$\left.\frac{\partial c_m}{\partial \delta_f}\right|_{EVD}$ is the program calculated sectional c_m for the fundamental case which defines the flap.

In order to apply these corrections to the program sectional data, equation (3.41) or (3.42) should be used to correct the camber/twist fundamental case and equation (3.43) should be used to correct the flap fundamental case. Then the corrected results can be appropriately added to form the required composite cases. However, for simplicity, applying only equation (3.43) to composite case data for flapped sections should suffice because the incremental pitching moment due to flap is usually the dominant effect. No data are presented for double-slotted flaps because of a lack of systematic data. For leading-edge devices the Datcom methods are based on potential flow methods only, and hence the program result should be used directly.

Blown Wing Sections

The empirical methods described above for unblown-wing sections are not applicable to jet-flapped wing sections because of the favorable boundary-layer-control effects of the jet. The reader is referred to Section 3.1.1.1 on lift for a complete discussion of the implications of blowing and the need for treating blown wing sections differently from unblown sections. Based on

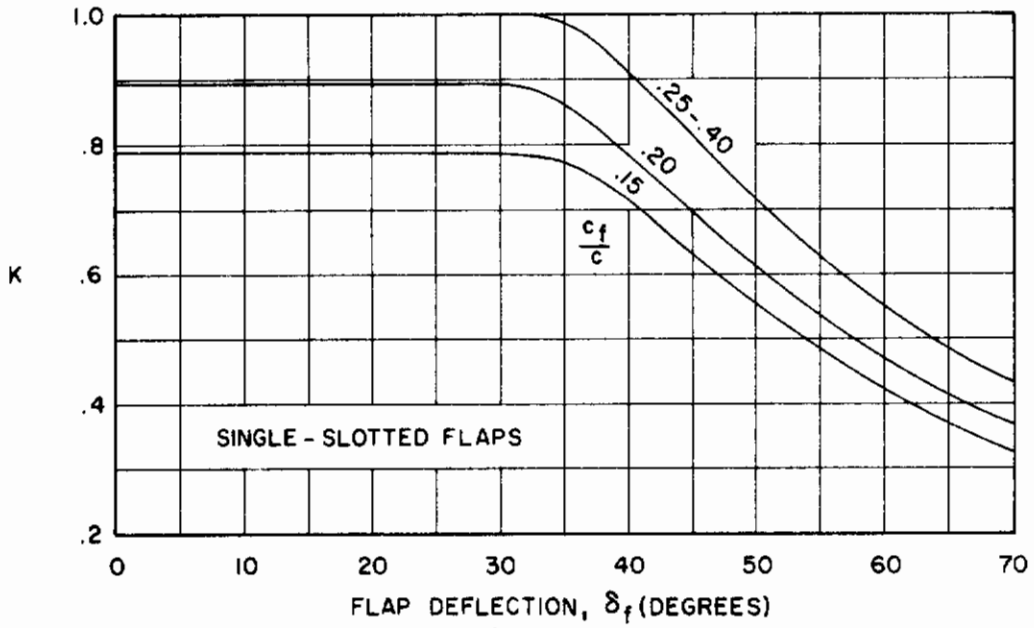

(a)

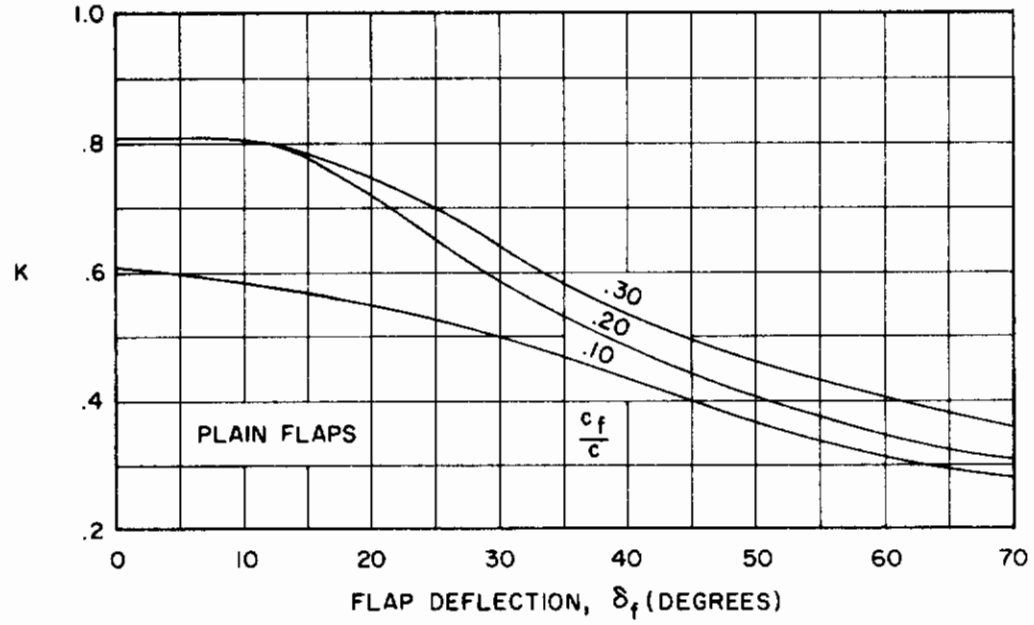

(b)

Figure (3.19). Empirical Correction to c_{m_o} for Boundary Layer Effects

an analogy with the discussion of that section, a simple correction for thickness effects can be applied to the circulation component of pitching moment, as

$$c_{m_\Gamma} = [1 + (K)t/c)]c_{m_\Gamma}\Big|_{EVD} \tag{3.44}$$

where equation (3.44) applies to both $c_{m_{\Gamma_0}}$ and $c_{m_{\Gamma_\alpha}}$ in equation (3.38a). The usual value K used in equation (3.44) is 0.8 for sections with sharp trailing edges.

Ground Effect

As discussed in the section on lift, the present ground-effect method is intended primarily to provide the relative magnitude of the ground effect compared to the free-air solution rather than the absolute magnitude of the changes due to ground proximity. Hence the changes in sectional pitching moment due to ground proximity should be expressed as

$$\frac{\Delta c_{m_{ground}}}{c_{m_{free\ air}}} = \frac{c_{m_{ground}} - c_{m_{free\ air}}}{c_{m_{free\ air}}} \tag{3.44}$$

Mechanical Flaps with Vectored Thrust

Corrections should be applied to the program calculated sectional pitching moments for mechanical flap systems with vectored thrust [equation (3.38e)] in the same manner as for unblown sections because there is no boundary-layer-control effect for this type of system as there is for jet-flap airfoils.

3.1.3.2 Total Wing Pitching Moment

The sectional pitching moments, which are referenced to the section leading edges, are integrated by the program along the span of the wing to determine the total wing pitching moment, which is referenced to the wing apex, by approximating the integral

$$C_{m_{apex}} = \frac{1}{S\bar{c}} \int_{-b/2}^{b/2} [c^2(y)c_{m_\Gamma}(y) - c(y)c_{\ell_\Gamma}(y)x_\ell(y)]dy + C_{m_J} + C_{m_T} \tag{3.45}$$

by a finite summation, treating $c_{m_\Gamma}(y)$, $c_{\ell_\Gamma}(y)$, $c(y)$, and $x_\ell(y)$ as constant over each spanwise division. In order to correct the total wing pitching moment for thickness and viscous effects, the corrected sectional c_{m_Γ}

calculated in Section 3.1.3.1 and the corrected sectional c_{ℓ_Γ} calculated in Section 3.1.1.1 must be reintegrated using the equation

$$c_{m_{apex}} = \frac{1}{S\bar{c}} \sum \left[c^2(y) c_{m_\Gamma}(y) \Big|_{corrected} - c(y) x_\ell(y) c_{\ell_\Gamma}(y) \Big|_{corrected} \right] \Delta y + c_{m_J}{}_{apex} + c_{m_T}{}_{apex} \quad (3.46)$$

where the summation is taken over the span of the wing. Then the total wing pitching moment can be transferred to the input moment reference center (x_{mc}) in the wing plane by

$$c_{m_{mc}} = c_{m_\Gamma}{}_{apex} + c_{L_\Gamma}\left(\frac{x_{mc}}{\bar{c}}\right) + c_{m_J}{}_{mc} + c_{m_T}{}_{mc} \quad (3.47)$$

where $c_{m_{\Gamma apex}}$ and c_{L_Γ} are quantities that have been corrected for thickness and viscous effects and the reaction components are calculated directly by the program.

A considerable simplification to the thickness and viscous corrections to total wing pitching moment, analogous to that presented for lift, involves applying a single correction factor to the program-calculated total wing pitching moment. The approximation employed is to assume that for unblown sections the thickness correction is cancelled by the viscous correction, leaving the program calculated c_{m_o} and c_{m_α} values; and that for blown wing sections the thickness correction of $[1 + K(t/c)]$ is applied to $c_{m_{o_\Gamma}}$ and $c_{m_{\alpha_\Gamma}}$. The resulting expression is

$$c_m = \left[1 + (K)\left(\frac{S_B}{S}\right)\frac{t}{c}\right] c_{m_\Gamma}\Big|_{EVD} \quad (3.48)$$

where S_B is defined in figure (3.7). Obviously this approximation will become less valid as angle of attack or flap deflection is increased and viscous effects, including boundary-layer-separation, become more important.

In a manner similar to that discussed at length for lift, the total wing pitching moment can be expressed in terms of derivatives which explicitly show the effects of angle of attack, flap deflection, slat deflection, jet-sheet deflection, etc. using the fundamental case structure of the program. This

can only be done for jet-wings or conventional wings in free air, and, within the context of linear theory, can be expressed as

$$C_m = C_{m_o} + \frac{\partial C_m}{\partial \alpha}\alpha + \frac{\partial C_m}{\partial \delta_f}\delta_f + \frac{\partial C_m}{\partial \delta_s}\delta_s + \frac{\partial C_m}{\partial \delta_J}\delta_J + \frac{\partial C_m}{\partial \delta_{sp}}\delta_{sp} \qquad (3.49)$$

These terms represent the basic pitching moment, the pitching moment curve slope, and the change in pitching moment due to deflection of flap, slat, jet sheet, and spoiler, respectively. Each of these terms can be calculated directly by the program, except the spoiler term. The procedure to calculate each of these terms is identical to that fully discussed in Section 3.1.1.2 for lift and will not be repeated here. When following that procedure it must be remembered to apply the appropriate corrections for pitching moment, equation (3.46) or (3.48).

3.1.3.3 Empennage Pitching Moment

The empennage contribution to aircraft pitching moment is due only to the horizontal tail and depends on both the geometry of the tailplane and the downwash field induced by the jet-wing high-lift system. Tailplane pitching moment is calculated by the program both for the tail by itself (isolated tail analysis) and for the tail in the induced flow field of the jet-wing (interference tail analysis). The tailplane contributes to pitching moment both through a pure couple about its own aerodynamic center and through the moment about the aircraft moment center due to the lift on the tailplane. The pitching moment due to drag on the empennage is small compared to the other contributions and is not calculated by the program, but corrections for it are discussed here.

For the isolated tail analysis, the program calculated horizontal tail pitching moment can be expressed in the form

$$C_{m_H} = C_{m_{o_H}} + \left(\frac{\partial C_{m_H}}{\partial \alpha}\right)_{Isol}\alpha \qquad (3.50)$$

where $C_{m_{o_H}}$ is the basic pitching moment of the horizontal tail and includes the effects of any input surface deflections, such as tail camber, elevator deflection, and tail incidence (other than angle of attack); and $\left(\partial C_{m_H}/\partial\alpha\right)_{Isol}$ is the pitching moment curve slope of the horizontal tail. For the interference

tail analysis, the program-calculated installed horizontal tail pitching moment is expressed as

$$\left(C_{m_H}\right)_{\text{Installed}} = C_{m_H}(\alpha) \qquad (\alpha = 0,\ 5,\ 10,\ 15,\ 20 \text{ degrees}) \qquad (3.51)$$

For other angles of attack within this range, either graphical or numerical interpolation of equation (3.51) should be used.

The program output, equation (3.51),includes the effect of the horizontal tail lift and pitching moment. In order to include the pitching moment contribution of the horizontal tail drag, it is necessary to modify the program calculated horizontal tail drag for viscous effects. This has been discussed in Section 3.1.2.3 and the result is summarized in equations (3.32), (3.33), and (3.34). The pitching moment contribution of the empennage drag is then

$$C_m(\alpha,\beta)\Big|_{\text{tail drag}} = C_{D_H}(\alpha,\beta)\left[\frac{\ell_H}{\bar{c}}\sin\alpha + \frac{\Delta z_H}{\bar{c}}\cos\alpha\right] + C_{D_V}(\alpha,\beta)\left[\frac{\ell_V}{\bar{c}}\sin\alpha + \frac{\Delta z_V}{\bar{c}}\cos\alpha\right] \qquad (3.52)$$

where Δz_H is the height of the horizontal tail above (or below) the aircraft moment center, Δz_V is the height of the vertical tail aerodynamic center above the aircraft moment center, α and β are the wing angle of attack and angle of sideslip, respectively, and C_{D_H} and C_{D_V} are the total horizontal and vertical tail drag coefficients, respectively. Except for cases of extreme vertical tail loading, such as in a crosswind or in an engine-out condition, the vertical tail contribution in equations (3.52) can be neglected. Also, for conventional tailplane locations, the horizontal tail contribution in equation (3.52) can be neglected.

3.1.1.4 Fuselage Pitching Moment

The fuselage contribution to total aircraft pitching moment can be regarded as arising from two effects. One is due to the carryover of lift, and hence pitching moment, from the wing to the fuselage. This effect is accounted for in the present method by extending the wing planform to the aircraft plane of symmetry, and, therefore, it is an integral part of the

total wing pitching moment calculated in equation (3.45). The other effect is the pitching moment due to the noncirculatory flow about the fuselage, which is calculated directly by the computer program using a modified slender-body approach described in Volume I. The interference of the jet-wing is included in the computer methods, and because of the nonlinear nature of the interference, the program calculated fuselage pitching moment must be expressed as

$$C_{m_F} = C_{m_F}(\alpha) \qquad (\alpha = 0, 5, 10, 15, 20 \text{ degrees}) \qquad (3.53a)$$

The program-calculated C_{m_F}, equation (3.53a), should be corrected to account for boundary-layer separation and vortex shedding from the fuselage afterbody. Based on the approximate methods of Datcom (Section 4.2.2.1), equation (3.53a) can be corrected and is expressed as

$$C_{m_F}(\alpha)\Big|_{\text{corrected}} = C_{m_F}(\alpha) - \Delta C_{m_F}(\alpha) + \frac{2\alpha^2}{(57.3)^2 S\bar{c}} \int_{x_0}^{x_E} \eta r(\xi)\, c_{d_c}(x_{mc} - \xi)\, d\xi \qquad (3.53b)$$

where the first term is the program-calculated fuselage pitching moment; the second term accounts for non-potential flow effects on the after-body and is evaluated by summing the program-calculated fuselage sectional pitching moments from body station X_0 to X_E; and the third term accounts for the pitching moment due to viscous cross-flow drag on the fuselage afterbody. The terms in equation (3.53b) are defined in the text following equation (3.21).

3.2 Lateral Static Coefficients and Derivatives

Methods for calculating the lateral static coefficients and derivatives are discussed in the following sections. The procedure used to calculate the lateral aerodynamic characteristics of an aircraft configuration requires that the configuration be analyzed in a sideslipped condition (with the exception of the engine-out case). Such a procedure introduces a basic asymmetry into the problem which significantly complicates the solution.

The theoretical methods and associated computer programs discussed in Volumes I and II have been formulated to allow the sideslip condition to be treated, but additional approximations must be made, some of which may be significant. In sideslip, interferences become more difficult to handle

analytically, and the semi-empirical methods presented in Datcom and other references are based on sparse experimental data. It is the intention here to integrate the analytical methods developed in this work with existing semi-empirical techniques to provide a rational basis for estimating lateral aerodynamic characteristics.

3.2.1 Side Force

For an aircraft in normal flight through still air, there is no side force. However, for sideslipping flight (such as in a cross-wind) or for asymmetrical configurations (such as exists when there is an engine failure), there will be a nonzero side force on the aircraft which must be trimmed out by actuation of the appropriate controls. In this section, methods to calculate this side force are discussed. These methods are applicable to both sideslip and to asymmetrical configurations.

3.2.1.1 Total Wing Side Force

For conventional aircraft the primary contribution to side force is due to the fuselage and the vertical tail, the wing contribution being small by comparison. It is necessary to look more closely at the wing contribution for STOL aircraft employing a jet flap, however, to ascertain whether the jet sheet contributes significantly to side force. Unfortunately, within the context of the assumptions of the EVD method, the y-component of jet momentum is assumed to be negligibly small compared to the x- and z-components. Hence, in order to analytically treat a yawed jet-wing, it is necessary to yaw the wing but to leave the jet momentum confined to planes parallel to the x-z-plane, as illustrated in figure (3.20). According to the mathematical model, there is no side force component of the jet sheet reaction. Obviously the assumption of a negligible y-component of jet momentum for the sideslip case is incorrect since the ducting of the jet exit will be designed to insure emission of the jet in planes parallel to the aircraft plane of symmetry. Therefore, in the sideslip case some side force will be required to turn the jet so that it emits parallel to the x-z-plane. There is no analytical means by which to calculate this side force, however, since in practice the turning of the jet to the freestream direction will be accomplished both by the ducting of the jet flap and by the freestream itself. An estimate of the upper

limit of this side force would be to assume that the jet-flap ducting does no turning of the jet sheet, and then the side force is simply the jet reaction:

$$C_{Y_J} = -\frac{\sin \beta}{S} \int_{-b/2}^{b/2} c(y)\, c_\mu(y) \cos \theta(y) dy \approx -C_J \beta \qquad (3.54)$$

However, the actual jet contribution to C_Y may be less than that predicted by equation (3.54) because of the internal jet turning mechanism of the jet-flap ducting.

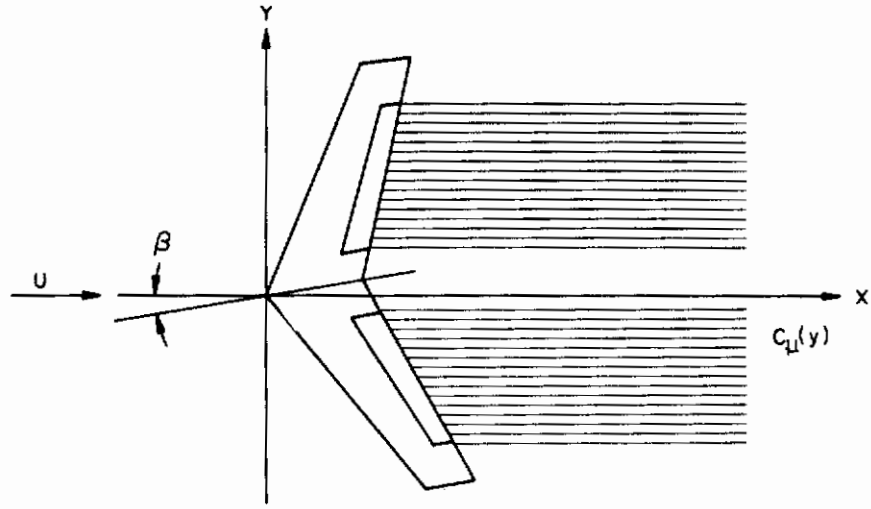

Figure (3.20). Illustration of Yawed Jet-Wing as Treated by the EVD Method.

To calculate the wing contribution to side force, the wing planform should be treated as asymmetrical and input as illustrated in figure (3.20). As discussed in Section 2.0, certain approximations to the planform must be made in this case, such as approximating the skewed wing tip by a tip parallel to the streamwise direction. In addition, flap edges must be approximated so that they are parallel to the freestream direction. Also, the jet momentum distribution must be altered to account for the sideslip angle β, which can simply be done by assuming

$$c_\mu(y)\Big|_\beta = c_\mu(y) \cos \beta \tag{3.55}$$

For internally ducted jet flaps, equation (3.55) should apply reasonably well for moderate sideslip angles, although for externally blown jet flaps the entire nature of the spreading and turning characteristics of the flap may change. Section 7.0 discusses further the nature of EBF systems.

The program calculated wing circulation side force is expressed in the form

$$C_{Y_\Gamma}(\alpha,\beta) = C_{Y_{\Gamma_O}}(\beta) + \left[\frac{\partial C_{Y_\Gamma}}{\partial \alpha}(\beta)\right]\alpha + \left[\frac{\partial^2 C_{Y_\Gamma}}{\partial \alpha^2}(\beta)\right]\alpha^2 \tag{3.56}$$

where each coefficient in equation (3.56) is implicitly a function of β. In order to determine C_Y over a range of β, it would be necessary to calculate C_Y for several sideslip angles and curve fit the coefficients of equation (3.56). In cases where only small sideslip angles need be considered, a reasonable engineering approximation would be to treat each of the coefficients in equation (3.56) as linear in β and then solve the sideslip problem for one particular β (say $\beta = 5°$ and $10°$) to determine the slope of the assumed linear curve. In this case C_Y can be expressed as

$$C_Y(\alpha,\beta) = \left[\frac{\partial C_{Y_{\Gamma_O}}}{\partial \beta}\right]\beta + \left[\frac{\partial^2 C_{Y_\Gamma}}{\partial \alpha \partial \beta}\right]\alpha\beta + \left[\frac{\partial^3 C_{Y_\Gamma}}{\partial^2 \alpha \partial \beta}\right]\alpha^2\beta \tag{3.57a}$$

and

$$\frac{\partial C_{Y_{\Gamma_O}}}{\partial \beta} = \frac{C_{Y_{\Gamma_O}}}{\beta}; \quad \frac{\partial^2 C_{Y_\Gamma}}{\partial \alpha \partial \beta} = \frac{1}{\beta}\frac{\partial C_{Y_\Gamma}}{\partial \alpha}; \quad \frac{\partial^3 C_{Y_\Gamma}}{\partial^2 \alpha \partial \beta} = \frac{1}{\beta}\frac{\partial^2 C_{Y_\Gamma}}{\partial \alpha^2} \tag{3.57b}$$

where β is the sideslip angle actually used to calculate the above terms. There is an additional contribution to the wing side force due to dihedral,

which can be calculated approximately by the program by defining a fundamental case with the twist distribution

$$\alpha_o(y) = \frac{\beta \cdot \Gamma(y)}{57.3} \frac{y}{|y|} \tag{3.58}$$

where Γ is the dihedral angle in degrees and β is the sideslip angle in degrees. Note that this fundamental case must be run for the yawed (asymmetrical) wing and that this twist distribution is actually anti-symmetrical. The fundamental case defined by equation (3.58) can be combined into a composite case just as any other type of fundamental case, but it is only applicable for small dihedral angles. An alternate approximation to the dihedral effect on C_Y is given by Datcom to be

$$C_Y\Big|_{\text{dihedral}} = -0.0001\Gamma\beta \qquad (\Gamma,\beta \text{ degrees}) \tag{3.59}$$

The total jet-wing side force coefficient can be determined from equations (3.54) and either (3.56) or (3.57). Because of the relative unimportance of the jet-wing contribution to C_Y and a general lack of understanding of the complex flow phenomenon occurring on a wing in sideslip, no viscous or thickness corrections are applied to these results.

3.2.1.2 Fuselage Side Force

The contribution of the fuselage to side force can be calculated in essentially the same manner as the lift on the fuselage is calculated (Section 3.1.1.4). Of course, there is a wing carryover side force as there was for lift, but the primary contribution to side force on the fuselage is due to boundary-layer separation and vortex shedding from the fuselage afterbody. Hence, the fuselage contribution to side force is

$$C_{Y_F} = -K_{WB}\left[\frac{2(K_M)A_o}{(57.3)S}\right]\beta + \frac{2}{(57.3)^2 S}\beta^2 \int_{x_o}^{x_E} \eta r c_d c\, dx \tag{3.60}$$

where

K_{WB} is an empirical wing-body interference factor from Datcom (Section 5.2.1.1) and plotted in figure (3.21).

β is the sideslip angle in degrees

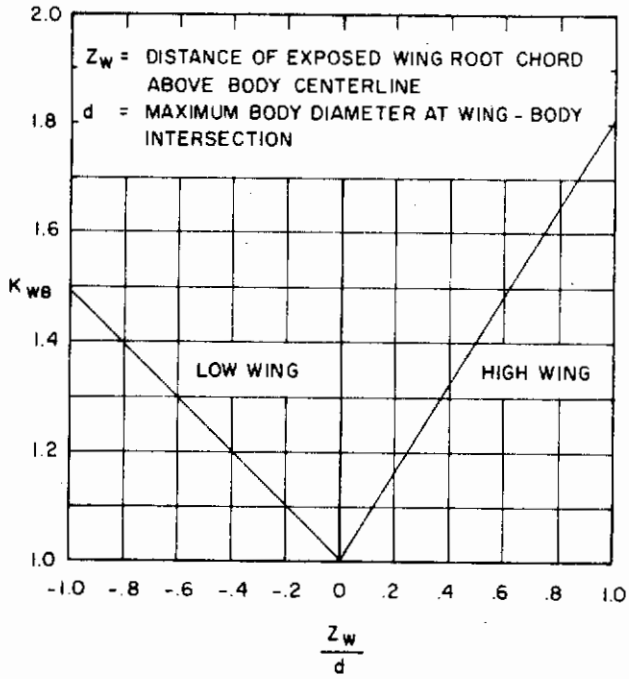

Figure (3.21). Empirical Wing-Body Interference Factor.

and the remaining terms are defined following equation (3.21).

The magnitude of C_{Y_F} is at least the same order as the wing side force and hence cannot be neglected.

3.2.1.3 Empennage Side Force

The empennage side force contribution is derived solely from the vertical tail and is calculated directly by the program, including the end-plate effects of the fuselage and horizontal tail and the external flow field influence of the jet-wing high lift system. The procedure used to calculate C_{Y_V} is similar to that employed for C_{L_H}, the lift contribution of the horizontal tail. Tail side force is calculated for the tail by itself (isolated tail analysis) in the form

$$\left(C_{Y_V}\right)_{Isol} = C_{Y_{o_V}} + \frac{\partial C_{Y_V}}{\partial \beta}\,\beta \qquad (3.61)$$

where the first term is the basic load level and includes the effects of any input surface deflections, particularly rudder deflection; and the second term is the slope of the linearized vertical tail side force curve. Tail side force is also calculated by the program for the tail within the induced flow field of the jet-wing (interference tail analysis) in the form

$$\left[C_{Y_V}(\alpha,\beta)\right]_{Installed} = C_{Y_V}(\alpha) \quad (\alpha=0,\ 5,\ 10,\ 15,\ 20 \text{ degrees}) \qquad (3.62)$$

where the β-variation can only be determined by running a range of sideslip angles. The sidewash gradient, $\partial\sigma/\partial\beta$, cannot be calculated accurately by the present methods and may be important for computing C_{Y_V}.

3.2.2 Rolling Moment

For STOL aircraft employing powered lift systems, there can be contributions to the aircraft rolling moment both from the aerodynamic forces on the airframe and from the reaction force of the jet sheet or vectored jets for sideslipping flight or for asymmetrical configurations. The methods discussed in this section are composed of the theoretical methods developed in Volume I and semi-empirical methods presented in Datcom.

3.2.2.1 Total Wing Rolling Moment

Unlike side force, the wing contribution to rolling moment can be significant. It is calculated directly by the program by defining the planform as in figure (3.20) for a sideslipping jet-wing or as in figure (3.22) for an asymmetrical configuration; in this case engine-out flight. The program calculated wing rolling moment is expressed in the form

$$C_l = C_{l_\Gamma} + C_{l_J} \qquad (3.63)$$

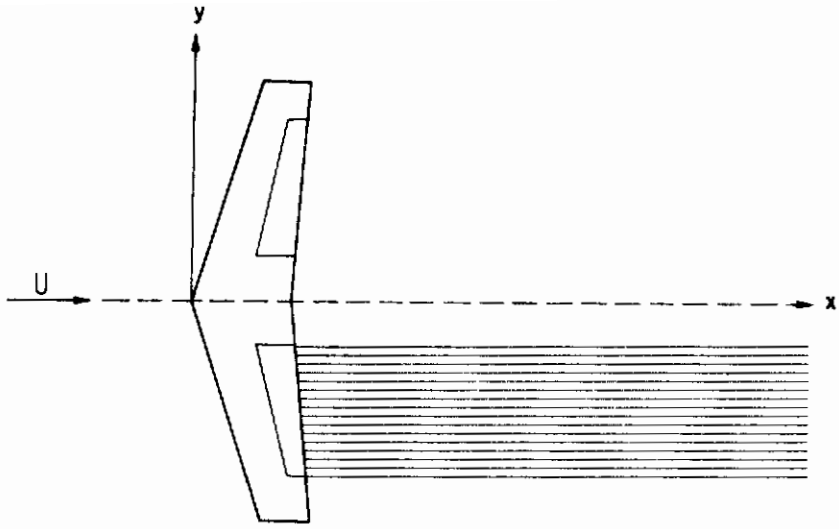

Figure (3.22). Illustration of an Asymmetrical Jet-Wing (Engine-Out Configuration).

where C_{l_Γ} is the wing circulation rolling moment and C_{l_J} is the jet-reaction rolling moment. Each of these terms is expressed as a function of angle of attack for a composite case in the form

$$C_{l_\Gamma}(\alpha,\beta) = C_{l_{\Gamma_o}}(\beta) + \left[\frac{\partial C_{l_\Gamma}}{\partial \alpha}(\beta)\right]\alpha \qquad (3.64a)$$

$$C_{l_J}(\alpha,\beta) = C_{l_{J_o}}(\beta) + \left[\frac{\partial C_{l_J}}{\partial \alpha}(\beta)\right]\alpha \qquad (3.64b)$$

where the β-dependence is implicit and can be determined by running several sideslip angles and curve fitting the coefficients of equation (3.64). For a jet-wing in ground-effect equation (3.64) must be modified to be

$$C_{l_\Gamma}(\alpha,\beta) = C_{l_{\Gamma_o}}(\beta) + \left[\frac{\partial C_{l_\Gamma}}{\partial \alpha}(\beta)\right]\alpha + \left[\frac{\partial^2 C_{l_\Gamma}}{\partial \alpha^2}(\beta)\right]\alpha^2 \qquad (3.64c)$$

while the mechanical flap systems with vectored thrust

$$C_{l_\Gamma}(\alpha,\beta) = C_{l_\Gamma}(\alpha,\beta) \qquad (\alpha = 0, 5, 10, 15, 20 \text{ degrees}) \qquad (3.64d)$$

While the longitudinal aerodynamic characteristics of a jet-wing are not critically dependent on the spanwise distribution of jet momentum, for the lateral characteristics, particularly rolling moment and yawing moment, it is imperative that the jet momentum distribution $c_\mu(y)$ be known accurately. Therefore, the simplified distributions of jet momentum for EBF systems suggested in Section 7.0 are not likely to be adequate for the calculation of lateral aerodynamic characteristics; and experimentally determined momentum distributions will be required.

One of the more important contributing factors to rolling moment is the effect of wing dihedral, Γ. Positive dihedral has the effect of increasing the angle of attack on the right wing by

$$\Delta\alpha = \sin\beta \sin\Gamma \approx \beta\Gamma \tag{3.65}$$

and decreasing the angle of attack on the left wing by the same amount (for positive β), resulting in a negative rolling moment. As discussed previously, dihedral can be accounted for by defining a fundamental case with the anti-symmetric twist distribution

$$\alpha_o(y) = \frac{\beta\Gamma(y)}{57.3}\frac{y}{|y|} \tag{3.66}$$

Equation (3.66) is applicable only to small dihedral angles and small sideslip angles.

If only small sideslip angles are to be considered, the β-dependence implied in equations (3.64) can be defined explicitly in the same manner as described for side force [equation (3.57)]. That is, solve the sideslip problem at a particular (small) β and then assume linear variation of each coefficient in equation (3.64) with β.

3.2.2.2 Fuselage Rolling Moment

The program does not calculate any influence of the body on rolling moment. However, the effect of the body in sideslip has been shown experimentally to change the wing rolling moment. First, the body changes the effective dihedral of the wing because the cross flow around the body locally induces a change in effective angle of attack of the wing. As illustrated in figure (3.23), the effective change in wing dihedral caused by the body is to

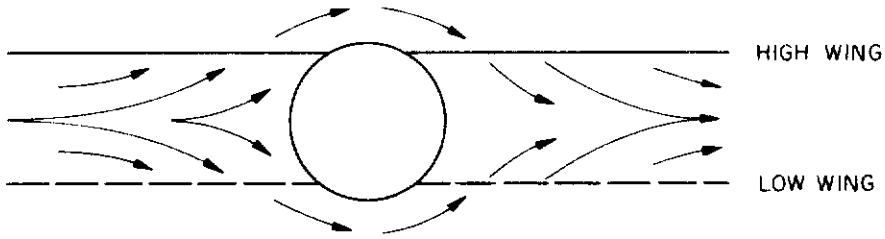

Figure (3.23). Illustration of the Change in Effective Wing Dihedral Induced by the Body in Sideslip.

increase the dihedral for high wings and to decrease the dihedral for low wings. Secondly, there is a decrease in the effective wing dihedral with increasing fuselage length, the decrease being a result of the fuselage reducing the effective sideslip angle on the wing as illustrated in figure (3.24).

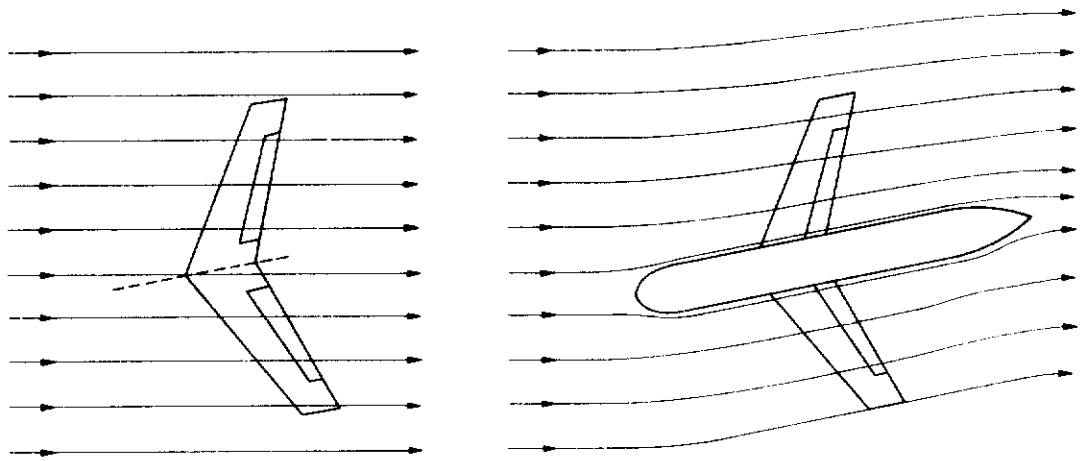

Figure (3.24). Illustration of the Decrease in Effective Wing Sideslip Angle with Increasing Fuselage Length.

Limited experimental studies have shown that the parameters of primary importance in determining the fuselage effect on rolling moment are the vertical position of the wing relative to the fuselage and the fuselage length ahead of the wing. The first effect can be approximately calculated using the semi-empirical relation

$$C_{l_{fuselage}} = -0.0005(AR)^{1/2}\left(\frac{d}{b}\right)^2 \Gamma\beta + 0.04188(AR)^{1/2}\left(\frac{z_w}{b}\right)\left(\frac{d}{b}\right)\beta \qquad (3.67)$$

where the first term accounts for the body-induced effect on wing dihedral for a wing located at the midfuselage height and the second term accounts for wings located above or below the midfuselage height, and where

$\frac{d}{b}$ is the average fuselage diameter at the wing root, normalized by the wing span.

$\frac{z_w}{b}$ is the height of the fuselage centerline relative to the quarter-chord root point of the wing, positive for the fuselage centerline above the wing.

$\overline{\Gamma}$ is the average wing dihedral angle, in degrees.

β is the sideslip angle, in degrees.

The effect of fuselage length forward of the wing can be approximately accounted for by applying a correction to the program calculated wing circulation rolling moment, equation (3.64), in the form

$$C_{l_{\Gamma_{wing\text{-}fuselage}}} = K_F C_{l_{\Gamma_{wing}}} \qquad (3.68)$$

where

K_F is the empirical fuselage length effect factor obtained from figure (3.25).

$\frac{\ell_F}{b}$ is the fuselage length ahead of the wing-tip half-chord point, normalized by wing span.

$C_{l_{\Gamma_{wing}}}$ is the program calculated circulation rolling moment, equation (3.64).

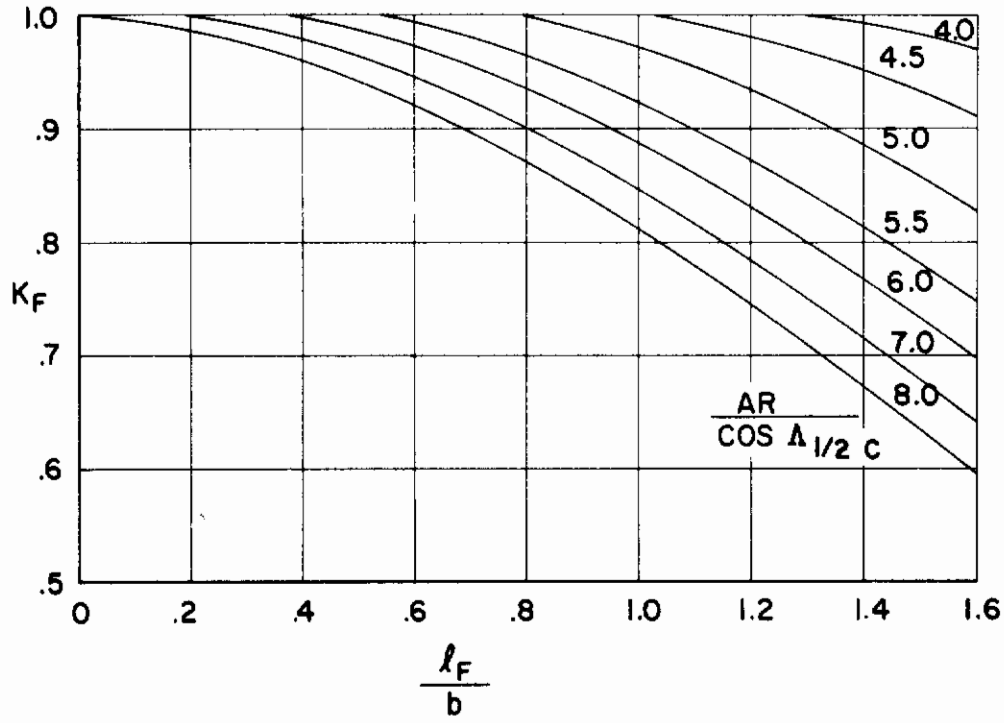

Figure (3.25). Empirical Fuselage Length Effect Factor.

3.2.2.3 Empennage Rolling Moment

The empennage rolling moment contribution is due to both the horizontal and vertical tails and is calculated directly by the program, including the endplate effect of the fuselage and the external flow field influence of the jet-wing. The empennage rolling moment is first calculated for the tail by itself (isolated tail analysis) in the form

$$C_{l_{tail}} = C_{l_{o_H}} + C_{l_{\alpha_H}} + C_{l_{o_V}} + C_{l_{\beta_V}}\beta \qquad (3.69)$$

where the first term is due to horizontal tail camber, elevator deflection, and the antisymmetric load induced on the horizontal tail by the vertical tail; and the third term is due to vertical tail surface deflection, in particular rudder deflection. The empennage rolling moment contribution is also calculated by the program for the tail within the induced flow field of the jet-wing (interference tail analysis) in the form

$$C_{l_H} = C_{l_H}(\alpha,\beta) \qquad (\alpha = 0,\ 5,\ 10,\ 15,\ 20 \text{ degrees}) \qquad (3.70a)$$

$$C_{l_V} = C_{l_V}(\alpha,\beta) \qquad (\alpha = 0, 5, 10, 15, 20 \text{ degrees}) \qquad (3.70b)$$

where the β-dependence is implicit and can only be calculated by running a range of sideslip angles. For small sideslip angles equation (3.69) should provide a sufficient estimate of $C_{l_{tail}}$ for preliminary design purposes.

3.2.3 Yawing Moment

Both aerodynamic forces on the airframe and the reaction force of the jet sheet or vectored jets contribute to aircraft yawing moment for STOL aircraft employing powered lift systems. It is necessary to calculate the yawing moment contribution of each aircraft component for sideslipping flight or for asymmetrical configurations, such as flight with an inoperative engine. The methods discussed in this section are based on the theoretical methods developed in Volume I and semi-empirical methods developed in Datcom.

3.2.3.1 Total Wing Yawing Moment

For jet-wings, the wing contribution to yawing moment can be significant, particularly for asymmetric jet momentum distributions. It is calculated directly by the program by defining the planform as in figure (3.20) for a sideslipping jet-wing or as in figure (3.22) for an asymmetrical configuration. The program calculated wing yawing moment is expressed in the form

$$C_n = C_{n_\Gamma} + C_{n_J} \qquad (3.71)$$

where C_{n_Γ} is the wing circulation yawing moment and C_{n_J} is the jet reaction yawing moment. The circulation contribution is due to the asymmetrical induced drag distribution and hence can be expressed, for a composite case, in the form

$$C_{n_\Gamma}(\alpha,\beta) = C_{n_{\Gamma_o}}(\beta) + \left[\frac{\partial C_{n_\Gamma}}{\partial \alpha}(\beta)\right]\alpha + \left[\frac{\partial^2 C_{n_\Gamma}}{\partial \alpha^2}(\beta)\right]\alpha^2 \qquad (3.71a)$$

while the reaction contribution can be expressed as

$$C_{n_J}(\alpha,\beta) = C_{n_{J_o}}(\beta) + \left[\frac{\partial C_{n_J}}{\partial \alpha}(\beta)\right]\alpha + \left[\frac{\partial^2 C_{n_J}}{\partial \alpha^2}(\beta)\right]\alpha^2 \qquad (3.71b)$$

where the β-dependence is implicit and can be determined by running several sideslip angles. It may be necessary to account for the asymmetrical distribution of profile drag as well, particularly for the engine-out case where loss of power can also mean loss of boundary-layer control and hence flow separation can occur asymmetrically. For example, consider the jet-wing configuration of figure (3.22). A good assumption to calculate the profile drag contribution to yawing moment would be to assume that the friction drag on each panel is the same, the only asymmetry being in drag due to separation. Assuming fully attached flow for the left wing panel (with blowing present), the yawing moment can be calculated solely for the right panel, being of magnitude

$$C_n\Big|_{\substack{\text{profile}\\\text{drag}}} = \Delta c_{d_{flap}} K_b \left(\frac{\bar{y}_{flap}}{b}\right) \tag{3.72}$$

where

$\Delta c_{d_{flap}}$ is the incremental sectional profile drag coefficient due to flap deflection, plotted in figures (3.15a) and (3.15b) for plain and single-slotted flaps, respectively.

K_b is a factor to account for partial span flaps, plotted in figure (3.16).

$\left(\frac{\bar{y}_{flap}}{b}\right)$ is the mean spanwise position of the flap, normalized by wing span.

Variations of equation (3.72) can easily be formulated subject to the nature of the case of interest.

Just as for rolling moment, it is necessary that the jet momentum distribution $c_\mu(y)$ be known accurately in calculating yawing moment since the spanwise location of the jet reaction enters directly in the integral for reaction yawing moment, as

$$C_{n_J} = \frac{1}{Sb} \int_{-b/2}^{b/2} c(y) c_{d_\mu}(y) y dy$$

Section 7.0 discusses empirical methods to estimate momentum distributions for EBF wings.

3.2.3.2 Fuselage Yawing Moment

The fuselage contribution to aircraft yawing moment is calculated in a manner similar to pitching moment. The yawing moment can be regarded as arising from two effects. One is due to the carryover of load from the wings onto the fuselage, and this effect is accounted for in the present method by extending the wing planform to the aircraft plane of symmetry. The other effect is the yawing moment due to the noncirculatory flow about the fuselage, which is calculated directly by the program using the modified slender-body fuselage analysis discussed in Volume I, and is expressed in the form

$$C_{n_F} = C_{n_F}(\alpha,\beta) \qquad (\alpha = 0,\ 5,\ 10,\ 15,\ 20 \text{ degrees}) \qquad (3.73)$$

The program calculated C_{n_F} includes the interference effects of the jet-wing, and the β-dependence can be determined by running several sideslip angles. A correction to C_{n_F} to account for boundary-layer separation and vortex shedding from the fuselage afterbody can be formulated in a manner analogous to equation (3.53b) for pitching moment, as

$$C_{n_F}(\alpha,\beta)\Big|_{\text{corrected}} = C_{n_F}(\alpha,\beta) - \Delta C_{n_F}(\alpha,\beta) + \frac{2\beta^2}{(57.3)^2 S\bar{c}} \int_{x_o}^{x_E} \eta r(\xi) c_{d_c} (x_{mc} - \xi)\, d\xi \qquad (3.74)$$

where the first term is the program calculated fuselage yawing moment; the second term accounts for non-potential flow effects on the after-body and is evaluated by summing the program-calculated fuselage sectional yawing moments from body station x_o to x_E; and the third term accounts for the yawing moment due to viscous cross-flow drag on the fuselage afterbody. The terms in equation (3.74) are defined in the text following equation (3.21).

3.2.3.3 Empennage Yawing Moment

It is assumed in the present analysis that only the vertical tail contributes to the empennage yawing moment, the yawing moment on the horizontal tail due to any asymmetrical loading distribution being of much smaller order and hence negligible. The program calculates the vertical tail yawing moment

first for the tail by itself (isolated tail analysis), but including the endplate effects of the fuselage and horizontal tail, in the form

$$\left(C_{n_V}\right)_{Isol} = C_{n_{0V}} + C_{n_{\beta V}}\beta \qquad (3.75)$$

where the first term is due to any input camber on the vertical tail, in particular rudder deflection. The tail yawing moment is also calculated for the tail within the induced flow field of the jet-wing (interference tail analysis) in the form

$$\left(C_{n_V}\right)_{Installed} = C_{n_V}(\alpha,\beta) \qquad (\alpha = 0, 5, 10, 15, 20 \text{ degrees}) \qquad (3.76)$$

where the β-dependence is implicit and can only be calculated by running a range of sideslip angles. For small sideslip angles, equation (3.75) should provide a sufficient estimate of $C_{n_{tail}}$ for preliminary design purposes.

4.0 STABILITY AND CONTROL ANALYSIS OF STOL AIRCRAFT

The subject of airplane stability and control has existed as a recognizable entity since before the first powered flight of the Wright brothers in 1903. Lanchester (reference 16) and Bryan (reference 17) are largely credited with the pioneering work in this field, although others, including the Wright brothers, made significant contributions to the early work. During this century airplane stability and control has developed into a complex science, taking a position of primary importance in the design of aircraft. The motion of an aircraft in flight is determined by the aerodynamic characteristics of the airframe, the reaction force supplied by the propulsive system, the force of gravity, the inertial characteristics of the airplane, and the nature of the atmosphere through which the airplane flies. For STOL aircraft employing powered lift systems, the propulsive system assumes a more important role than for conventional aircraft, influencing the aerodynamic characteristics of the airframe as well as providing large reaction forces.

The equations of motion for STOL aircraft are derived in the same manner as for conventional aircraft, equating the rate of change of momentum of the aircraft to the forces applied to it and the rate of change of angular momentum of the aircraft to the torque applied to it. These equations can fundamentally be written as

$$\begin{aligned} \Sigma F_x &= \frac{d}{dt}(mU) \\ \Sigma F_y &= \frac{d}{dt}(mV) \\ \Sigma F_z &= \frac{d}{dt}(mW) \end{aligned} \qquad (4.1)$$

$$\begin{aligned} \Sigma L &= \frac{dh_x}{dt} \\ \Sigma M &= \frac{dh_y}{dt} \\ \Sigma N &= \frac{dh_z}{dt} \end{aligned} \qquad (4.2)$$

where (U,V,W) are the total aircraft velocities in the (x,y,z) directions, respectively; and (h_x, h_y, h_z) are the components of angular momentum. As done in most classical treatments of the subject, a stability axis coordinate

system, illustrated in figure (4.1), will be used in this work. These axes are chosen such that the x-axis points in the direction of motion in a reference steady state condition; the z-axis is in the aircraft plane of symmetry, perpendicular to x-axis, positive down; and the y-axis forms a right-handed coordinate, positive on the right wing. The origin of this coordinate system is located at the wing apex, although for the purpose of calculating stability derivatives the rotation of the aircraft is assumed to be about the aircraft center of gravity (see Volume I, Section 2.2.4). (NOTE: This axis system, in some cases, differs from that used in DATCOM.)

The equations of motion, equations (4.1) and (4.2), can be expanded so that the aerodynamic, gravity, control system, and propulsive system forces and moments are explicitly defined. It is neither the purpose nor the intent of this work to derive the dynamic equations of motion for STOL aircraft, however, and the reader is referred to references 5, 7, and 8 for such derivations. It should be noted that although the final forms of the dynamic equations presented in each reference are slightly different, the equations are in essence the same, the differences being due to slightly different formulations of the basic problem. But each formulation does reduce to the same set of stability and control derivatives, the calculation of which is a primary objective of this work. It is necessary here, however, to examine the dynamic equations of motion, or rather their solution, in order to establish basic accuracy requirements for the stability and control derivatives.

Consistent with standard formulations of the non-dimensional small disturbance dynamic equations of motion, modified for power effects associated with STOL aircraft, the following aerodynamic and stability and control coefficients and derivatives are required, some of which have already been discussed in Section 3.0:

I. Longitudinal Characteristics:

   a. Static characteristics: C_L, C_{L_α}, C_D, C_{D_α}, C_m, C_{m_α}.

   b. Dynamic stability derivatives: C_{L_u}, C_{D_u}, C_{m_u}, $C_{L_{\dot\alpha}}$, $C_{m_{\dot\alpha}}$, C_{L_q}, C_{m_q}.

   c. Control derivatives: $C_{L_{\delta_e}}$, $C_{D_{\delta_e}}$, $C_{m_{\delta_e}}$, $C_{L_{\delta_s}}$, $C_{D_{\delta_s}}$, $C_{m_{\delta_s}}$, $C_{D_{\delta_a}}$.

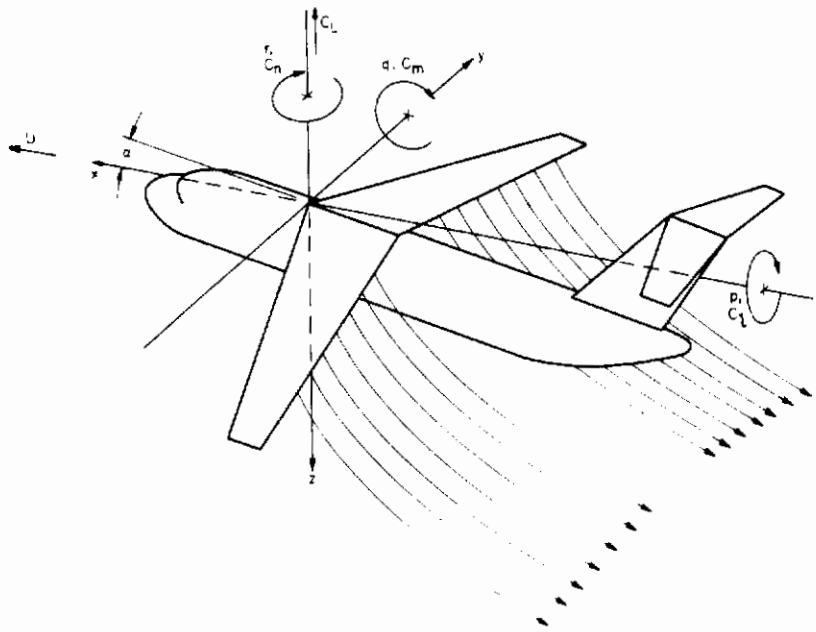

Figure (4.1). Reference Coordinate System for Dynamic Stability Derivatives.

II. Lateral Characteristics:

a. Static characteristics: C_{Y_β}, C_{l_β}, C_{n_β}.

b. Dynamic stability derivatives: $C_{Y_{\dot\beta}}$, $C_{l_{\dot\beta}}$, $C_{n_{\dot\beta}}$, C_{Y_p}, C_{l_p}, C_{n_p}, C_{Y_r}, C_{l_r}, C_{n_r}.

c. Control derivatives: $C_{Y_{\delta_a}}$, $C_{l_{\delta_a}}$, $C_{n_{\delta_a}}$, $C_{Y_{\delta_r}}$, $C_{l_{\delta_r}}$, $C_{n_{\delta_r}}$, $C_{Y_{\delta_{sp}}}$, $C_{l_{\delta_{sp}}}$, $C_{n_{\delta_{sp}}}$.

The static characteristics have been thoroughly discussed in Section 3.0; the dynamic stability derivatives are the subject of Section 5.0, and the control derivatives are the subject of Section 6.0.

4.1 Accuracy Requirements for Stability and Control Derivatives

In an analysis of this type, it is prudent to determine the importance of each influencing parameter on the final stability characteristics of the aircraft so that an estimate of the accuracy requirements for analytical methods can be established. Hence, a study was initiated at Douglas using available test data and previously established prediction techniques to determine the impact of each of the derivatives on the frequency and damping of the longitudinal and lateral-directional oscillatory modes. For this purpose, a complete set of aerodynamic data was generated for a typical STOL aircraft. The model selected for this study is based on the Douglas Aircraft Company Model D-915F, a configuration employing an externally blown jet flap, illustrated in figure (4.2). Baseline values of the aerodynamic and stability and control coefficients and derivatives, based to a large extent on wind tunnel test data, were used to establish reference values for the frequency and damping of the short-period response, the phugoid mode, Dutch-roll oscillation, roll mode, and spiral stability. Each coefficient and derivative was then varied from this baseline to establish its impact on the shape of the oscillatory modes, and these resulting modes were compared with the flying qualities criteria of MIL-F-83300. The relative magnitude of the variations in frequency and damping are considered to be indicative of the level of accuracy required of the prediction methods. In selecting a set of tolerances

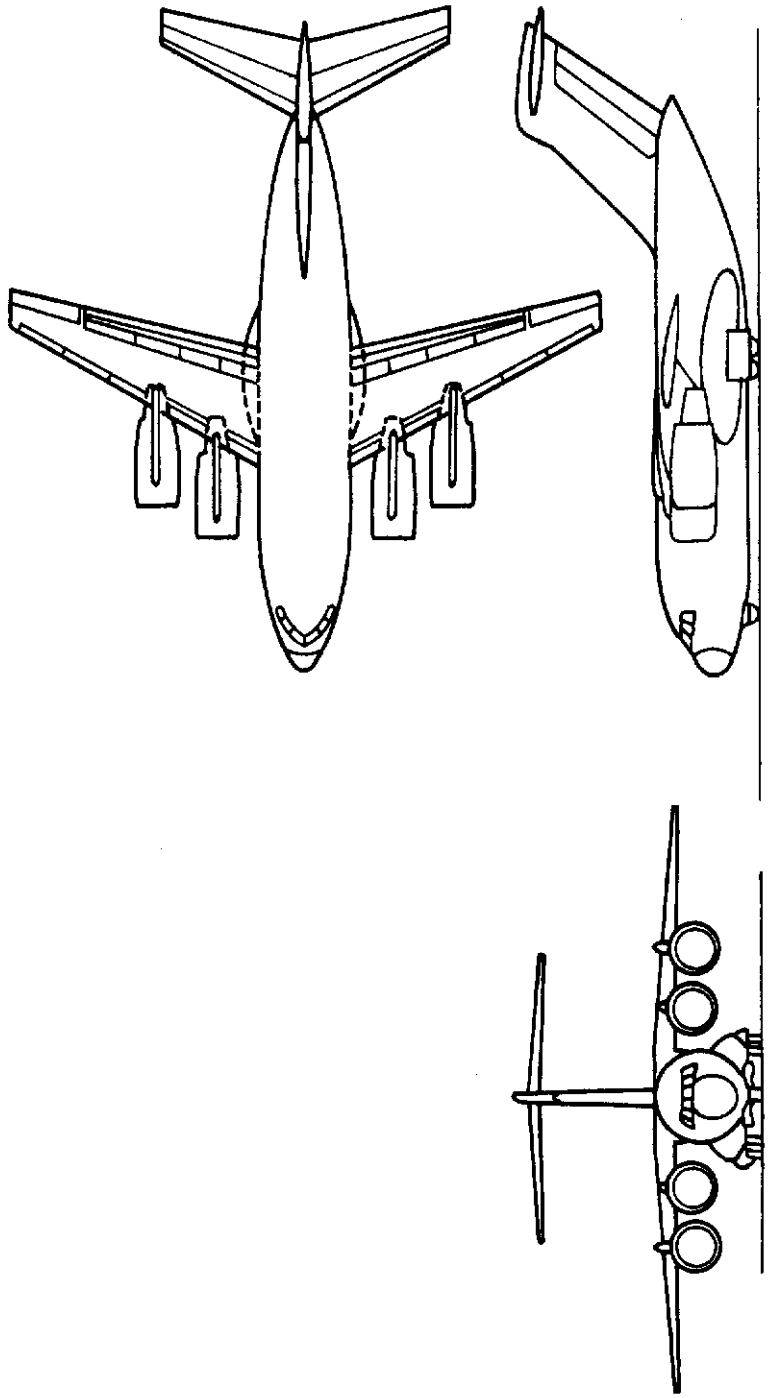

Figure (4.2). STOL Transport Model Employed in Sensitivity Study.

for these derivatives, consideration has been given to the relative importance of each derivative, to the critical nature of the flying qualities, and to the degree to which the derivatives can be controlled in configuration design work. Consideration has also been given to variations in the mass characteristics of the aircraft.

4.1.1 Baseline Configuration

The aircraft configuration employed in this study is based on the Douglas Aircraft Company Model D-915F, a STOL transport model employing externally blown jet flaps and illustrated in figure (4.2). The geometric and mass characteristics of the aircraft are tabulated in table (4.1), and the estimated longitudinal and lateral aerodynamic characteristics, based largely on wind tunnel test data presented in reference 18, are tabulated in tables (4.2) and (4.3), respectively. Some of these data are from reference 19 and are based on existing methods in Datcom.

Prior studies coupled with simulator experience have shown landing to be the most critical flight condition for STOL aircraft, and for this reason only one basic flight condition was considered in this study. A representative power approach condition with the airplane trimmed to a speed of 75 knots and with sufficient power to maintain a 7.5 degree glideslope has been used. A nominal center of gravity location of 25% MAC was used.

Table (4.1) Model D-915F Baseline Configuration

b 114.6 ft	b_H 58.6 ft	b_V 17 ft
S 1875 ft^2	S_H 640 ft^2	S_V 560 ft^2
AR 7.0	AR_H 5.0	AR_V 1.0
λ 0.3	λ_H 0.25	λ_V 0.75
$\Lambda c/4$ 25°	$\Lambda_{Hc/4}$ 25°	$\Lambda_{Vc/4}$ 42°
C.G. 25% MAC	ℓ_H 63 ft	ℓ_V 46 ft
W 150000 lbs	Iy 2.67×10^6 slug-ft^2	Ix 1.55×10^6 slug-ft^2
I_Z 3.98×10^6 slug-ft^2	I_{XZ} 5×10^5 slug-ft^2	δ_f 30°/20°

Table (4.2) Estimated Longitudinal Aerodynamic Characteristics of Baseline Configuration (references 18 and 19)

C_{L_α}	0.12325 deg^{-1}	$\partial\epsilon/\partial\alpha$	0.638
C_{D_α}	0.0525 deg^{-1}	$\partial C_L/\partial C_\mu$	1.2346
C_{m_α}	-0.03288 deg^{-1}	$\partial C_D/\partial C_\mu$	-0.11963
$C_{L_{\dot\alpha}}$	0.10208	$\partial C_m/\partial C_\mu$	-0.7616
$C_{m_{\dot\alpha}}$	-0.3583	$\partial F_g/\partial V_T^{\dagger}$	9.18
C_{L_q}	0.2294	$\partial F_R/\partial V_T^{\ddagger}$	17.9
C_{m_q}	-0.5936		
$C_{m_{i_H}}$	-0.080 deg^{-1}		

† Change in gross thrust with airspeed (lb/ft/sec)

‡ Change in ram drag with airspeed (lb/ft/sec)

Table (4.3) Estimated Lateral Aerodynamic Characteristics of Baseline Configuration (references 18 and 19)

C_{Y_β}	-0.0362 deg^{-1}	C_{Y_r}	0.0154
C_{l_β}	-0.00693 deg^{-1}	C_{l_r}	0.02095
C_{n_β}	0.00808 deg^{-1}	C_{n_r}	-0.01008
C_{Y_p}	0.00825	$C_{Y_{\dot\beta}}$	0.00023
C_{l_p}	-0.0112	$C_{Y_{\dot p}V_T}$	-0.092
C_{n_p}	-0.00601	$C_{l_{\dot\beta}}$	0.00005

4.1.2 Dynamic Analysis

Using the baseline configuration aerodynamic data as a reference point, baseline values of the frequency and damping ratios of the oscillatory modes have been calculated using Douglas in-house dynamic analysis methods. These methods essentially calculate the coefficients of the linearized three-degree-of-freedom equations of motion, both longitudinal and lateral, and also calculate the roots of the characteristic equations. Once the baseline mode shapes were determined, then variations of the baseline derivatives of up to ±50 percent were made, and their effects on the oscillatory modes were determined.

4.1.2.1 Longitudinal Modes

The effects on the frequency and damping of the longitudinal modes caused by variations in the parameters listed in table (4.2) are presented in figures (4.3) and (4.4). The baseline values of the damping and frequency ratios for the longitudinal modes have been calculated to be

$$\text{Short-period:} \quad \begin{aligned} \zeta_{sp} &= 0.862 \\ \omega n_{sp} &= 0.822 \ \text{sec}^{-1} \end{aligned} \tag{4.1}$$

$$\text{Phugoid:} \quad \begin{aligned} \zeta_{p} &= 0.01 \\ \omega n_{p} &= 0.350 \ \text{sec}^{-1} \end{aligned} \tag{4.2}$$

These data show that the baseline configuration is stable and meets the Level 1 requirements of paragraph 3.3.2 of MIL-F-83300 (i.e., all roots of the characteristic equation are stable). Figures (4.3) and (4.4) show the relative sensitivity of the frequency and damping ratio of each of the modes to changes in each of the derivatives. These figures show the effects of a one percent change in the derivatives and indicate the direction of change of each derivative required to effect an increase in frequency and damping. It should be noted that changes in any of the derivatives of up to 50 percent from the baseline value are acceptable for the short period mode since the oscillation remains damped. However, the baseline phugoid mode is

SHORT PERIOD MODE

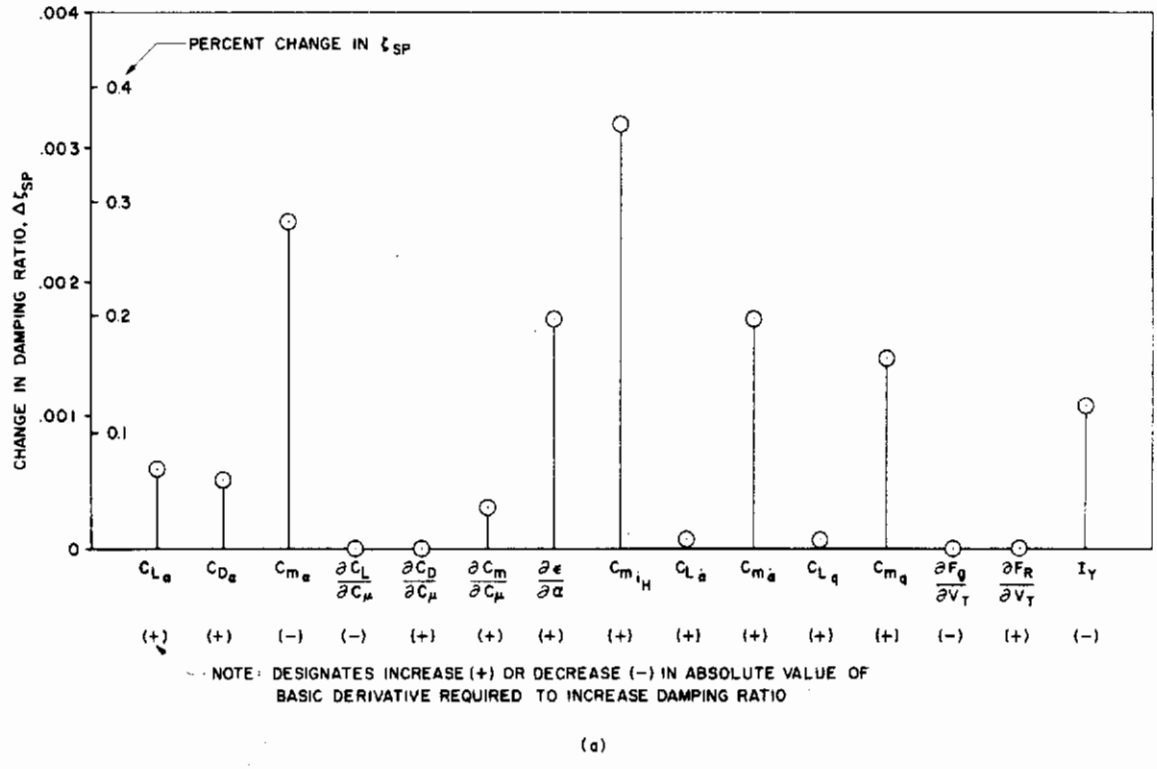

(a)

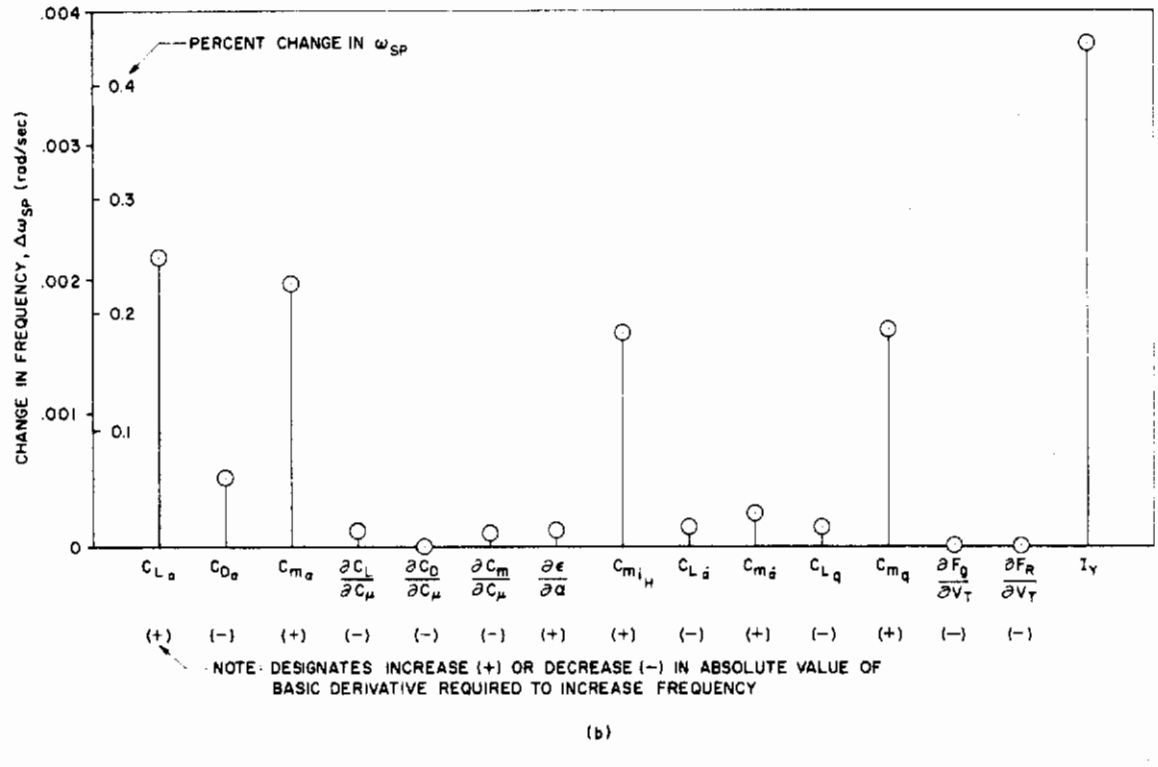

(b)

Figure (4.3). Incremental Change in Damping and Frequency of Short Period Oscillation Due to a One-Percent Change in Each Derivative.

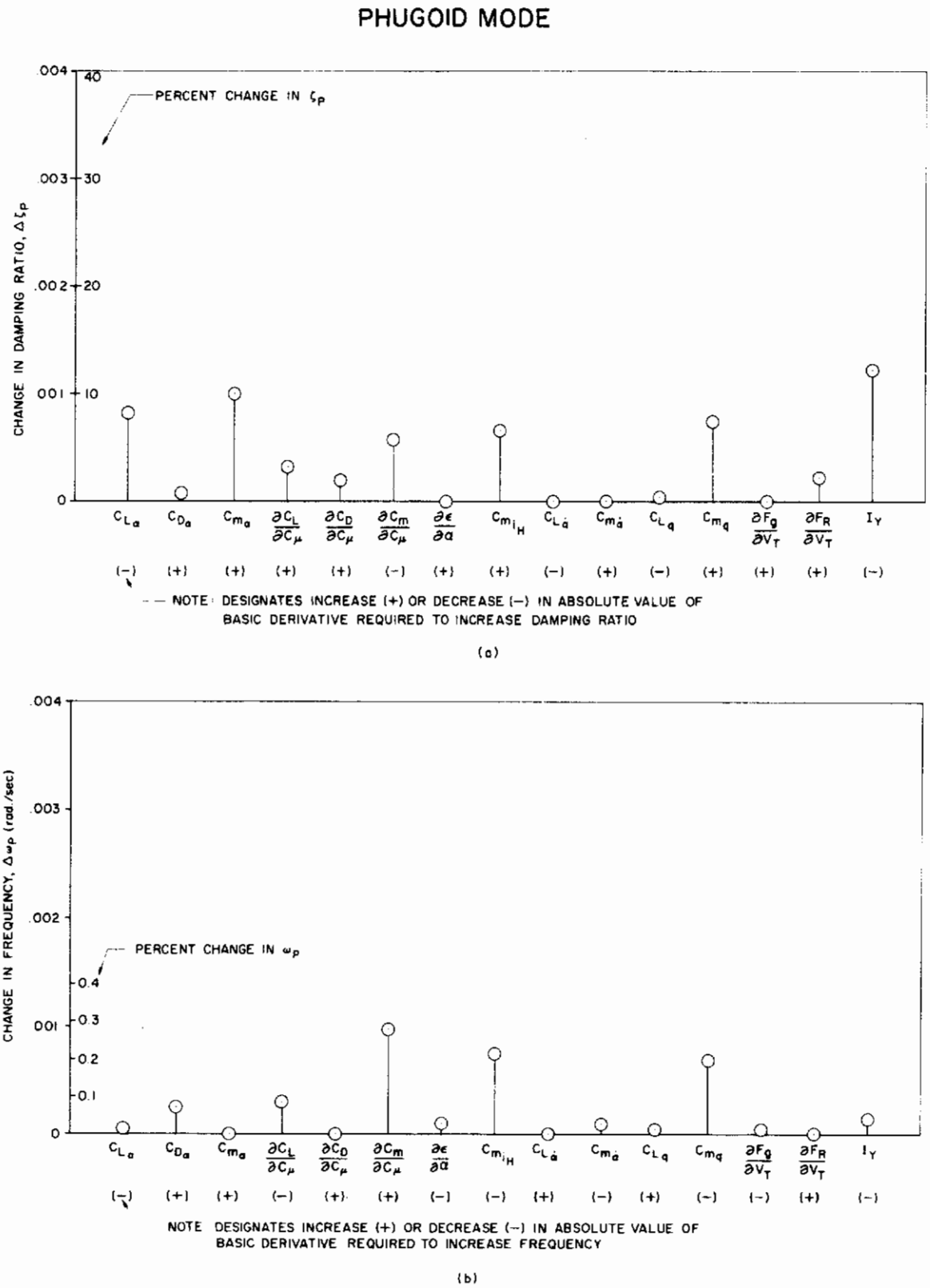

Figure (4.4). Incremental Change in Damping and Frequency of Phugoid Oscillation Due to a One-Percent Change in Each Derivative.

lightly damped and can become divergent for changes in some derivatives (e.g., C_{m_α}, I_Y) of only 10 percent. In none of the cases examined, however, does the time to double amplitude of the phugoid become less than the Level 2 limit of 12 seconds, which is considered acceptable for the phugoid mode.

Based on an extensive analysis of the data summarized in figures (4.3) and (4.4), tolerances for each of the derivatives can be established which will result in a negligibly small inaccuracy in the estimated longitudinal dynamic characteristics. The following tolerances have been established as a guideline:

(a) 5% tolerance on I_Y, C_{L_α}, C_{m_α}, $\frac{\partial \epsilon}{\partial \alpha}$, $C_{m_{i_H}}$, $C_{m_{\dot{\alpha}}}$, C_{m_q}.

(b) 25% tolerance on C_{D_α}, $\frac{\partial C_L}{\partial C_\mu}$, $\frac{\partial C_m}{\partial C_\mu}$, $\frac{\partial F_R}{\partial V_T}$, $\frac{\partial C_D}{\partial C_\mu}$.

(c) 100% tolerance on $C_{L_{\dot{\alpha}}}$, C_{L_q}, $\frac{\partial F_g}{\partial V_T}$.

This is not to imply that a larger tolerance or uncertainty in any of these quantities would lead to an inadequate dynamic analysis, but in order to allow for the build up of error, these tolerances have been made more stringent than may actually be required.

4.1.2.2 Lateral-Directional Modes

The effects on the frequency, damping ratio, and time constants of the lateral-directional modes caused by variations in the parameters listed in table (4.3) are presented in figures (4.5) and (4.6). The baseline values of the frequency, damping ratio, and time constants for the lateral-directional modes have been calculated to be

$$\text{Dutch-roll:} \quad \zeta_D = 0.104 \qquad \omega_{n_D} = 0.95 \text{ sec}^{-1} \tag{4.3}$$

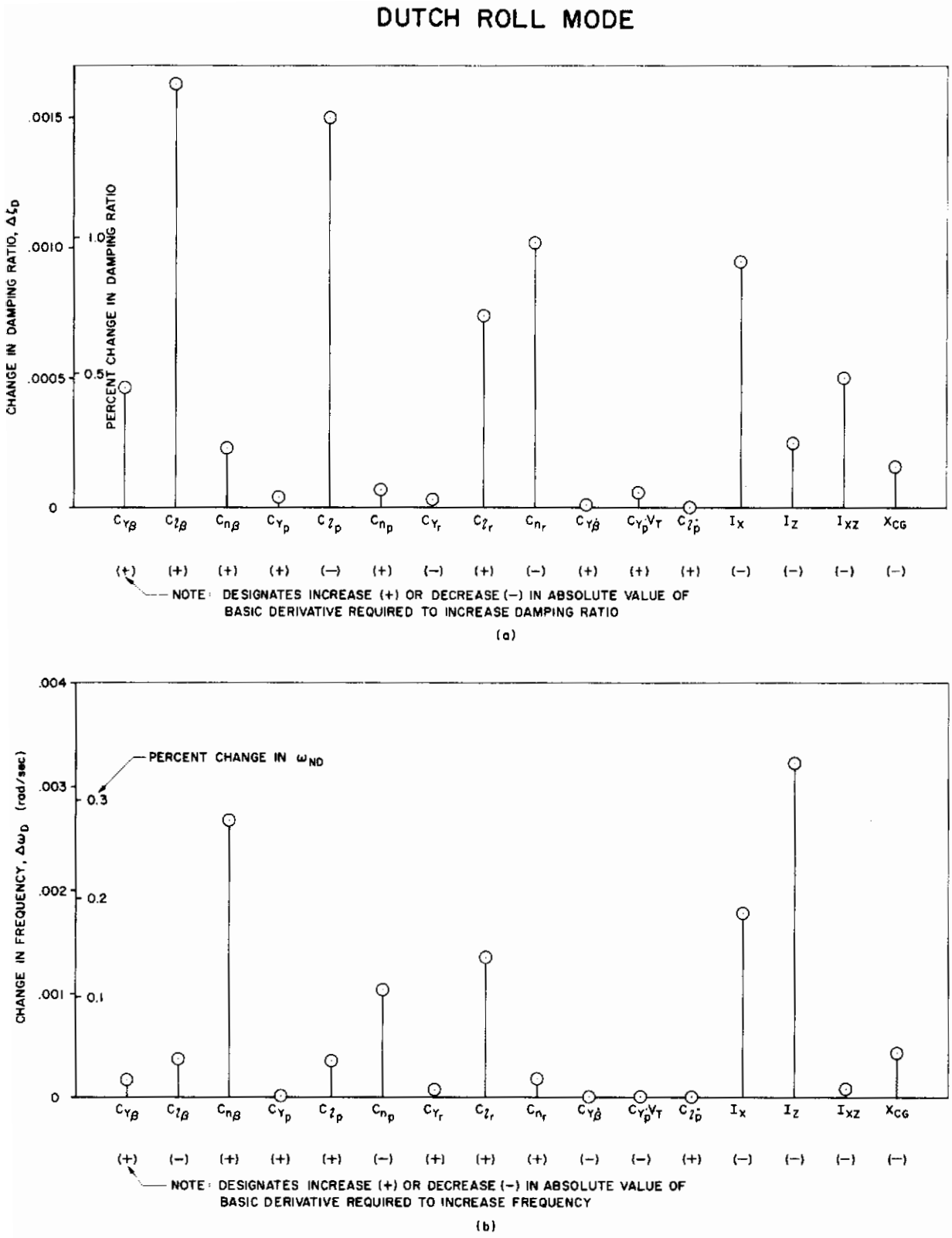

Figure (4.5). Incremental Change in Damping and Frequency of Dutch Roll Oscillation Due to a One-Percent Change in Each Derivative.

ROLL MODE & SPIRAL MODE

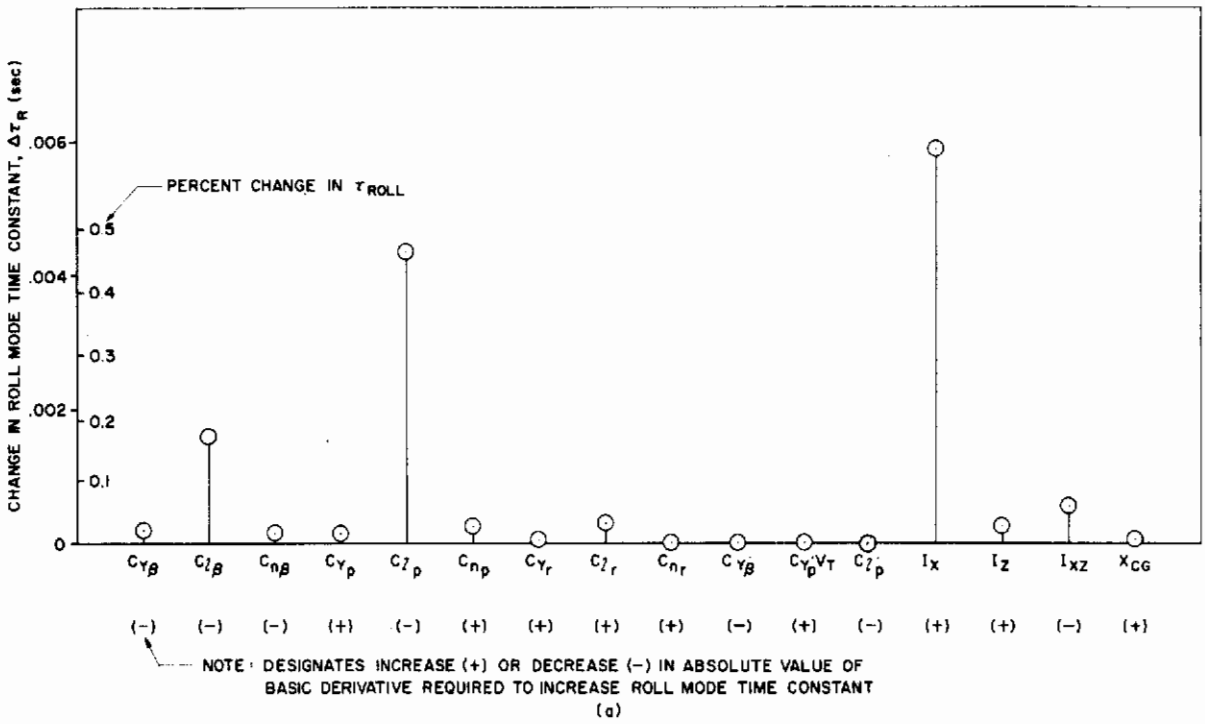

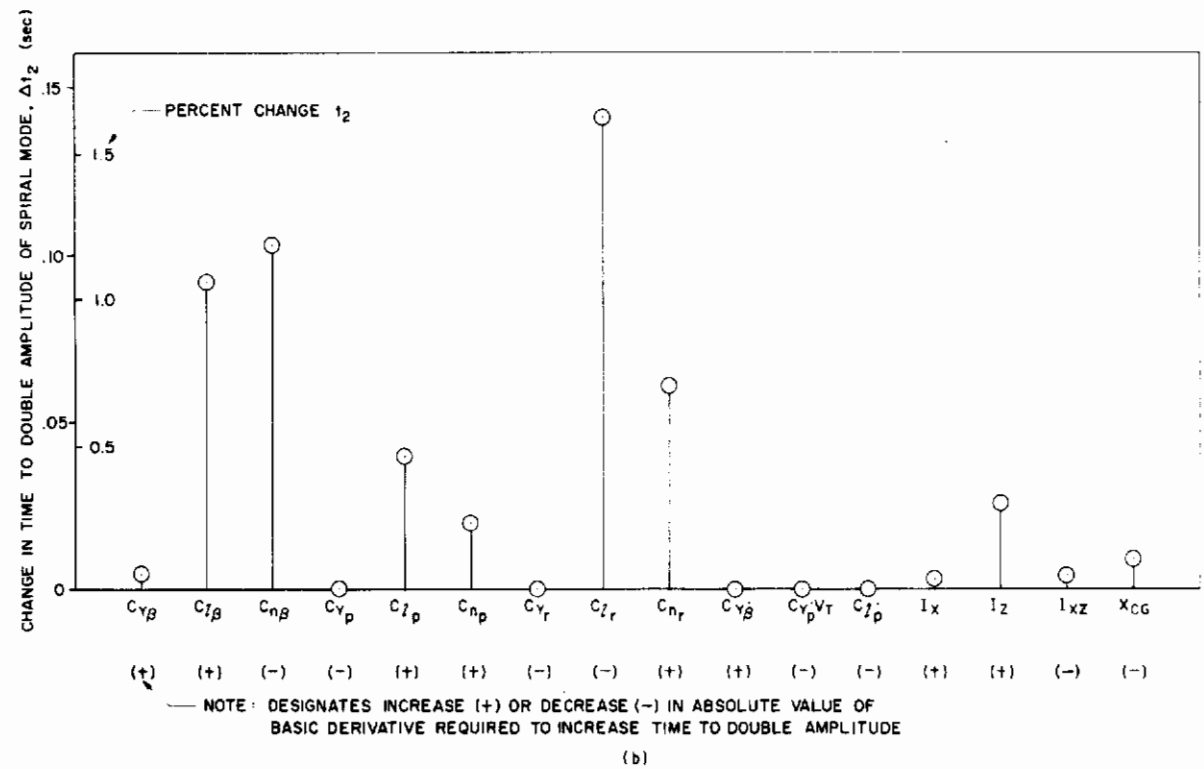

Figure (4.6). Incremental Change in Roll Mode Time Constant and Time to Double Amplitude of Spiral Mode Due to a One-Percent Change in Each Derivative.

Roll Mode: τ_R = 0.94 sec (time constant) (4.4)

Spiral Mode: t_2 = 7.7 sec (time to double amplitude) (4.5)

These data show that the Dutch-roll mode of the baseline configuration is stable and meets Level 1 requirements. The roll mode time constant, τ_R, is satisfactory, being less than one second, and falls well below the Level 1 limit. However, for the baseline configuration the spiral stability is divergent and marginal in that it meets only the Level 3 requirement. Figures (4.5) and (4.6) indicate the relative sensitivity of the mode shapes to changes in each of the pertinent aerodynamic parameters, showing the effects of a one percent change in each derivative. These figures indicate that the derivatives of major impact on the Dutch-roll and spiral modes are the rolling and yawing moments due to sideslip (C_{l_β} and C_{n_β}), due to roll rate (C_{l_p} and C_{n_p}), and due to yaw rate (C_{l_r} and C_{n_r}). The roll mode time constant is dependent primarily on the rolling moments due to sideslip and roll rate (C_{l_β} and C_{l_p}).

Based on an analysis of the data summarized in figures (4.5) and (4.6), tolerances for each of the pertinent derivatives can be established as for the longitudinal modes. These are as follows:

(a) 5% tolerance on C_{l_β}, C_{l_p}, C_{l_r}, C_{n_β}, C_{n_p}, C_{n_r}.

(b) 20% tolerance on C_{Y_β}

(c) 100% tolerance on C_{Y_p}, $C_{Y_{\dot{\beta}}}$, C_{Y_r}, $(C_{Y_p}.V_T)$

5.0 DYNAMIC STABILITY DERIVATIVES

The dynamics of the airframe and the aerodynamics of the airplane are related through the stability derivatives. Indeed, the equations of motion, equations (4.1) and (4.2), are applicable to the motion of any mechanical system; and the introduction of aerodynamics to the problem is brought about only by defining certain forces as aerodynamic forces and certain moments as aerodynamic moments. Suitable non-dimensionalization of the equations of motion (e.g., see reference 5) leads to the complete set of static and dynamic stability derivatives.

It has been shown in Section 4.1 that small changes in the values of some of the stability derivatives can produce large changes in the response of the airframe to disturbances. Hence, a knowledge of the values of the stability derivatives is required in the preliminary design of the airframe, control systems, and certain avionics systems. A knowledge of the variations of these derivatives with changes in the airframe configuration is also vital to the design engineer.

In the following sections each of the dynamic stability derivatives required to calculate the response characteristics of STOL aircraft to disturbances in flight conditions is discussed in detail, including discussions concerning those factors that affect the value of each derivative and methods for calculating each of the derivatives. Most of the prediction methods discussed in the following sections are based on the theoretical methods developed in Volume I of this report, implemented through use of the STOL Aerodynamic Methods Program (STAMP), described in Volume II. In addition, for those derivatives not amenable to theoretical treatment, semi-empirical methods are presented.

In the calculation of the dynamic stability derivatives, certain assumptions have been made which can limit the scope of applicability of the results, and hence it is necessary at this time to discuss these assumptions and their implications. Perhaps the most important assumption made in this work (and in most classical treatments of dynamic stability) is that the stability derivatives can be calculated in a quasi-steady state. That is, it is assumed

that the aerodynamic forces and moments acting on the airplane are dependent on only the velocities (both linear and angular) of the airplane, which implies that the forces and moments during a dynamic motion are the same as those acting on the airplane in steady flight with the same velocities as at some instant of the dynamic motion. This is equivalent to assuming that the entire flow field adjusts instantaneously to any perturbation in the flight condition, and hence the history of the motion is neglected. In light of this assumption, forces and moments dependent on the rates of change of velocity are neglected. However, as will be shown later, it is necessary to account for certain acceleration effects insofar as the interaction between the wing and tail are concerned, these effects normally being treated using the so-called $\dot{\alpha}$ and $\dot{\beta}$ derivatives. The applicability of the quasi-steady approach to jet-wings, where the dynamic motions can result in perturbations to the jet sheet shape which may be of importance, remains to be satisfactorily determined, and at this time an experimental investigation may be warranted.

In addition to the quasi-steady assumption, several other assumptions have been made which limit the range of applicability of the stability analysis, but these assumptions are consistent with classical theory and are not considered to be overly restrictive. These assumptions include:

1. The airplane is assumed to be a rigid body.
2. The atmosphere is assumed to be fixed and uniform.
3. Changes in the mass of the airplane during the dynamic motion are assumed to be negligible.
4. Disturbances from the steady flight condition are assumed to be small such that products of the disturbances are assumed to be negligible and that the sine and tangent of disturbance angles can be taken to be the angle itself and the cosine to be equal to 1.0.
5. In the steady flight condition, the airplane is assumed to be in straight level flight, with all velocity components except U and W equal to zero ($V = P = Q = R = 0$).

It is an unfortunate fact that stability derivatives appear in various treatments of the subject in a number of different forms. Both dimensional

and non-dimensional stability derivatives are in common usage, and there are also stability derivative parameters in use which involve the moments of inertia as well as the terms in the standard derivatives. In this work only the non-dimensional stability derivatives will be used, which correspond to the non-dimensional equations of motion. The notation used here is the same as that defined by NACA and that used by Etkin (reference 7). The basic non-dimensionalizing variables are the time constant $t^* = \ell/U$, the characteristic length $\ell = \frac{1}{2}\bar{c}$ for the longitudinal derivatives, and the characteristic length $\ell = \frac{1}{2}b$ for the lateral derivatives. Finally, all stability derivatives are calculated in the stability axis system illustrated in figure (4.1).

5.1 Longitudinal Dynamic Stability Derivatives

Methods for calculating the dynamic stability derivatives pertinent to the longitudinal oscillatory modes are presented in the following sections. In conjunction with the stability sensitivity study presented in Section 4.1, the importance of each of the derivatives to the short-period mode and the phugoid oscillation are also discussed. Table (5.1) summarizes the terms required for the longitudinal stability analysis and indicates for which aircraft components methods are required to calculate each term.

Table (5.1) Longitudinal Stability Parameters

Stability Parameter	Contribution				Section Number
	Jet-Wing	Fuselage	Horizontal Tail	Vertical Tail	
C_L, C_{L_α}	●	●	●		3.1.1
C_D, C_{D_α}	●	●	●	●	3.1.2
C_m, C_{m_α}	●	●	●		3.1.3
C_{L_u}	●		●		5.1.1.1
C_{D_u}	●		●		5.1.1.2
C_{m_u}	●		●		5.1.1.3
C_{L_q}	●		●		5.1.2.1
C_{m_q}	●	●	●		5.1.2.2
$C_{L_{\dot{\alpha}}}$	●		●		5.1.3.1
$C_{m_{\dot{\alpha}}}$	●		●		5.1.3.2

5.1.1 Variation of Forward Speed Derivatives

The variation of forward speed or "u" derivatives relate the effect on the aerodynamic forces and moments of an increase in the forward speed of the aircraft, the angle of attack, control angles, and power setting remaining constant. The u derivatives arise from the effects of Mach number and Reynolds number, both of which increase with forward speed. In addition, aeroelastic effects can be regarded as dependent on forward speed. Finally, the variation of jet momentum coefficient with forward speed must be considered, this effect being predominant for STOL aircraft employing powered lift systems where the engine thrust contributes both to wing circulation and jet reaction. In fact, if it were not for the thrust effect, it may be argued that the u derivatives could be neglected for the STOL phase of flight.

In the following sections the u derivatives are derived based on the non-dimensional forward speed $\hat{u} = (u+U)/U$ where u is the change in forward speed and U is the reference forward speed.

5.1.1.1 Change in Lift Due to Variation in Forward Speed (C_{L_u})

The derivative expressing the change in lift due to variation in forward speed is defined as

$$C_{L_u} = \left(\frac{\partial C_L}{\partial \hat{u}}\right)_o = U\left(\frac{\partial C_L}{\partial u}\right)_o \tag{5.1}$$

the subscript zero indicating that the derivative is to be evaluated at the reference condition. The Reynolds number and aeroelastic effects are considered to be negligibly small, and the Mach number effect, expressed as

$$C_{L_u}\Big|_{Mach} = M\left(\frac{\partial C_L}{\partial M}\right)_o \tag{5.2}$$

is important only in the high speed flight regime, which is not of interest in this work. The remaining effect is that due to the variation with forward speed of the jet momentum. This effect is manifested in the jet momentum coefficient, C_J, since for constant engine thrust C_J is a function of

forward speed, as can be expressed as

$$C_J = \frac{J}{\frac{1}{2}\rho(U+u)^2 S} \tag{5.3}$$

It is also possible, however, that the jet momentum J is also a function of forward speed, even at a constant throttle setting, so that the variation of C_J with forward speed can be expressed as

$$\left.\frac{\partial C_J}{\partial u}\right|_o = \frac{1}{\frac{1}{2}\rho U^2 S} \left.\frac{\partial J}{\partial u}\right|_o - \frac{1}{\frac{1}{2}\rho U^2 S} \frac{2J}{U} \tag{5.4}$$

The derivative $\left.\frac{\partial J}{\partial u}\right|_o$ is a characteristic of the engine/airframe and must be determined from flight test, although it is common practice to neglect the term since it is usually small. The second term of equation (5.4) must be considered, however, since it can significantly affect both the circulation and reaction lift components. The reaction term can be computed in a straightforward manner as

$$\left.\frac{\partial C_{L_J}}{\partial u}\right|_o = - C_J\left(\frac{2}{U}\right) \theta \tag{5.5}$$

where θ is the jet deflection angle relative to the freestream (in radians). The corresponding term for circulation lift C_{L_Γ} cannot be so simply calculated, however, owing to the complex relationship between C_{L_Γ} and C_J. It is recommended, therefore, that to determine C_{L_u} that the computer program be run over a range of jet momentum coefficients corresponding to a range of forward speeds, and then the derivative C_{L_u} can be calculated from the program solution as

$$C_{L_{\Gamma u}} = \left(\frac{\partial C_{L_\Gamma}}{\partial \hat{U}}\right)_o = U\left(\frac{\partial C_{L_\Gamma}}{\partial u}\right)_o \approx U\left(\frac{\Delta C_{L_\Gamma}}{\Delta u}\right)_o \tag{5.6}$$

The forward speed variation Δu in equation (5.6) is calculated by assuming the jet momentum J to be constant and can be expressed as

$$\frac{\Delta u}{U} = \frac{\sqrt{C_{J_o}}}{\sqrt{C_{J_2}} - \sqrt{C_{J_1}}} \tag{5.7}$$

where C_{J_0} is the reference momentum coefficient and C_{J_1} and C_{J_2} are the momentum coefficients corresponding to C_{L_1} and C_{L_2}, where $\Delta C_L = C_{L_2} - C_{L_1}$.

The C_{L_u} derivative is considered to be relatively unimportant in the dynamic stability analysis of conventional aircraft, although there is some evidence that it does affect the phugoid mode in such a manner that an increase in C_{L_u} can decrease the period of oscillation. For STOL aircraft, this derivative is likely to be more important, although further research is required to establish any trends.

5.1.1.2 Change in Drag Due to Variation in Forward Speed (C_{D_u})

The derivative expressing the change in drag due to variation in forward speed is defined as

$$C_{D_u} = \left(\frac{\partial C_D}{\partial \hat{u}}\right)_o = U\left(\frac{\partial C_D}{\partial u}\right)_o \tag{5.8}$$

and is known as the speed damping derivative, since it gives the resistance to an increase in speed. As was done for C_{L_u}, the Reynolds number and aeroelastic effects are neglected, and the Mach number effect,

$$C_{D_u}\Big|_{Mach} = M\left(\frac{\partial C_D}{\partial M}\right)_o \tag{5.9}$$

need be considered only in the speed regime where the drag rise is appreciable. The effect due to the variation with forward speed of the jet momentum coefficient is again of paramount importance, and can again be expressed as in equation (5.4). For jet aircraft, it is common to neglect the term $\frac{\partial J}{\partial u}\Big|_o$, but the effect on C_{D_Γ} and C_{D_J} must be considered. The reaction term can be quickly estimated to be

$$\frac{\partial C_{D_J}}{\partial u}\Big|_o = -C_J\left(\frac{2}{U}\right)\left(1 - \frac{\theta^2}{2}\right) \tag{5.10}$$

but the circulation term must be calculated in a manner similar to that described earlier for C_{L_Γ}. That is, run the program for a range of momentum coefficients corresponding to the range of velocities as calculated in

equation (5.7), and then calculate the speed damping derivative from

$$C_{D_{T_u}} = \left(\frac{\partial C_{D_T}}{\partial \hat{u}}\right)_o = U\left(\frac{\partial C_{D_T}}{\partial u}\right)_o \approx U\left(\frac{\Delta C_{D_T}}{\Delta u}\right)_o \qquad (5.11a)$$

The effect of a positive value of C_{D_u} is to increase the damping ratio of the phugoid oscillation, but, at least for conventional aircraft, it is not considered to be an important quantity so far as flying qualities are concerned. Actually C_{D_u} is more important from a performance standpoint, particularly for high speed flight where a small drag rise is desirable.

There is also a change in ram drag with forward speed, which is expressed as

$$\frac{\partial C_{D_R}}{\partial \hat{u}} = U\left(\frac{\partial C_{D_R}}{\partial u}\right) = \frac{2N}{\rho US}\frac{\partial Q_i}{\partial u} - \frac{2NA_o}{US} \qquad (5.11b)$$

where the first term expresses the change in ram drag due to changes in the engine inlet mass flow Q_i with forward speed, and where

N is the number of engines
A_o is the capture area of each engine
U is the reference forward speed

5.1.1.3 Change in Pitching Moment Due to Variation in Forward Speed (C_{m_u})

The stability derivative expressing the change in pitching moment due to variation in forward speed is defined as

$$C_{m_u} = \left(\frac{\partial C_m}{\partial \hat{u}}\right)_o = U\left(\frac{\partial C_m}{\partial u}\right)_o \qquad (5.12)$$

Unlike the C_{L_u} and C_{D_u} derivatives previously discussed, aeroelastic effects can be significant for the C_{m_u} derivative, largely due to the flexibility of the fuselage which can change the effective incidence of the horizontal tail. Based on a very simple analysis presented in reference 7, the aeroelastic contribution of the tail can be calculated from

$$C_{m_u}\Big|_{\substack{\text{aeroelastic}\\ \text{tail}}} = -C_{m_t}\Big|_o \frac{\rho U^2 K a_H S_H}{1+\frac{1}{2}\rho U^2 K a_H S_H} \qquad (5.13)$$

where $C_{m_t}|_o$ is the reference state value of tail pitching moment (calculated by the program; see Section 3.1.3.3); a_H and S_H are the lift curve slope and planform area of the horizontal tail, respectively; and K is an aeroelastic parameter which relates the change in tail incidence to tail lift, as

$$\Delta\alpha_H = - KL_H \tag{5.14}$$

Equation (5.13) is presented only for reference, however, and it is suggested that a more thorough aeroelastic analysis be made. Mach number effects for C_{m_u} can be treated as before, as

$$C_{m_u}\Big|_{Mach} = M\left(\frac{\partial C_m}{\partial M}\right)_o \tag{5.15}$$

but again this effect is regarded as negligible for the speeds of interest in STOL operations. The effect of variation of forward speed on the jet momentum coefficient is again the predominant effect for STOL aircraft. In analogy with the methods presented for C_{L_u} and C_{D_u}, the variation of pitching moment with forward speed can be obtained from the program by running a range of C_J corresponding to a range of velocities, the final result being

$$C_{m_u} = \left(\frac{\partial C_m}{\partial \hat{u}}\right)_o = U\left(\frac{\partial C_m}{\partial u}\right)_o \approx U\left(\frac{\Delta C_m}{\Delta u}\right)_o \tag{5.16}$$

For conventional aircraft it is known that C_{m_u} generally affects both the period and damping of the phugoid mode, positive values of C_{m_u} tending to decrease both. For STOL aircraft this derivative is likely to be of greater importance because of the influence of the jet sheet.

5.1.2 Pitching Rate Derivatives

The pitching rate or "q" derivatives represent the effect on the aerodynamic forces and moments of rotation of the airplane about an axis through the aircraft center of gravity (c.g.) parallel to the y-axis while angle of attack remains constant. An example of this type of motion is the steady pull-up maneuver. The primary effect of a pitching motion is the rotation of the aircraft which induces a flow normal to the wing, the horizontal tail, and the fuselage; and this induced flow can be regarded as

inducing aerodynamic forces and moments on the aircraft. The predominant effect of rotation is on the horizontal tail. In addition to the rotation effect, it has been shown that aeroelastic effects are also of considerable importance for the pitching rate derivatives. Although aeroelastics will be discussed briefly in the following sections, no methods are presented in this report to consider aeroelastic effects.

The q derivatives discussed in the following sections are based on the non-dimensional* pitching rate $\hat{q} = q\bar{c}/2U$ where q is the rate of pitch in radians per second.

5.1.2.1 Lift Due to Rate of Pitch (C_{L_q})

The derivative expressing the change in lift due to rate of pitch q is defined as

$$C_{L_q} = \left(\frac{\partial C_L}{\partial \hat{q}}\right)_o = \frac{2U}{\bar{c}} \left(\frac{\partial C_L}{\partial q}\right)_o \tag{5.17}$$

where the subscript zero indicates that the derivative is to be evaluated at the reference condition, usually defined to be zero angle of attack. The lift induced on the wing and the horizontal tail by the rotation rate is calculated directly by the computer program when the dynamic stability derivative option is requested (see Volume II). The wing contribution is printed as $C_L(\hat{q})$, expressed in the form

$$C_L(\hat{q})\Big|_{wing} = C_{L_q}\,\hat{q} \tag{5.18a}$$

for the free air case, and as

$$C_L(\hat{q})\Big|_{wing} = (C_{L_{q_o}} + C_{L_{q_\alpha}}\alpha)\hat{q} + C_{L_{q^2}}\,\hat{q}^2 \tag{5.18b}$$

in ground effect. The free air expression, equation (5.18a), is printed in the standard form of a stability derivative. The ground effect expression is not truly in the form of a derivative, however, because there is a dependence on angle of attack and the rotation rate. What this means is that within the context of the assumptions employed in Volume I that C_{L_q} in ground

* STAMP evaluates derivatives based on reference chord $\bar{c}$.

effect is non-linear, and its use in the linearized equations of motion, which are derived by assuming constant stability derivatives, is not justified. However, for most configurations the terms $C_{L_{q_\alpha}}$ and $C_{L_{q^2}}$ are negligibly small, and equation (5.18b) reduces to the same form as equation (5.18a). If, however, either of these terms is not negligibly small, then use of the linearized equations of motion is subject to question, and a higher order dynamic stability analysis may be required. This situation occurs for several other stability derivatives, as will be seen in subsequent sections.

The horizontal tail contribution to C_{L_q} is usually considerably more important than the wing contribution and is calculated directly by the computer program as $C_{L_q}\big|_{tail}$.

Aeroelastic effects arise from the centripetal force on the airframe which can cause the wings to twist or the tail incidence angle to change. The wing twist effect has been shown to be of particular importance when overhanging nacelles, typical of modern jet transport aircraft, are used.

5.1.2.2 Pitching Moment Due to Rate of Pitch (C_{m_q})

The derivative expressing the change in pitching moment due to rate of pitch is defined as

$$C_{m_q} = \left(\frac{\partial C_m}{\partial \hat{q}}\right)_0 = \frac{2U}{\bar{c}}\left(\frac{\partial C_m}{\partial q}\right)_0 \qquad (5.19)$$

and is commonly called the pitch damping derivative. The computer program calculates the contribution to C_{m_q} due to the wing, fuselage, and horizontal tail. The wing contribution is calculated in the same manner as C_{L_q} and is printed in the form of equations (5.18). The fuselage and horizontal tail contributions are calculated and printed in the form $C_{m_q}\big|_{fuselage}$ and $C_{m_q}\big|_{tail}$ (i.e., constant derivatives).

The C_{m_q} derivative is quite important in the longitudinal dynamics of the airplane, as has been shown in the sensitivity study (Section 4.1), primarily affecting the damping of the short period oscillation. The primary contribution to the damping, for conventional aircraft at least, is from

the horizontal tail, and tailless aircraft have characteristically poorly damped short period oscillations. For adequate damping a large negative value of C_{m_q} is desirable.

5.1.3 The $\dot{\alpha}$ Derivatives

The $\dot{\alpha}$ stability derivatives are the only longitudinal stability derivatives considered which cannot be calculated based on the quasi-steady assumptions adopted heretofore. They owe their existence to the fact that the flow field does not adjust itself instantaneously to changes in angle of attack, but rather some finite time is required for the pressures and induced flows to adjust to a new equilibrium value. The $\dot{\alpha}$ derivatives are sometimes referred to as vertical acceleration derivatives. They represent unsteady flow phenomena and must be included in longitudinal dynamic stability analyses simply because experiment has shown them to be of some importance, particularly in the damping characteristics of the short period mode.

There is a lack of general analytical methods for calculating the unsteady flow phenomena associated with the $\dot{\alpha}$ derivatives. Simple methods applicable to wings have been developed, but in most methods (e.g., that of Datcom) the range of applicability is quite limited and the unsteady flow models employed are quite crude. For jet-wings, the problem is further complicated by the presence of the jet sheet, whose shape may become quite complex in an oscillatory mode. Consider, for example, a jet-wing undergoing a damped sinusoidal oscillation in angle of attack, such as in the short period mode. The jet shape, which is a function of the wing loading, the instantaneous jet emission angle, and the momentum coefficient, will not be sinusoidal in correspondence with the angle of attack since the history of the flow will affect its shape. The influence of the wing bound vortices, whose strength is constantly changing with time, will reach different parts of the jet sheet at different times. Thus, because of this lag effect, the jet shape will be exceedingly complex and virtually impossible to calculate. However, the lag effect on the jet shape can, for many cases of interest, be neglected because of the high velocity of the jet (on the order of ten times the forward speed of the aircraft) which, in effect, rapidly moves perturbations in the jet shape downstream where their effect on the aircraft will not be important.

The lag effect which is usually predominant and is considered in most conventional stability analyses is that due to the lag in downwash at the horizontal tail. The approximate method for calculating this effect entirely neglects the unsteady character of the lift response of the tail to changes in effective tail incidence, but considers instead the fact that the downwash at the tail does not respond instantaneously to changes in wing angle of attack. It is assumed that the downwash at the tail is primarily dependent on the strength of the wing trailing vorticity in the region of the tail, and then it is assumed that trailing vorticity shed by the wing moves downstream with the velocity of the freestream. Hence, the change in downwash at the tail lags any change in angle of attack at the wing by the time

$$\Delta t = \frac{\ell_H}{U} \tag{5.20}$$

where ℓ_H is the horizontal tail length. Therefore, the downwash at the tail $\epsilon(t)$ corresponds to the wing angle of attack $\alpha(t-\Delta t)$, so the change in tail-plane downwash can be expressed as

$$\frac{\Delta\epsilon}{\Delta t} \approx \frac{\partial\epsilon}{\partial\alpha}\frac{\partial\alpha}{\partial t} = \frac{\partial\epsilon}{\partial\alpha}\dot{\alpha} \tag{5.21}$$

so that with equation (5.20)

$$\Delta\epsilon \approx \frac{\partial\epsilon}{\partial\alpha}\dot{\alpha}\frac{\ell_H}{U} \tag{5.22}$$

Obviously the assumption that vorticity propagates downstream at the free-stream velocity is not correct (and is rather unsatisfactory to the fluid dynamicist), but such an assumption has proven to be satisfactory within the context of stability work.

The methods presented herein for calculating the $\dot{\alpha}$ stability derivatives consider only the lag in downwash effect on the horizontal tail and neglect entirely the unsteady effects associated with the lag in pressures on the wing. The authors believe that the latter effect requires further study and experimental work since the presence of the jet sheet may accentuate unsteady effects. However, an unsteady flow analysis is clearly beyond the

scope of the present study.

The $\dot{\alpha}$ derivatives discussed in the following sections are based on the non-dimensional rate of change of angle of attack $\hat{\dot{\alpha}} = \dot{\alpha}\bar{c}/2U$ where $\dot{\alpha}$ is the rate of change of angle of attack in radians per second.

5.1.3.1 Lift Due to $\dot{\alpha}$ ($C_{L_{\dot{\alpha}}}$)

The change in lift on the horizontal tail due to a rate of change of angle of attack is calculated from the lag in downwash, equation (5.22), expressed as

$$\Delta C_L = -57.3\, C_{L_{\alpha_H}} \Delta\varepsilon = -57.3\, C_{L_{\alpha_H}} \dot{\alpha}\, \frac{\ell_H}{U}\, \frac{d\varepsilon}{d\alpha} \qquad (5.23)$$

In this expression $C_{L_{\alpha_H}}$ is the lift curve slope of the horizontal tail non-dimensionalized by wing area and calculated directly by the program (isolated tail analysis), and $\frac{d\varepsilon}{d\alpha}$ is the rate of change of tailplane downwash, which can be calculated from the program results as discussed in Section 3.1.1.3. Equation (5.23) can easily be put in the form of a dynamic stability derivatives:

$$C_{L_{\dot{\alpha}}} = \left(\frac{\partial C_L}{\partial \hat{\dot{\alpha}}}\right)_0 = \frac{\partial C_L}{\partial\left(\frac{\dot{\alpha}\bar{c}}{2U}\right)} = -2(57.3)\, C_{L_{\alpha_H}} \frac{\ell_H}{\bar{c}}\, \frac{d\varepsilon}{d\alpha} \qquad (5.24)$$

There can also be aeroelastic contributions to $C_{L_{\dot{\alpha}}}$ arising from bending of the fuselage as α is changing, which changes the effective incidence angle of the tail, and from twisting of the wings.

The $C_{L_{\dot{\alpha}}}$ derivative is not important in determining the shape of the longitudinal oscillatory modes, as is shown in figures (4.3) and (4.4) for the short period and phugoid modes, respectively. It is usually neglected unless it happens to be large.

5.1.3.2 Pitching Moment Due to $\dot{\alpha}$ ($C_{m_{\dot{\alpha}}}$)

The change in pitching moment of the horizontal tail due to a rate of angle of attack is calculated from the lag in downwash, as

$$\Delta C_m = -57.3\, C_{m_{\alpha_H}} \Delta\varepsilon = -57.3\, C_{m_{\alpha_H}} \dot{\alpha}\, \frac{\ell_H}{U}\, \frac{d\varepsilon}{d\alpha} \qquad (5.25)$$

where $C_{m_{\alpha_H}}$ is the slope of the pitching moment curve, calculated directly by the program (isolated tail analysis). In the form of a dynamic stability derivative equation (5.25) becomes

$$C_{m_{\dot{\alpha}}} = \left(\frac{\partial C_m}{\partial \hat{\dot{\alpha}}}\right)_o = \frac{\partial C_m}{\partial\left(\frac{\dot{\alpha}\bar{c}}{2U}\right)} = -2(57.3)C_{m_{\alpha_H}}\frac{\ell_H}{U}\frac{d\epsilon}{d\alpha} \qquad (5.26)$$

The $C_{m_{\dot{\alpha}}}$ derivative is quite important in the longitudinal dynamics, affecting primarily the damping characteristics of the short period oscillation, as shown in figure (4.3). A negative value of $C_{m_{\dot{\alpha}}}$ increases the damping of the short period mode.

5.2 Lateral Dynamic Stability Derivatives

Methods for calculating the dynamic stability derivatives pertinent to the lateral oscillatory and aperiodic modes are presented in the following sections. The importance of each derivative to the Dutch roll oscillation, the roll mode, and the spiral mode is discussed, including the implications of the sensitivity study presented in Section 4.0. Table (5.2) summarizes the terms required for the lateral stability analysis and indicates for which aircraft components methods are required to calculate each term.

5.2.1 Rolling Rate Derivatives

The rolling rate or "p" derivatives represent the effect on the aerodynamic forces and moments of rotation of the airplane about the x-axis [see figure (4.1)]. The motion can be visualized by observing that the wing tips trace a helix during the rolling maneuver. The primary effect of rolling the aircraft is an induced flow on the wing, the horizontal tail, and the vertical tail; and this induced flow can be regarded as effective twist on each surface. Contributions from the wing and each tail surface can be of similar magnitude and hence, each must be considered carefully. Aeroelastic effects in the lateral modes are not regarded to be of importance as they may be for the longitudinal modes, and hence, they are neglected herein.

The p derivatives discussed in the following sections are based on the non-dimensional rolling rate $\hat{p} = pb/2U$ where p is the rate of roll in radians per second.

Table (5.2) Lateral Stability Parameters

Stability Parameter	CONTRIBUTION				Section Number
	Jet-Wing	Fuselage	Horizontal Tail	Vertical Tail	
C_Y, C_{Y_β}	●	●		●	3.2.1
C_l, C_{l_β}	●	●	●	●	3.2.2
C_n, C_{n_β}	●	●		●	3.2.3
C_{Y_p}	●			●	5.2.1.1
C_{l_p}	●		●	●	5.2.1.2
C_{n_p}	●			●	5.2.1.3
C_{Y_r}	●			●	5.2.2.1
C_{l_r}	●			●	5.2.2.2
C_{n_r}	●	●		●	5.2.2.3
$C_{Y_{\dot\beta}}$	●			●	5.2.3.1
$C_{l_{\dot\beta}}$	●			●	5.2.3.2
$C_{n_{\dot\beta}}$	●			●	5.2.3.3

5.2.1.1 Side Force Due to Rate of Roll (C_{Y_p})

The derivative expressing the change in side force due to rate of roll p is defined as

$$C_{Y_p} = \left(\frac{\partial C_Y}{\partial \hat{p}}\right)_0 = \frac{2U}{b}\left(\frac{\partial C_Y}{\partial p}\right)_0 \tag{5.27}$$

where the subscript zero indicates that the derivative is to be evaluated at the reference condition, usually defined to be zero angle of sideslip. The primary contributions to C_{Y_p} are from the wing and the vertical tail, and in this work the contributions from the horizontal tail and the fuselage are neglected. In addition, the helical nature of the vortex sheet, which is a consequence of the motion, has been neglected here; but for the small rates of roll admissible in linear theory, this effect has been shown to have a negligible influence.

The wing contribution to C_{Y_p} can be calculated using the results of the computer program in conjunction with some semi-empirical methods in Datcom (Section 7.1.2.1). Expressing the wing term in the form $C_Y(\hat{p})$, the following relation can be used to calculate wing C_{Y_p}:

$$C_Y(\hat{p})\Big|_{wing} = \left[\left(C_{Y_{p_0}} + C_{Y_{p_\alpha}}\,\alpha\right)\hat{p} + C_{Y_{p^2}}\,\hat{p}^2\right] + \left(\Delta C_{Y_p}\right)_\Gamma\,\hat{p} \tag{5.28}$$

where the terms within the square brackets are calculated directly by the program and where $(\Delta C_{Y_p})_\Gamma$ is the increment in C_{Y_p} due to dihedral given in Datcom by the expression

$$\left(\Delta C_{Y_p}\right)_\Gamma = \left[3 \sin\Gamma \left(1 + 2\,\frac{z}{b/2}\sin\Gamma\right)\right]\left(C_{l_p}\right)_{\substack{\Gamma = 0 \\ C_L = 0}} \tag{5.29}$$

where

Γ is the geometric dihedral angle in degrees

z is the vertical distance between the airplane c.g. and the wing root chord, positive for the wing above the c.g.

$(C_{l_p})_{\substack{\Gamma = 0 \\ C_L = 0}}$ is the roll damping derivative of the wing at zero C_L with no dihedral effect, obtained in the next section.

Equation (5.28) is not in the form of a stability derivative as conceived by Bryan, however, since in his formulation the derivatives are independent of the motion. $C_Y(\hat{p})$ in equation (5.28) is dependent on both the angle of attack and the rate of roll $(C_{Y_{p^2}})$, and, therefore, in that form its use in the linearized equations of motion is not justified. In many cases of interest, however, the $C_{Y_{p^2}}$ terms are insignificant, and the remainder of the expression is then independent of the motion. The program output should be carefully examined to ascertain if these terms are negligible.

In general, the wing contribution to C_{Y_p} is small compared to that due to the vertical tail. The program result, $C_{Y_p}|_{tail}$, can be used directly.

C_{Y_p} is generally unimportant in the lateral dynamic characteristics of the airplane, as shown in figures (4.5) and (4.6), and it is common engineering practice to neglect this term in stability analysis. Experimental verification of this is needed, however, for jet-wing configurations where the helical shape of the jet may be of some significance.

5.2.1.2 Rolling Moment Due to Rate of Roll (C_{l_p})

The derivative expressing the change in rolling moment due to rate of roll p is defined as

$$C_{l_p} = \left(\frac{\partial C_l}{\partial \hat{p}}\right)_0 = \frac{2U}{b}\left(\frac{\partial C_l}{\partial p}\right) \qquad (5.30)$$

and is referred to as the roll damping derivative. The primary contributions to C_{l_p} are from the wing, the horizontal tail, and the vertical tail. For aircraft with large tail surfaces, C_{l_p} for the tail can be very important. As for C_{Y_p}, the helical nature of the jet-wing wake has been neglected in this analysis.

The wing contribution to the roll damping derivative can be calculated

using the results of the computer program in conjunction with Datcom methods (Section 7.1.2.2). Expressing the wing term in the form $C_l(p)$, the roll damping is expressed as

$$C_l(\hat{p}) = K\left[C_{l_p}\,\hat{p}\right] \tag{5.31a}$$

for the free air case, and as

$$C_l(\hat{p}) = K\left[\left(C_{l_{p_o}} + C_{l_{p_\alpha}}\,\alpha\right)\hat{p} + C_{l_{p^2}}\,p^2\right] \tag{5.31b}$$

in ground effect. The factor K in equation (5.31) is a correction for dihedral from Datcom given by

$$K = \left[1 + 2\,\frac{z}{b/2}\sin\Gamma + 3\left(\frac{z}{b/2}\right)^2\sin^2\Gamma\right] \tag{5.32}$$

where

Γ is the geometric dihedral angle in degrees

z is the vertical distance between the airplane c.g. and the wing root chord, positive for the wing above the c.g.

As for C_{Y_p}, the equation for C_{l_p} in ground effect is not in the form of a stability derivative because of the α and p dependence, but in many cases the $C_{l_{p_\alpha}}$ and $C_{l_{p^2}}$ terms are negligible.

The program calculates tail contributions to C_{l_p} in stability derivative form $C_{l_p}\big|_{\text{hor.tail}}$ and $C_{l_p}\big|_{\text{vert.tail}}$.

The C_{l_p} derivative is extremely important in determing the lateral dynamic characteristics of the aircraft, as clearly shown in figures (4.5) and (4.6). It is important in establishing the time constants for the spiral and roll modes and the damping ratio of the Dutch roll oscillation. In conjunction with the roll mode, C_{l_p} is important in establishing the effectiveness of ailerons for roll control since it is a measure of the resistance of the aircraft to rolling motions.

5.2.1.3 Yawing Moment Due to Rate of Roll (C_{n_p})

The derivative expressing the change in yawing moment due to rate of roll is defined as

$$C_{n_p} = \left(\frac{\partial C_n}{\partial \hat{p}}\right)_o = \frac{2U}{b}\left(\frac{\partial C_n}{\partial p}\right)_o \tag{5.33}$$

and is referred to as a cross derivative since it couples the rolling and yawing motions. The primary contributions to C_{n_p} are from the wing and the vertical tail, the latter being the predominant term, especially for the large tails typical of STOL aircraft.

Dihedral does not significantly influence C_{n_p}, and hence the wing contribution is calculated directly by the computer program, printed as $C_n(p)$ and expressed in the form

$$C_n(\hat{p})_{wing} = \left(C_{n_{p_o}} + C_{n_{p_\alpha}}\,\alpha\right)\hat{p} + C_{n_{p^2}}\,\hat{p}^2 \tag{5.34}$$

for either the free air case or in ground effect. The program output should be carefully examined to determine whether equation (5.34) must be used as such or whether the lift and roll rate dependence is negligible so that the standard stability derivative form can be used. The vertical tail contribution is calculated directly by the computer program, neglecting the helical nature of the jet-wing vortex sheet, in the stability derivative form $C_{n_p}\big|_{tail}$.

The C_{n_p} derivative is primarily important in lateral dynamics in determining the shape of the Dutch roll mode. It affects both the frequency and damping of the mode, and its effect on ζ_D can be more important than that illustrated in figure (4.5a). In general, a positive value of C_{n_p} is desirable since that leads to a damped Dutch roll oscillation.

5.2.2 Yawing Rate Derivatives

The yawing rate or "r" derivatives represent the effect on the aerodynamic forces and moments of rotation of the airplane about the z_s-axis [see figure (4.1)]. The primary effect of yawing the aircraft is an induced flow on the wing, which can be regarded as an antisymmetric onset flow distribution

with a resulting asymmetric loading, and an induced flow on the vertical tail, which can be regarded as an effective camber distribution on the tail. In addition, the yawing motion effectively induces a sidewash distribution on the fuselage. The contribution to the r derivatives of the horizontal tail is small and is neglected, as are aeroelastic effects.

The r derivatives discussed in the following sections are based on the non-dimensional yawing rate $\hat{r} = rb/2U$, where r is the rate of roll in radians per second.

5.2.2.1 Side Force Due to Rate of Yaw (C_{Y_r})

The derivative expressing the change in side force due to rate of yaw r is defined as

$$C_{Y_r} = \left(\frac{\partial C_Y}{\partial \hat{r}}\right)_0 = \frac{2U}{b}\left(\frac{\partial C_Y}{\partial r}\right)_0 \tag{5.35}$$

The primary contribution to C_{Y_r} is from the vertical tail, although in some cases the wing contribution may be of some significance. Contributions from the horizontal tail and the fuselage are small and have been neglected in this work. The yawing motion leads to an asymmetrical jet-wing vortex wake which can induce additional forces and moments on the tail and fuselage, but for the small rates of yaw admissible in linear theory neglecting the wake distortion should not be an unreasonable assumption. However, it has yet to be determined whether this interaction is important for jet-wing high lift systems.

Datcom offers no method to calculate wing C_{Y_r}. Hence, the program result is all that is available, printed as $C_Y(\hat{r})$ and expressed in the form

$$\begin{aligned} C_Y(\hat{r})\Big|_{wing} = &\left(C_{Y_{r_0}} + C_{Y_{r_\alpha}}\,\alpha + C_{Y_{r_{\alpha^2}}}\,\alpha^2\right)\hat{r} \\ &+ \left(C_{Y_{r^2_0}} + C_{Y_{r^2_\alpha}}\,\alpha + C_{Y_{r^2_{\alpha^2}}}\alpha^2\right)\hat{r}^2 \end{aligned} \tag{5.36}$$

in free air or in ground effect. Although equation (5.36) appears foreboding, in most circumstances many of the terms are negligible and a simpler relation

remains. Since the wing contribution is typically small compared to that of the tail, it is probably necessary to consider only the $C_{Y_{r_o}}$ term in equation (5.36). The vertical tail contribution to C_{Y_r} is calculated by the program in stability derivative form $C_{Y_r}\big|_{tail}$.

C_{Y_r} is of little importance in conventional aircraft lateral dynamics and is usually neglected.

5.2.2.2 Rolling Moment Due to Rate of Yaw (C_{l_r})

The derivative expressing the change in rolling moment due to rate of yaw r is defined as

$$C_{l_r} = \left(\frac{\partial C_l}{\partial \hat{r}}\right)_o = \frac{2U}{b}\left(\frac{\partial C_l}{\partial r}\right)_o \tag{5.37}$$

and is also referred to as an aerodynamic cross derivative, as was C_{n_p}. The primary contributions to C_{l_r} are from the wing and the vertical tail. Contributions from the horizontal tail and the fuselage are small and have been neglected in this work.

The wing contribution to C_{l_r} is calculated using the computer program in conjunction with some methods presented in Datcom (Section 7.1.3.2). Expressed in the form $C_l(r)$, the wing C_{l_r} can be calculated from

$$C_l(\hat{r})\big|_{wing} = \left[C_{l_{r_o}} + C_{l_{r_\alpha}}\,\alpha\right]\hat{r} + \frac{z}{b/2}\,C_Y(\hat{r}) + \left(\Delta C_{l_{r_\Gamma}}\right)\hat{r} \tag{5.38a}$$

for the free air case, and as

$$\begin{aligned} C_l(\hat{r})\big|_{wing} = {} & \left[\left(C_{l_{r_o}} + C_{l_{r_\alpha}}\,\alpha + C_{l_{r_{\alpha^2}}}\alpha^2\right)\hat{r}\right. \\ & \left. + \left(C_{l_{r^2_o}} + C_{l_{r^2_\alpha}}\,\alpha + C_{l_{r^2_\alpha}}\,\alpha^2\right)\hat{r}^2\right] + \frac{z}{b/2}\,C_Y(\hat{r}) \\ & + \left(\Delta C_{l_r}\right)_\Gamma \hat{r} \end{aligned} \tag{5.38b}$$

in ground effect. The terms within the square brackets are calculated directly by the computer program for the jet-wing and indicate that C_{l_r} can be a

function of both angle of attack and the rate of yaw, although, as for the previously discussed stability derivatives, most of the higher order terms are negligible. The second term in each of equations (5.38) accounts for the rolling moment due to C_{Y_r} when the wing plane is displaced vertically from the center of gravity, while the last term is intended to account for the dihedral effect. In equations (5.38)

z is the vertical distance of the wing relative to the c.g., positive for the wing above the c.g.

$C_Y(\hat{r})$ is the side force due to yawing, from equation (5.36)

$\Delta C_{l_{r_\Gamma}}$ is the increment in C_{l_r} due to dihedral, given in Datcom by

$$\Delta C_{l_{r_\Gamma}} = \frac{1}{12} \frac{\pi AR \sin \Lambda_{c/4}}{AR+4 \cos \Lambda_{c/4}} \quad \text{(per radian}^2\text{)} \qquad (5.39)$$

$\Lambda_{c/4}$ is the quarter-chord sweep of the wing

Γ is the wing dihedral in radians.

The vertical tail contribution to C_{l_r} is calculated directly by the program in the form of a stability derivative $C_{l_r}\big|_{tail}$.

C_{l_r} can be an important derivative in lateral dynamic calculations, particularly in the Dutch roll and spiral modes, as has been shown in figures (4.5) and (4.6), although it is not considered to be a preliminary design parameter.

5.2.2.3 Yawing Moment Due to Rate of Yaw (C_{n_r})

The derivative expressing the change in yawing moment due to rate of yaw r is defined as

$$C_{n_r} = \left(\frac{\partial C_n}{\partial \hat{r}}\right)_0 = \frac{2U}{b}\left(\frac{\partial C_n}{\partial r}\right)_0 \qquad (5.40)$$

and is commonly referred to as the yaw damping derivative. The wing, vertical tail, and fuselage each contribute to C_{n_r}, but the horizontal tail contribution is relatively small and has been neglected here. The vertical contribution is by far the most important, often contributing as much as 80 to 90

per cent of the total C_{n_r}.

The wing contribution to C_{n_r} is calculated using the potential flow value for a jet-wing from the program in conjunction with the semi-empirical methods from Datcom which account for asymmetrical changes in profile drag due to the yawing motion. Expressed as $C_n(\hat{r})$, the wing contribution can be calculated from

$$C_n(\hat{r})_{wing} = \left[\left(C_{n_{r_0}} + C_{n_{r_\alpha}}\alpha + C_{n_{r_{\alpha^2}}}\alpha^2\right)\hat{r} + \left(C_{n_{r^2_0}} + C_{n_{r^2_\alpha}}\alpha + C_{n_{r^2_{\alpha^2}}}\right)\alpha^2\ \hat{r}^2\right] + \left(\frac{C_{n_r}}{C_{D_0}}\right)C_{D_0}\hat{r} \quad (5.41)$$

where the terms within the square brackets are calculated directly by the program, and in most cases the higher order terms are negligible. The second term is to account for asymmetries in profile drag due to the yaw rate and is based on a simplified approach which is a function of wing planform only. These terms are defined as

$\frac{C_{n_r}}{C_{D_0}}$ is the low speed profile drag yaw damping parameter obtained from figure (5.1) as a function of aspect ratio, sweep, and c.g. position

C_{D_0} is the wing profile drag coefficient, obtained from Section 3.1.2.1.

The vertical tail contribution to C_{n_r}, usually the most important term, is calculated directly by the computer program in the form $C_{n_r}|_{tail}$. The fuselage contribution is calculated by assuming a sidewash distribution on the fuselage due to the yawing motion and is expressed in standard stability derivative form $C_{n_r}|_{fuselage}$.

In lateral dynamic stability analysis the yaw damping derivative is particularly important since it is a primary contributor to the yaw damping of the Dutch roll oscillatory mode, as shown in figure (4.5). It is also of importance in the spiral mode. Large negative values of C_{n_r} are desirable for adequate damping characteristics. The yaw damping derivative can be an

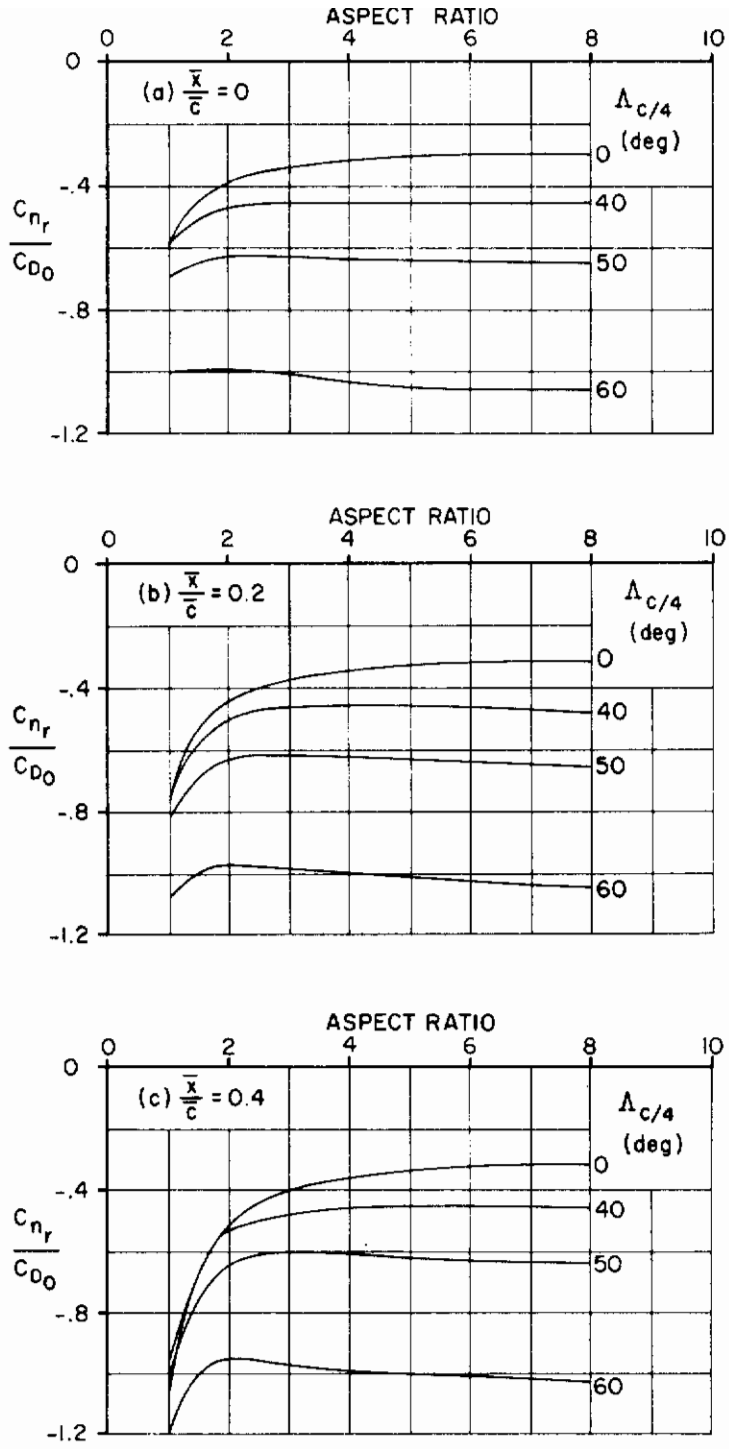

Figure (5.1). Low Speed Profile Drag Yaw Damping Parameter

important parameter in sizing the vertical tail for proper Dutch roll characteristics.

5.2.3 The $\dot{\beta}$ Derivatives

In correspondence with the $\dot{\alpha}$ derivatives discussed in Section 5.1.3 in conjunction with longitudinal dynamics, the $\dot{\beta}$ stability derivatives are the only lateral stability derivatives which require consideration of unsteady flow phenomena. They owe their existence to the fact that the flow field does not adjust instantaneously to changes in sideslip β, but rather some finite time is required for the pressures and induced flows to adjust to a new equilibrium value. As are the $\dot{\alpha}$ derivatives, the $\dot{\beta}$ derivatives are referred to as acceleration derivatives.

Calculation of the $\dot{\beta}$ derivatives can, in general, be done in a manner analogous to the $\dot{\alpha}$ derivatives, which implies that only the lag in induced flow at the tail can be considered. Hence, equation (5.20) is applicable, except that it must be rewritten as

$$\Delta t = \frac{\ell_V}{U} \tag{5.42}$$

where ℓ_V is the vertical tail length, and Δt is the lag time between a change in conditions at the wing and change in sidewash at the tail. Hence, letting $\sigma(t)$ denote the sidewash angle at the tail at any time corresponding to a wing sideslip angle $\beta(t-\Delta t)$, the change in tailplane sidewash can be expressed as

$$\frac{\Delta\sigma}{\Delta t} \approx \frac{\partial\sigma}{\partial\beta}\,\frac{\partial\beta}{\partial t} = \frac{\partial\sigma}{\partial\beta}\,\dot{\beta} \tag{5.43}$$

and with equation (5.42)

$$\Delta\sigma \approx \frac{\partial\sigma}{\partial\beta}\,\dot{\beta}\,\frac{\ell_V}{U} \tag{5.44}$$

Calculation of the $\dot{\beta}$ derivatives, namely $C_{Y_{\dot{\beta}}}$, $C_{l_{\dot{\beta}}}$, and $C_{n_{\dot{\beta}}}$, would then proceed in a manner analogous to that used for the $\dot{\alpha}$ derivatives. However the term $\frac{\partial\sigma}{\partial\beta}$ in equation (5.44) cannot be as simply determined as $\frac{\partial\varepsilon}{\partial\alpha}$ in equation (5.22) because it requires running the computer program in its

asymmetric mode at a number of sideslip angles (which is a lengthy and costly process), and also fuselage effects, which are not included in the program calculation of external flow fields, will be important. In general, $\frac{\partial \sigma}{\partial \beta}$ is determined experimentally. However, the $\dot{\beta}$ derivatives are not generally of importance in lateral dynamic stability analysis and hence it is not considered to be a serious matter that their analytical estimation is not possible.

6.0 CONTROL DERIVATIVES

Changes in the aerodynamic forces and moments due to the actuation of a control system can be expressed in terms of a set of non-dimensional control derivatives. These derivatives are important both in static stability analysis and in the dynamic response characteristics of the airframe. In the following sections methods are presented for calculating the appropriate derivatives for elevator, rudder, aileron, and spoiler systems; but it is a straightforward extension of these methods to apply them to a variety of unusual control systems, such as flaperons and elevons.

The importance of some of the control derivatives discussed below in stability analysis is likely to be increased for STOL aircraft because of the large moments resulting from the deflected jet sheet or vectored jets which must be trimmed out in steady flight by actuation of the control systems. Hence, while some of these control derivatives are generally neglected for conventional aircraft, it is recommended that for STOL configurations the magnitude of each derivative be examined to ascertain if its omission in stability and control analyses is justified.

In the following sections control derivatives for each of the conventional control systems are discussed in detail, including methods for calculating each derivative and a discussion of the importance of each term. As for the dynamic stability derivatives (Section 5.0), most of the prediction methods presented herein are based on the theoretical methods developed in Volume I, implemented through use of the STOL Aerodynamic Methods Program, described in Volume II. Semi-empirical methods have also been included, where applicable, most notably to the analysis of spoilers.

Control rate derivatives (e.g. $C_{L_{\dot{\delta}_e}}$) have not been included in this report because they basically involve the dynamics of the control system as well as the aerodynamics. Their analysis is beyond the scope of this work in that unsteady aerodynamic theory is required, and since their analysis for STOL aircraft is likely to be identical to that required for conventional aircraft, existing methods can be employed. Nevertheless, for dynamic

stability and control work with controls free, these derivatives are important, and it is likely that further work in their prediction is required. Datcom offers no methods to calculate these derivatives.

6.1 Elevator Derivatives

The elevator is the primary longitudinal control system for conventional wing-tail configurations such as those typical STOL transport aircraft, although for tailless aircraft, such as slender delta wing configurations, elevons (symmetrically deflected ailerons) or some similar device would be used for longitudinal control. The elevator may be used in conjunction with an all-movable horizontal tail, which effectively changes the incidence of the entire tailplane, or there may be no elevator at all but just an all-movable tailplane. In the following discussion both conventional elevators and all-movable tails will be discussed, but extension to less common systems is a straightforward task.

A positive elevator deflection will be defined as down elevator, and tailplane incidence will be defined in the same sense as angle of attack. The control derivatives derived here are defined per degree of control deflection.

6.1.1 Lift Due to Elevator Deflection ($C_{L_{\delta_e}}$)

The derivative expressing the change in lift due to a change in elevator angle is defined as

$$C_{L_{\delta_e}} = \frac{\partial C_L}{\partial \delta_e} \tag{6.1}$$

where C_L is total aircraft lift coefficient. $C_{L_{\delta_e}}$ is generally positive since a positive elevator deflection leads to an increase in tailplane lift. Since deflection of the elevator can be regarded as an effective change in tailplane camber, $C_{L_{\delta_e}}$ will be nearly constant over a range of tailplane incidences and elevator angles where the flow remains essentially attached, but once separation occurs $C_{L_{\delta_e}}$ will become a function of both tailplane incidence and elevator deflection angle. Aeroelastic effects, primarily a change in fuselage bending with elevator deflection, may require consideration for highly flexible aircraft.

Within the range of incidence for which the flow is essentially attached $C_{L_{\delta_e}}$ can be calculated by the computer program by defining the only horizontal tail camber as the elevator deflected downward one degree (or one radian if $C_{L_{\delta_e}}$ per radian is desired). $C_{L_{\delta_e}}$ is not labelled explicitly in the program output, but it is normally printed as the tail lift coefficient for the camber case in the isolated tail analysis. In addition, for an all-movable horizontal tail the derivative

$$C_{L_{i_H}} = \frac{\partial C_L}{\partial i_H} \tag{6.2}$$

where i_H is the incidence of the horizontal tail in degrees, is simply the tail lift curve slope, also printed in the isolated tail analysis. The derivatives expressed by equations (6.1) and (6.2) will suffice for most stability and control analyses since usually large tailplane incidences are not considered. However, if viscous and thickness corrections to $C_{L_{\delta_e}}$ or $C_{L_{i_H}}$ are required, the methods of section 3.1.1 can be implemented.

Although for conventional aircraft the change in lift due to elevator deflection is often small and hence neglected, STOL aircraft are often characterized by large wing pitching moments (primarily due to jet reaction) and hence large tails and elevators for trim, so the lift changes associated with elevator deflection can be significant.

6.1.2 Drag Due to Elevator Deflection ($C_{D_{\delta_e}}$)

The derivative expressing the change in drag due to a change in elevator angle is defined as

$$C_{D_{\delta_e}} = \frac{\partial C_D}{\partial \delta_e} \tag{6.3}$$

and is a portion of the tail contribution to what is generally known as trim drag. $C_{D_{\delta_e}}$ is always positive since an increase in elevator angle is always accompanied by an increase in tail induced drag. $C_{D_{\delta_e}}$ can be calculated by treating the elevator in the same manner as described in the previous section. Hence, $C_{D_{\delta_e}}$ is the resulting induced drag in the camber case of the isolated tail analysis. However, since induced drag is a quadratic function of incidence, the effects of other incidences (angle of attack, tail incidence, jet-wing induced flow, etc.) cannot be separated, so the change in drag due to elevator

deflection must actually be calculated as

$$C_D\big|_{\delta_e} = C_D\big|_{\delta_e=\delta} - C_D\big|_{\delta_{e=0}} \tag{6.4}$$

Viscous and thickness effects can be included using the methods of section 3.1.2.

Drag due to elevator deflection (trim drag) is an important quantity in take-off and landing performance, and its importance may be increased due to the large trim requirements of STOL aircraft.

6.1.3 Pitching Moment Due to Elevator Deflection ($C_{m_{\delta e}}$)

The derivative expressing the change in pitching moment due to a change in elevator angle is defined as

$$C_{m_{\delta e}} = \frac{\partial C_m}{\partial \delta_e} \tag{6.5}$$

and is commonly referred to as the elevator effectiveness or elevator power. $C_{m_{\delta e}}$ is normally negative in sign. Since the primary function of the elevator is to control angle of attack and hence flight speed, the effectiveness of the elevator, $C_{m_{\delta e}}$, is of great importance in preliminary design.

$C_{m_{\delta e}}$ can be calculated in essentially the same manner as $C_{L_{\delta e}}$, defining the only horizontal tail camber as that of the elevator deflected one degree, and taking $C_{m_{\delta e}}$ directly from the isolated tail analysis segment of the program output. In addition, for an all-movable horizontal tail the derivative

$$C_{m_{i_H}} = \frac{\partial C_m}{\partial i_H} \tag{6.6}$$

is simply the pitching moment curve slope of the horizontal tail. If thickness and viscous corrections need be applied to equations (6.5) and (6.6), the methods of section 3.1.3 can be utilized.

6.2 Rudder Derivatives

The rudder is the primary yaw control system for conventional configurations, although some degree of yaw control can be obtained from the ailerons. Since a primary consideration in designing the vertical tail and rudder is

engine-out operation, which can be critical for STOL aircraft because of high thrust-to-weight ratios and the need for placing engines outboard on the wing (for blown flap configurations) to obtain the jet-flap effect over a significant portion of the span, a large vertical tail and rudder will probably be required. Multiply segmented rudders, which are already in use for conventional aircraft, will undoubtedly be used on future STOL configurations.

In the following sections the side force, drag, rolling moment, and yawing moment due to rudder deflection, expressed as non-dimensional control derivatives, will be discussed. A positive rudder deflection is defined as a deflection where the trailing edge of the rudder moves in the -y direction. Rudder control derivatives have been derived per degree of rudder deflection.

6.2.1 Side Force Due to Rudder Deflection ($C_{Y_{\delta r}}$)

The derivative expressing the change in airplane side force due to a change in rudder deflection is defined as

$$C_{Y_{\delta r}} = \frac{\partial C_Y}{\partial \delta_r} \tag{6.7}$$

This derivative is generally positive. It can be calculated from the program by defining the only vertical tail camber as that for one degree of rudder deflection, and $C_{Y_{\delta r}}$ is then the side force for the camber case of the isolated tail analysis. $C_{Y_{\delta r}}$ is generally unimportant for lateral control design.

6.2.2 Drag Due to Rudder Deflection ($C_{D_{\delta r}}$)

The derivative expressing the change in drag due to a change in rudder deflection is defined as

$$C_{D_{\delta r}} = \frac{\partial C_D}{\partial \delta_r} \tag{6.8}$$

and is another portion of the tail contribution to trim drag, as was $C_{D_{\delta e}}$. $C_{D_{\delta r}}$ is always positive and can be calculated by treating the rudder in the same manner as in the previous section. $C_{D_{\delta r}}$ can be important for takeoff and landing performance in a cross-wind or in an engine-out condition.

6.2.3 Rolling Moment Due to Rudder Deflection ($C_{l_{\delta r}}$)

The derivative expressing the change in aircraft rolling moment due to a change in rudder deflection is defined as

$$C_{l_{\delta r}} = \frac{\partial C_l}{\partial \delta_r} \tag{6.9}$$

Although the ailerons are intended for roll control, deflection of the rudder does produce a rolling moment because of the position of the vertical tail above the center of gravity and because of the anti-symmetrical load distribution induced on the horizontal tail by the vertical tail with deflected rudder. The rolling moment due to these effects is calculated directly by the program by defining the deflected rudder as in Section 6.2.1. The computer program output prints explicitly the vertical tail rolling moment and the horizontal tail rolling moment in the isolated tail analysis segment of the program.

$C_{l_{\delta r}}$ is generally not considered to be an important control derivative for conventional aircraft, but the more powerful rudders required for STOL aircraft may make this derivative of greater importance.

6.2.4 Yawing Moment Due to Rudder Deflection ($C_{n_{\delta r}}$)

The derivative expressing the change in aircraft yawing moment due to a change in rudder deflection is defined as

$$C_{n_{\delta r}} = \frac{\partial C_n}{\partial \delta_r} \tag{6.10}$$

and is commonly referred to as the rudder effectiveness or rudder power. $C_{n_{\delta r}}$ is always negative. The primary contribution to $C_{n_{\delta r}}$ is due to the side force on the vertical tail, and this effect is calculated directly by the program. In addition, the anti-symmetrical lift distribution induced on the horizontal tail by the vertical tail results in an asymmetrical induced drag distribution along the span of the horizontal tail and hence a yawing moment, but this effect should be relatively small and has been neglected in this work. $C_{n_{\delta r}}$ is calculated directly by the computer program in the isolated tail analysis segment by defining the rudder as described in Section 6.2.1, and it is printed as total vertical tail yawing moment for the camber case.

$C_{n_{\delta_r}}$ is an important design parameter in determining the lateral-directional control characteristics of the aircraft. Such parameters as directional control in crosswinds, engine-out flight, and counteracting adverse yaw in rolling maneuvers must be considered in determining the rudder power ($C_{n_{\delta_r}}$) required.

6.3 Aileron Derivatives

Ailerons are the primary roll control system for conventional configurations, although some degree of roll control is obtained from the rudder and aerodynamic cross-coupling (i.e., rolling moment due to sideslip, C_{l_β}, the dihedral effect). In addition, the ailerons also provide some degree of yaw control, although the effect is often not desirable (adverse yaw due to aileron deflection). For STOL aircraft the possibility of using blown ailerons also exists, so boundary layer control and even jet-flap effects may need consideration. The use of spoilers in conjunction with ailerons for roll control is discussed in Section 6.4.

In the following sections the side force, rolling moment, and yawing moment due to aileron deflection, expressed as non-dimensional control derivatives, will be discussed. The aileron deflection δ_a is defined as the mean angular displacement of the ailerons, positive when the right aileron movement is downward and the left aileron movement is upward. All aileron derivatives are defined per degree of aileron deflection. Ailerons are the only controls discussed thus far which are part of the wing, and hence their analysis involves use of the EVD segment of STAMP. The flexibility of EVD can thus be fully exploited for analysis of ailerons, but it must be remembered that aileron deflection is inherently anti-symmetrical and the ensuing computational requirements can be restrictive.

6.3.1 Side Force Due to Aileron Deflection ($C_{Y_{\delta_a}}$)

The derivative expressing the change in side force due to a change in aileron deflection is defined as

$$C_{Y_{\delta_a}} = \frac{\partial C_Y}{\partial \delta_a} \qquad (6.11)$$

Such a side force arises from the asymmetrical leading edge suction distribution $c_s(y)$ due to aileron deflection, and hence $C_{Y_{\delta_a}}$ is dependent on leading edge sweep and is zero for a wing with no leading edge sweep. $C_{Y_{\delta_a}}$ can be calculated by the computer program, but this requires that either an anti-symmetric or asymmetric run be made. That is, the ailerons can be defined either by running the EVD segment of STAMP in its anti-symmetric mode (see Volume II) and defining the aileron on the right wing panel as if it were a flap deflected one degree, treating this as a fundamental case; or by running the program in its asymmetric mode and defining the ailerons by a fundamental case with the right aileron down and the left aileron up. The former method is more computationally expedient because it takes advantage of anti-symmetry, but cross-product terms (which arise from the non-linear nature of leading edge suction) which may involve wing camber, flap deflection, etc., will be ignored. Hence some inaccuracies can arise. The latter method can include all the cross-product terms through use of the composite case capability of the program, but being asymmetric the computational task is increased enormously. It is believed that for most cases of interest, however, the cross-product terms will be negligible and the more efficient anti-symmetric mode can be used. Running the program in this manner will yield $C_{Y_{\delta_a}}$ as the side force for the aileron fundamental case. If the program is run in the asymmetric mode, $C_{Y_{\delta_a}}$ is calculated as the difference in C_Y with ailerons and without from the composite case output.

$C_{Y_{\delta_a}}$ is usually quite small except for highly swept configurations, and it is neglected in most conventional aircraft lateral-directional control analysis.

6.3.2 Rolling Moment Due to Aileron Deflection ($C_{l_{\delta_a}}$)

The derivative expressing the change in airplane rolling moment due to a change in aileron deflection is defined as

$$C_{l_{\delta_a}} = \frac{\partial C_l}{\partial \delta_a} \tag{6.12}$$

and is commonly referred to as aileron effectiveness or aileron power. According to the definition of aileron deflection used here, $C_{l_{\delta_a}}$ will usually be negative, or, in other words, a positive aileron deflection will produce a negative rolling moment.

$C_{l_{\delta_a}}$ can be calculated in essentially the same manner as $C_{Y_{\delta_a}}$ described in the previous section, but since rolling moment is calculated from sectional lift rather than sectional drag, there are no cross-product terms and hence the anti-symmetric and asymmetric modes will yield exactly the same result. In either case $C_{l_{\delta_a}}$ will be the rolling moment calculated for the aileron fundamental case. If the ailerons are blown, incidentally, there will be a jet reaction term for $C_{l_{\delta_a}}$. If large aileron deflections are anticipated, it may be desirable to correct program results for viscous and thickness effects. This can be done by calculating corrections to sectional c_ℓ by the procedure of section 3.1.1.1, treating each aileron as a flap deflected $\pm\delta$, and then integrating the resulting sectional lift correction Δc_ℓ as

$$\Delta C_l = \frac{1}{Sb}\int_{-b/2}^{b/2} y\Delta c_\ell(y)\, dy \qquad (6.13)$$

Such a correction would be required for each desired aileron deflection.

$C_{l_{\delta_a}}$ is the most important control derivative in lateral-directional dynamics. Aileron effectiveness in conjunction with the roll damping derivative (C_{l_p}) establishes the maximum rate of roll available, which is critical in low speed flight in counteracting gust-induced rolling moments. For fighter aircraft the maximum rate of roll is a direct measure of the aircraft maneuverability.

6.3.3 Yawing Moment Due to Aileron Deflection ($C_{n_{\delta_a}}$)

The derivative expressing the change in aircraft yawing moment due to a change in aileron deflection is defined as

$$C_{n_{\delta_a}} = \frac{\partial C_n}{\partial \delta_a} \qquad (6.14)$$

and, if positive according to the sign definitions used here, is commonly referred to as the adverse yaw coefficient due to ailerons. The sign of $C_{n_{\delta_a}}$ depends mainly on the rigging of the ailerons (e.g., plain ailerons, Frise ailerons, etc.) and the angle of attack. The ailerons can be treated as discussed in section 6.3.1, and again cross-product terms will be lost if the anti-symmetric mode is used since $C_{n_{\delta_a}}$ depends on sectional induced drag. In addition, viscous effects may be important in calculating $C_{n_{\delta_a}}$,

especially for Frise-type ailerons (which are rigged such that the nose of the upward deflected aileron protrudes below the wing lower surface to achieve favorable yaw). Analysis of these effects cannot be handled by any simple methods, and experimental data will most likely be required. Since $C_{n_{\delta_a}}$ is a very important quantity in lateral-directional control dynamics, it is recommended that further work be done to provide a reliable semi-empirical technique to augment program calculated derivatives.

6.4 Spoiler Derivatives

Unlike the analyses presented in the previous sections for elevator, rudder, and aileron derivatives, potential flow methods cannot be used as the basis for estimating the aerodynamic derivatives for spoiler deflection. Spoilers, as most appropriately indicated by their name, spoil the nearly potential flow over the wing. They deliberately force flow separation forward of the trailing edge, and hence even at small angles of attack the assumptions of classical lifting surface theories do not apply. Treatment of spoilers in the literature is, therefore, largely empirical. Much of this empirical work is summarized in Datcom (section 6.2.1.1 for rolling moment due to asymmetrical spoiler deflection, and section 6.2.2.1 for yawing moment due to spoiler deflection), and some of that work will be discussed here. However, the actual methods of Datcom will not be repeated here, and the reader is referred to Datcom for the details of their implementation.

The bulk of the work done to date on spoiler analysis has been experimental in nature. Attempts to systematize such empirical data have been made, as can be found in several of the cited references in Datcom; but the lack of generality of these data precludes its usefulness in analyzing arbitrary spoilers with arbitrary wing planforms. In addition, it is the opinion of the authors that the fundamental nature of the flow around a wing section with a deflected spoiler, which is characterized by a region of fully separated flow behind the spoiler, may be radically altered when a deflected jet is present. For sufficiently strong jets at large deflection angles, it is possible that the suction pressures prevalent near the jet may be strong enough to reattach the flow, resulting in a bubble behind the spoiler which may increase the effective airfoil camber. The authors know of no experimental evidence to

substantiate this phenomenon, and it is suggested that an experimental investigation of jet-wings with spoilers be made.

The methods presented in Datcom to handle asymmetrically deflected spoilers involve applying three-dimensional corrections to sectional spoiler data. The methods include some rather crude corrections to account for sweep and taper of the spoiler, spanwise flow on the wing, and spoiler-slot effects. However for the limited data correlations presented, the methods seem to be reasonably adequate. The reader should recognize the limited range of applicability of these methods and the total inapplicability of these methods to jet-wings, however, and within the current state of the art experimental data can provide the only reliable source of spoiler effectiveness. Spoiler derivatives, namely $\frac{\partial C_l}{\partial \delta_{sp}}$, $\frac{\partial C_n}{\partial \delta_{sp}}$, and $\frac{\partial C_Y}{\partial \delta_{sp}}$ for asymmetrically deflected spoilers, and $\frac{\partial C_L}{\partial \delta_{sp}}$, $\frac{\partial C_D}{\partial \delta_{sp}}$, and $\frac{\partial C_m}{\partial \delta_{sp}}$ for symmetrically deflected spoilers, are not of great importance in stability analysis and are of secondary importance in control analysis, and hence the lack of a reliable method for their prediction is not considered to be of great importance.

7.0 EMPIRICAL METHODS

7.1 Externally Blown Jet Flap

Estimation of the spreading and turning characteristics of externally blown jet flaps has been a subject of extensive experimental investigation for the past several years, and progress has been made in systematizing the data so that certain fundamental characteristics of the jet can be estimated with reasonable accuracy for configurations resembling those tested. However, general methods, applicable to arbitrary EBF configurations, have not yet been developed, and within the foreseeable future empirical methods are all that will be available. The complex flow phenomena associated with a high velocity jet impinging at an arbitrary skew angle to the lower (or upper) surface of a finite wing are, at this time, beyond the current state-of-the-art, although progress is being made in developing an analytical solution to treat three-dimensional wing/jet interactions including jet distortion influences (reference 20).

Application of the EVD jet-wing method to an externally blown flap configuration depends on the recognition that the details of the jet impingement/spreading/turning process are relatively unimportant as far as the overall aerodynamic characteristics are concerned. Only the end result of this process, the spanwise distribution of the momentum sheet at the trailing edge, has any significant influence on the overall aerodynamic forces and moments.

The jet impingement/spreading/turning involves the viscid/inviscid interaction of the jet with the wing, and it is not currently possible to determine analytically the details of this flow. The required information must be derived experimentally. The usual approach is to first measure the static turning performance of a particular configuration. This supplies the overall turning angle and thrust loss associated with the process. Next, the shape of the spanwise distribution of trailing edge momentum is determined, either by measuring the spanwise momentum distribution or by estimating the spanwise extent of the spread jet flow from the exit nozzle and assuming some spanwise distribution based on available data. The measured overall

static performance, applied over the assumed distribution, completely specifies the information required for input into the EVD segment of the program. This procedure assumes a correspondence between the static impingement/spreading/turning process and that at forward speed, and experiment has shown that EBF jet characteristics are nearly independent of forward speed.

Correlation studies have shown that the calculated results are not very sensitive to differences in the distribution of trailing edge jet momentum insofar as longitudinal aerodynamic characteristics are concerned, but depend mostly on the overall performance of the jet in terms of the turning efficiency, τ, and the turning angle, ν ($\nu=\delta_f+\delta_J$), measured statically. These quantities are very convenient to measure on a wind tunnel model and are routinely determined in most EBF STOL model tests. However, wind tunnel model results are seldom available for arbitrary configurations under study, making it necessary to make estimates based on tests of similar configurations. Lateral-directional aerodynamic characteristics, on the other hand, have been shown to be very sensitive to the spanwise distribution of trailing edge jet momentum, as was briefly mentioned in Section 3.2.2; hence, not only must τ and ν be experimentally determined, but so must $c_\mu(y)$ for calculating such quantities as C_Y, C_l, C_n.

In the following sections information based on experimental investigations and correlation studies is presented to provide design personnel with a rational approach in determining the characteristics of the impingement/spreading/turning process for use in the EVD segment of STAMP.

7.1.1 Static EBF Performance

Recently an experimental program was conducted at the Douglas Aircraft Company to measure the static turning characteristics of an EBF configuration over a wide range of geometric parameters. The hope was that some systematic basis could be laid for estimating EBF static performance. The model consisted of a rectangular wing panel and a single jet nozzle, illustrated in figure (7.1).

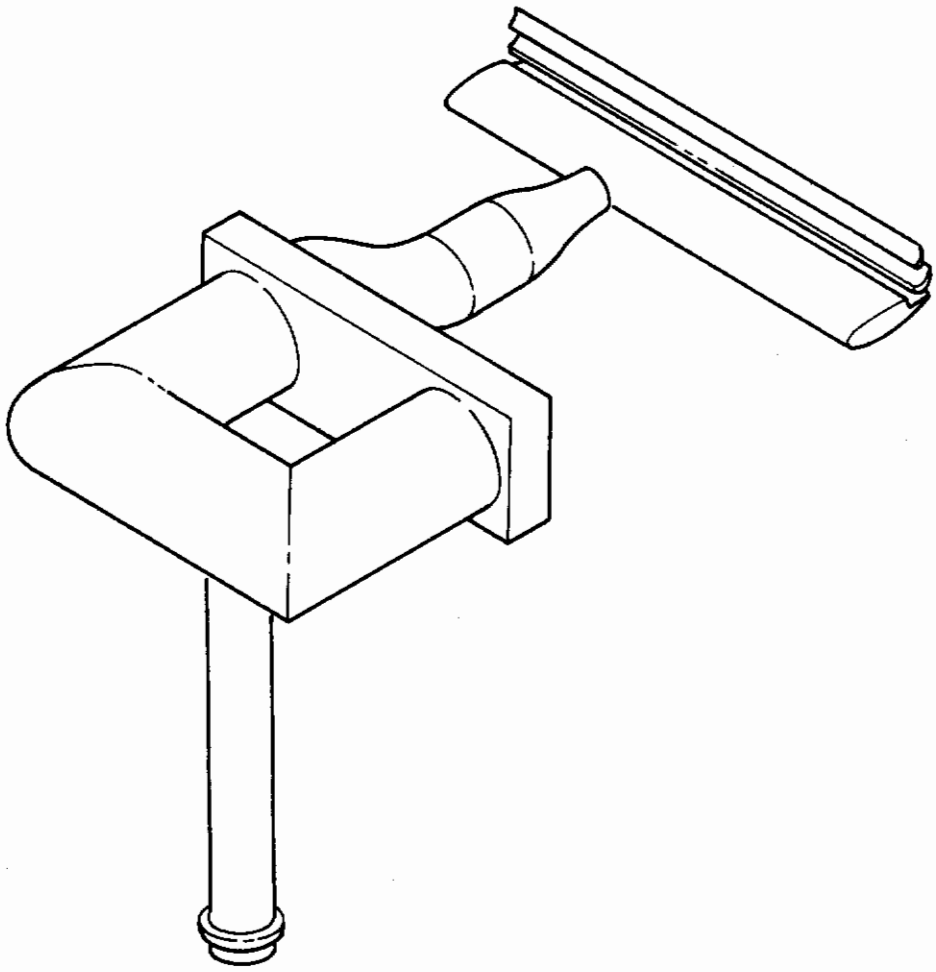

Figure (7.1). Illustration of Test Apparatus to Measure Static EBF Performance

The flap deflection was constant across the span and the aspect ratio was sufficiently high to contain all the jet flow after impingement. The forces and moments were measured on the wing and nozzle separately and summed to yield the overall turning efficiency, τ, and the turning angle, ν. The parametric quantities examined included flap deflection angle, flap chord, wing sweep angle, jet nozzle size and shape, jet pressure ratio, nozzle vertical and longitudinal position relative to the wing, and nozzle incidence angle. Some of these geometric quantities are defined in figure (7.2).

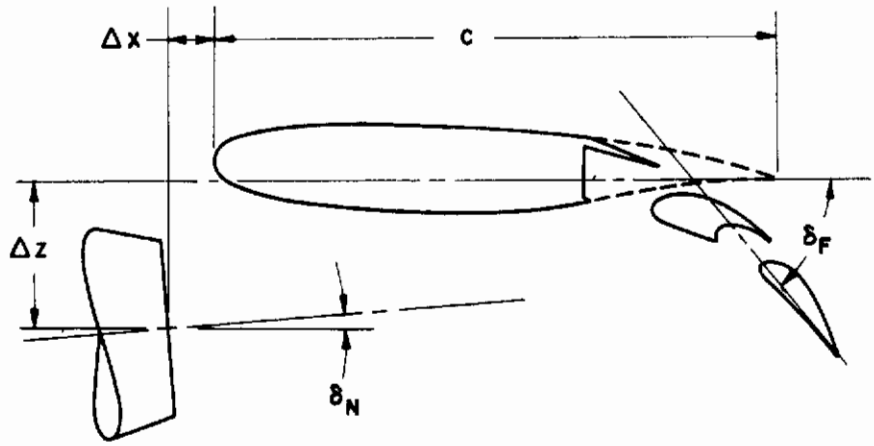

Figure (7.2). Geometric Arrangement of Static EBF Test Apparatus

In addition, limited examinations were conducted on the effects of a simulated fuselage, flap brackets, flap slot fairings, flap gap, and flap vertical position.

It should be obvious that any kind of systematic coverage of so many parameters must involve massive quantities of data, which is the case in this instance. Analysis of the data is still in progress, but it seems obvious that many of the observed trends cannot be satisfactorily generalized because of the great complexity of the flow situation. Nevertheless, some significant findings are evident which may usefully summarize the process. These are presented here.

At a particular flap angle, the most significant geometric parameter is the vertical displacement between the wing lower surface and the nozzle centerline. Figure (7.3) shows the static turning angle and turning efficiency as a function of vertical displacement non-dimensionalized by wing chord, $\Delta z/c$, for a typical configuration. Three curves are shown for different nozzle incidence angles, δ_N. Because of the geometry of the pivot arrangement, the longitudinal positions, $\Delta x/c$, were slightly different for each incidence angle, but this parameter has been shown to have negligible effect

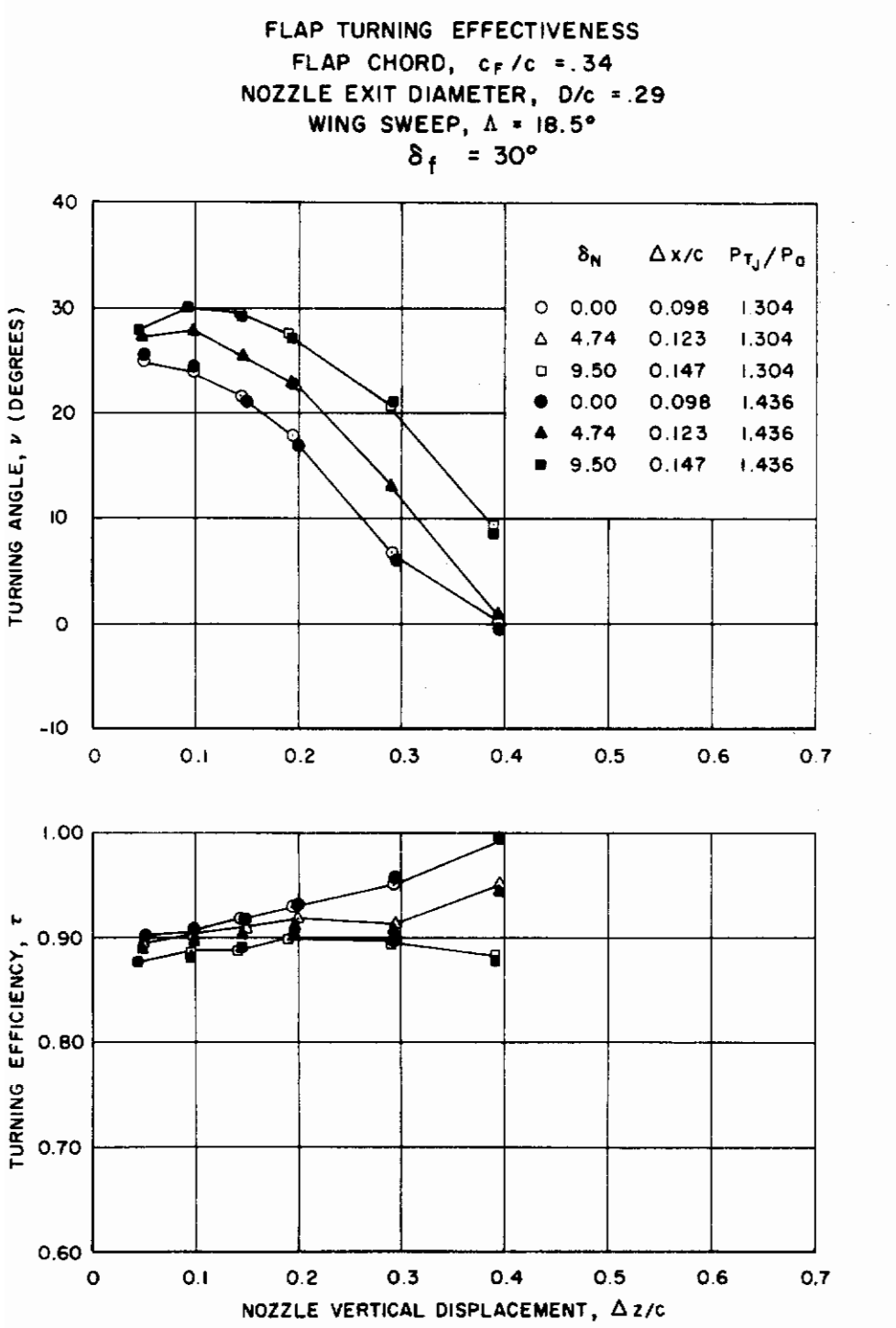

Figure (7.3). Typical Static EBF Performance Data

on the results. Data at two different nozzle pressure ratios (P_{T_J}/P_a) are presented in this figure that correspond approximately to takeoff and landing values, showing little effect of pressure ratio.

The principle trend of the data over the range of $\Delta z/c$ is to show a steady reduction in turning angle and increase in turning efficiency as the vertical displacement is increased. The maximum value of turning angle occurs close to the wing at a point where the turning efficiency varies slowly with $\Delta z/c$, so that an optimum vertical position is usually evident. At large displacements the turning angle and efficiency obviously must approach the nozzle incidence angle and unity, respectively.

It is clear that the variation of flap effectiveness at large displacements must be strongly correlated with the intersection of the jet extended centerline with the flap trailing edge. In fact, some more-or-less successful correlations have been made of the turning angle, ν, as a function of distance between the jet extended centerline and the flap trailing edge when this distance is less than the jet radius. However, the losses associated with this turning, expressed as the turning efficiency τ, show much less systematic behaviour, which makes a complete correlation more difficult. Efforts to develop a complete correlation of these data are continuing and will be the subject of a future Douglas Aircraft Company report.

More important than this problem, however, is the description of the flap effectiveness trends near the optimum nozzle location, since any viable STOL aircraft design would no doubt be operating near that point. In this case, the data clearly show that the distance between the flap trailing edge and the extended jet centerline has little correlation with the flap effectiveness. The optimum location is usually so close to the wing that the jet shape and trajectory is appreciably distorted before the trailing edge is reached.

As a first step in empirically describing the overall static flap effectiveness, the quantities τ and ν at the optimum nozzle location were examined over the range of flap angles and other geometric parameters tested. Figure (7.4) shows the customary polar presentation of the data. Two nozzle incidence angles are shown and the open symbols denote a single slot flap

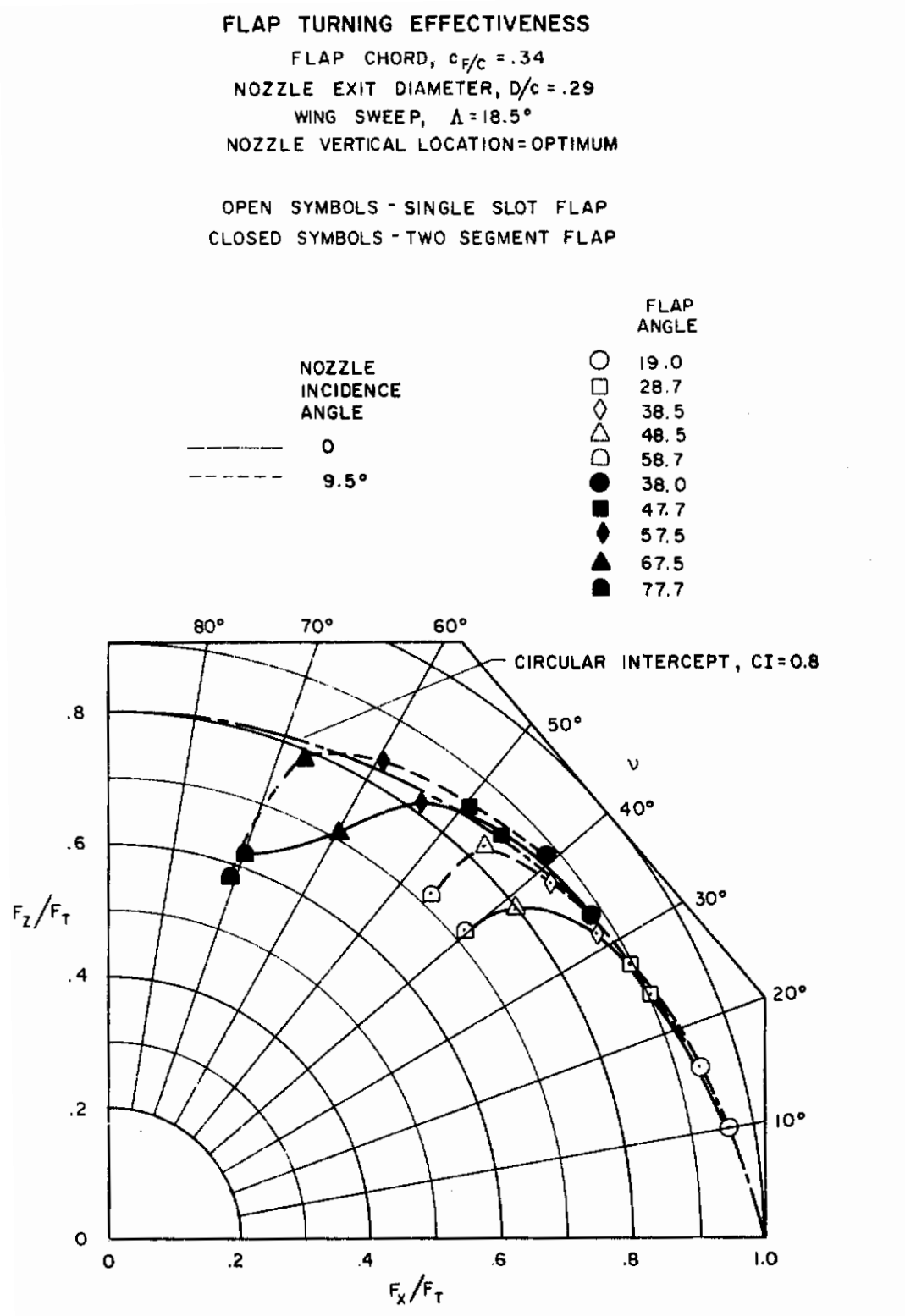

Figure (7.4). Polar Presentation of Static EBF Performance Data

configuration while the solid symbols denote a two segment flap. Inspection of this figure suggests that the data for the various combinations of flap angle, nozzle incidence angle, and flap configuration show an envelope of maximum performance that approximates a circular arc through the point $\nu = 0$, $\tau = 1.0$, with the center of the circle on the axis $\nu = 90°$. Such a circular arc can be specified with one quantity, and this has been taken to be the intercept of the arc with the axis $\nu = 90°$. This quantity has been called the circular intercept (CI). Thus, two variables, τ and ν, can be described with the single quantity, CI. The significance of this quantity can be appreciated by recognizing that increases in turning angle or turning efficiency can easily be achieved by changing the flap angle in the appropriate direction, but that τ and ν are coupled together such that CI is approximately constant. Any significant improvement in τ or ν requires that CI increase in value.

Having established the concept of the circular intercept, CI, it is now possible to present some limited data which can be used to estimate the turning effectiveness of various flap/nozzle arrangements. Such data are presented in figure (7.5), where CI and ν/δ_f are plotted as a function of the flap deflection angle. Although these data do not cover a complete matrix of the pertinent variables, there is enough coverage to make them useful for estimating the static turning performance of an EBF configuration. The procedure to follow in use of these data is to select the plot which most closely resembles the case of interest in terms of wing sweep, nozzle diameter, and flap chord ratio, and determine CI and ν as a function of flap deflection δ_f. Then a polar plot similar to figure (7.4) can be drawn to determine τ. The center of the circle to be drawn is located on the $\nu = 90°$ axis, located at

$$\frac{F_Z}{F_T} = \frac{(CI)^2 - 1}{2(CI)} \qquad (7.1)$$

which can be verified by simple analytic geometry. The center of the circle is always at a negative value of $\frac{F_Z}{F_T}$. By this procedure an envelope of τ and ν values can be estimated so that the turning effectiveness over a range of flap angles can be estimated. It must be emphasized, however, that the data of figure (7.5) are for optimum vertical positions $(\Delta z/c)$ of the nozzle

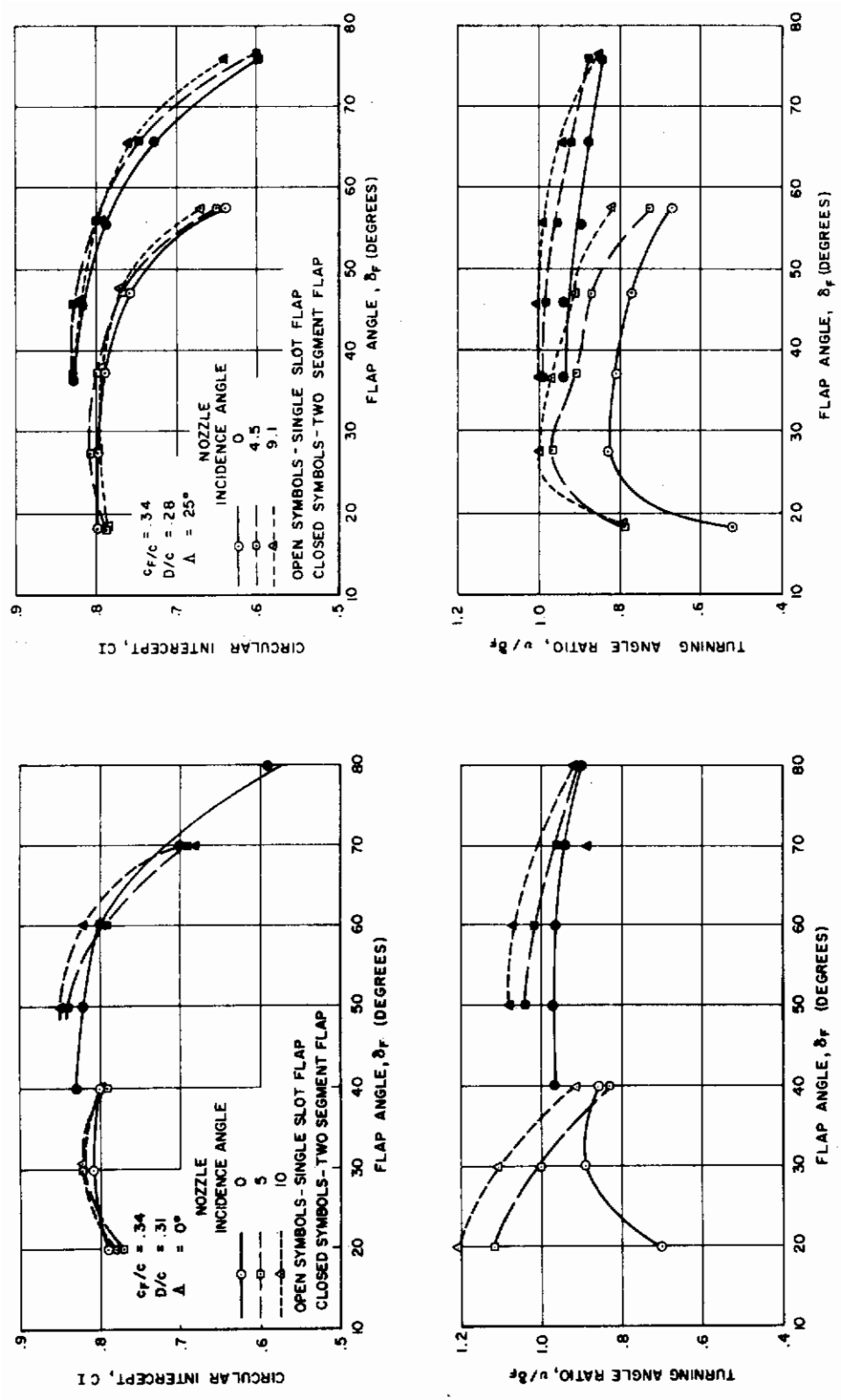

Figure (7.5). Summary of Experimentally Determined Static EBF Performance Data

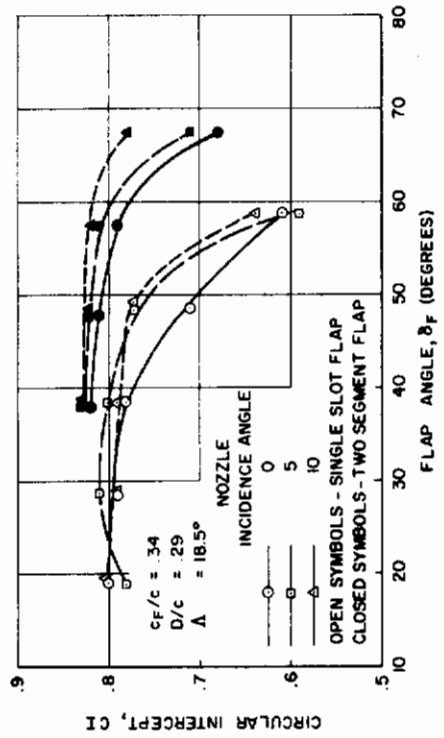

(d)

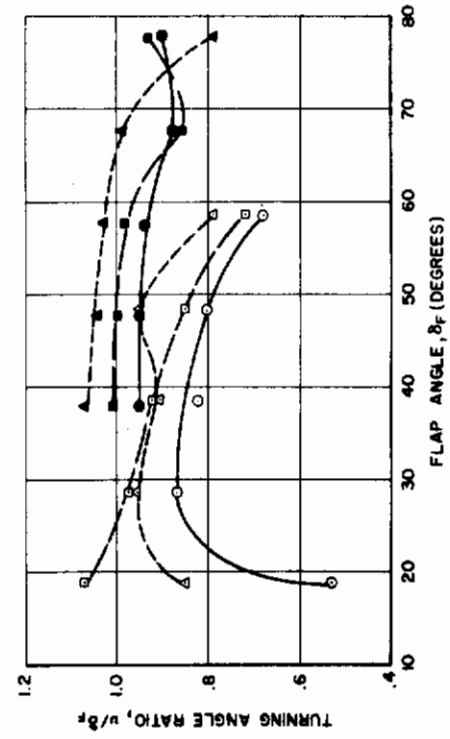

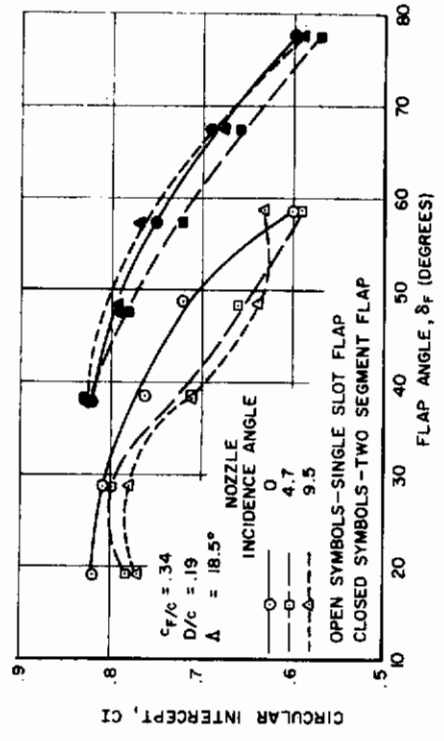

(c)

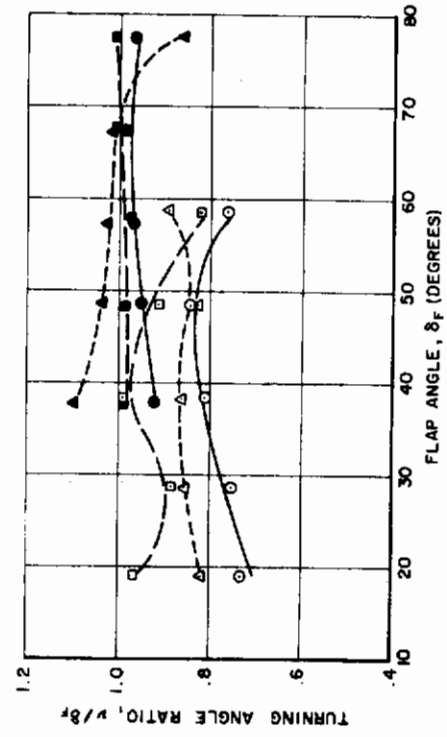

Figure (7.5) Continued

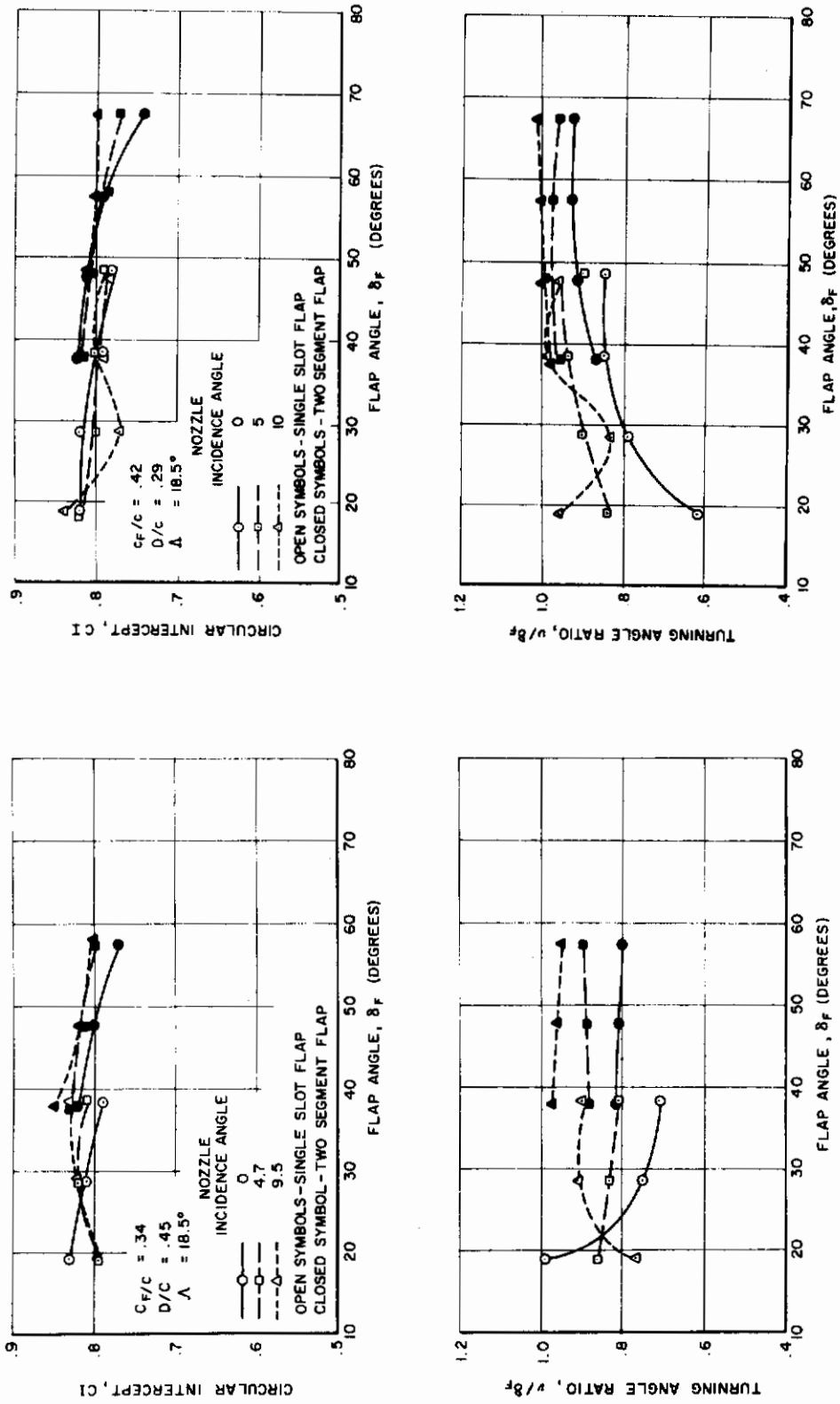

Figure (7.5) Continued

as determined from the experimental program described herein, but as yet no systematic means of determining this position has been found.

7.1.2 Jet Spreading

In the preceeding section the turning effectiveness of nozzle/flap combinations has been discussed, and empirical methods based on extensive experimental programs have been presented. The problem of jet spreading, however, is even more difficult to treat, and to date little in the way of analytical or empirical methods has been developed. Solution of the problem, which is simply to determine the spanwise distribution of trailing edge jet momentum $c_\mu(y)$, requires that the flow details of the impingement/spreading/turning process be known. Such a flow solution, which involves the viscid/inviscid interaction of the jet impinging on the wing/flap system, is clearly beyond the current state-of-the-art. The discussion here will be concerned primarily with experimentally determined spanwise momentum distributions and means of postulating such distributions for arbitrary nozzle/flap geometries.

In conjunction with static and forward speed EBF experimental programs conducted at the Douglas Aircraft Company, a limited number of jet momentum distributions have been measured using a 3-D hot film anemometer probe. Some of these data are presented in figure (7.6) for a complete EBF model. The curves in this figure correspond to power settings representative of total jet momentum coefficients C_J used in EBF forward speed tests. The general shape of these curves indicates that the greatest concentration of jet momentum is directly behind the engines, as would be expected, but considerable spreading of the jet is also indicated.

Data of the type presented in figure (7.6) are ideal for use in the program, but this type of information is rarely available, particularly in the preliminary design phase. Hence, there is a necessity to be able to postulate the spreading and distribution of the jet. The postulated spreading and momentum distribution suggested here are quite crude, but fortunately the longitudinal aerodynamic characteristics have been shown to be rather insensitive to the jet distribution. However, the lateral aerodynamic characteristics, particularly C_l and C_n, are strongly dependent on $c_\mu(y)$, and more adequate

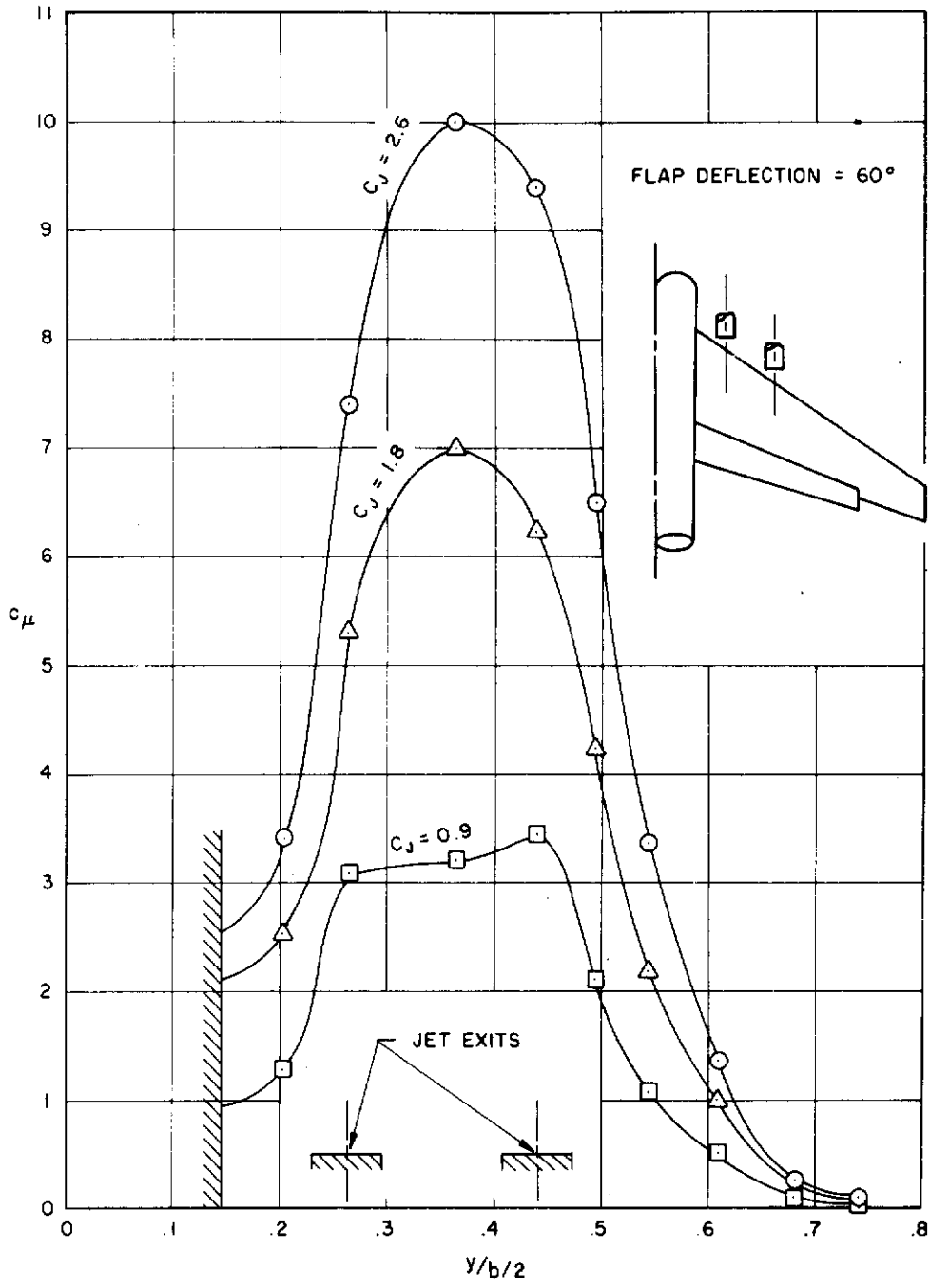

(a)

Figure (7.6). Trailing Edge Momentum Distribution for a Typical EBF Transport Model

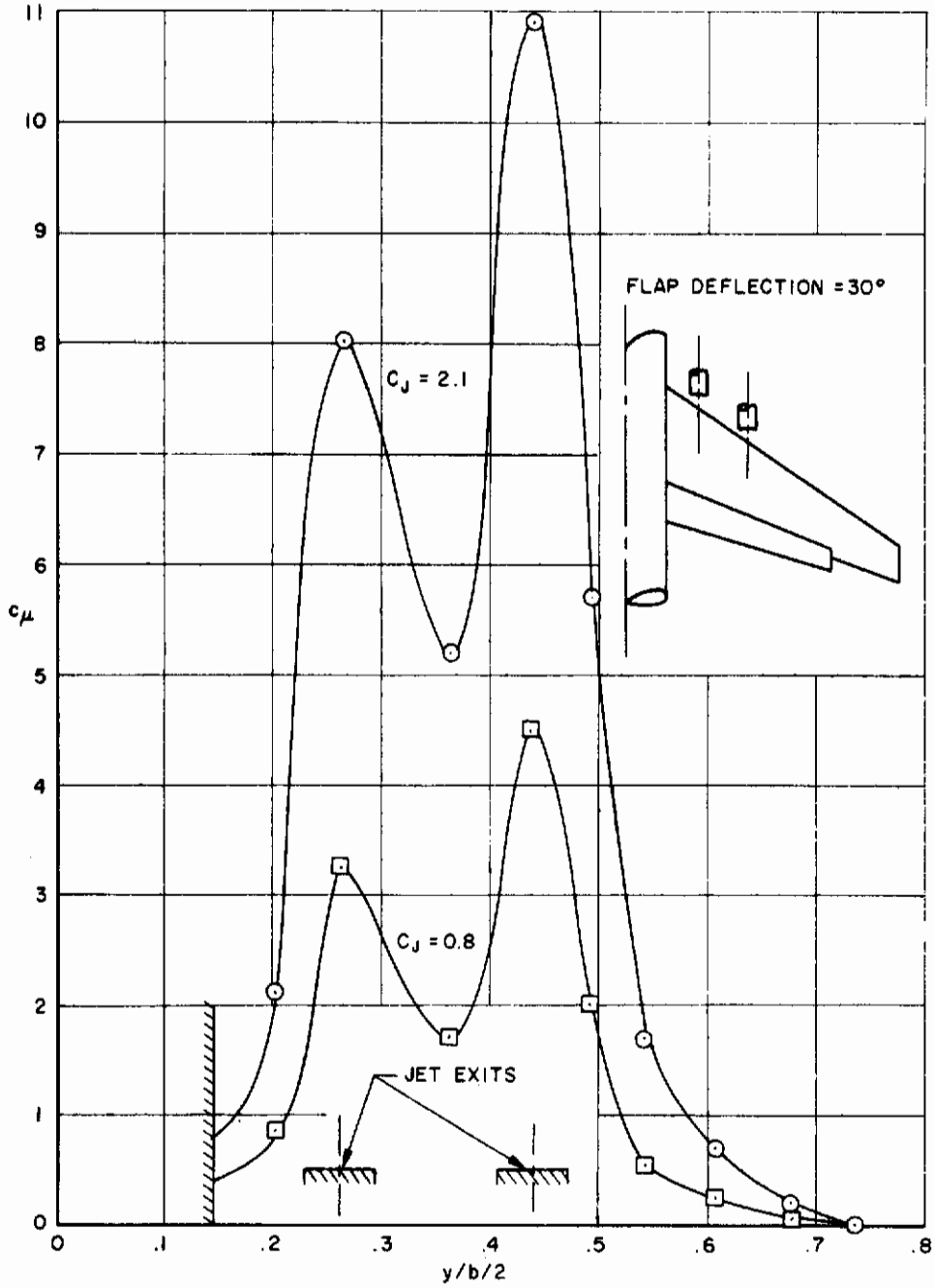

(b)

Figure (7.6) Continued

means of determining the momentum distribution will be required for them.

A procedure for estimating the jet momentum distribution for an EBF configuration is illustrated in figure (7.7). This procedure is based on experimental data similar to those presented in figure (7.6) and is intended to approximately predict the momentum distribution of an arbitrary configuration. A trapezoidal momentum distribution is assumed for each engine, with $c_\mu(y)$ constant across the face of each engine and decreasing linearly to zero on either side of the engine. The spanwise width of these trapezoids has been found to be primarily a function of the flap deflection, which is a measure of how much of the jet impinges on the wing lower surface. For the limited data available at this time, it can be said that for a 30 degree flap deflection each jet spreads approximately one jet diameter beyond each edge of the jet, while for a 60 degree flap deflection the spreading is approximately two jet diameters. For the inboard engine where the spreading region extends into the fuselage, the trapezoidal shape must be suitably modified. The magnitude of $c_\mu(y)$ is, of course, constrained by the requirement that

$$C_J = \frac{1}{S} \int_{-b/2}^{b/2} c(y)\, c_\mu(y)\, dy \qquad (7.2)$$

where C_J is the total jet momentum coefficient. To actually calculate the momentum distribution for an arbitrary EBF configuration, it is recommended that first the blown region be defined, as in figures (7.7a) and (7.7c). Then the c_μ-distribution for each engine can be determined. Consider the inboard engine for the configuration in figure (7.7). The blown region extends from point a' to point d. This region can be divided into three segments: the first extending from point a (inside the fuselage) to point b; the second from point b to point c across the face of the engine; and the third from point c to point d. Defining $C_{J_{Inboard}}$ as the total momentum coefficient of the inboard engine (which for a four engine airplane would be $\frac{1}{4} C_J$), and using the constraint implied by equation (7.2), the spanwise momentum distribution associated with this engine can be shown to be

$$c_\mu(y) = \frac{c_{\mu_{max}} (y-y_a)}{y_b-y_a} \qquad y_{a'} \le y \le y_b \qquad (7.3a)$$

$$c_\mu(y) = c_{\mu_{max}} \qquad y_b \le y \le y_c \tag{7.3b}$$

$$c_\mu(y) = \frac{c_{\mu_{max}}\,(y_d-y)}{y_d-y_c} \qquad y_c \le y \le y_d \tag{7.3c}$$

where

$$c_{\mu_{max}} = \frac{C_{J_{Inboard}}}{K_1+K_2+K_3} \tag{7.3d}$$

and

$$K_1 = \frac{1}{S}\left\{\frac{c_a}{y_b-y_a}\left[\frac{1}{2}\,(y_b^2-y_a^2,) - y_a\,(y_b-y_a,)\right]\right.$$

$$\left. + \frac{(c_b-c_a)}{(y_b-y_a)^2}\left[\frac{1}{3}(y_b^3-y_a^3,) - y_a(y_b^2-y_a^2,) + y_a^2(y_b-y_a,)\right]\right\} \tag{7.3e}$$

$$K_2 = \frac{1}{S}\left\{\frac{1}{2}(c_c+c_b)(y_c-y_b)\right\} \tag{7.3f}$$

$$K_3 = \frac{1}{S}\left\{\frac{1}{2}\,c_c(y_d-y_c) + \right.$$

$$\left. \frac{(c_d-c_c)}{(y_d-y_c)^2}\left[\frac{1}{6}(y_d^3-y_c^3) - \frac{1}{2}\,y_c y_d(y_d-y_c)\right]\right\} \tag{7.3g}$$

where S is the reference area and c is the local wing chord at spanwise station y. For the outboard engine these equations can similarly be derived by replacing a, a', b, c, d by e, e, f, g, h, respectively. Hence, a spanwise momentum distribution associated with each engine can be calculated in this manner, and the total sectional momentum coefficient $c_\mu(y)$ can then be calculated by summing the contribution from each engine, as illustrated in figures (7.7b) and (7.7d). Graphical evaluation of the c_μ-distribution as illustrated in figure (7.7) is adequate, although the value of $c_{\mu_{max}}$ must be determined from equation (7.3). These assumed distributions can be smoothed such that they more realistically represent distributions like those in figures (7.6).

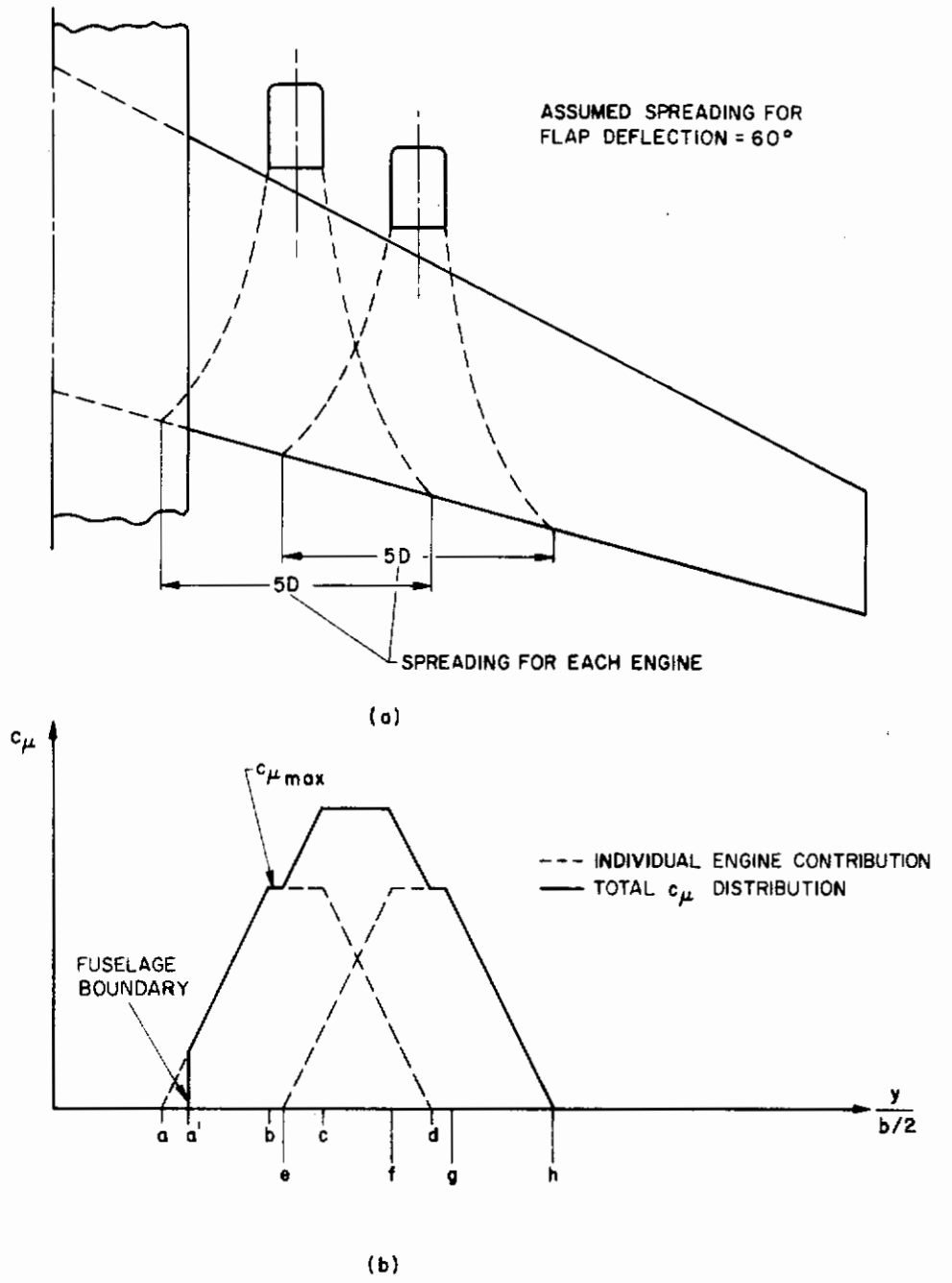

Figure (7.7). Procedure for Estimating the Spanwise Distribution of Jet Momentum

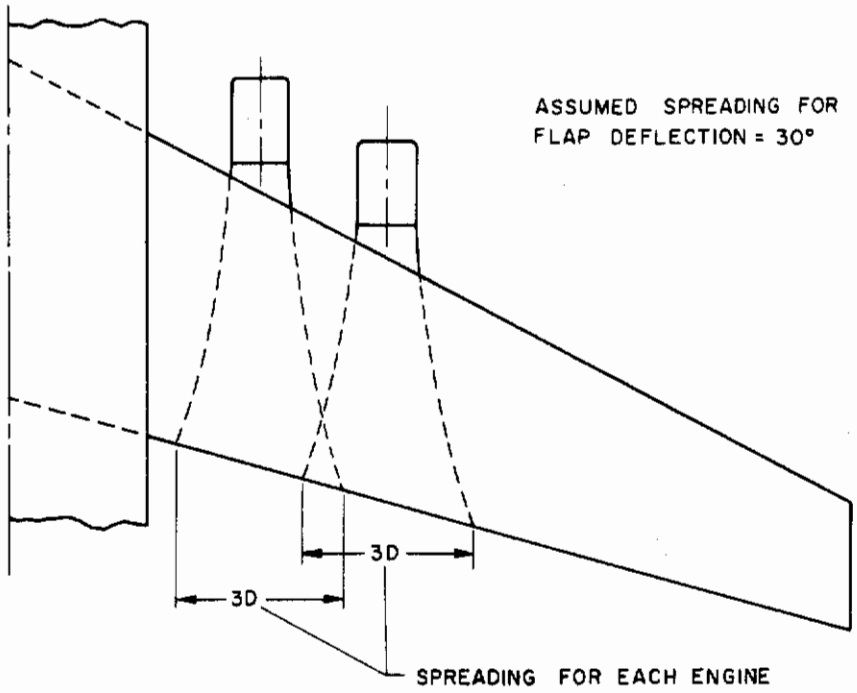

(c)

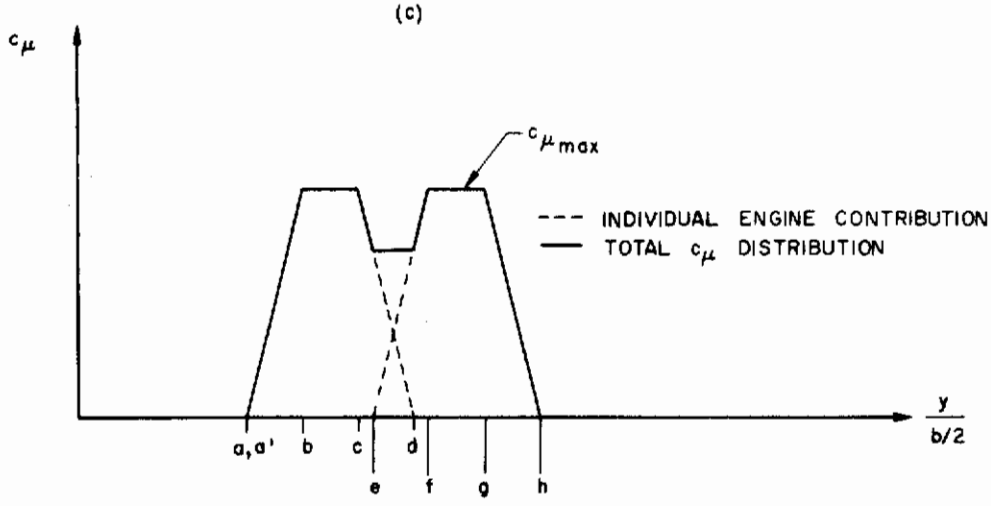

(d)

Figure (7.7) Continued

What has been provided in this section is no more than a preliminary empirical method to estimate the spanwise distribution of jet momentum for typical EBF configurations. The authors expect that, as more experimental data is obtained and reduced, more sophisticated empirical methods will be developed. In addition, efforts to solve the jet impingement/spreading/turning problem analytically will undoubtedly provide further capabilities in the future.

8.0 METHODS APPLICATIONS

The aerodynamic and stability and control prediction methods developed in this work have been applied to a number of complete STOL aircraft configurations for which experimental data is available in order to assess the validity of the methods and to demonstrate their applicability to practical STOL aircraft configurations. The configurations selected for presentation were tested by Convair Aerospace Division of General Dynamics Corporation in the AFFDL STOL Tactical Aircraft Investigation (STAI). This test program used a common basic aircraft configuration to test each of the STOL concepts under consideration in this report:

- Internally ducted jet flap, blown over a flap (IBF).
- Externally blown jet flap (EBF).
- Mechanical flap with vectored thrust (MF/VT).

These configurations have been analyzed using the STOL Aerodynamic Methods Program (STAMP), and the results of the computer generated aerodynamic data have been modified using the engineering methods presented in this volume. In the following sections each of the configurations is defined; preparation of the geometry for input to STAMP is discussed; application of the engineering methods to the computer data is presented; and the final results are compared with the available experimental data.

Some general comments concerning the availability and applicability of the Convair STAI data to this work must be made. It was originally intended that experimental data from the STAI would be used to improve the empirical methods presented in this volume. However, these data were not received by the Douglas Aircraft Company until late in the term of this contract, and hence the time constraint allowed for only direct comparisons to be made. Although the experimental data was received late, a preliminary test report (reference 26) was available, and the original STAMP computer runs were based on the configurations described therein. It has since been learned, however, that discrepancies exist between the model geometric details in reference 26 and those presented in the final wind tunnel data report, reference 27. Most notably in disagreement was the wing root chord which was listed as 12.05 inches in reference 26 and as 12.89 inches in reference 27. Since the former value was used in all computer runs, an error in wing area of approximately

five percent exists in all data presented herein. Another discrepancy involves double-slotted flap geometry. Reference 26 refers to flap F_{32} while reference 27 refers to flap F_{23}, yet no apparent difference has been found between these flaps.

Throughout the analysis some basic assumptions have been made which may not be obvious but which may be of some importance. As discussed in Section 2.0 of this volume, when Fowler flaps are considered, the composite case capability of STAMP can be used to evaluate several flap deflections only by choosing a mean planform representative of the mean flap extension. Otherwise, a new planform must be input for each flap angle. In the analyses presented here, the composite case feature has been used since it demonstrates the normal program usage; but the discrepancies due to Fowler flaps, especially for the EBF and MF/VT, must be remembered. Additionally, changes in flap turning efficiency with flap deflection cannot be treated using the composite case feature of STAMP, so instead a mean value of τ must be used. This results in a small discrepancy between experiment and the analysis for the trailing edge C_J. This effect is important only for the EBF, and the actual trailing edge C_J values have been listed to emphasize the discrepancy.

Finally, the authors have considerable concern over some of the techniques employed in the wind tunnel tests presented in references 26 and 27, particularly in regard to wall corrections, sting interference, wake blockage, and ground effects. Rather than discuss testing techniques here, however, these matters are fully discussed in later sections which compare experiment and predictions.

8.1 STOL Aircraft Employing Internally Ducted Jet Flap

An internally ducted jet flap system in which the jet is blown over the knee of a plain trailing edge flap was employed in the first phase of these comparisons. Such a high lift system is often referred to as an internally blown flap (IBF).

8.1.1 Configuration Description

The basic aircraft configuration is illustrated in figure (8.1). The model is typical of a four-engine, high wing, T-tail, subsonic STOL transport

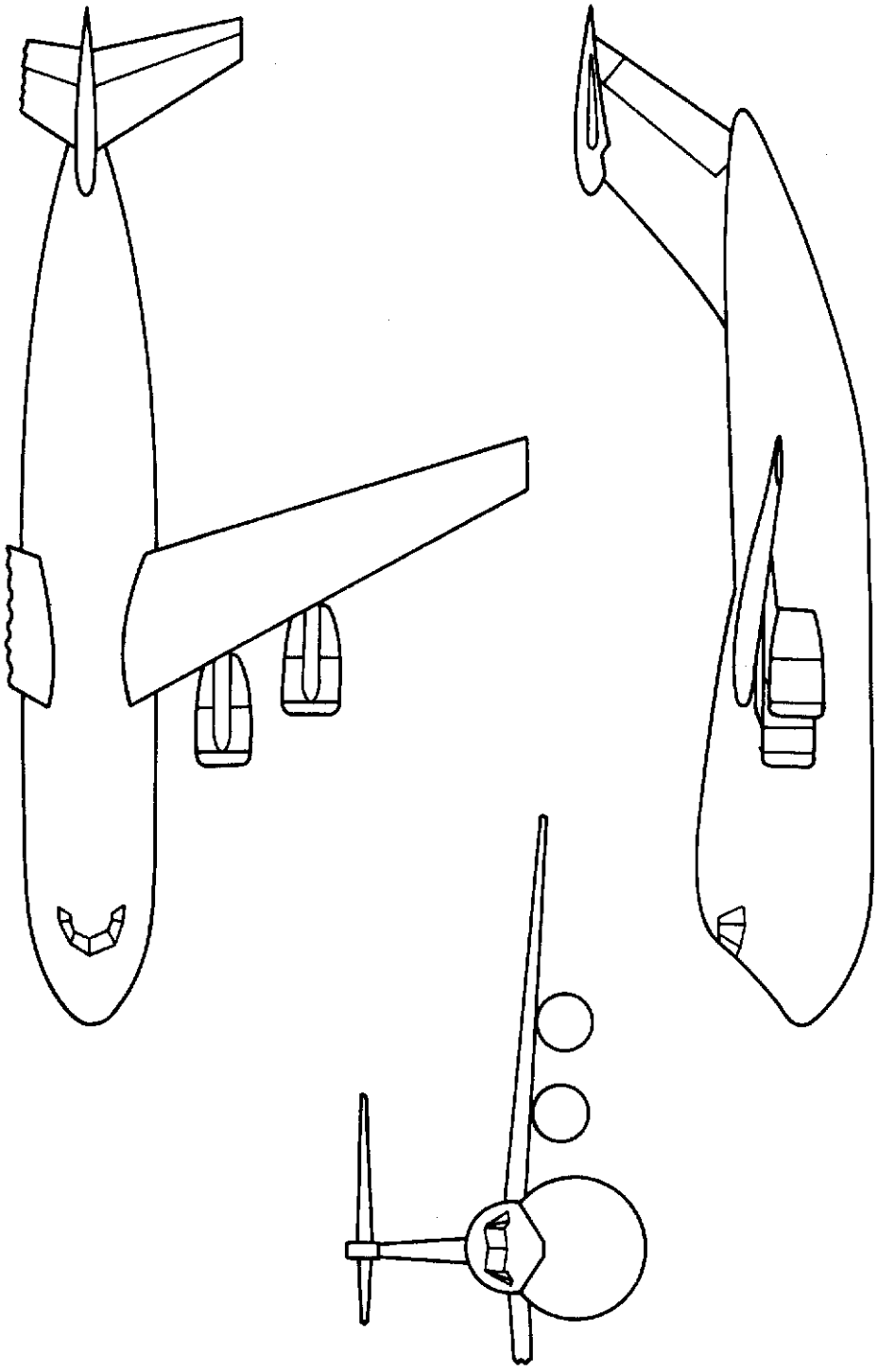

Figure (8.1). Basic Convair STAI Model Configuration

with a front-loading cargo fuselage. The basic wing geometric characteristics are listed in table (8.1).

Table (8.1). IBF Wing Geometric Characteristics

Aspect Ratio	8.0
Taper Ratio	0.334
1/4-Chord Sweep	25°
Span (in)	68.82
Area (in^2)	592.0
Dihedral	-3.5°
Incidence, root	3.5°
Chord, root (in)	12.05
tip (in)	4.33
MAC (in)	9.33
Airfoil, root	NACA 64A314
tip	NACA 64A410
Twist, root	0.0°
tip	-4.5°
MAC	-1.1°

The wing is equipped with a full span plain flap with flap-chord ratio and chord extension as listed in table (8.2).

Table (8.2). Plain Flap Geometric Characteristics

δ_f(deg)	C_f/C	C'/C
15	.255	1.013
30	.269	1.027
45	.285	1.043
60	.303	1.061

Since the wing is mounted high on the fuselage, the inboard edge of the flap actually extends inboard of the fuselage edge. However, for the purposes of analyzing such a geometry, the flap will be assumed to end at the outboard edge of the fuselage. Blowing over the flap was accomplished with a full span slot at the knee of the flap.

This wing is also equipped with a full span leading edge flap with a chord 15 percent of the local wing chord and a chord extension of 14.5 percent.

The empennage is a T-tail type. The primary geometric characteristics are listed in table (8.3).

Table (8.3) Empennage Geometric Characteristics

	Horizontal	Vertical
Aspect Ratio	4.50	0.95
Taper Ratio	0.40	0.65
1/4-Chord Sweep	25°	45°
Span (in)	24.394	11.811
Area (in^2)	132.19	146.88
MAC (in)	5.753	12.619

8.1.2 Geometry Preparation for Computer Analysis

In accordance with the geometry preparation procedures of Section 4.2 of Volume II, the wing planform is first defined by graphically extending the chord to account for flap and leading edge device deflections, as illustrated in figure (8.2). Note that a mean chord extension, calculated from the data in table (8.2), has been chosen. The inboard 16 percent semi-span is retained in its unextended form to account for the fuselage. Since the flap, leading edge flap, and jet are full span, the only regions where large spanwise loading gradients can be expected are near the wing tip and at the edge of the fuselage. Using this fact, the spanwise divisions are then selected based on the spacing guidelines presented in Volume II [see figure (8.2)]. Centerline locations of each section are most easily determined by choosing the edge of each section first and then calculating the centerline values. For this case, NROWS = 13 and the values of Y to be input are .985, .945, .885, .80, .675, .525, .375, .27, .215, .175, .145, .095, .03.

Division of each section in a chordwise sense is simplified by the fact that the first ten (outboard) sections have identical chordwise geometry, while the three inboard sections represent the fuselage cut out and require only simple definition. The basic chordwise geometry is that of a NACA 64A-series airfoil, with an a = 1.0 mean line, which has infinite camber at both

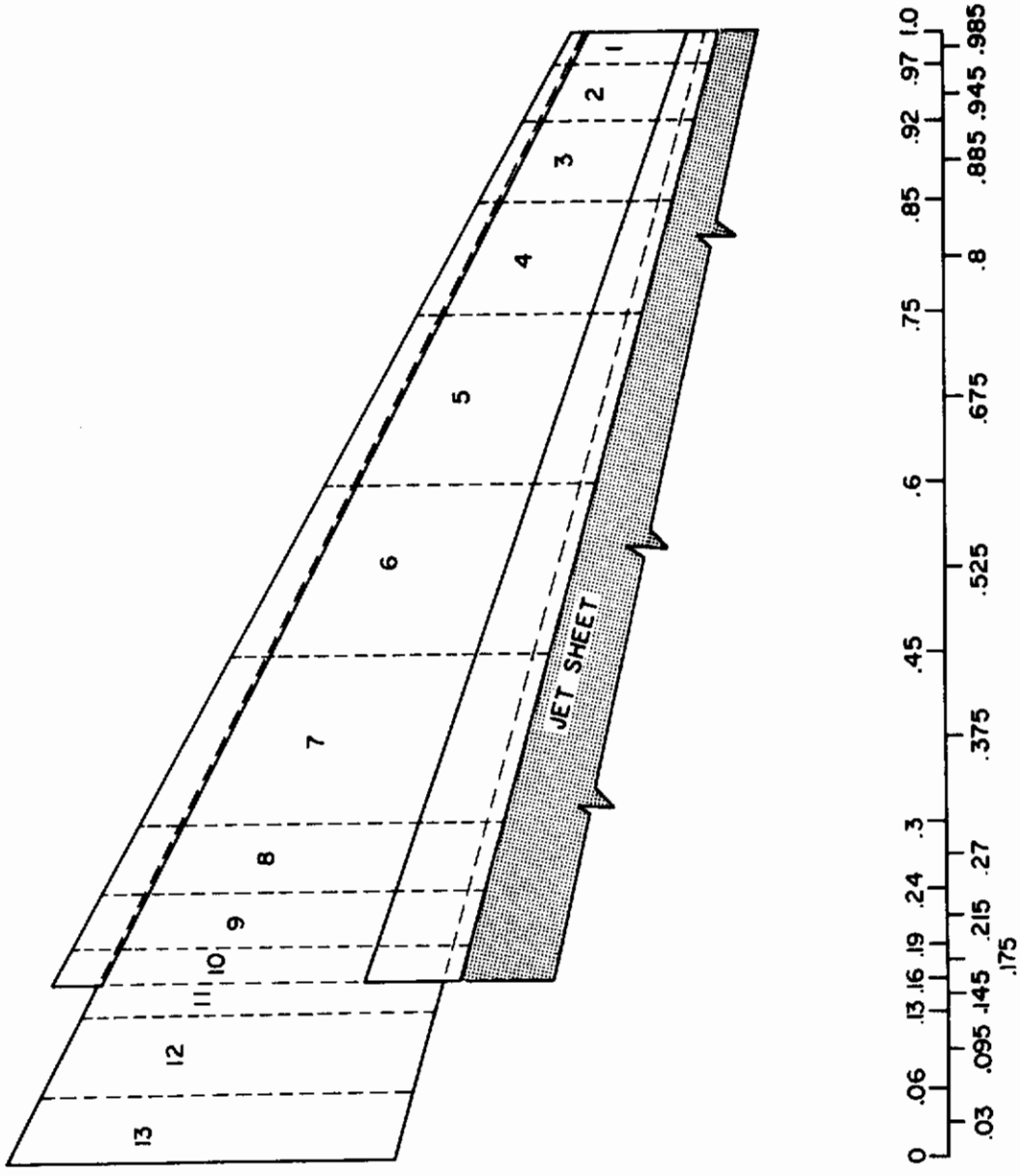

Figure (8.2). IBF Wing Planform Including Selected Spanwise Divisions

the leading and trailing edges. Hence camber can only be approximated for input to the computer program. In addition, there are two hinges in each section. From table (8.2) the average flap-chord extension is found to be 3.8 percent of the unextended chord, the leading edge extension is 14.5 percent of the unextended chord, and the extended chord c' is therefore

$$c' = (1.0 + 0.038 + 0.145)c = 1.183c$$

The leading edge flap hinge is located at the unextended leading edge, while the trailing edge flap hinge is located at 72.2 percent of the unextended chord. Therefore, the flap hinge lines, in terms of the extended chord, are located at

$$\frac{x}{c'} = \frac{0.145}{1.183} = 0.12 \qquad \text{(leading edge flap hinge)}$$

$$\frac{x}{c'} = \frac{0.145 + 0.038 + 0.722}{1.183} = 0.76 \qquad \text{(trailing edge flap hinge)}$$

The location of the hinges could also have been determined graphically. Figure (8.3) summarizes the various details of the chordwise geometry, including the $a = 1.0$ camber line, flap hinges, and the chosen chordwise spacing distribution. In addition, the spacing distribution for the three inboard sections is shown. The chosen divisions have 13 elements per section for the ten outboard sections and 9 per section for the three inboard sections, for a total of 157 elements on the semispan wing. In addition, the spacing on the jet sheet is also shown in figure (8.3) and has 6 elements per jet row for a total of 60 elements on the semispan jet. The semispan jet-wing configuration is defined by 217 EVD elements, and the symmetry option of the program will be utilized.

The wing is fully defined as in figures (8.2) and (8.3). The planform is input to the computer program in two trapezoidal sections using leading and trailing edge coordinates obtained graphically from figure (8.2) and tabulated below:

Y_{CL}	XLEAD	XTRAIL
0.985	17.72	22.37
0.175	1.72	14.28
0.145	2.72	13.56
0.03	0.585	12.35

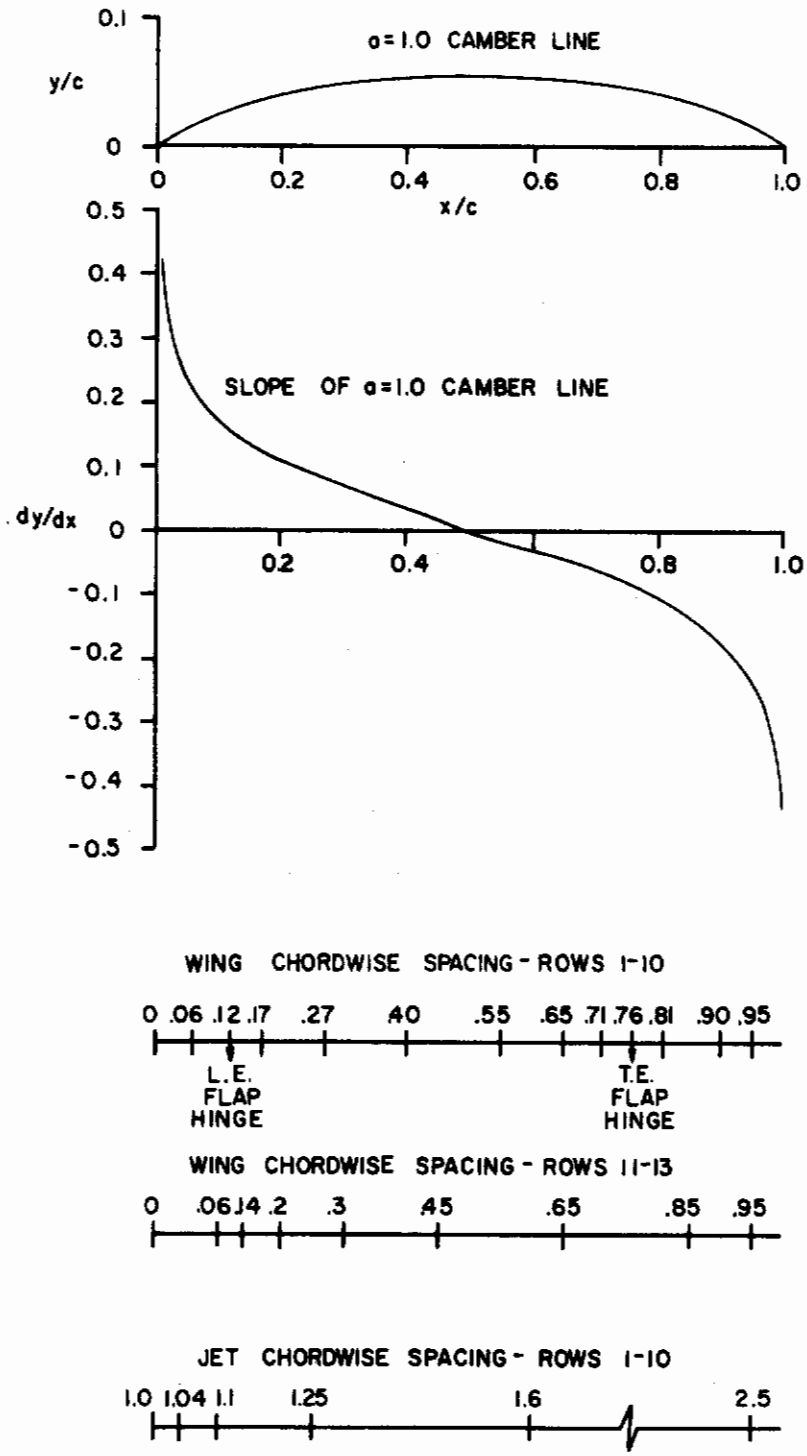

Figure (8.3). IBF Wing Chordwise Geometry Summary

This wing has been defined using five fundamental cases:

1. Angle of attack case.
2. Wing twist plus wing camber case.
3. Leading edge flap hinge case.
4. Trailing edge flap hinge case.
5. Jet deflection case.

The first case is defined by the program. Wing twist is plotted in figure (8.4), and camber has already been defined in figure (8.3). The leading edge hinge is defined for the first ten outboard wing rows at $x/c = 0.12$. The fundamental case deflection angle is input as one degree. Similarly, the trailing edge flap hinge is defined at $x/c = 0.76$ with a one degree deflection. A jet deflection fundamental case is required since the IBF jet turning differs from the flap deflection. Figure (8.5) indicates that the jet turning angle is approximately 10 degrees greater than the flap angle over the range of flap deflections considered. The jet turning fundamental case is defined as a uniform one degree deflection over the full span of the jet.

To evaluate the desired IBF configurations, four composite cases are required. Each case includes camber and twist (1.0 x CASE 2), leading edge flap deflection (55.0 x CASE 3), and a jet deflection of ten degrees (10.0 x CASE 5). Flap deflections of 60, 45, 30, and 15 degrees (60.0, 45.0, 30.0, 15.0 x CASE 4) are required for each composite case, respectively.

Calculation of jet strength input data for this IBF configuration is not difficult since the sectional jet momentum coefficient $c_\mu(y)$ is constant across the span. In this case the span of blowing is $0.16\ b/2 \le y \le 1.0\ b/2$, and the sectional momentum coefficient can be calculated from

$$c_\mu = C_{J_e} \frac{S}{S_B} \tau$$

where S_B is the blown wing area [see figure (3.7)] and τ is the turning efficiency of the flap. From figure (8.2) it can be determined graphically that $S_B/S = 0.84172$. The turning efficiency was measured statically and is plotted in figure (8.5). The mean value of τ over the range of flap deflections considered is 0.83. Hence the following table of gross engine thrust coefficient C_{J_e} versus trailing edge sectional thrust coefficient c_μ can be calculated:

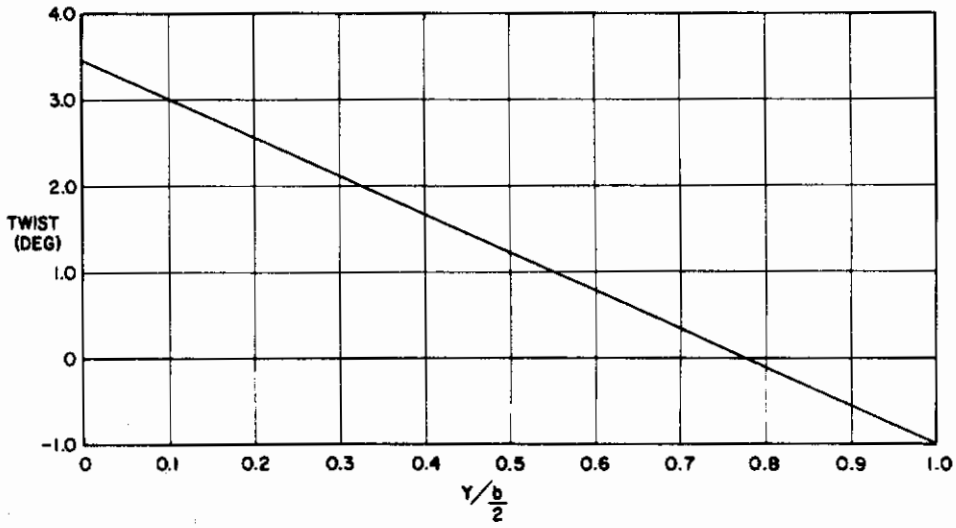

Figure (8.4). Wing Twist

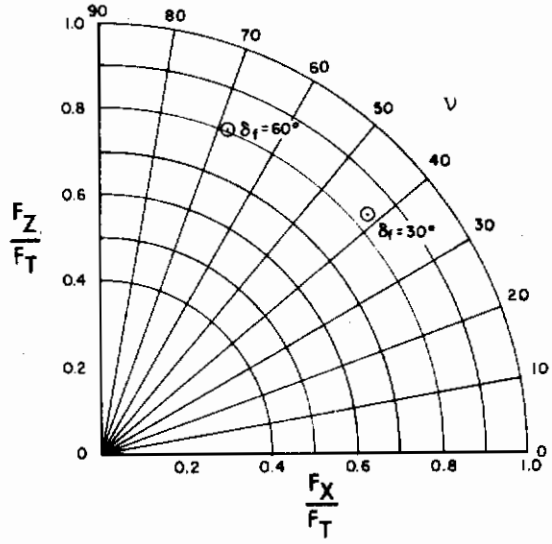

Figure (8.5). IBF Flap Turning Effectiveness (Test GDLST 612-3)

C_{Je}	C_{μ}
0	0
0.5	0.493
1.0	0.986
2.0	1.972
3.0	2.958
4.0	3.944

Empennage geometry is input using the geometric data in table (8.3). The apex-to-apex distances can be measured from figure (8.1) to be HL = 43.77, HH = 11.81, VL = 29.89, VH = 0.0. Since both panels of the horizontal tail must be input, 12 spanwise rows are required, while on the vertical tail only 6 rows are required. The centerlines of the chosen divisions are tabulated below:

YH = 0.975, 0.85, 0.65, 0.45, 0.25, 0.075, -0.075, -0.25, -0.45, -0.65, -0.85, -0.975

YV = 0.975, 0.85, 0.65, 0.45, 0.25, 0.075

The unusual fuselage geometry for this configuration, shown in figure (8.1), requires that the arbitrary cross-section input option be used for fuselage definition. Cross-sections for the forward portion of the fuselage with the upper deck have been assumed to be formed by two intersecting circles [see figure (8.6a)], while cross-sections for the remainder of the fuselage have been assumed to be elliptical. The fuselage has been divided into 37 streamwise segments based on the spacing guidelines presented in Section 4.2.3 of Volume II. Upsweep of the afterbody has been defined using the fuselage section vertical displacement input option. Figure (8.6) summarizes the fuselage geometry definition process. Details of the sectional geometric input are not presented because of the large amount of data involved, but the equivalent fuselage radius distribution and area distribution as calculated by the computer program are presented as a summary. These two quantities are a good check on the validity of the fuselage geometry input.

In addition to wing, jet sheet, empennage, and fuselage geometries, some basic parameters and control flags must be defined. The reference moment

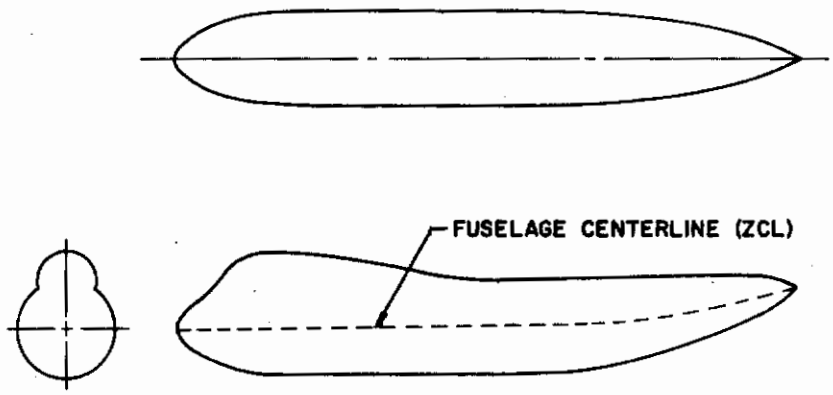

(a) FUSELAGE THREE-VIEW DRAWING

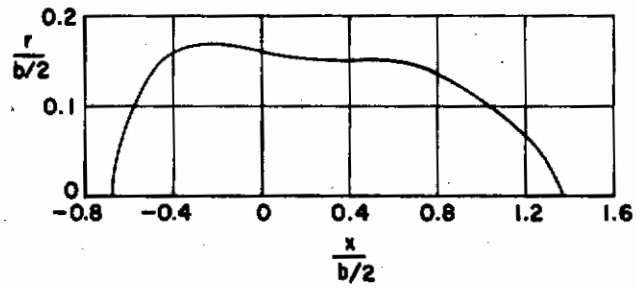

(b) EQUIVALENT FUSELAGE RADIUS DISTRIBUTION

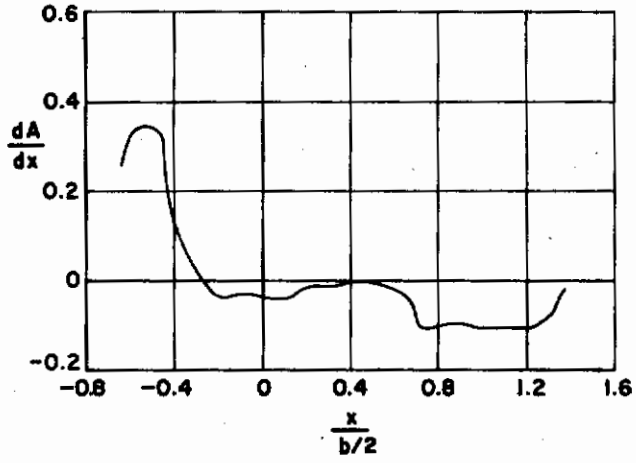

(c) EQUIVALENT FUSELAGE AREA GRADIENT DISTRIBUTION

Figure (8.6). Fuselage Geometry Summary

center (XMC) and center of gravity (XCG) are defined at the quarter-mean aerodynamic chord, which is x = 8.775. The mean thickness-chord of the wing is 9.47 percent. The following control flag inputs are required:

NROWS = 13	Thirteen spanwise rows on the right wing panel
NCASES = 5	Five fundamental cases, including the internally generated alpha case
ISYMM = 0	Configuration is symmetric
IPRINT = 0	Normal print option
JETFLG = 0	There is a jet sheet
IGTYPE = 1	Wing planform is completely arbitrary (i.e., not trapezoidal)
IHINGE = 0	No special Hinge EVD's
IDERIV = 1	Dynamic stability derivatives desired
IGRND = 0	No ground effect
IFFLD = 1	Jet-wing loading will be punched on cards for later use
NPOINT = 0	No off-body flow fields desired
NROWH = 12	Twelve horizontal tail spanwise rows
ICAMH = 0	No horizontal tail camber
NROWV = 6	Six vertical tail spanwise rows
ICAMV = 0	No vertical tail camber
NSEG = 37	Thirty-seven fuselage segments
ISECT = 1	Arbitrary fuselage cross-sections
ICAMF = 1	There is fuselage centerline camber

The computer run parameter estimates were 30 minutes of IBM/370 CPU time, 30 minutes of I/O time, 50,000 lines of print, and 4,000 punched output cards.

8.1.3 Interpretation of Computer Data

This section presents the computer generated aerodynamic data for the IBF configuration and demonstrates the application of the engineering methods presented in this volume thus leading to the complete aerodynamic analysis. Both predicted aerodynamic parameters and experimental results are presented here, but a discussion of the comparison between the predictions and experiment is presented in Section (8.1.4).

The actual STAMP computer analysis for this IBF configuration was run

on the McDonnell Douglas IBM 370/165 computer system and required 17.9 minutes of CPU time. Application of the engineering methods to these data is presented below:

Lift: IBF lift curves are plotted in Figure (8.7) for gross engine thrust coefficients C_{J_e} of 0.0, 0.5, 1.0, and 2.0. The solid curves represent corrected jet-wing plus fuselage lift. Tailplane lift is not included here.

Jet-wing lift has been corrected for viscous and thickness effects, for power-on cases, using equation (3.13), with S_B measured graphically to be 499.29 in^2:

$$C_{L_\Gamma} = \left[1.0 + 0.8\left(\frac{499.29}{592.0}\right)(0.106)\right] C_{L_\Gamma}\Big|_{EVD} = 1.072\ C_{L_\Gamma}\Big|_{EVD}$$

Both $C_{L_{\Gamma_0}}$ and $C_{L_{\Gamma_\alpha}}$ are corrected in this manner, and then $C_{L_{J_0}}$ and $C_{L_{J_\alpha}}$ are added, respectively, to yield the corrected jet-wing lift curves.

For the power-off case, sectional lift (c_ℓ) must first be corrected. For c_{ℓ_α}, using equation (3.3), it is found from figure (3.2a) that $K_1 = 1.1$. For the 64A-series airfoil $\phi_{TE} = 14.1$ degrees, and the Reynolds number is computed as

$$R_\ell = \frac{\rho U \ell}{\mu} = \frac{U\ell}{\nu} = \frac{(100\ \text{ft/sec})(0.78\ \text{ft})}{1.564 \times 10^{-4}\ \text{ft}^2/\text{sec}} = 5.0 \times 10^5$$

where ℓ = MAC = 0.78 ft and U = 100 ft/sec is a typical speed for the STOL phase of flight. Hence from figure (3.2b) $K_2 = 0.7$ and equation (3.3) yields

$$c_{\ell_\alpha} = (1.05)(1.1)(0.7)\, c_{\ell_\alpha}\Big|_{EVD} = 0.81\, c_{\ell_\alpha}\Big|_{EVD}$$

For c_{ℓ_0} equation (3.6) for plain flaps is used. With $c_f/c = 0.24$ and $t/c = 0.106$, figure (3.3a) gives $K_3 = 1.07$, figure (3.3b) gives $K_4 = 0.67$, and from figure (3.3c)

$$K_5 = \begin{Bmatrix} 0.97 \\ 0.65 \\ 0.54 \\ 0.48 \end{Bmatrix} \quad \text{for} \quad \delta_f = \begin{Bmatrix} 15° \\ 30° \\ 45° \\ 60° \end{Bmatrix}$$

Therefore, from equation (3.6)

$$c_{\ell_0} = K_3K_4K_5c_{\ell_0}\Big|_{EVD} = \begin{Bmatrix} 0.702 \\ 0.470 \\ 0.391 \\ 0.347 \end{Bmatrix} c_{\ell_0}\Big|_{EVD} \text{ for } \delta_f = \begin{Bmatrix} 15° \\ 30° \\ 45° \\ 60° \end{Bmatrix}$$

Strictly, the sectional c_{ℓ_α} and c_{ℓ_0} values calculated above should be

integrated along the span of the wing using equation (3.12), but since the correction applies over nearly the full span of the wing, these corrections have been applied directly to total wing quantities.

Fuselage cross-flow drag lift is calculated using equation (3.21). In figure (8.6b), the equivalent fuselage radius distribution is plotted, and the maximum radius is found to be 0.17 b/2. Hence the fineness ratio is

$$\frac{\ell}{2r_{max}} = \frac{70.65 \text{ in}}{2(.17)(34.41 \text{ in})} = 6.03$$

From figure (3.10a) Munk's apparent mass factor K_M is found to be 0.83. From figure (8.6c), $\frac{dA(x)}{dx}$ first reaches its maximum negative value at 85 percent of the fuselage length (i.e., x_1/ℓ), and from figure (3.10b) $x_o/\ell = 0.82$. At this fuselage station r = 0.115 b/2 = 3.96 and, therefore, $A_o = 49.2$. The integral in equation (3.21) must be evaluated using a finite summation technique. From figure (3.10), $c_{d_c} = 1.2$ and $\eta = 0.64$, and the integral is evaluated from $\frac{x_o}{b/2} = .99$ to $\frac{x_e}{b/2} = 1.37$. Compute $\int r(x)dx$ as:

$\frac{x}{b/2}$	$\frac{r}{b/2}$	$\frac{\Delta x}{b/2}$
1.053	.097	.073
1.126	.083	.073
1.192	.068	.059
1.242	.054	.043
1.279	.043	.029
1.308	.032	.029
1.337	.019	.029
1.361	.006	.020

$$\frac{1}{(b/2)^2} \sum r(x)\Delta x = .0223$$

The divisions used here are the same as those used in the fuselage analysis portion of STAMP. Evaluating equation (3.21),

$$C_{L_F} = \frac{2(0.83)(49.2)}{(57.3)(592.0)}\alpha + \frac{2(0.64)(1.2)(0.0223)(34.41)^2}{(57.3)^2(592.0)}\alpha^2$$

$$= .0024\alpha + .000021\alpha^2 \qquad (\alpha \text{ in degrees})$$

It should be noted that the fuselage cross-flow drag lift is quite small, being only 0.06 at α = 20 degrees.

The corrected lift data presented in figure (8.7) includes corrected jet-wing lift and fuselage lift.

Tailplane lift data is not presented, although the isolated analysis yielded

$$C_{L_{\alpha_{H\ Isol}}} = 0.0153$$

$$C_{m_{\alpha_{H\ Isol}}} = 0.0648$$

However, installed tailplane lift has been used to calculate mean tailplane downwash using equation (3.20), and these data are presented in figure (8.8). The gradient of tailplane downwash, $\frac{d\epsilon}{d\alpha}$, which is a quantity of primary importance in stability analyses, is simply the slope of the ϵ versus α curves in figure (8.8). It should be noted that tailplane downwash as plotted in figure (8.8) is based on lift curves which are corrected only by a simple thickness factor. For blown cases this should be acceptably accurate, but for the unblown cases where the corrected lift (i.e., C_L) is considerably different from the lift predicted directly by EVD, it may be desirable to ratio ϵ by the ratio $(C_L)/(C_{L\ EVD})$.

Drag: IBF drag polars are plotted in figure (8.9) for gross engine thrust coefficients C_{J_e} of 0.0, 0.5, 1.0, and 2.0. The solid curves are total jet-wing plus fuselage drag. Since most of the pertinent wind tunnel data was taken tail-off, empennage drag is not presented.

Induced drag calculated by the computer program has been corrected for thickness and viscous effects using equation (3.27), while profile drag (form and friction drag) has been calculated entirely using the methods of Section 3.1.2.1. Beginning with $C_{D_{o\ profile}}$, it has already been computed that $R_\ell = 5.0 \times 10^5$, and assuming an aerodynamically smooth surface, figure (3.11) gives $c_f = 0.005$. The profile drag is calculated from equation (3.24) as follows: Since $(t/c)_{max}$ for a NACA 64A-series airfoil is located at $x/c > 0.3$, $L = 1.2$. From figure (3.14) it is found that $R_{LS} = 1.07$. Flap incremental profile drag for the blown case is assumed to be zero because of the boundary layer control effect of the jet-sheet, but for the unblown case it is obtained from Figure (3.15a) to be the following:

IBF LIFT

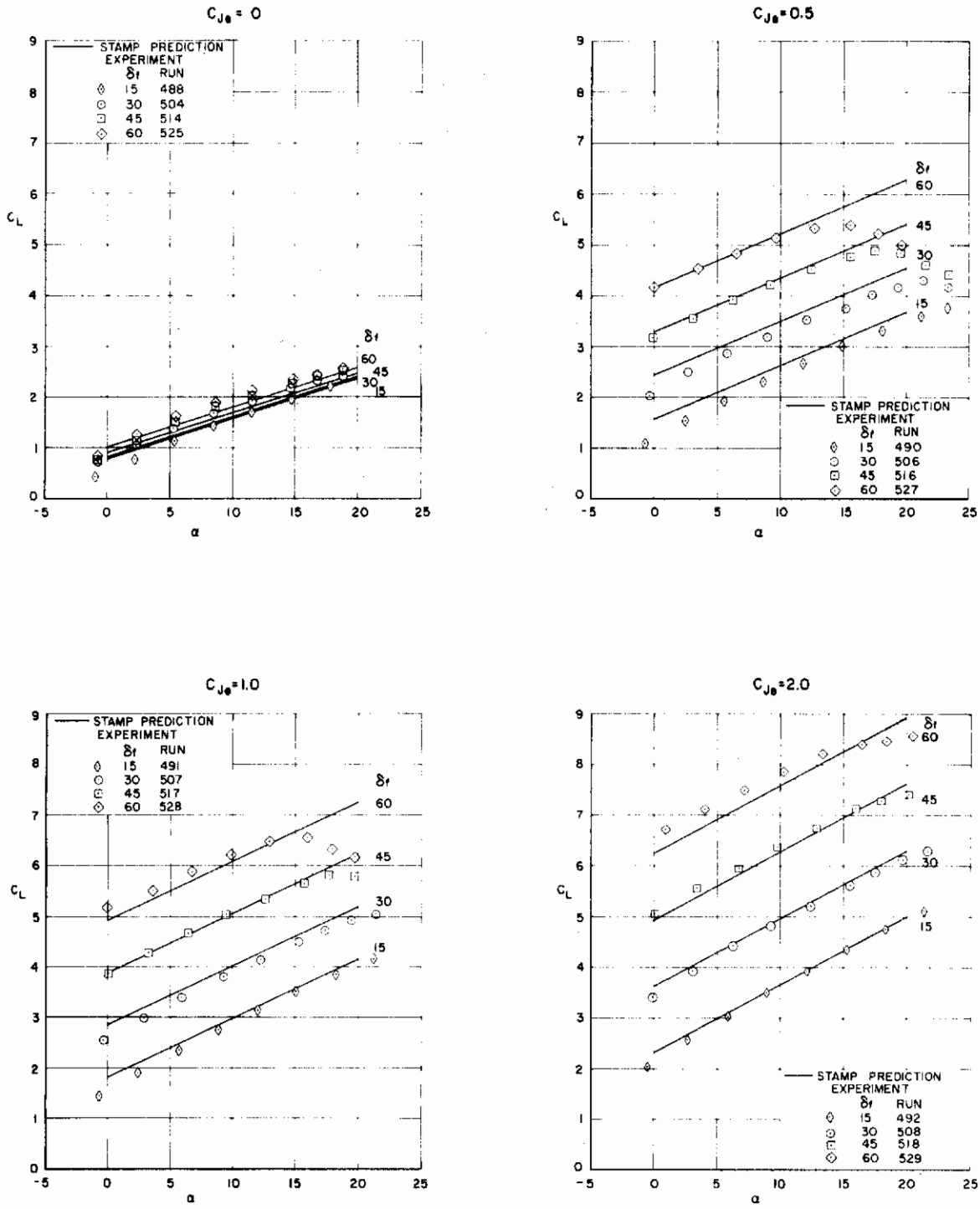

Figure (8.7). IBF Lift Comparisons (Test GDLST 612-3)

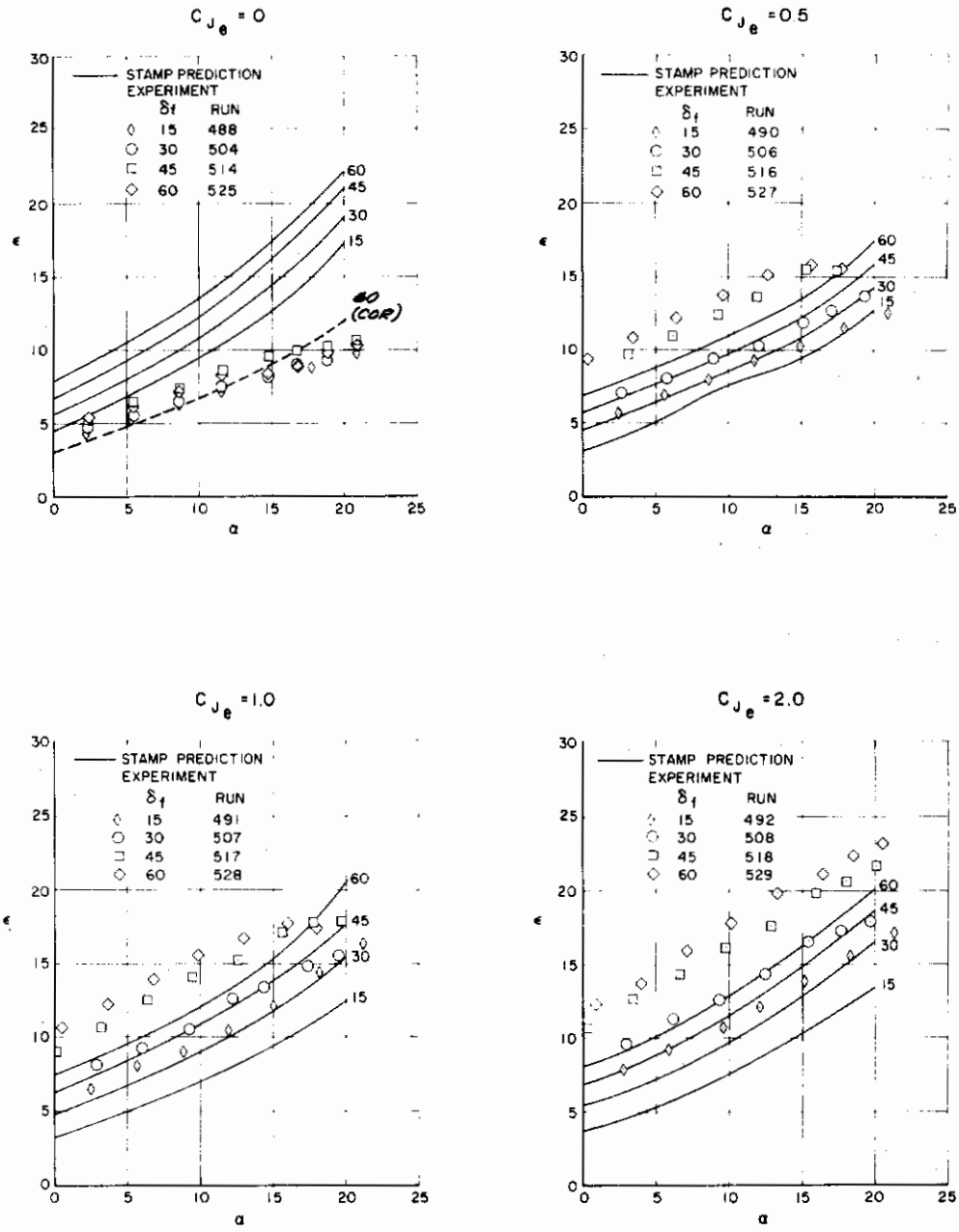

Figure (8.8). IBF Tailplane Downwash Comparisons (Test GDLST 612-3)
[NOTE: Except for the $C_{J_e} = 0$, $\delta_f = 60°$ case, ε has not been corrected by the ratio $(C_L/C_{L_{EVD}})$. This correction is most important for the unblown case.]

δ_f	$\Delta c_{d_{flap}}$
15°	0.014
30°	0.055
45°	0.112
60°	0.18

From figure (3.16),

$$K_b = K_b(1.0) - K_b(0.16) = 1.0-0.21 = 0.79$$

Hence the profile drag coefficient is calculated from equation (3.14):

$$C_{D_o}\Big|_{profile} = \left\{(0.005)\left[1 + 1.2(0.106) + 100(0.106)^4\right](1.07)\right\}\frac{998.5}{592.0}$$

$$+ 0.79\left(\Delta c_{d_{flap}}\right)$$

where $S_{wet} = 998.5$ in^2. Therefore,

Blown cases: $C_{D_{o_w}}\Big|_{profile} = 0.010647$

Unblown cases: $C_{D_{o_w}}\Big|_{profile} = \begin{pmatrix}0.021701\\0.054098\\0.099128\\0.152848\end{pmatrix}$ for $\delta_f = \begin{pmatrix}15°\\30°\\45°\\60°\end{pmatrix}$

Application of equation (3.27) to induced drag data calculated by the computer program to correct for viscous and thickness effects is a straightforward task, although somewhat tedious because of the large number of cases considered here. A sample set of these calculations is presented below. It has been found that evaluating $C_{D_{i_w}}$ at specific angles of attack is the most expedient means of applying equation (3.27). The following sample calculations are for the $C_{J_e} = 0.5$ case.

δ_f (deg)	α (deg)	C_L	$C_{L_{EVD}}$	$\frac{C_L}{C_{L_{EVD}}}$	$C_{D_{i_o}}\|_{EVD}$	$\frac{\partial C_{D_i}}{\partial \alpha}\|_{EVD}$	$\frac{\partial^2 C_{D_i}}{\partial \alpha^2}\|_{EVD}$	$C_{D_{i_w}}$
15	0	1.565	1.4579	1.073	0.11924	0.01184	0.0003629	0.1279
15	10	2.595	2.4127	1.076	"	"	"	0.2977
15	20	3.625	3.3675	1.076	"	"	"	0.5512
30	0	2.429	2.2637	1.073	0.29366	0.01849	0.0003629	0.3151
30	10	3.459	3.2185	1.075	"	"	"	0.5564
30	20	4.489	4.1733	1.076	"	"	"	0.8819
45	0	3.294	3.0695	1.073	0.54621	0.02515	0.0003629	0.5861
45	10	4.324	4.0243	1.074	"	"	"	0.8986
45	20	5.354	4.9791	1.075	"	"	"	1.2957
60	0	4.159	3.875	1.073	0.8758	0.0318	0.0003629	0.9397
60	10	5.189	4.830	1.074	"	"	"	1.3240
60	20	6.219	5.785	1.075	"	"	"	1.7929

Similar calculations have been made for each jet momentum coefficient.

Fuselage drag is calculated from equations (3.28) and (3.29). The fuselage Reynolds number based on its length $\ell = 70.65$ in $= 5.89$ ft is

$$R_\ell = \frac{(100 \text{ ft/sec})(5.89 \text{ ft})}{1.56 \times 10^{-4} \text{ft}^2/\text{sec}} = 3.75 \times 10^6$$

Figure (3.11) gives $c_f = 0.0035$. The fuselage fineness ratio has already been calculated to be 6.03, and the wetted area is calculated from

$$S_{wet} = 2\pi \int r(x)dx \approx 2\pi \sum r(x)\Delta x$$

where $r(x)$ is the equivalent fuselage radius distribution plotted in figure (8.6b). This integral is easily evaluated using a finite summation approximation to be $S_{wet} = 2038.7$ in^2. There is no base area for this fuselage, and hence equation (3.28) is evaluated as

$$C_{D_{o_F}} = 0.0035 \left[1 + \frac{60}{(6.03)^3} + 0.0025\,(6.03)\right] \frac{2038.7}{592.0} = 0.0156$$

For the lift dependent fuselage drag, the values of the terms in equation (3.29) are the same as used for the fuselage lift computations, and hence

$$C_{D_F}(\alpha) = \frac{2(0.83)(49.2)}{(57.3)^2(592.0)}\alpha^2 + \frac{2(0.64)(1.2)(0.0285)(34.41^2)}{(57.3)^3\,(592.0)}\,\alpha^3$$

$$= 4.2\text{x}10^{-5}\alpha^2 + 4.7\text{x}10^{-7}\,\alpha^3$$

Total wing-body drag is calculated using equation (3.30), where R_{WB} is found from figure (3.17) to be 1.07. For these IBF tests the engines were not operating (even though the trailing edge C_J was non-zero), so ram drag is taken to be ram drag for $C_{J_e} = 0$, which was measured to be 0.05.

The total jet-wing-fuselage drag is then calculated using equation (3.36) and is plotted in figure (8.9).

Pitching Moment: IBF pitching moment is plotted in figure (8.10) for gross engine thrust coefficients C_{J_e} of 0.0, 0.5, 1.0, and 2.0. The solid curves represent predicted jet-wing plus fuselage pitching moment. Tailplane pitching moments have been calculated but are not presented here because most of the wind tunnel data is for tail-off configurations.

For power on cases the total wing pitching moment is corrected for thickness and viscous effects directly using equation (3.48):

$$C_{m_\Gamma} = \left[1.0 + 0.8\left(\frac{499.29}{592.0}\right)(0.106)\right] C_{m_\Gamma}\Big|_{EVD} = 1.072\ C_{m_\Gamma}\Big|_{EVD}$$

Both $C_{m_{\Gamma_o}}$ and $C_{m_{\Gamma_\alpha}}$ are corrected in this manner, and then C_{m_J} and C_{m_T} are added to the corrected C_{m_Γ} values.

For power off case, the sectional pitching moment (c_m) must first be corrected. For c_{m_α}, using equation (3.40), it is found from figure (3.18) that for $\phi_{TE} = 14.1$ degrees and t/c = 0.106, K = 1.00. The ratio of corrected to EVD lift curve slope was previously calculated to be 0.925, and hence

$$c_{m_\alpha} = (1.00)(0.925)\ c_{m_\alpha}{}_{EVD} = 0.925\, c_{m_\alpha}{}_{EVD}$$

For c_{m_o}, equation (3.43) for plain flaps is used, and as discussed in Section 3.1.3.1 this correction is applied to the composite sectional c_{m_o}. K is taken from figure (3.19a) with $c_f/c = 0.24$ and the corrected c_{m_o} is tabulated below:

δf (deg)	K	C_{m_o}
15	0.78	-0.424
30	0.62	-0.496
45	0.48	-0.507
60	0.37	-0.487

IBF DRAG

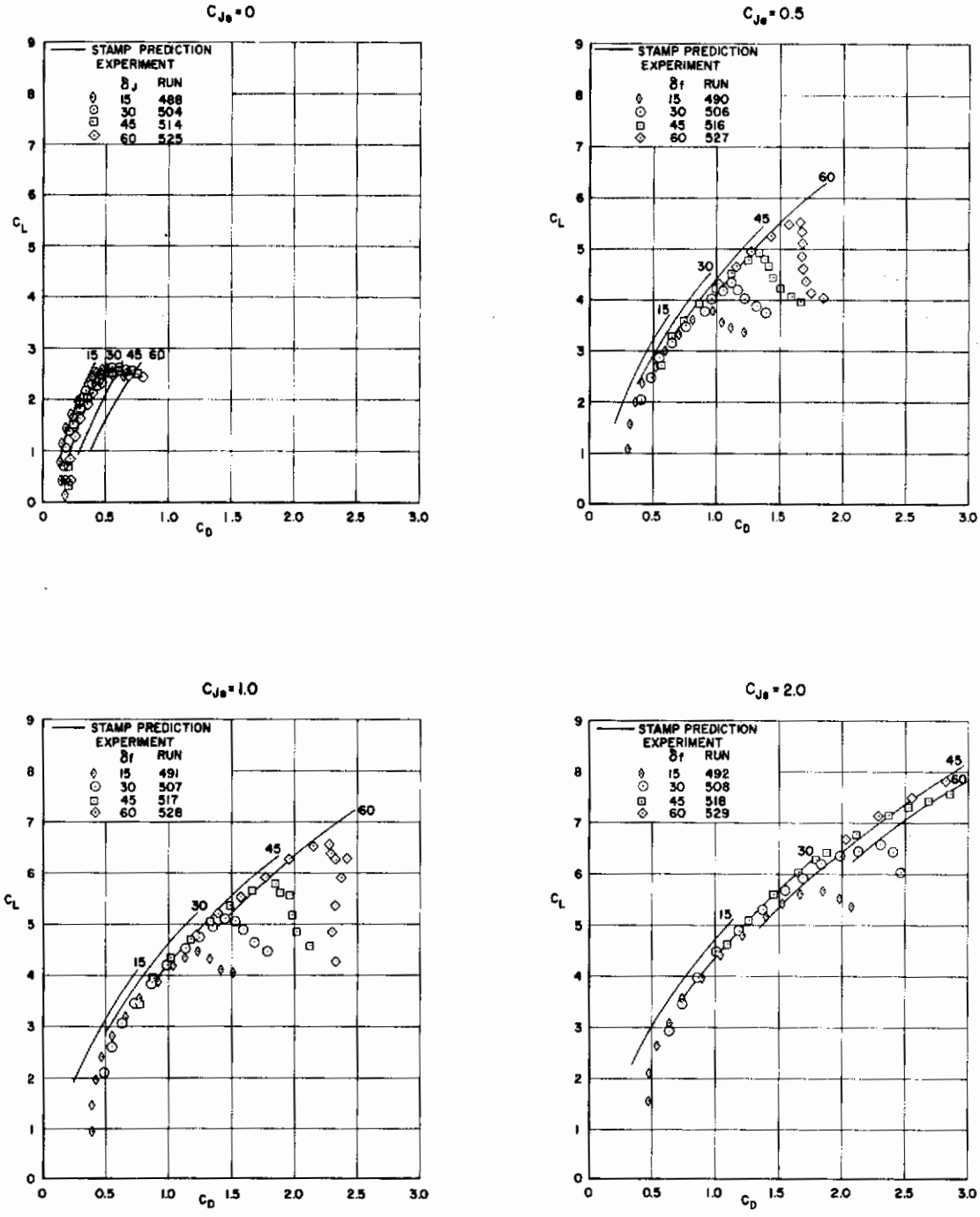

Figure (8.9). IBF Drag Comparisons (Test GDLST 612-3)

In a strict sense the sectional pitching moment, as for lift, should be integrated along the wing span, using equations (3.46) and (3.47). However, since the correction applies over nearly the full span of the wing, these corrections have been applied directly to total wing quantities. It should be noted that all pitching moment data presented here are based on a moment center at the quarter-mean aerodynamic chord point.

The fuselage contribution to pitching moment calculated by the computer program has been modified using equation (3.53b). The correction to account for non-potential flow effects on the after-body, ΔC_{m_F}, is calculated by summing the sectional c_{m_F} values calculated by the computer program from $\frac{x_o}{b/2} = 0.99$ to $\frac{x}{b/2} = 1.37$. The correction to account for viscous cross-flow is evaluated in a manner similar to that used for fuselage lift. Compute $\int r(\xi)(X_{mc}-\xi)d\xi$ as:

$\frac{x}{b/2}$	$\frac{x_{mc}-x}{b/2}$	$\frac{\Delta x}{b/2}$	$\frac{r}{b/2}$
1.053	-0.798	.073	.097
1.126	-0.871	.973	.083
1.192	-0.937	.059	.068
1.242	-0.987	.043	.054
1.279	-1.024	.029	.043
1.308	-1.053	.029	.032
1.337	-1.082	.029	.019
1.361	-1.106	.020	.006

$$\frac{1}{(b/2)^3}\sum r(x)(x_{mc}-x)\Delta x = -.0200$$

Hence evaluating equation (3.53b),

$$C_{m_F}(\alpha)\Big|_{\text{corrected}} = C_{m_F}(\alpha) - \Delta C_{m_F}(\alpha) + \frac{2(0.64)(1.2)(-.0200)(34.41^3)}{(57.3)^2(592.0)(9.33)}\ \alpha^2$$

$$= C_{m_F}(\alpha) - \Delta C_{m_F}(\alpha) - 0.000069\ \alpha^2$$

Values of $C_{m_F}(\alpha)$ are taken directly from the computer program output.

An additional contribution to pitching moment comes from the ram drag. Referring to the sketch below, the ram drag pitching moment, C_{m_R},

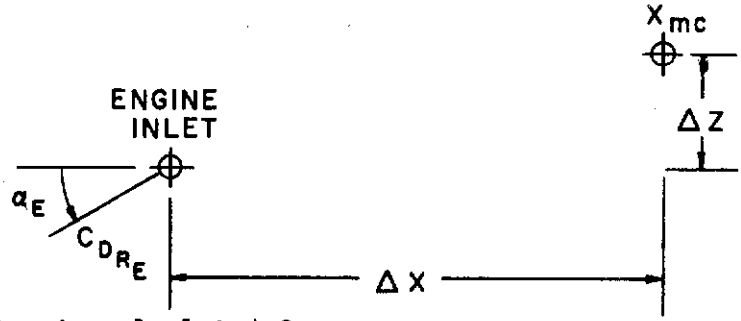

for each engine is calculated from

$$C_{m_R} = \left(\frac{\Delta Z}{C} \cos \alpha_E - \frac{\Delta X}{C} \sin \alpha_E\right) C_{D_{R_E}}$$

where $C_{D_{R_E}}$ is the ram drag for each engine. From figure (8.1), the engine locations have been measured to be

	Inboard	Outboard
$\frac{\Delta Z}{C}$	-0.483	-0.516
$\frac{\Delta X}{C}$	0.848	0.498

Since there are four engines on this model, the final expression obtained for C_{m_R} is

$$C_{m_R} = 2C_{D_{R_E}} \left(-0.999 \cos \alpha_E + 1.346 \sin \alpha_E\right)$$

The predicted pitching moment data presented in figure (8.10) include corrected jet-wing pitching moment, corrected fuselage pitching moment, and the ram drag pitching moment (with $C_{D_R} = 0.05$ in all cases).

Dynamic Stability Derivatives: Although there is no experimental data for comparison, a complete set of dynamic stability derivatives have been generated for this IBF configuration. These data are presented below, including application of the engineering methods of Section 5.0 where appropriate.

C_{L_u}: The C_{L_u} derivative is calculated from equations (5.6) and (5.7) for the circulation component and from equation (5.5) for the reaction component. The $\frac{\Delta u}{U}$ term is evaluated by choosing a C_{J_o}, letting

$$C_{J_1} = C_{J_o} - 0.1$$

$$C_{J_2} = C_{J_o} + 0.1$$

IBF PITCHING MOMENT

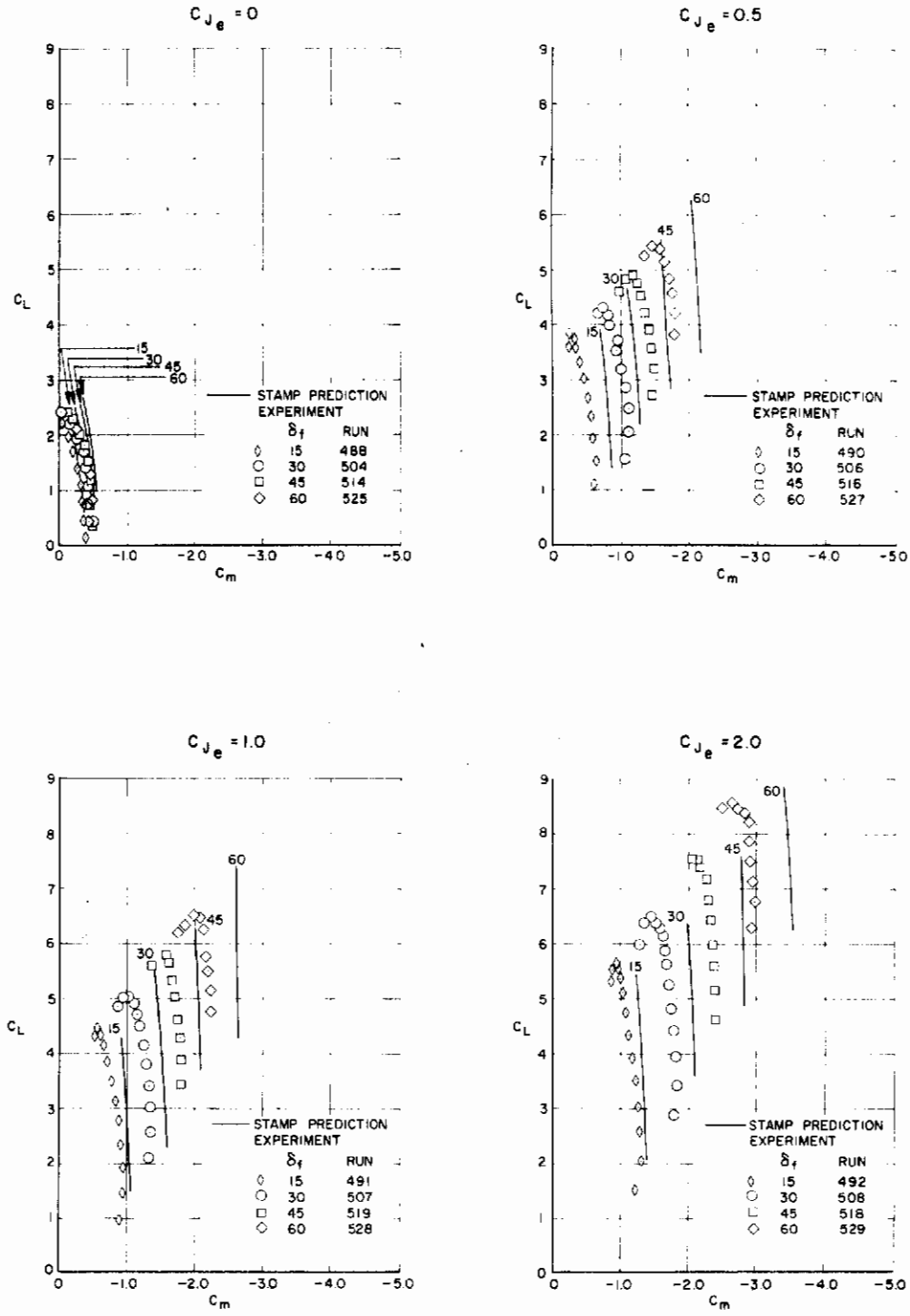

Figure (8.10). IBF Pitching Moment Comparisons (Test GDLST 612-3) (Tail Off)

and then calculating by equation (5.7)

$$\frac{\Delta u}{U} = \frac{\sqrt{C_{J_o}}}{\sqrt{C_{J_o} + 0.1} - \sqrt{C_{J_o} - 0.1}}$$

This quantity is plotted in figure (8.11a). The ΔC_{L_Γ} term is evaluated by plotting $C_{L_{\Gamma_o}}$ and $C_{L_{\Gamma_\alpha}}$ versus C_J, as in figure (8.11b), and then graphically determining

$$C_{L_1} = C_L(C_{J_o} - 0.1)$$

$$C_{L_2} = C_L(C_{J_o} + 0.1)$$

Small differences in C_L must be resolved from figure (8.11b), so care must be taken in constructing such a plot. The values for $C_{L_{\Gamma_u}}$ calculated for the IBF configuration are tabulated below:

Table (8.4). IBF C_{L_u} Stability Derivatives

C_{J_e}	$\frac{\partial C_{L_{\Gamma_o}}}{\partial u}$				$\frac{\partial C_{L_{\Gamma_\alpha}}}{\partial u}$
	$\delta_f = 15°$	$\delta_f = 30°$	$\delta_f = 45°$	$\delta_f = 60°$	
0.5	0.020	0.050	0.062	0.064	0.0007
1.0	0.004	0.005	0.005	0.005	0.0001
2.0	0.002	0.003	0.003	0.003	0.0001

The jet reaction portion of the term, $C_{L_{J_u}}$, is simply calculated from equation (5.5) and is not tabulated here.

C_{D_u}: The speed damping derivative is calculated from equations (5.10) and (5.11) using a procedure identical to that described above for C_{L_u}. C_D versus C_J is plotted in figure (8.12) for $\alpha = 10$ degrees, and the calculated values of C_{D_u} are tabulated below:

Table (8.5.) IBF C_{D_u} Stability Derivatives

C_{J_e}	$\frac{\partial C_D}{\partial u}$			
	$\delta_f = 15°$	$\delta_f = 30°$	$\delta_f = 45°$	$\delta_f = 60°$
0.5	0.016	0.024	0.038	0.058
1.0	0.006	0.012	0.016	0.020
2.0	0.002	0.004	0.007	0.009

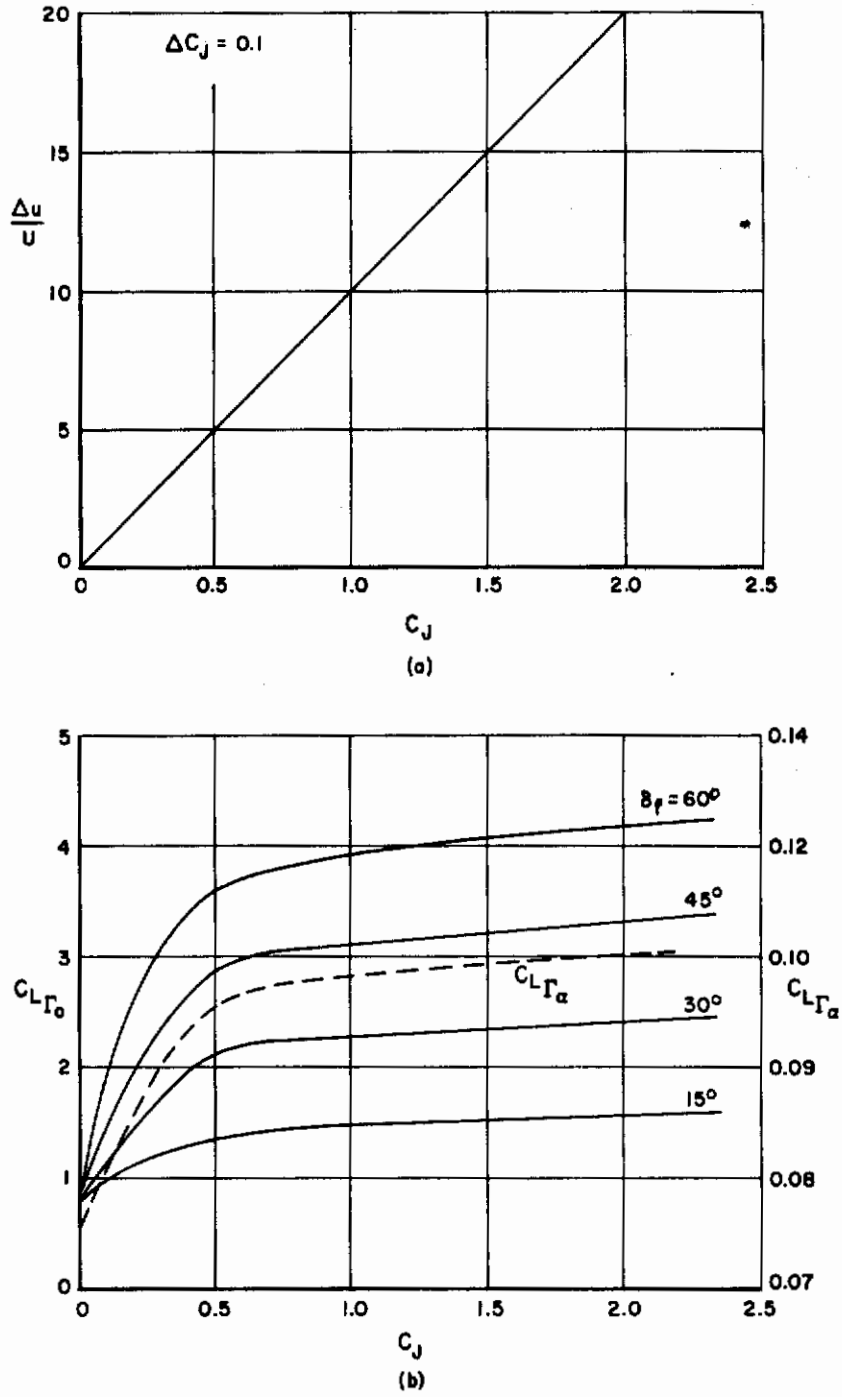

Figure (8.11). Graphical Procedure for Calculating the C_{L_u} Stability Derivative

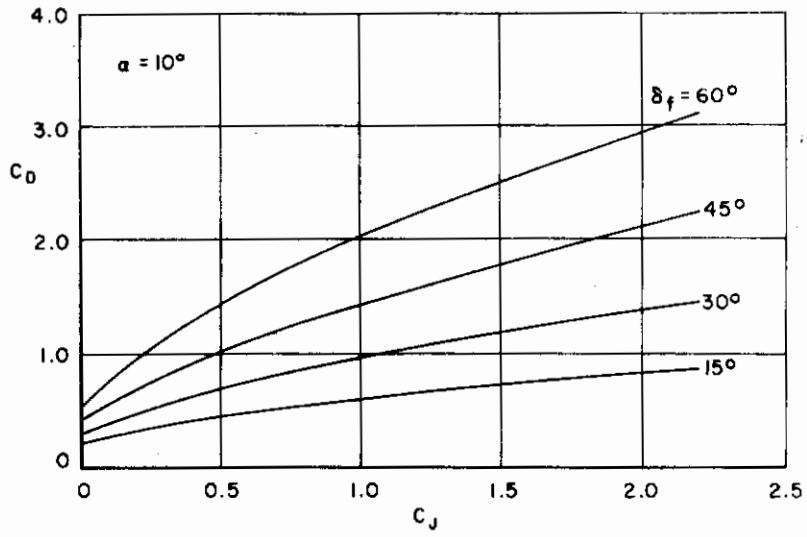

Figure (8.12). Graphical Procedure for Calculating C_{D_u} Stability Derivative

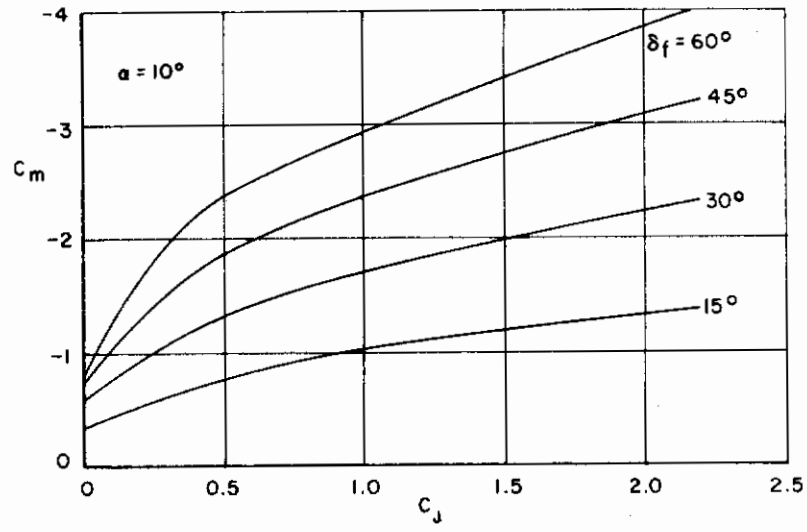

Figure (8.13). Graphical Procedure for Calculating C_{m_u} Stability Derivative

These data include both reaction and circulation components of C_{D_u}, and hence equation (5.10) is not needed.

C_{m_u}: The aerodynamic portion of C_{m_u}, tail off, was calculated in a manner similar to C_{L_u} and C_{D_u}. C_m versus C_J for the various flap angles at α = 10 degrees is plotted in figure (8.13), and the calculated values of C_{m_u} are tabulated below. Note that because of the non-linearity of the predicted C_D and C_m curves, it is easier to evaluate the C_{D_u} and C_{m_u} derivatives at some specific angle of attack whereas C_{L_u} can be treated using $\frac{\partial C_{L_o}}{\partial u}$ and $\frac{\partial C_{L_\alpha}}{\partial u}$.

Table (8.6). IBF C_{m_u} Stability Derivatives

C_{J_e}	$\frac{\partial C_m}{\partial u}$			
	δ_f = 15°	δ_f = 30°	δ_f = 45°	δ_f = 60°
0.5	-0.026	-0.040	-0.052	-0.060
1.0	-0.008	-0.012	-0.017	-0.021
2.0	-0.0025	-0.0055	-0.0055	-0.0095

q Derivatives: The pitching rate derivatives are calculated directly by the the computer program for the jet-wing, empennage, and fuselage. Within the context of linearized theory, C_{L_q} and C_{m_q} are independent of α and q. They are tabulated below:

Table (8.7). IBF Pitching Rate Stability Derivatives

	C_{L_q}	C_{m_q}
Jet-Wing		
C_{J_e} = 0	5.528	-2.473
C_{J_e} = 0.5	6.311	-2.835
C_{J_e} = 1.0	6.649	-2.984
C_{J_e} = 2.0	7.052	-3.160
Empennage	7.947	-33.644
Fuselage	-	-5.105

The fuselage contribution to C_{L_q} could, conceivably, be calculated using a cross-flow drag technique as was used for the steady-state fuselage lift. However, it should be negligibly small and has not been computed here.

$\dot{\alpha}$ Derivatives: Methods presented in this volume to calculate the $\dot{\alpha}$ stability derivatives consider only the lag in downwash at the horizontal tail. $C_{L_{\dot{\alpha}}}$ and $C_{m_{\dot{\alpha}}}$ are calculated from equations (5.24) and (5.26), respectively. In terms of model scale, ℓ_H = 43.77 inches, $\bar{c}$ = 9.33 inches, $C_{L_{\alpha_H}}$ = 0.0155 (isolated), and $C_{m_{\alpha_H}}$ = 0.0657 (isolated). With $\frac{d\varepsilon}{d\alpha}$ determined graphically from the STAMP predictions of figure (8.8), the following table of $\dot{\alpha}$ stability derivatives can be computed:

Table (8.8). IBF $\dot{\alpha}$ Stability Derivatives

C_{J_e}	δ_f (deg)	$\frac{d\varepsilon}{d\alpha}$	$C_{L_{\dot{\alpha}}}$	$C_{m_{\dot{\alpha}}}$
0	15	0.49	4.083	-16.408
	30	0.51	4.250	-18.014
	45	0.55	4.583	-19.427
	60	0.56	4.666	-19.780
0.5	15	0.46	3.833	-16.248
	30	0.40	3.333	-14.124
	45	0.40	3.333	-14.129
	60	0.40	3.333	-14.129
1.0	15	0.40	3.333	-14.129
	30	0.42	3.500	-14.835
	45	0.46	3.833	-16.248
	60	0.46	3.833	-16.248
2.0	15	0.39	3.250	-13.776
	30	0.43	3.583	-15.188
	45	0.47	3.917	-16.601
	60	0.48	4.000	-16.955

p Derivatives: The rolling rate derivatives are calculated using output directly from STAMP along with several empirical terms presented in Section 5.2.1. The roll damping derivative, C_{l_p}, is calculated from equations (5.31a) and (5.32), with dihedral Γ = -3.5° and z = 1.04 inches (distance of root chord above moment center, model scale). Hence equation (5.32) is evaluated as

$$K = \left[1 + 2\left(\frac{1.04}{34.41}\right)\sin(-3.5^0) + 3\left(\frac{1.04}{34.41}\right)^2 \sin^2(-3.5^0)\right] = 0.996$$

Applying equation (5.31a) to the computer program calculated C_{l_p} for the jet-wing, the following table can be formed:

Table (8.9). IBF C_{l_p} Stability Derivatives

	C_{l_p}
Jet-Wing	
C_{J_e} = 0	-0.492
C_{J_e} = 0.5	-0.522
C_{J_e} = 1.0	-0.535
C_{J_e} = 2.0	-0.551
Horizontal Tail	-0.0276
Vertical Tail	-0.0103
Fuselage	-

Although the yawing moment due to rate of roll, C_{n_p}, is not expressed in the form of a stability derivative [equation (5.34)], the second order term, $C_{n_{p^2}}$, is identically zero for symmetric configurations. Hence, there is only an alpha-variation to consider. For the various IBF configurations run, the $C_{n_{p_o}}$ and $C_{n_{p_\alpha}}$ terms are presented in table (8.10) below, as well as the empennage contribution to C_{n_p}.

Table (8.10). IBF C_{n_p} and C_{Y_p} Stability Derivatives

Wing	C_{J_e}	δ_f (deg)	$C_{n_{p_o}}$	$C_{n_{p_\alpha}}$	$C_{Y_{p_o}}$	$C_{Y_{p_\alpha}}$
	0	15	-0.111	-0.130	-0.285	0.230
		30	-0.172	-0.060	-0.181	0.115
		45	-0.234	-0.026	-0.077	0.057
		60	-0.296	-0.009	0.027	0.029
	0.5	15	-0.130	-0.138	-0.261	0.244
		30	-0.206	-0.065	-0.131	0.122
		45	-0.281	-0.028	-0.002	0.061
		60	-0.357	-0.009	0.127	0.030
	1.0	15	-0.142	-0.143	-0.246	0.251
		30	-0.225	-0.066	-0.104	0.125
		45	-0.308	-0.029	0.038	0.063
		60	-0.391	-0.010	0.180	0.031
	2.0	15	-0.158	-0.148	-0.226	0.260
		30	-0.250	-0.069	-0.068	0.130
		45	-0.342	-0.030	0.089	0.065
		60	-0.434	-0.010	0.247	0.033
Vertical Tail			0.160	-	-0.046	-

It is apparent from these data that neglecting the angle of attack variation is not permissible since the $C_{n_{p_\alpha}}$ term is often the same order as the $C_{n_{p_o}}$ term. Hence, for this configuration, use of the linearized equations of motion should be questioned. Note also that the predicted sign of $C_{n(p)}$ is indicative of an undamped Dutch roll mode.

Also tabulated above are the STAMP predictions for the side force due to rate of roll. To these values must be added an increment for dihedral, calculated by equation (5.29):

$$\left(\Delta C_{Y_p}\right)_\Gamma = \left[3 \sin(-3.5^0)\left(1 + 2\left(\frac{1.04}{34.41}\right)\sin(-3.5^0)\right)\right]\left(C_{l_p}\right)\Big|_{\substack{\Gamma = 0 \\ C_L = 0}}$$

$$= -0.182\left(C_{l_p}\right)_{\substack{\Gamma = 0 \\ C_L = 0}} \begin{Bmatrix} 0.090 \\ 0.095 \\ 0.097 \\ 0.100 \end{Bmatrix} \text{for } C_{J_e} = \begin{Bmatrix} 0 \\ 0.5 \\ 1.0 \\ 2.0 \end{Bmatrix}$$

Again it should be noted that the $C_{Y_{p_\alpha}}$ term is of a similar order to the $C_{Y_{p_o}}$ term and hence must be considered in a dynamic stability analysis.

r Derivatives: The yawing rate derivatives are calculated by the methods presented in Section 5.2.2 using derivatives calculated directly by the STAMP computer program in conjunction with several empirical terms. The side force due to rate of yaw for the jet-wing is calculated directly by STAMP in the form of equation (5.36), but since the configuration considered here is symmetric, all r^2-dependent derivatives are identically zero. However, the r-dependent portion of $C_Y(r)$ is a function of angle of attack, and the data generated by the computer program indicate that these terms cannot be neglected. The vertical tail contribution to C_{Y_r} is several orders of magnitude greater than the wing contribution, however, as indicated in table (8.11).

The rolling moment due to yawing is calculated from equation (5.38a). The first two terms which are calculated by the computer program, are tabulated in table (8.11), and it is apparent that the $C_{l_{r_\alpha}}$ term is negligible. The remaining terms in equation (5.38a) are calculated below:

$$C_l(r)\Big|_{wing} = \left[C_{l_{r_o}} + C_{l_{r_\alpha}}{}^{\alpha}\right]\hat{r} + \frac{(1.04)}{(34.41)} C_Y(\hat{r})\hat{r} + \left(\frac{1}{12}\right)\frac{\pi(8.0)(\sin 25^\circ)}{8.0 + 4\cos 25^\circ}\hat{r}$$

$$= \left[C_{l_{r_o}} + C_{l_{r_\alpha}}\right]\hat{r} + 0.030\, C_Y(\hat{r})\hat{r} + 0.076\,\hat{r}$$

where $C_{l_{r_o}}$, $C_{l_{r_\alpha}}$, and $C_Y(\hat{r})$ can all be determined from table (8.11).

The yaw damping derivative for the jet-wing is calculated using equation (5.41). The quantities within the square brackets are presented in table (8.11). The additional term, which accounts for asymmetries in C_{D_o}, is found from figure (5.1) to be

$$-0.4\, C_{D_o}\,\hat{r}$$

where C_{D_o} is the wing profile drag coefficient, tabulated earlier in this section. This additional term is, therefore:

$$-0.00426\,\hat{r} \qquad \text{Blown cases}$$

$$\begin{Bmatrix} -0.00868\,\hat{r} \\ -0.02164\,\hat{r} \\ -0.03965\,\hat{r} \\ -0.06114\,\hat{r} \end{Bmatrix} \quad \text{for } \delta_f = \begin{Bmatrix} 15^\circ \\ 30^\circ \\ 45^\circ \\ 60^\circ \end{Bmatrix} \qquad \text{Unblown cases}$$

Control Derivatives: Elevator and rudder control derivatives have been

Table (8.11). IBF Yawing Rate Stability Derivatives

	C_{J_e}	δ_f (deg)	$C_{Y_{r_o}}$	$C_{Y_{r_\alpha}}$	$C_{Y_{r_{\alpha^2}}}$	$C_{n_{r_o}}$	$C_{n_{r_\alpha}}$	$C_{n_{r_{\alpha^2}}}$	$C_{l_{r_o}}$	$C_{l_{r_\alpha}}$
Wing	0	15	-0.08734	0.07052	-0.00401	0.00443	-0.03890	0.00226	0.14252	0.00862
		30	-0.04841	0.02958	-0.00200	-0.02523	-0.01597	0.00106	0.22282	0.00862
		45	-0.02137	0.01138	-0.00100	-0.05658	-0.00671	0.00045	0.30312	0.00862
		60	-0.00623	0.00295	-0.00050	-0.08962	-0.00326	0.00015	0.38342	0.00862
	0.5	15	-0.07527	0.06911	-0.00425	-0.00109	-0.03822	0.00241	0.16002	0.00914
		30	-0.03370	0.02670	-0.00213	-0.03353	-0.01463	0.00113	0.25461	0.00914
		45	-0.00936	0.00830	-0.00106	-0.06652	-0.00554	0.00048	0.34920	0.00914
		60	-0.00226	-0.00006	-0.00053	-0.10001	-0.00242	0.00016	0.44378	0.00914
	1.0	15	-0.06879	0.06810	-0.00438	-0.00386	-0.03768	0.00249	0.16942	0.00938
		30	-0.02700	0.02509	-0.00210	-0.03663	-0.01383	0.00116	0.26998	0.00938
		45	-0.00529	0.00666	-0.00110	-0.06891	-0.00484	0.00050	0.37055	0.00938
		60	-0.00366	-0.00164	-0.00055	-0.10071	-0.00188	0.00017	0.47111	0.00938
	2.0	15	-0.06112	0.06679	-0.00454	-0.00701	-0.03697	0.00250	0.18060	0.00966
		30	-0.01973	0.02306	-0.00228	-0.03956	-0.01278	0.00121	0.28803	0.00966
		45	-0.00216	0.00459	-0.00114	-0.07006	-0.00391	0.00052	0.39547	0.00966
		60	-0.00841	-0.00362	-0.00057	-0.09853	-0.00114	0.00018	0.50290	0.00966
Vertical Tail			0.422	-	-	-1.398	-	-	0.0738	-
Fuselage			-	-	-	-0.355	-	-	-	-

calculated for the empennage configuration employed in these tests by using the STAMP computer program for the empennage alone. This was done so that a more detailed tail loading could be obtained than was obtained in the complete airplane computer runs. In the complete runs the tail was defined by a minimal number of elements to minimize computation time.

The horizontal tail was equipped with a full span plain elevator with a chord $c_e = 0.35\ c_H$. Treating the elevator as a plain flap deflected one degree, as discussed in Section 6.1, the following derivatives have been calculated:

$$C_{L_{\delta_e}} = 0.0112$$
$$C_{m_{\delta_e}} = 0.0486$$
$$C_{D_{\delta_e}} = 0.0003$$

These derivatives are based on wing reference area and chord, airplane moment center, and are per degree of elevator deflection. The horizontal tail incidence derivatives, which express changes in aerodynamic parameters with a change in tailplane incidence, are identical to the tailplane α-derivatives:

$$C_{L_{i_H}} = C_{L_{\alpha_H}} = 0.0155$$
$$C_{m_{i_H}} = C_{m_{\alpha_H}} = -0.0658$$

The vertical tail was equipped with a full span rudder of chord $c_r = 0.25c_V$. Treating the rudder as discussed in Section 6.2, the following control derivatives have been computed:

$$C_{Y_{\delta_r}} = 0.0038$$
$$C_{n_{\delta_r}} = -0.0140$$
$$C_{D_{\delta_r}} = 0.0003$$
$$C_{l_{\delta_r}} = \begin{cases} 0.000665 & \text{(Vertical Tail)} \\ -0.000478 & \text{(Horizontal Tail)} \end{cases}$$

It will be noted that the rudder deflection induces an asymmetrical loading on the horizontal tail, and hence there are two contributions to $C_{l_{\delta_r}}$. The vertical tail β-derivatives are

$$C_{Y_\beta} = 0.0068$$

$$C_{n_\beta} = -0.0228$$

Ground Effect: A simplified version of the IBF configuration has been used to predict the influence of ground proximity on the static aerodynamic characteristics. Only the jet-wing portion of the configuration was used in the STAMP computer program analysis for ground effect since only incremental lift, drag, and pitching moment data were desired. Input to the computer program for the jet-wing differs from the free-air case only in that the control flag IGRND=1 and ground heights must be input. Two mean ground heights were used, h = 13.76 and 20.65 inches, which correspond to h = 0.4 b/2 and h = 0.6 b/2, respectively. The first ground height is representative of "wheels on the ground" case and is the most severe condition.

Predicted incremental aerodynamic characteristics due to ground proximity have been calculated by taking uncorrected STAMP data for free air and ground effect runs to calculate ΔC_L, ΔC_m, and ΔC_D, and dividing these increments by corrected free air predictions to obtain percentage ground effect influence. Inherent in this procedure is the assumption that ground proximity influences only the potential flow aspects of the problem and neglects any viscous flow changes due to ground effect. Predictions of ground effect for lift, drag, and pitching moment are presented in figures (8.14), (8.15), and (8.16), respectively.

8.1.4 Comparison with Experiment (IBF)

Comparisons between the predictions of the methods developed in this report and wind tunnel test data for the IBF configuration have been presented in figures (8.7), (8.8), (8.9), and (8.10) for lift, tailplane downwash, drag, and pitching moment, respectively. In addition, comparisons have also been presented for the IBF in ground effect in figures (8.14), (8.15), and (8.16). In this section these comparisons are discussed to assess the validity of the present prediction methods and to ascertain where further work is required. It should be reiterated here that, as discussed in Section 8.0, certain discrepancies must be expected due to assumptions made concerning mean flap extension and mean jet turning efficiencies. Fortunately, for the IBF neither of these effects is expected to be important.

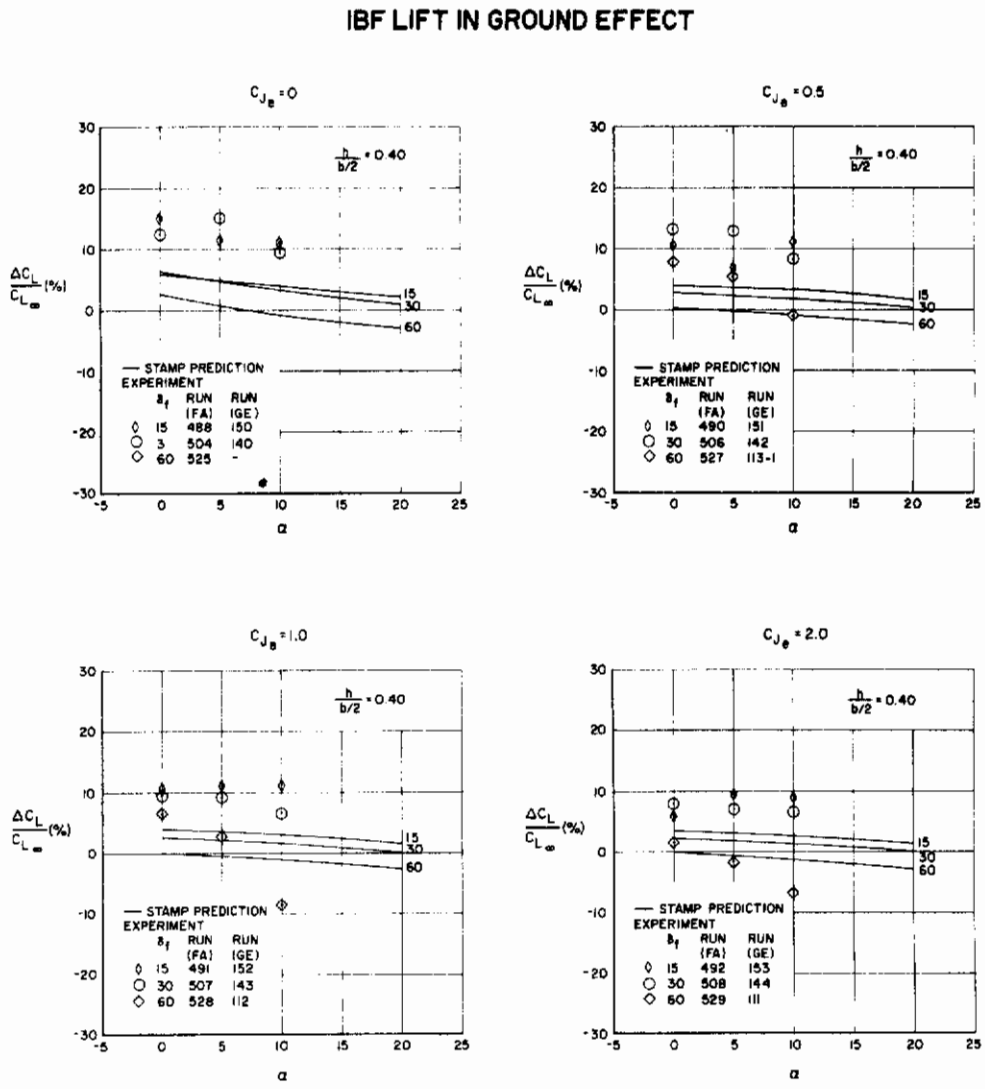

Figure (8.14). IBF Ground Effect Lift Comparisons (Test GDLST 621 and GDLST 612-3)

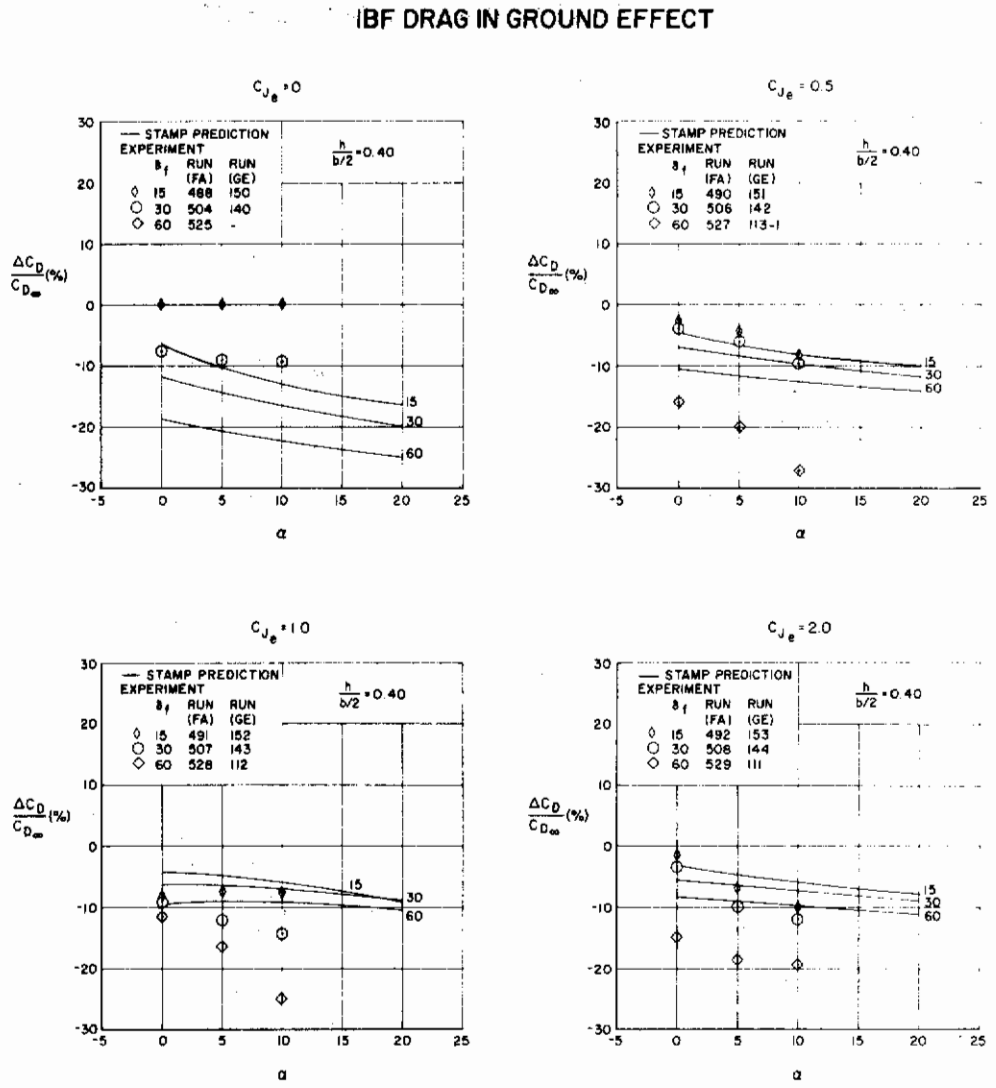

Figure (8.15). IBF Ground Effect Drag Comparisons (Tests GDLST 621 and GDLST 612-3)

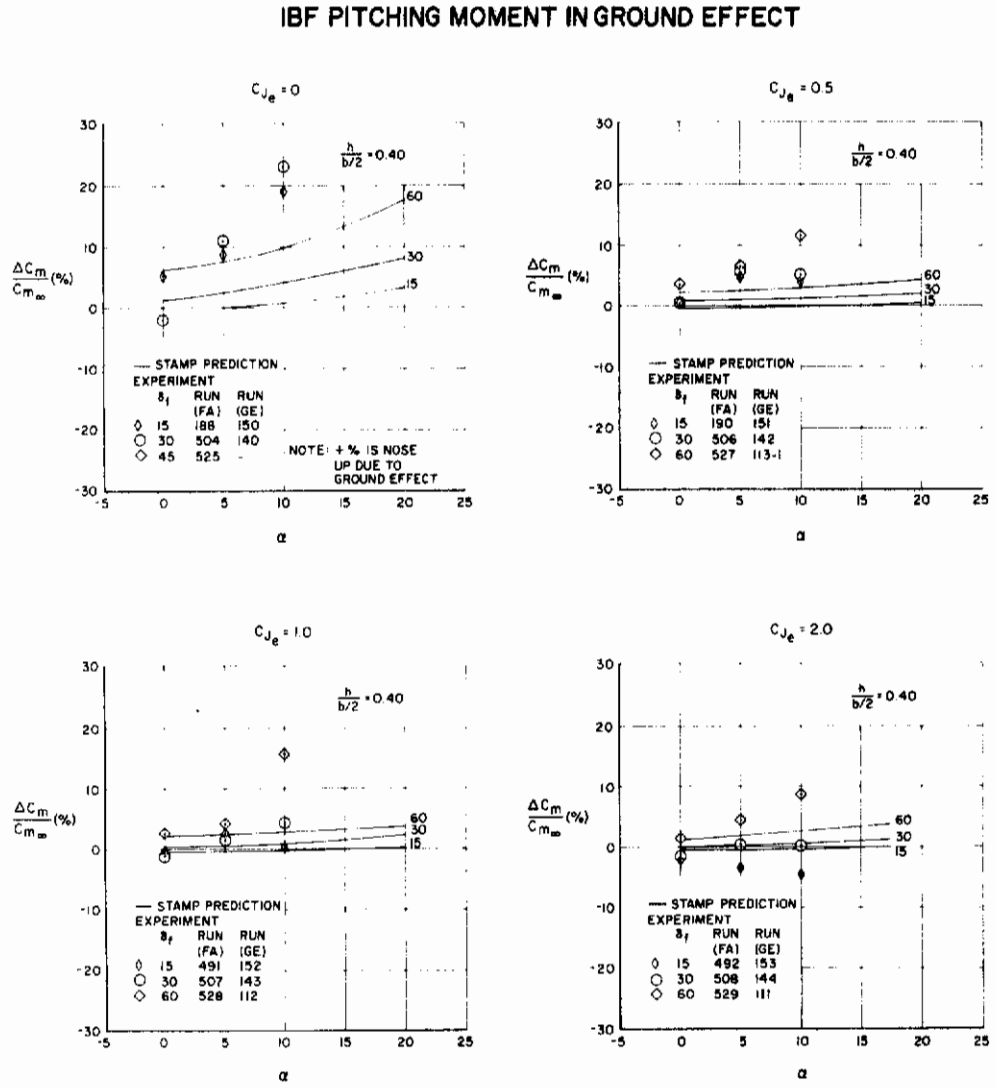

Figure (8.16). IBF Ground Effect Pitching Moment Comparisons (Tests GDLST 621 and GDLST 612-3)

Prior to discussing the comparisons of data, a few comments concerning the Convair STOL Tactical Aircraft Investigation Wind Tunnel program will be made. The 5.69-foot span IBF model was tested in the 8- by 12-foot test section of the General Dynamics Low Speed Wind Tunnel. The model was mounted on a single 5-inch diameter sting which entered the model in the upswept fuselage afterbody. Standard jet-flapped wing wind tunnel wall corrections, discussed in references (21, 22, and 23), were applied by Convair. It is suggested by Anscombe and Williams (reference 22) that the model/tunnel size relationship should be such that tunnel interference correction, $\Delta\alpha$, be less than two degrees. This correction, based on a simple lifting line representation of the wing, is expressed as

$$\Delta\alpha = \frac{57.3}{1 + \frac{2C_J}{\pi AR}} \delta \frac{S}{C} C_L$$

For a tunnel height-to-width of 2:3, reference 21 gives $\delta \approx 0.11$. The wing reference area $S = 4.11$ ft^2, the tunnel cross-sectional area is $C = 96$ ft^2, and $AR = 8.0$. Hence

$$\Delta\alpha = \begin{Bmatrix} 0.27C_L \\ 0.26C_L \\ 0.25C_L \\ 0.23C_L \end{Bmatrix} \quad \text{for} \quad C_{J_e} = \begin{Bmatrix} 0 \\ 0.5 \\ 1.0 \\ 2.0 \end{Bmatrix}$$

Therefore allowable maximum values of C_L to meet the $\Delta\alpha \leq 2$ degrees criterion are

$$C_L = \begin{Bmatrix} 7.42 \\ 7.70 \\ 8.00 \\ 8.70 \end{Bmatrix} \quad \text{for} \quad C_{J_e} = \begin{Bmatrix} 0 \\ 0.5 \\ 1.0 \\ 2.0 \end{Bmatrix}$$

Most of the test data falls within this somewhat arbitrary limit.

Wake blockage and solid blockage, which combine to increase the effective tunnel dynamic pressure, are quite difficult to estimate. Reference 23 suggests that q be corrected as follows:

$$q_{blocked} = q(1 + 2\varepsilon)$$

where $\varepsilon \approx \frac{1}{4} \frac{\text{(Model frontal area)}}{\text{(Test section area)}}$.

However it is difficult to estimate the model frontal area since the deflected jet sheet also acts to block partially the tunnel freestream. Reference 22 contends that blockage effects at very high lift coefficients are not significant. Reference 29, on the other hand, states that for jet-flapped wings wake blockage effects are very important but that little is known concerning their estimation. It is uncertain whether Convair actually applied wake blockage corrections, but based on their list of references it is likely that they did not.

Although it appears that the tunnel wall constraints are at an acceptable level, there are several other matters which deserve consideration. The large sting support system used in these tests can interfere significantly with the model flow field, particularly in the vicinity of the fuselage afterbody. Since no tares were taken, the magnitude of these interferences is unknown. An exploratory analytical investigation based on slender body methods shows that a 30 percent underprediction in nose-up pitching moment due to the fuselage can be made if the presence of the sting is ignored. The remainder of the model support system and air supply feed system, located several feet downstream of the model, may also interfere with the model flow field and may also add to tunnel blockage corrections. Again aerodynamic tares would have been valuable to assess these interferences.

In conclusion, with the exception of unresolved aerodynamic interferences, the test conditions provided an adequate means of measuring the necessary aerodynamic parameters. For the purposes of the following data comparisons, it must be assumed that special problems, such as air supply bridging and wind tunnel flow angularity, had been properly handled by the wind tunnel test contractor.

The following paragraphs discuss comparisons made between the experimental data and the predictions of the methods developed in this work.

Lift: Figure (8.7) indicates that generally excellent agreement with experiment is obtained for the predicted lift curves, both in slope (C_{L_α}) and in level (C_{L_o}). The good agreement obtained for the unblown case ($C_{J_e} = 0$) confirms the validity of the empirical curves presented in figure (3.2) for plain flaps. These empirical curves seem to account properly for severe

separations characteristic of highly deflected plain flaps. It should be mentioned that the predicted lift level taken directly from the EVD portion of STAMP for the unblown case at δ_f = 60 degrees, for example, was C_{L_o} = 2.90. Since the experimental C_{L_o} = 1.00, it is obvious that, for the unblown case, the empirical corrections are vitally important.

Agreement for the blown cases is also quite good, and the small variations shown can be partially attributed to variations in the flap turning efficiency τ with flap deflection [figure (8.5)]. A strange experimental result, however, is the severe break in the $\delta_f = 60°$ lift curves for each of the C_{J_e} plots. This may be due to impingement of the highly deflected jet sheet on the tunnel floor, although there is no experimental verification of such an occurrence.

Tailplane Downwash: The comparisons presented in figure (8.8) indicate generally good agreement for $\frac{d\varepsilon}{d\alpha}$, the parameter of primary importance for stability analyses, except for the unblown case. The agreement for ε_o is generally within three degrees, which can affect tail sizing and tailplane incidence limits. The poor agreement obtained for the unblown case is not surprising in light of the discussion of flow fields in Volume I, since the location of the vortex wake for a conventional wing is not constrained by a dynamic boundary condition as is the jet sheet. Although the present method for locating the trailing vorticity is approximate, it has been shown to work in many cases. The failure here is, most likely, due to the extreme trailing edge flow separation characteristics of plain flaps. For the unblown case, ε_o and $\frac{d\varepsilon}{d\alpha}$ predictions can be improved by multiplying the predicted values by $(C_L/C_{L_{EVD}})$.

Drag: IBF drag comparisons are presented in figure (8.9). Looking first at the C_{J_e} = 0.5 plot, excellent agreement between experiment and the predictions are indicated for all flap deflection angles. Fairly good agreement is also obtained for the C_{J_e} = 1.0 runs, except for the highest flap deflection. The experimental data shows virtually no shift in the drag polars between the 45 and 60 degree flap deflections. This unusual trend is even further exaggerated for the C_{J_e} = 2.0 curves, where it can be seen that the drag polar for 60 degrees flap deflection is actually at a lower level than the 45 degree

polar. Such behavior is contrary to expectations. However, based on the observations made from the lift data, where a severe break in the $\delta_f = 60^\circ$ lift curve which was attributed to impingement of the jet sheet on the tunnel floor was noted, the unusual drag trends can be explained. It appears that for the higher jet momentums and deflection angles tested there was inadequate clearance with the tunnel walls, so the data are actually as if the model were in ground effect.

Looking now at the unblown case drag comparison, good agreement is obtained for the 15 and 30 degree flap deflection angles, but the drag has been over-predicted for the 45 and 60 degree flap deflections. Since lift has been properly predicted for this case, failure to predict drag accurately indicates a poor prediction of the profile drag due to flap deflection. Although this may be indicative of inadequate empirical data in figure (3.15a) for plain flap profile drag, another possibility is that the leading edge blowing used in this configuration provided enough boundary layer control to alter the flow separation characteristic of plain trailing edge flaps.

Drag for this IBF has been predicted with reasonable accuracy, particularly when it is considered that drag is a relatively unimportant aerodynamic parameter for stability and control analyses.

Pitching Moment: IBF pitching moment comparisons are presented in figure (8.10). The pitching moments are referenced about the quarter mean aerodynamic chord point of the wing. For the unblown case, the agreement between experiment and prediction is good, both for C_{m_o} and C_{m_α}. For the blown cases, however, the predicted C_{m_o} is more nose down than is shown by the experimental data, but there is good agreement for C_{m_α}, the pitching moment curve slope. The discrepancies in C_{m_o} shown in figure (8.10) can, in part, be attributed to the fuselage. The jet-wing alone C_{m_o} predicted by the EVD portion of STAMP was in better agreement with experiment than the final prediction, but its C_{m_α} prediction was poor, generally being of the wrong sign. Inclusion of the modified slender body solution fuselage pitching moment, including jet-wing interference effects, yielded a good estimate of C_{m_α} but caused an unfavorable shift in C_{m_o}. Fuselage C_{m_α} depends primarily on the body fineness ratio and not on the specific body geometric details, so an accurate estimate of C_{m_α} is expected. However, C_{m_o} is strongly dependent on body

upsweep, cross-section, etc.; and since the fuselage used in the Convair STAI tests was of complex design, the relatively simple fuselage methods in STAMP cannot be expected to predict $C_{m_o}|_{Fuselage}$ well. In addition, the empirical afterbody separation methods presented in Section 3.1.1.4 can only be expected to qualitatively predict C_{m_o}.

There are additional factors which can also be contributing to the C_{m_o} discrepancy. First is interference from the sting/support system. It was mentioned earlier that such interferences could alter the fuselage C_{m_o} by as much as 30 percent (nose up). Second is the close proximity of the jet sheet to the tunnel floor, which has been discussed earlier. Finally, variations in the spanwise distribution of jet momentum from that postulated, due to variations in the trailing edge blowing slot geometry from design, can alter the jet reaction pitching moment.

Ground Effect: Comparisons of the effect of ground proximity on lift, drag, and pitching moment are presented in figures (8.14), (8.15), and (8.16). These plots present the percentage change of each aerodynamic parameter from its corresponding free-air value in percent of the free-air value. The ground height selected for this comparison, $h = 0.40\ b/2$, is representative of the height of the wing above the ground when the landing gear are on the ground. Experimental data have been taken from Convair Test GDLST 612-3 for free-air runs and from Convair Test GDLST 621 for ground effect runs.

The ground effect lift comparisons presented in figure (8.14) show only qualitative agreement between experiment and the prediction methods. For the unblown case, experiment shows a strong favorable ground effect of up to 15 percent, while the theoretical methods predict only 5 percent favorable ground effect. Similar trends exist for the blown cases. Significant impingement of the jet sheet on the ground plane should be noted for the 60 degree deflection angle.

Similarly, figure (8.15) for drag indicates qualitative agreement only, showing generally large decreases in drag experimentally and smaller predicted drag reduction. Note that experiment shows nearly a 30 percent decrease in drag for the 60 degree flap deflection case where jet impingement is evident.

Finally, pitching moment in ground effect comparisons are presented in figure (8.16) and again indicate qualitative agreement between experiment and the prediction methods. For nearly all conditions tested, there is a decrease in the nose down pitching moment.

Special consideration of wind tunnel wall effects for ground effect runs must be made, particularly in light of the poor agreement obtained. Reference 28 indicates that reference 30 was used to modify δ, the wall correction factor, for ground effect runs. The method presented in reference 30 is quite simple in many respects, ignoring offset of the model from the tunnel centerline, non-rectangular tunnel geometries, spanwise loading variations, etc. and the 10 percent uncertainty in δ that is mentioned in reference 30 may very likely increase for jet-wings. Hence there is reason to believe that some of the discrepancies shown in figures (8.14), (8.15), and (8.16) are due to wind tunnel wall corrections, which can be on the same order as the ground effects themselves.

8.2 STOL Aircraft Employing Externally Blown Jet Flap

An externally blown jet flap system in which the efflux of four pod-mounted jet engines is directed to impinge on a large-chord double-slotted flap system was employed in the second phase of these comparisons. The basic EBF model tested was similar to the IBF model analyzed in Section 8.1, the differences being primarily in the flap system, engine position, and of course the means by which the jet-flap effect was achieved. The analysis presented in the following sections is abbreviated to avoid repeating work presented for the IBF analysis.

8.2.1 Configuration Description

The basic aircraft configuration is illustrated in figure (8.1). The model is typical of a four-engine, high wing, T-tail, subsonic STOL transport with a front-loading cargo fuselage. The basic wing geometric characteristics are listed in table (8.1).

The wing is equipped with a full span double-slotted flap with pertinent flap geometric characteristics as listed in table (8.12).

Table (8.12). Double-Slotted Flap Geometric Characteristics

δ_{f_1}(deg)	c_1/c	δ_{f_2}(deg)	c_2/c	δ_{f_2}(deg)
30	0.274	16.5	0.329	13.5
45	0.274	28.5	0.329	16.5
60	0.274	28.5	0.329	31.5

In addition, the wing is equipped with a full span leading edge flap with a chord 15 percent of the local wing chord and a chord extension of 14.5 percent. Empennage and fuselage geometric characteristics are identical to those described in Section 8.1 for the IBF configuration.

8.2.2 Geometry Preparation for Computer Analysis

The wing planform is first defined by graphically extending the chord to account for flap and leading edge device deflections. Although there is a considerable amount of Fowler action involved in the double-slotted flap motion, a mean flap-chord extension was used, to simplify the analysis, being representative of the planform over the range of flap deflection angles to be considered. Illustrated in figure (8.17) is the procedure used to determine a mean c_f/c. First a sectional mean line is constructed for each flap deflection, and then the flap segments are rotated about their assumed hinge points back to the section chord line. For the particular flap used in this test it has been determined that the flap-chord extensions are approximately 34 and 38 percent of the local chord for deflection angles of 30 and 60 degrees respectively. Hence a 36 percent mean flap-chord extension has been used to define this planform, as illustrated in figure (8.18). The leading edge device extension, 14.5 percent, is the same as used for the IBF configuration.

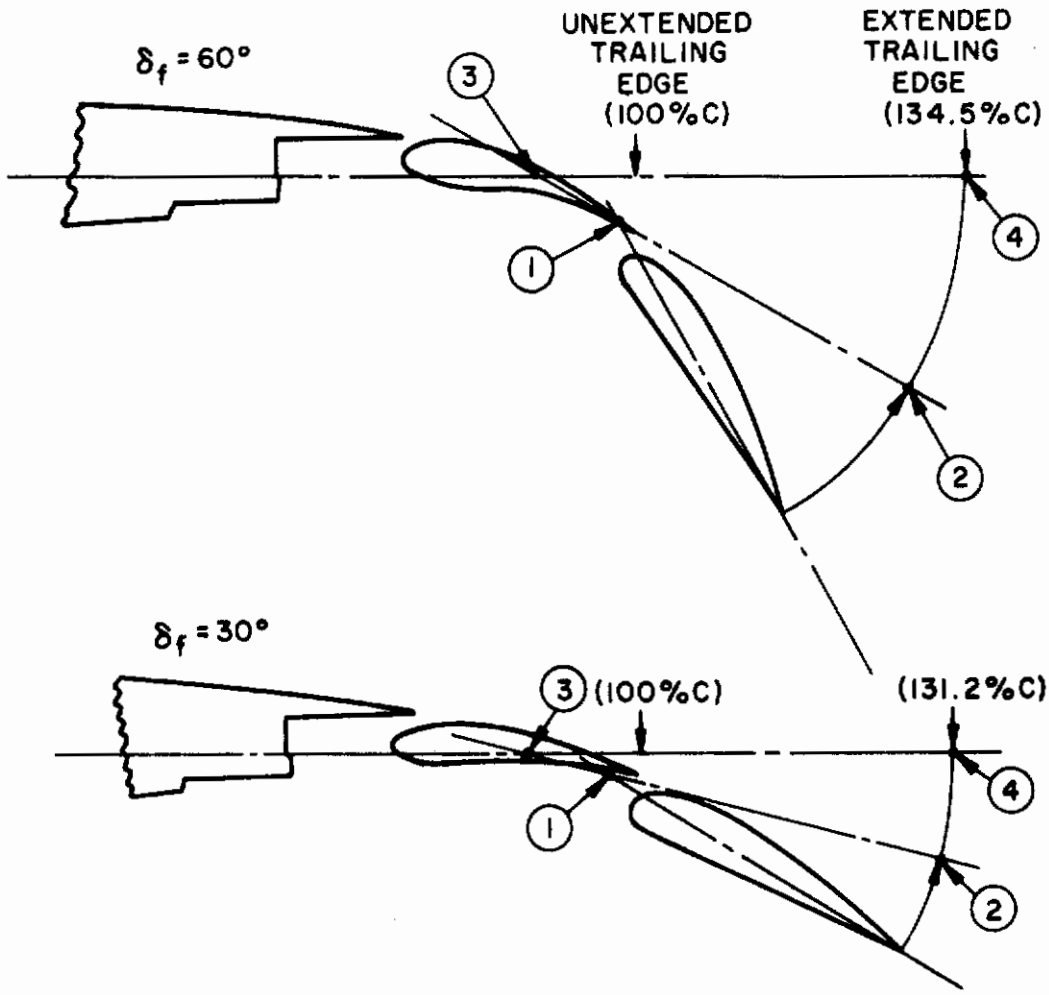

Figure (8.17). EBF Flap Sectional Geometry and Illustration of Chord Rotation Procedure for Fowler Flaps

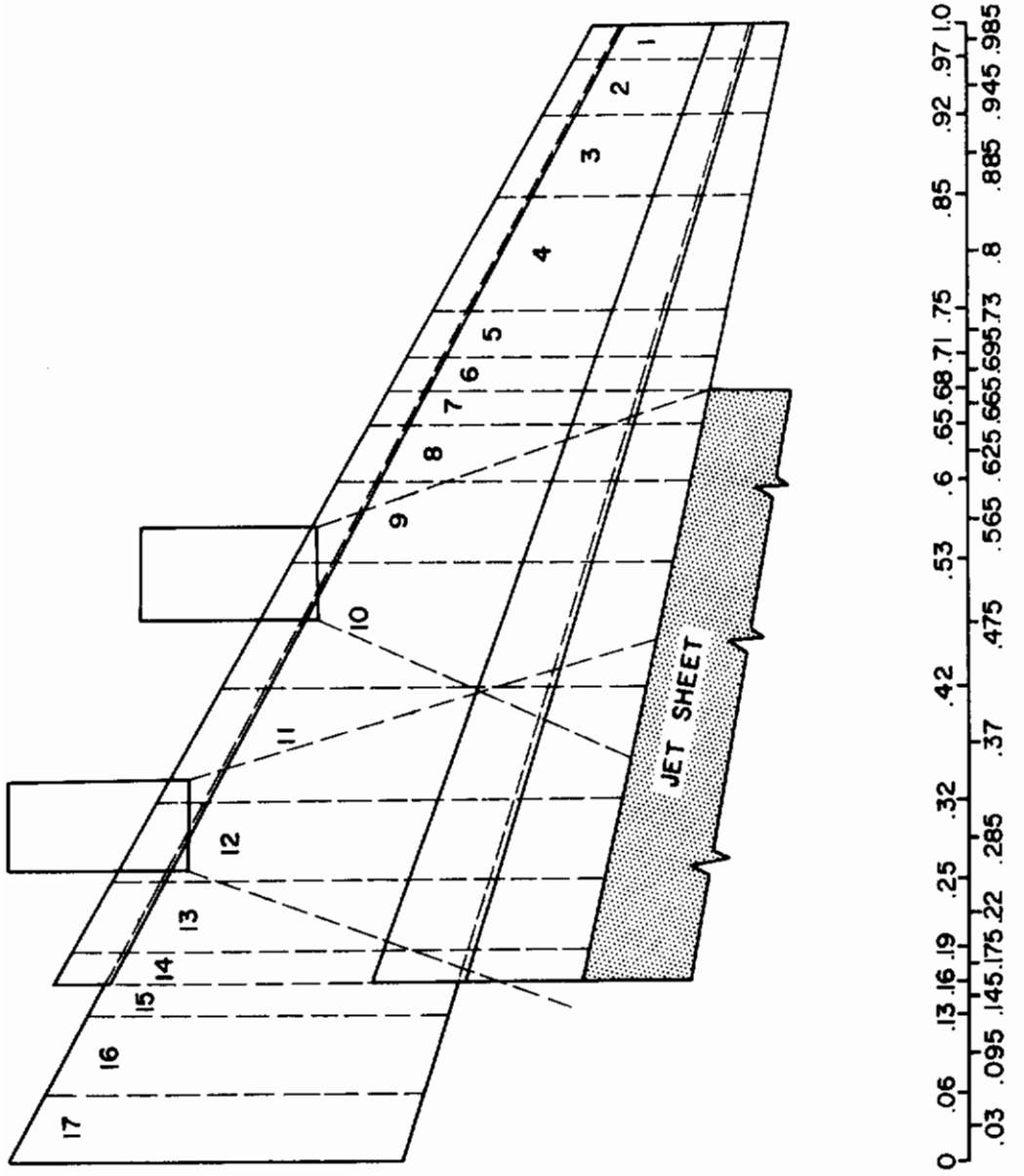

Figure (8.18). EBF Wing Planform Including Selected Spanwise Divisions and Assumed Jet Spreading

Note that the inboard 16 percent semi-span is retained in its unextended form to account for the fuselage.

Unlike the IBF configuration where the only regions of expected large spanwise loading gradients are near the wing tip and at the edge of the fuselage break, for the EBF the blowing region is not full span, so another significant spanwise loading gradient can be expected at the outboard edge of the jet sheet. Hence postulated jet spreading characteristics, based on the empirical methods of Section 7.1.2, must first be determined before an appropriate distribution of spanwise rows can be chosen.

Referring to the discussion of Section 7.1.2, it is said that a jet spreading of 3 and 5 jet exit diameters for flap deflections of 30 and 60 degrees, respectively, has been observed experimentally. Therefore, for the range of flap deflections of interest a reasonable mean jet spreading is 4 jet exit diameters. Since the exit duct of the jet engines is of diameter 0.08 b/2, the "trailing-edge plume" for each engine is 0.32 b/2, as shown is figure (8.18). Referring to figure (7.7), the following parameters necessary for the evaluation of equations (7.3) can be graphically determined:

Point	$\frac{y}{b/2}$	$\frac{c}{b/2}$
a	0.14	0.475
a'	0.16	0.470
b	0.26	0.435
c	0.34	0.407
d	0.46	0.365
e	0.36	0.400
f	0.48	0.357
g	0.56	0.330
h	0.68	0.285

Applying equations (7.3), it can be shown that

$$K_1 = 0.05227$$

$$K_2 = 0.06740$$

$$K_3 = 0.04719$$

Hence the maximum sectional momentum coefficients are

$$c_{\mu_{max}}\Big|_{Inboard} = 5.993\ C_J\Big|_{Inboard}$$

$$c_{\mu_{max}}\Big|_{Outboard} = 7.278\ C_J\Big|_{Outboard}$$

EBF turning characteristics are presented in figure (8.19). Over the range of flap deflections of interest the mean jet turning efficiency $\tau = 0.76$. Also, the mean jet turning angle $\nu = \delta_f - 10°$. Based on these values, the engine momentum coefficients (C_{J_e}), trailing edge jet momentum (C_J), trailing edge jet momentum for each engine (C_J per engine), and maximum sectional jet momentum coefficients ($c_{\mu_{max}}\Big|_{Inboard}$ and $c_{\mu_{max}}\Big|_{Outboard}$) are tabulated below:

Table (8.14). EBF Jet Momentum Characteristics

C_{J_e}	C_J	C_J per Engine	$c_{\mu_{max}}\Big\|_{Inbd}$	$c_{\mu_{max}}\Big\|_{Otbd}$
0	0	0	0	0
0.5	0.38	0.095	0.569	0.691
1.0	0.76	0.190	1.139	1.383
2.0	1.52	0.380	2.277	2.765

Returning now to the spanwise division problem, it can now be inferred from figure (8.18) that significant spanwise loading gradients will occur near the wing tip, at the fuselage edge, and near the outboard edge of the jet sheet at $y = 0.68\ b/2$. The spanwise divisions are then selected based on the spacing guidelines presented in Volume II. Referring to figure (8.18), 17 divisions have been selected for this case and the centerline values of y to be input are .985, .945, .885, .80, .73, .695, .665, .625, .565, .475, .37, .285, .22, .175, .145, .095, .03.

Now knowing the jet momentum characteristics from table (8.14) and the spanwise divisions as listed above, values of the sectional jet momentum coefficients to be input can be calculated using equations (7.3a), (7.3b),and (7.3c). These values are tabulated below. It should be noted that the postulated trapezoidal momentum distributions overlap on the $y = 0.37\ b/2$ spanwise row, and both the inboard engine and outboard engine c_μ-contributions to this row are listed.

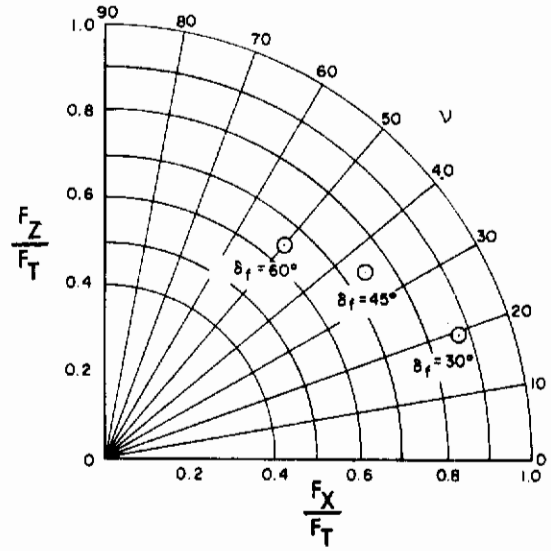

Figure (8.19). EBF Flap Turning Effectiveness (Test GDLST 612-3)

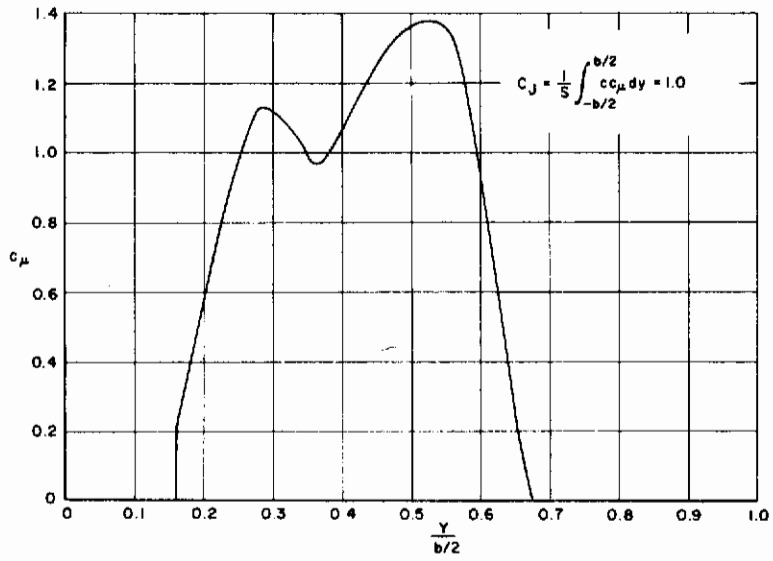

Figure (8.20). Postulated EBF Trailing Edge Momentum Distribution

Table (8.15). EBF Sectional Jet Momentum Coefficients

$\frac{y}{b/2}$	Engine	$c_\mu(y)$ for C_{J_e}=0.5	$c_\mu(y)$ for C_{J_e}=1.0	$c_\mu(y)$ for C_{J_e}=2.0
0.665	Outboard	0.086	0.172	0.344
0.625		0.317	0.634	1.265
0.565		0.663	1.326	2.652
0.475		0.663	1.326	2.652
0.370		0.057	0.114	0.228
0.370	Inboard	0.427	0.854	1.708
0.285		0.569	1.139	2.277
0.220		0.379	0.758	1.516
0.175		0.166	0.332	0.664

The postulated sectional momentum distribution for $C_{J_e} = 1.0$ is presented in figure (8.20)

Chordwise geometry is defined in a manner similar to that for the IBF configuration. The fourteen outboard rows have identical chordwise geometry, including a leading edge hinge and two trailing edge hinges; while the three inboard rows represent the fuselage cutout and require only simple definition. The basic chordwise geometry is that of a NACA 64A-series airfoil, with an a = 1.0 camber line, which is highly cambered at both the leading and trailing edges. The leading edge flap hinge is located at the unextended leading edge. The extended chord c' is

$$c' = (1.0 + 0.36 + 0.145)c = 1.505c$$

so the leading edge hinge is located at

$$\frac{x}{c'} = \frac{0.145}{1.505} = 0.096 \qquad \text{(leading edge flap hinge)}$$

The trailing edge hinges are located at 75.8 percent and 103.8 percent of the unextended chord for a mean deflection, or in terms of the extended chord

$$\frac{x}{c'} = \frac{0.145 + 0.758}{1.505} = 0.60 \quad \text{(trailing edge flap hinge 1)}$$

$$\frac{x}{c'} = \frac{0.145 + 1.038}{1.505} = 0.786 \quad \text{(trailing edge flap hinge 2)}$$

The chosen chordwise division for the fourteen flapped rows required 14 elements per row, while the three inboard rows were divided into 9 elements per section [figure (8.21)]. Jet sheet spacing is the same as was used for the IBF. Hence the wing is defined by 223 EVD elements and the jet by 48 elements for a total of 271 EVD elements.

The EBF wing planform is fully defined by figures (8.18) and (8.21). The planform is input into the computer program in two trapezoidal sections using leading and trailing edge coordinates obtained graphically from figure (8.18) and tabulated below:

Y	X_{LEAD}	X_{TRAIL}
0.985	17.72	23.85
0.175	1.72	17.69
0.145	2.72	13.56
0.03	0.585	12.35

The jet-wing has been defined using six fundamental cases:

1. Angle of attack case
2. Wing twist plus wing camber case
3. Leading edge flap hinge case
4. Trailing edge flap hinge case
5. Trailing edge flap hinge case
6. Jet deflection case

The first case is defined by the computer program. The second case is essentially the same as for the IBF. The leading edge flap hinge is defined for the fourteen outboard rows at x/c = 0.10 with a fundamental case input of one degree. The trailing edge hinges are defined at x/c = 0.6 and x/c = 0.786, each deflected one degree for the respective fundamental cases. The jet deflection fundamental case defines the jet deflected one degree (downward) relative to the wing trailing edge.

To evaluate the desired EBF configurations, three composite cases are required. Each case includes camber and twist (1.0 x CASE 2), leading edge flap deflection (55.0 x CASE 3), and a jet deflection of ten degrees less than the flap deflection angle (-10.0 x CASE 6). The flap deflections are input as follows: 30 degrees as (16.5 x CASE 4 plus 13.5 x CASE 5); 45 degrees

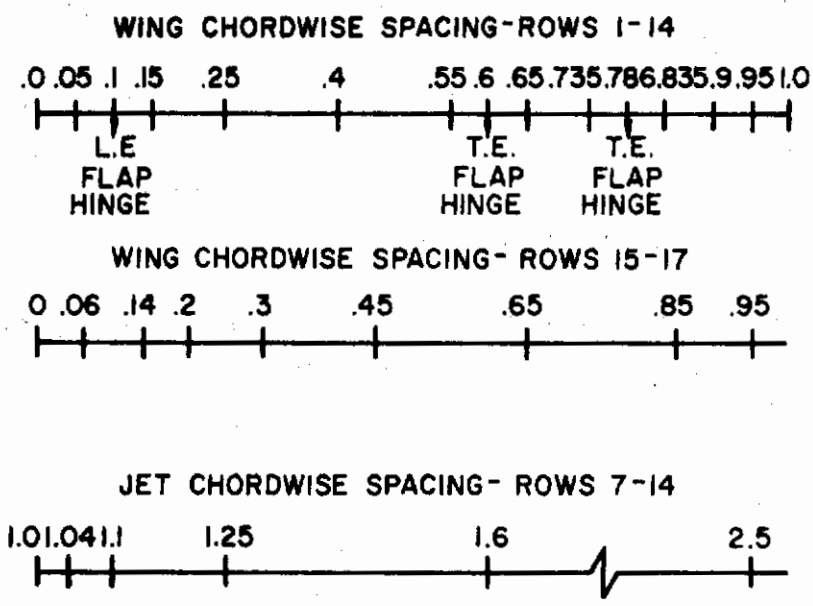

Figure (8.21). EBF Chordwise Geometry Summary

as (28.5 x CASE 4 plus 16.5 x CASE 5); and 60 degrees as (28.5 x CASE 4 plus 31.5 x CASE 5).

Basic case parameters are input essentially the same as for the IBF case except for the EBF case NROWS = 17 and NCASES = 6. The computer run parameter estimates were 30 minutes of IBM/370 CPU time, 30 minutes of I/O time, 50,000 lines of print, and 4,000 punched output cards.

8.2.3 Interpretation of Computer Data

This section presents the computer generated aerodynamic data for the EBF configuration and demonstrates application of the engineering methods presented in this volume to complete the aerodynamic analysis. Both predicted aerodynamic parameters and experimental results are presented here, but a discussion of the comparison between the predictions and experiment is reserved for the next section. Certain portions of the EBF analysis are identical to the IBF analysis, particularly with regard to the fuselage viscous corrections, and these portions are not repeated here.

The actual STAMP computer analysis for this EBF configuration was run on the McDonnell Douglas IBM 370/165 computer system and required 24.8 minutes of CPU time. Application of the engineering methods to these data is presented below:

Lift: EBF lift curves are plotted in figure (8.22) for gross engine thrust coefficients C_{J_e} of 0.0, 0.5, 1.0, and 2.0. The solid curves represent corrected jet-wing plus fuselage lift. Tailplane lift is not included here.

Jet-wing lift has been corrected for viscous and thickness effects using equation (3.12). This requires that the sectional lift coefficients first be corrected. For blown wing sections equation (3.9) is used to correct circulation lift for thickness effects, with K = 0.8 and $t/c' = 0.083$. Hence

$$c_{\ell_\Gamma}\Big|_{\text{Blown}} = [1.0 + 0.8(0.083)]c_{\ell_\Gamma}\Big|_{\substack{\text{EVD}\\\text{Blown}}}$$

To each corrected $c_{\ell_\Gamma}\Big|_{\text{Blown}}$ value must be added the appropriate reaction lift,

c_{ℓ_μ}. The above correction applies both to $c_{\ell_{\Gamma_o}}$ and $c_{\ell_{\Gamma_\alpha}}$ for blown sections. For unblown wing sections a different correction is required for c_{ℓ_o} and c_{ℓ_α}. For c_{ℓ_α}, equation (3.3) is used. For the EBF, $K_1 = 1.07$, $R_\ell = 5.0 \times 10^5$, and $K_2 = 0.7$. Hence

$$c_{\ell_\alpha}\Big|_{\text{Unblown}} = 1.05(1.07)(0.7)c_{\ell_\alpha}\Big|_{\substack{\text{EVD}\\\text{Unblown}}} = 0.79\, c_{\ell_\alpha}\Big|_{\substack{\text{EVD}\\\text{Unblown}}}$$

For c_{ℓ_o}, equation (3.8) is used. $K_6|_{\text{FWD}}$ is obtained from figure (3.4) with $c_1/c_a' = 0.236$ (from wing geometry), and is

$$K_6|_{\text{FWD}} = \begin{Bmatrix}0.48\\0.44\\0.44\end{Bmatrix} \text{ for } \delta_{f_1} = \begin{Bmatrix}16.5°\\28.5°\\28.5°\end{Bmatrix}$$

$K_6|_{\text{AFT}}$ is also obtained from figure (3.4) with $c_2/c_1 = 0.215$, and is

$$K_6|_{\text{AFT}} = \begin{Bmatrix}0.45\\0.45\\0.40\end{Bmatrix} \text{ for } \delta_{f_2} = \begin{Bmatrix}13.5°\\16.5°\\31.5°\end{Bmatrix}$$

K_3 is obtained from figure (3.2a) based on c_1/c_a' and c_2/c_1 and is found to be

$$K_3|_{\text{FWD}} = 1.07 \qquad K_3|_{\text{AFT}} = 1.05$$

Therefore, equation (3.8) is evaluated as

$$c_{\ell_o}\Big|_{\text{Unblown}} = \left[\begin{Bmatrix}0.48\\0.44\\0.44\end{Bmatrix}(1.07) + 0.72\begin{Bmatrix}0.45\\0.45\\0.40\end{Bmatrix}(1.05)\right] c_{\ell_o}\Big|_{\substack{\text{EVD}\\\text{Unblown}}}$$

$$= \begin{Bmatrix}0.8538\\0.8110\\0.7732\end{Bmatrix} c_{\ell_o}\Big|_{\substack{\text{EVD}\\\text{Unblown}}} \text{ for } \delta_f = \begin{Bmatrix}30°\\45°\\60°\end{Bmatrix}$$

All of the necessary lift corrections have now been made, and all that remains is to extract the appropriate sectional lift values from the computer program output, apply the appropriate corrections, and re-integrate the lift using equation (3.12). These integrations have been done using a small Fortran computer program, which can easily be written tailored to the nature of a particular case (or which can be done by hand). Finally, fuselage lift, as calculated for the IBF configuration, is added to the corrected jet-wing lift to yield the curves in figure (8.22).

Mean tailplane downwash is calculated using equation (3.20) and is

EBF LIFT

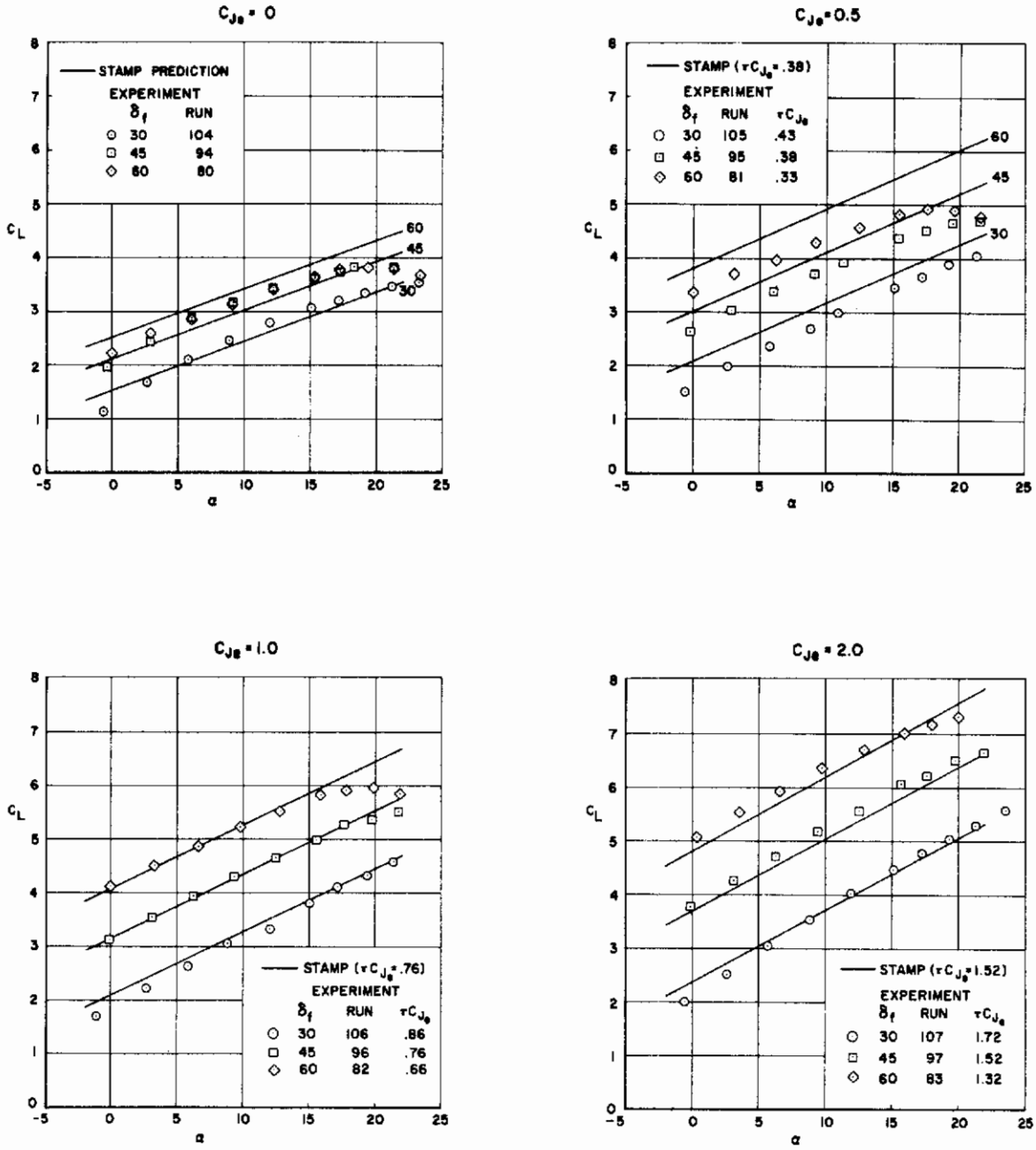

Figure (8.22). EBF Lift Comparisons (Test GDLST 612-3)

plotted in figure (8.23). Note that ε has not been corrected for discrepancies between the predicted C_L and $C_{L_{EVD}}$. The gradient of tail-plane downwash, $\frac{d\varepsilon}{d\alpha}$, which is a quantity of primary importance in stability and control analyses, is the slope of the ε versus α curves in figure (8.23).

Drag: EBF drag polars are plotted in figure (8.24) for gross engine thrust coefficients C_{J_e} of 0.0, 0.5, 1.0, and 2.0. The solid curves are total jet-wing plus fuselage drag. Since most of the pertinent wind tunnel data was taken tail-off, empennage drag is not presented. Note that the quantity plotted in figure (8.24) is actually

$$C_D = \tau C_{J_e} - C_T$$

where τ is the mean turning efficiency of the EBF and C_{J_e} is the gross engine thrust coefficient.

Induced drag calculated by the computer program has been corrected for thickness and viscous effects using equation (3.27), while profile drag (form and friction drag) has been calculated entirely using the methods of Section 3.1.2.1. Beginning with $C_{D_o}|_{profile}$, the skin friction coefficient is the same as for the IBF, i.e., $c_f = 0.005$. As for the IBF, $R_{LS} = 1.07$, $L = 1.2$, and $t/c = 0.125$ ($t/c' \approx 0.083$). Calculating flap incremental profile drag for this EBF configuration is a difficult task, both for blown and unblown wing sections, because there is little existing empirical data for double-slotted Fowler flaps which can be applied with any generality, especially when it is remembered that the effects of boundary layer control can only be estimated based on the postulated jet spreading (Section 8.2.2). Data for the flap term in equation (3.24), $\Delta c_{d_{flap}} K_b$, is presented only for plain and single-slotted flaps because so little in the way of systematic studies of double-slotted flaps has been done.

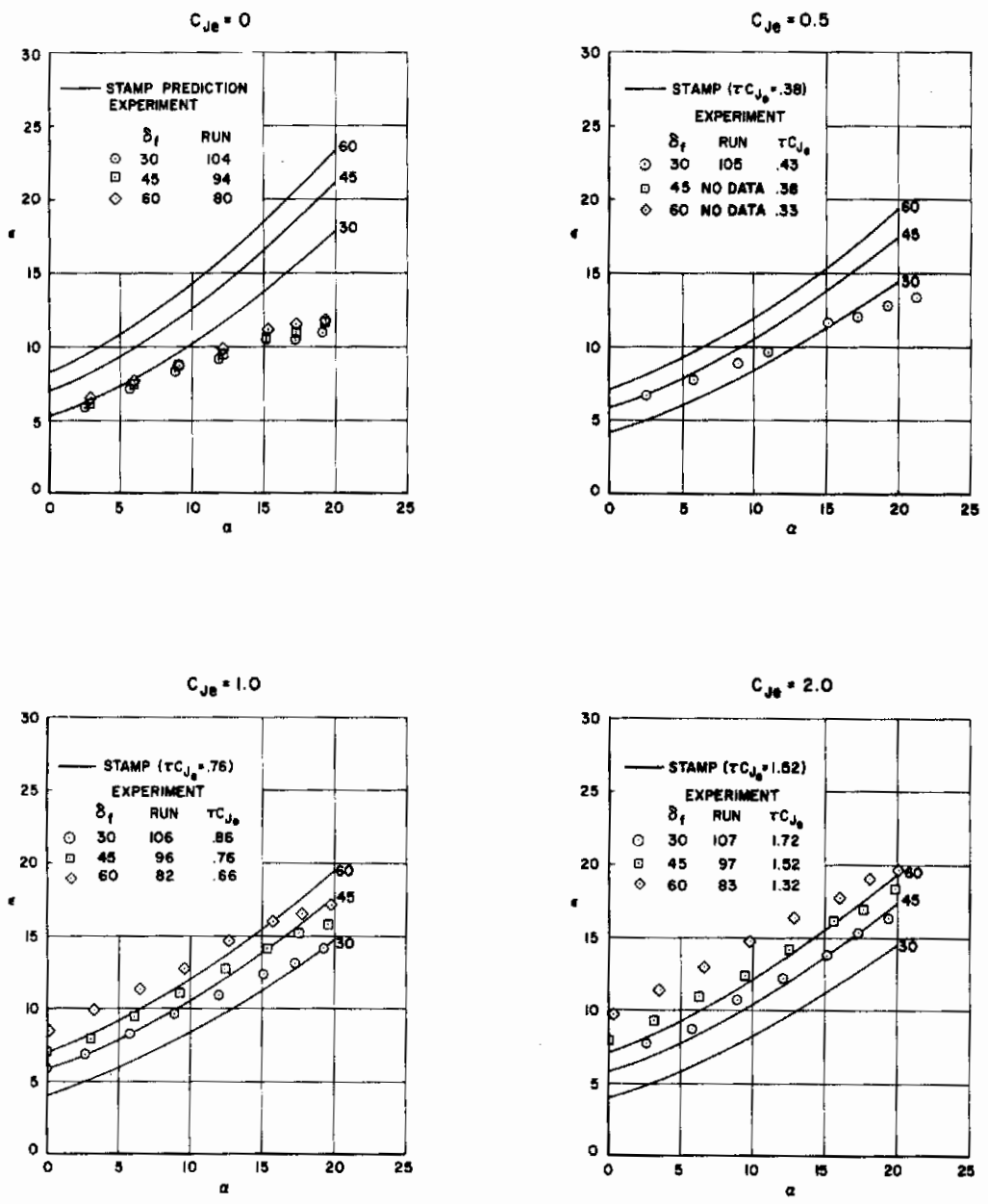

Figure (8.23). EBF Tailplane Downwash Comparisons (Test GDLST 612-3)
[NOTE: ε has not been corrected by the ratio $(C_L/C_{L_{EVD}})$]

This is largely due to the complex geometry of a double-slotted high lift system which leads to a tremendous array of possible configurations. Parameters such as flap-chord ratios of both flap segments, the relative displacement, overlap, gap, and deflection of each segment, and the amount of Fowler motion for each flap segment must be considered. Of the limited flight test and wind tunnel data for $\Delta c_{d_{flap}}$ existing for CTOL aircraft with single-, double-, and triple-slotted flap systems, some of the data indicate similar incremental profile drag coefficients for single- and double-slotted systems, some data indicate smaller $\Delta c_{d_{flap}}$ for double-slotted relative to single-slotted systems, while other data show smaller $\Delta c_{d_{flap}}$ for triple-slotted systems relative to both of the others. At this time no improved double-slotted flap data can be presented, so single-slotted flap data will be used. It is expected that for the unblown case C_{D_o} will be over-predicted. For the EBF blown cases, the $\Delta c_{d_{flap}}$ term will be assumed to be zero over the blown extent of the wing ($0.16\ b/2 \leq y \leq 0.68$) and hence only for the span from $0.68\ b/2 < y \leq 1.0\ b/2$ will a $\Delta c_{d_{flap}}$ be applied. For the unblown case, the term will be applied from $0.16\ b/2 \leq y \leq 1.0\ b/2$. From figure (3.16),

$$K_b\Big|_{Blown} = K_b(1.0) - K_b(0.68) = 1.0 - 0.84 = 0.16$$

$$K_b\Big|_{Unblown} = K_b(1.0) - K_b(0.16) = 1.0 - 0.21 = 0.79$$

Using the single-slotted flap data in figure (3.15b) with $c_f/c = 0.40$

δf (deg)	$\Delta C_{d_{flap}}$
30	0.06
45	0.15
60	0.30

The value for $\Delta c_{d_{flap}}$ at $\delta_f = 60$ degrees was determined by cross-plotting $\Delta c_{d_{flap}}$ versus δ_f with $c_f/c = 0.40$. Hence the profile drag coefficient is calculated from equation (3.14):

$$C_{D_o\ profile} = \left\{(0.005)[1 + 1.2(0.083) + 100(0.083)^4](1.07)\right\}\left\{\frac{1283.0}{592.0}\right\} + \Delta c_{d_{flap}} K_b$$

where S_{wet} = 1283.0 in^2. Therefore

$$\underline{\text{Blown cases}}: \left.C_{D_o}\right|_{\text{profile}} = \begin{Bmatrix}0.0257\\0.0437\\0.0737\end{Bmatrix} \text{ for } \delta_f = \begin{Bmatrix}30°\\45°\\60°\end{Bmatrix}$$

$$\underline{\text{Unblown cases}}: \left.C_{D_o}\right|_{\text{profile}} = \begin{Bmatrix}0.0629\\0.1367\\0.2597\end{Bmatrix} \text{ for } \delta_f = \begin{Bmatrix}30°\\45°\\60°\end{Bmatrix}$$

Application of equation (3.27) to induced drag calculated by the computer program to correct for viscous and thickness effects is done in the same manner for the EBF as was outlined for the IBF in Section 8.1.3. Because of the length of these calculations, none of the tabular results is presented.

Fuselage drag and engine ram drag are calculated in the same manner as for the IBF configuration. There it was calculated that the fuselage drag coefficient is

$$C_{D_{o_F}} = 0.0156$$

and the fuselage lift dependent drag is

$$C_{D_F}(\alpha) = 4.2 \times 10^{-5}\alpha^2 + 4.7 \times 10^{-7}\alpha^3$$

Ram drag was measured to be as tabulated below:

C_{J_e}	0	0.5	1.0	2.0
C_{D_R}	0.05	0.134	0.177	0.221

The total EBF jet-wing-fuselage plus ram drag is calculated using equation (3.36) and is plotted in figure (8.24).

Pitching Moment: EBF pitching moment is plotted in figure (8.25) for gross engine thrust coefficients C_{J_e} of 0.0, 0.5, 1.0, and 2.0. The solid curves represent predicted jet-wing plus fuselage pitching moment. Tailplane pitching moments have been calculated but are not presented here because most of the wind tunnel data is for tail-off configurations.

Jet-wing pitching moment has been corrected for viscous and thickness effects using equation (3.46). This requires that the sectional pitching moments first be corrected. For blown wing sections equation (3.44) is used to correct circulation pitching moment for thickness effects, with K = 0.8 and t/c = 0.083. Hence

$$c_{m_\Gamma}\Big|_{\text{Blown}} = [1.0 + 0.8(0.083)]c_{m_\Gamma}\Big|_{\substack{\text{EVD}\\\text{Blown}}}$$

To each corrected c_{m_Γ} must be added the appropriate reaction lift and thrust terms, c_{m_μ} and c_{m_T}. The above correction applies both to $c_{m_{\Gamma_0}}$ and $c_{m_{\Gamma_\alpha}}$ for blown sections. For unblown wing sections a different correction is required for c_{m_0} and c_{m_α}. For c_{m_α} equation (3.40) is used. For the EBF, ϕ_{TE} = 14.1 degrees and t/c = 0.083, hence K = 0.99 from figure (3.18) The ratio of corrected to EVD lift curve slope was previously calculated to be 0.925, and hence

$$c_{m_\alpha} = (0.99)(0.925)c_{m_\alpha}\Big|_{\text{EVD}} = 0.915\ c_{m_\alpha}\Big|_{\text{EVD}}$$

For c_{m_0}, equation (3.43) for single-slotted flaps is used, and, as discussed in Section 3.1.3.1, this correction is applied to the composite sectional c_{m_0}. K is taken from figure (3.19b) with c_f/c = 0.40 and is found to be (1.0, 0.8, 0.35) for δ_f = (30, 45, 60) degrees. All of the necessary sectional pitching moment corrections have now been made, and all that remains is to extract the necessary sectional pitching moment values from the computer program output, apply the appropriate corrections, and re-integrate the pitching moment using equations (3.46) and (3.47). Again these integrations have been performed by writing a small Fortran computer program tailored to this particular case.

Fuselage pitching moment has been calculated in a manner identical to that used for the IBF, but of course the jet-wing interferences as calculated

EBF DRAG

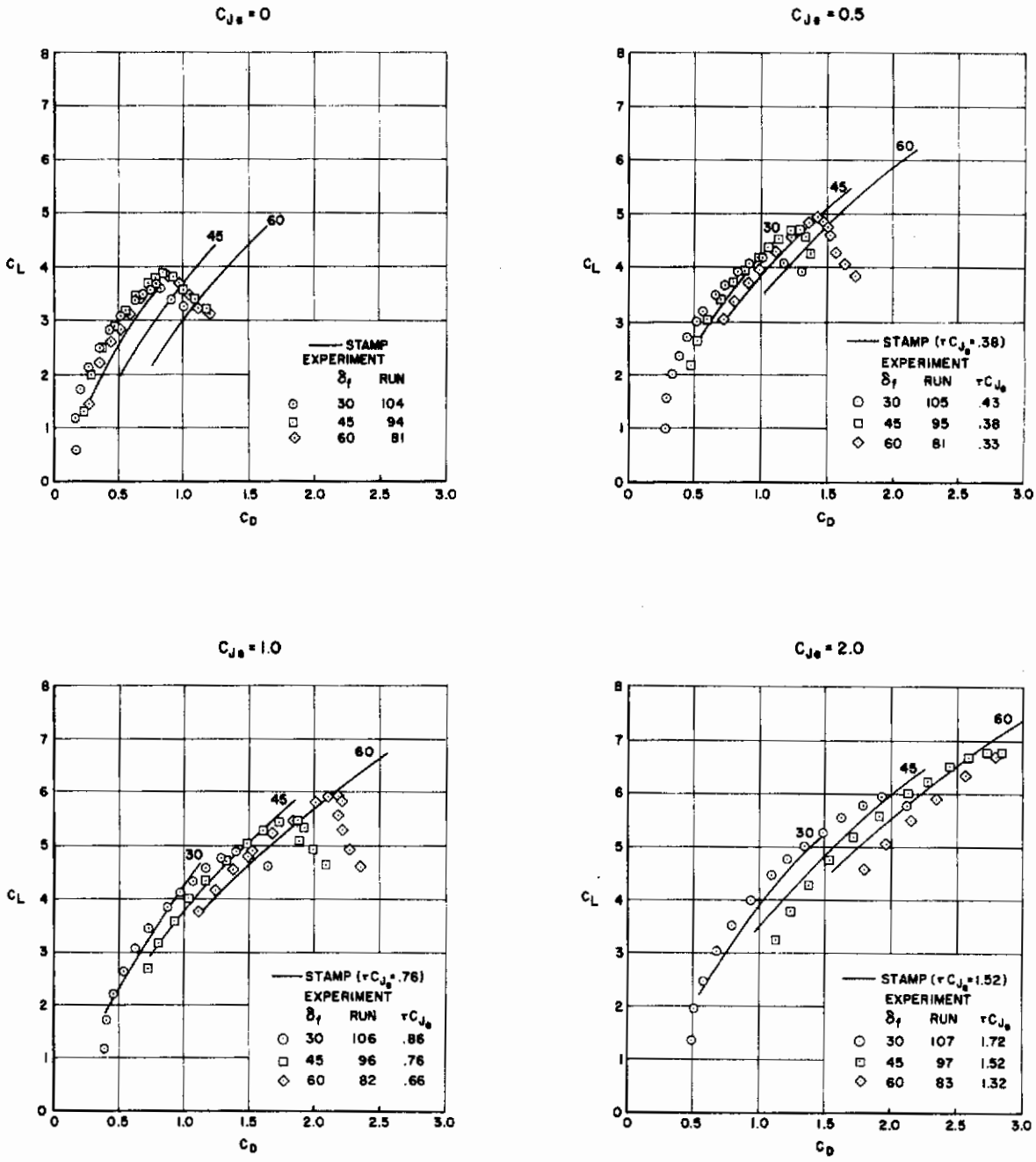

Figure (8.24). EBF Drag Comparisons (Test GDLST 612-3)
(Note: $C_D = \tau C_{J_e} - C_T$)

by the computer program are different. Viscous effects are assumed to be the same. Ram drag pitching moment is calculated using the procedure discussed for the IBF, but here C_{D_R} varies with C_{J_e}. The predicted pitching moment data presented in figure (8.25) includes corrected jet-wing pitching moment, corrected fuselage pitching moment, and the ram drag pitching moment.

Dynamic Stability Derivatives: Although there is no experimental data for comparison, a complete set of dynamic stability derivatives has been generated for this EBF configuration. These data are presented in the same format as the IBF dynamic stability derivatives.

C_{L_u}: The C_{L_u} derivative is calculated from equations (5.6) and (5.7) for the circulation component and from equation (5.5) for the reaction component. The circulation term, $\frac{\partial C_{L_\Gamma}}{\partial u}$, is presented in table (8.16).

Table (8.16). EBF C_{L_u} Stability Derivatives

C_{J_e}	$\frac{\partial C_{L_{\Gamma_o}}}{\partial u}$			$\frac{\partial C_{L_{\Gamma_\alpha}}}{\partial u}$
	$\delta_f = 30°$	$\delta_f = 45°$	$\delta_f = 60°$	
0.5	0.010	0.022	0.028	0.0004
1.0	0.009	0.010	0.010	0.00005
2.0	0.002	0.002	0.003	0.00002

C_{D_u}: The speed damping derivative is calculated from equation (5.10) and (5.11) using a procedure indentical to that described above for C_{L_u}. The total C_{D_u} stability derivatives for α = 10 degrees are presented in table (8.17). These data include the circulation and reaction portions of C_{D_u}. As for the IBF, the ram drag term cannot be calculated since the variation of Q_j with U is unknown.

EBF PITCHING MOMENT

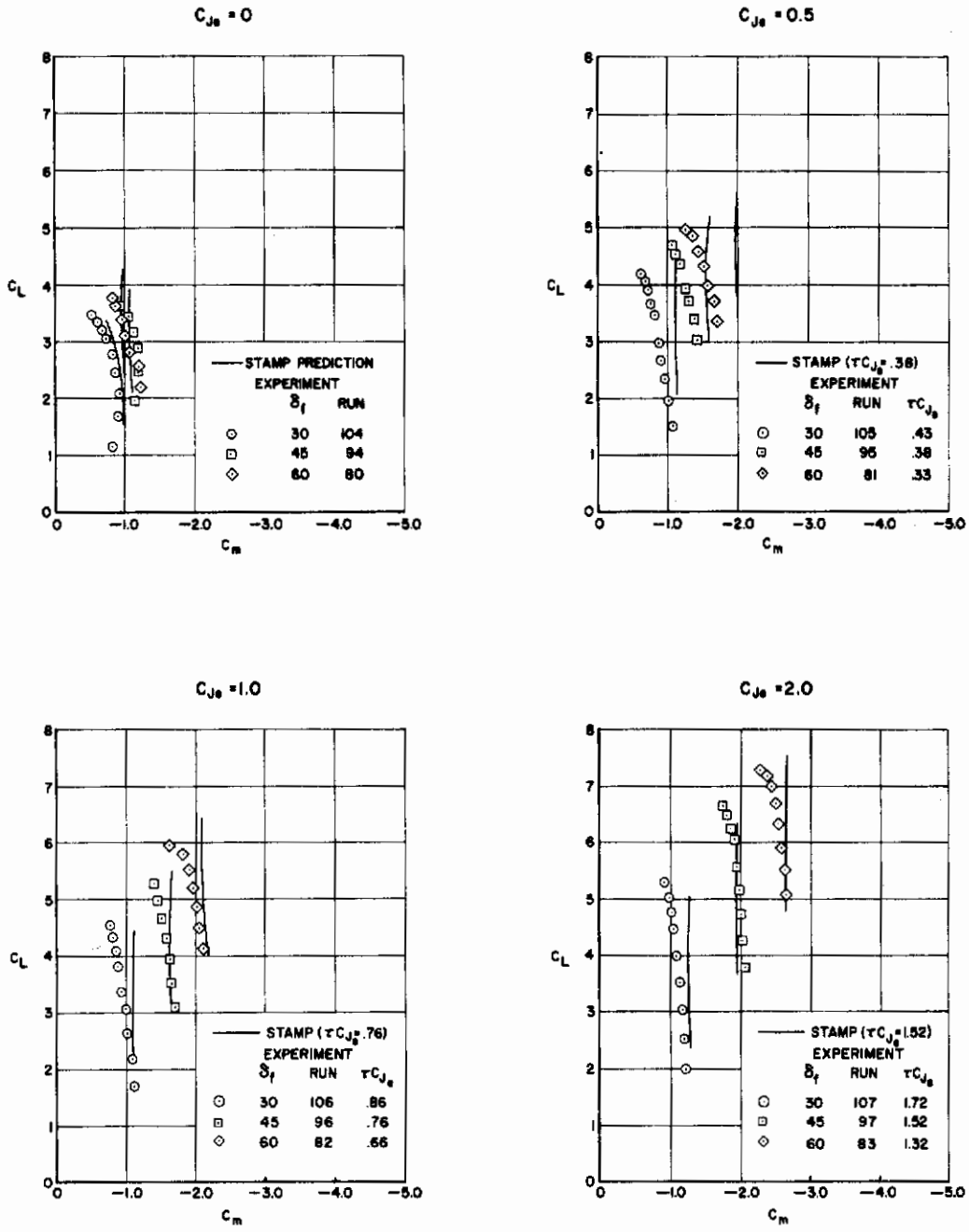

Figure (8.25). EBF Pitching Moment Comparisons (Test GDLST 612-3) (Tail off)

Table (8.17). EBF C_{D_u} Stability Derivatives

C_{J_e}	$\frac{\partial C_D}{\partial u}$		
	$\delta_f = 30°$	$\delta_f = 45°$	$\delta_f = 60°$
0.5	0.011	0.020	0.038
1.0	0.0040	0.0065	0.0085
2.0	0.0014	0.0018	0.0030

$\frac{C_{m_u}}{C_{D_u}}$: The C_{m_u} derivative is calculated in a manner similar to C_{L_u} and C_{D_u}. Table (8.18) presents the calculated values of C_{m_u} at angle of attack $\alpha = 10$ degrees for the various jet momentum coefficients and flap deflection angles tested.

Table (8.18). EBF C_{m_u} Stability Derivatives

C_{J_e}	$\frac{\partial C_m}{\partial u}$		
	$\delta_f = 30°$	$\delta_f = 45°$	$\delta_f = 60°$
0.5	-0.008	-0.024	-0.042
1.0	-0.002	-0.006	-0.010
2.0	-0.0002	-0.0005	-0.002

q - Derivatives: The pitching rate derivatives are calculated directly by the computer program for the jet-wing, empennage, and fuselage. Within the context of linearized theory, C_{L_q} and C_{m_q} are independent of α and q. They are tabulated below:

Table (8.19). EBF Pitching Rate Stability Derivatives

	C_{L_q}	C_{m_q}
Jet-Wing		
C_{J_e} 0	8.058	-4.091
C_{J_e} 0.5	8.749	-4.463
C_{J_e} 1.0	8.996	-4.587
C_{J_e} 2.0	9.251	-4.711
Empennage	7.947	-33.644
Fuselage	-	-5.105

$\dot{\alpha}$ - Derivatives: The $\dot{\alpha}$ stability derivatives for the EBF are computed in a manner identical to that for the IBF. However, different values of $\frac{d\varepsilon}{d\alpha}$ have been predicted, so the stability derivatives are also different. Predicted values of $\frac{d\varepsilon}{d\alpha}$, $C_{L_{\dot{\alpha}}}$, and $C_{m_{\dot{\alpha}}}$ for the EBF are tabulated below:

Table (8.20). EBF $\dot{\alpha}$ Stability Derivatives

C_{J_e}	δ_f (deg)	$\frac{d\varepsilon}{d\alpha}$	C_{L_α}	C_{m_α}
0	30	0.52	4.316	-18.297
	45	0.57	4.716	-19.992
	60	0.60	4.974	-21.087
0.5	30	0.41	3.425	-14.517
	45	0.46	3.817	-16.177
	60	0.48	4.017	-17.025
1.0	30	0.43	3.542	-15.012
	45	0.46	3.867	-16.389
	60	0.49	4.083	-17.308
2.0	30	0.42	3.500	-14.835
	45	0.46	3.825	-16.213
	60	0.48	4.033	-17.096

p - Derivatives: The rolling rate stability derivatives are calculated using output directly from STAMP along with several empirical terms presented in Section 5.2.1. The roll damping derivative, C_{l_p}, is calculated using equations (5.31a) and (5.32), where K has been calculated for the IBF to be 0.996. C_{l_p} is tabulated below:

Table (8.21). EBF C_{l_p} Stability Derivatives

	C_{l_p}
Jet-Wing	
C_{J_e} = 0	-0.554
C_{J_e} = 0.5	-0.567
C_{J_e} = 1.0	-0.572
C_{J_e} = 2.0	-0.577
Horizontal Tail	-0.0276
Vertical Tail	-0.0103
Fuselage	-

Although the yawing moment due to rate of roll, C_{n_p}, is not expressed in the form of a stability derivative [equation (5.34)], the second order term, $C_{n_{p^2}}$, is identically zero for symmetric configurations. Hence, there is only an alpha-variation to consider. Table (8.22) presents the calculated $C_{n_{p_o}}$ and $C_{n_{p_\alpha}}$ terms for the various EBF cases considered.

Table (8.22). EBF C_{n_p} and C_{Y_p} Stability Derivatives

	C_{J_e}	δ_f (deg)	$C_{n_{p_o}}$	$C_{n_{p_\alpha}}$	$C_{Y_{p_o}}$	$C_{Y_{p_\alpha}}$
Wing	0	30	-0.152	-0.064	-0.189	0.122
		45	-0.221	-0.027	-0.060	0.061
		60	-0.275	-0.009	0.030	0.031
	0.5	30	-0.155	-0.065	-0.183	0.125
		45	-0.229	-0.028	-0.044	0.063
		60	-0.290	-0.009	0.060	0.031
	1.0	30	-0.147	-0.066	-0.196	0.126
		45	-0.224	-0.028	-0.051	0.063
		60	-0.288	-0.009	0.058	0.032
	2.0	30	-0.148	-0.067	-0.194	0.128
		45	-0.228	-0.028	-0.044	0.064
		60	-0.295	-0.009	0.071	0.128
Vertical Tail			0.160	-	-0.046	-

It is apparent from these data that neglecting the angle of attack variation is not permissible since the $C_{n_{p_\alpha}}$ term is often the same order of magnitude as the $C_{n_{p_o}}$ term. Hence, for this configuration, use of the linearized equations of motion should be questioned.

Also tabulated above are the STAMP predictions for the EBF side force due to rate of roll. To these values must be added an increment for dihedral, calculated by equation (5.29):

$$\left(\Delta C_{Y_p}\right)_\Gamma = -0.182(C_{l_p})_{\substack{\Gamma=0 \\ C_L=0}} = \begin{Bmatrix} 0.101 \\ 0.104 \\ 0.105 \\ 0.105 \end{Bmatrix} \quad \text{for} \quad C_{J_e} = \begin{Bmatrix} 0 \\ 0.5 \\ 1.0 \\ 2.0 \end{Bmatrix}$$

Again it should be noted that the $C_{Y_{p_\alpha}}$ term is of a similar order to the $C_{Y_{p_o}}$ term and hence must be considered in a dynamic stability analysis.

r - Derivatives: The yawing rate derivatives are calculated by the methods presented in Section 5.2.2 using derivatives calculated directly by the STAMP computer program in conjunction with several empirical terms. The side force due to rate of yaw for the jet-wing is calculated directly by STAMP in the form of equation (5.36), but since the configuration is symmetric, all r^2-dependent derivatives are identically zero. However, the r-dependent portion of $C_Y(r)$ is a function of angle of attack, and the data generated by the computer program [table(8.23)] indicate that these terms cannot be neglected.

The rolling moment due to yawing is calculated from equation (5.38a). The first two terms, which are calculated by the computer program, are tabulated in table (8.23). It is apparent that the $C_{l_{r_\alpha}}$ term is negligible. The remaining terms in equation (5.38a) are evaluated in the same manner as for the IBF:

$$\left(C_l(\hat{r})\right)_{wing} = \left[C_{l_{r_o}} + C_{l_{r_\alpha}}\,\alpha\right]\hat{r} + 0.030\, C_Y(\hat{r})\hat{r} + 0.076\,\hat{r}$$

where $C_{l_{r_o}}$, $C_{l_{r_\alpha}}$, and $C_Y(\hat{r})$ are presented in table (8.23).

The yaw damping derivative for the jet-wing is calculated using equation (5.41). The quantities within the square brackets are presented in table (8.23). The additional term, which accounts for asymmetries in C_{D_o}, is found from figure (5.1) to be

Table (8.23). EBF Yawing Rate Stability Derivatives

	C_{J_e}	δ_f (deg)	$C_{Y_{r_o}}$	$C_{Y_{r_\alpha}}$	$C_{Y_{r_{\alpha^2}}}$	$C_{n_{r_o}}$	$C_{n_{r_\alpha}}$	$C_{n_{r_{\alpha^2}}}$	$C_{l_{r_o}}$	$C_{l_{r_\alpha}}$
Wing	0	30	-0.05001	0.03174	-0.00213	-0.03031	-0.01779	0.00111	0.23083	0.00971
		45	-0.01745	0.01141	-0.00106	-0.07688	-0.00778	0.00047	0.33863	0.00971
		60	-0.00464	0.00331	-0.00053	-0.11944	-0.00464	0.00015	0.42596	0.00971
	0.5	30	-0.04804	0.03188	-0.00219	-0.03114	-0.01792	0.00114	0.23318	0.00994
		45	-0.01438	0.01094	-0.00109	-0.07943	-0.00767	0.00048	0.34638	0.00994
		60	-0.00165	0.00254	-0.00055	-0.12415	-0.00448	0.00015	0.44048	0.00994
	1.0	30	-0.05152	0.03285	-0.00221	-0.02814	-0.01836	0.00115	0.22573	0.01002
		45	-0.01573	0.01133	-0.00111	-0.07697	-0.00781	0.00049	0.34084	0.01002
		60	-0.00187	0.00264	-0.00055	-0.12221	-0.00450	0.00016	0.43726	0.01002
	2.0	30	-0.05070	0.03295	-0.00224	-0.02854	-0.01843	0.00117	0.22664	0.01011
		45	-0.01443	0.01115	-0.00112	-0.07792	-0.00775	0.00050	0.34368	0.01011
		60	-0.00072	0.00232	-0.00056	-0.12364	-0.00441	0.00016	0.44240	0.01011
Vertical Tail			0.422	-	-	-1.398	-	-	0.0737	-
Fuselage			-	-	-	-0.355	-	-	-	-

$$-0.4\ C_{D_o}\ r$$

where C_{D_o} is the wing profile drag coefficient, tabulated earlier in this section. This additional term is:

$$\begin{Bmatrix} -0.01028\ \hat{r} \\ -0.01748\ \hat{r} \\ -0.02948\ \hat{r} \end{Bmatrix} \quad \text{for} \quad \delta_f = \begin{Bmatrix} 30° \\ 45° \\ 60° \end{Bmatrix} \qquad \text{Blown Cases}$$

$$\begin{Bmatrix} -0.02516\ \hat{r} \\ -0.05468\ \hat{r} \\ -0.10388\ \hat{r} \end{Bmatrix} \quad \text{for} \quad \delta_f = \begin{Bmatrix} 30° \\ 45° \\ 60° \end{Bmatrix} \qquad \text{Unblown Cases}$$

8.2.4 Comparison with Experiment (EBF)

Data comparisons for the EBF configuration are presented in figures (8.22), (8.23), (8.24), and (8.25) for lift, tailplane downwash, drag, and pitching moment, respectively. These comparisons between experiment and the prediction methods are discussed in this section. It should be reiterated that certain inaccuracies in the analysis are expected due to assumptions concerning mean flap extensions, mean turning efficiencies, etc.

Lift: Figure (8.22) indicates poor agreement in lift for engine gross thrust coefficients C_{J_e} of 0 and 0.5, but good agreement for C_{J_e} of 1.0 and 2.0. Looking first at $C_{J_e} = 0$ data, reasonably good agreement is obtained for flap deflections of 30 and 45 degrees, but lift for 60 degrees flap deflection is considerably over-predicted. Also, a distinct non-linearity in the experimental lift curves is noted. The non-linearity can be explained by the presence of the engine nacelles, since similar data obtained from these tests without engines did not exhibit such behavior. The negligible increase in C_{L_o} from 45 to 60 degrees flap deflection is indicative of flow separation from the flap. The empirical correction to lift, which utilizes figure (3.4), does not predict such a severe loss in lift. This indicates that some refinement in the empirical curves is required, although the magnitude of disagreement seems to imply that the flap is poorly designed.

For the power-on cases, the experimental lift curves do not show the non-linearities obtained for the unblown case. For $C_{J_e} = 0.5$, a consistent

over-prediction in C_{L_o} is obtained, but C_{L_α} has been well predicted. Apparently the complete effects of boundary layer control have not been realized at this low power setting. Since the jet does spread in a manner similar to that shown in figure (8.20), it is likely that some of the sectional jet momentum coefficients (c_μ) are insufficient to maintain attached flow. The empirical corrections applied to these data assume that fully attached flow is maintained over the span of the jet sheet. For C_{J_e} = 1.0 and 2.0, much better agreement for C_{L_o} is obtained, and again C_{L_α} is well predicted. The small error in prediction of C_{L_o} for C_{J_e} = 2.0 can be easily explained, since the actual trailing edge jet momentum coefficient (τC_{J_e}) used in the STAMP computer run did not agree exactly with that tested. This was necessitated by the fact that a mean turning efficiency of $\tau = 0.76$ was used, while over the range of flap deflections tested τ varied from 0.66 to 0.86 [see figure (8.19)]. Had the correct values of C_{J_e} been used, C_{L_o} would have increased by 0.2 for δ_f = 30 degrees and decreased by 0.2 for δ_f = 60 degrees. The changes in C_{L_α} would be considerably smaller.

Tailplane Downwash: The comparisons presented in figure (8.23) indicate generally good agreement for $\frac{d\varepsilon}{d\alpha}$, the tailplane downwash gradient, except for the unblown case. The agreement for ε_o is generally within three degrees, which can affect tail sizing and tailplane incidence limits. These tailplane downwash comparisons are comparable in agreement to those obtained for the IBF. Again, better agreement can be obtained for the unblown case if the predicted values are multiplied by the ratio of corrected lift to $C_{L_{EVD}}$.

Drag: EBF drag comparisons are presented in figure (8.24). Looking first at the power-on drag polars, reasonably good agreement is obtained for C_{J_e} = 1.0 and 2.0. Better agreement than that indicated for the C_{J_e} = 2.0 case is actually obtained when the discrepancies in τC_{J_e} tested and run in the computer program are accounted for. For the C_{J_e} = 0 and 0.5 cases, however, the predicted drag polars indicate a higher drag level than that measured. This is consistent with lift predictions for these cases. However, a part of the over-prediction in drag level is due to inadequacies in the empirical flap profile drag methods. Referring to equation (3.24) and figure (3.15), it is seen that empirical curves for $\Delta c_{d_{flap}}$ are presented only for plain and

single-slotted flaps. These plots, taken from Datcom (reference 3), are based on a large body of wind tunnel data. Similar attempts to systematize profile drag data for double-slotted flaps have not been successful, however, partially due to a scarcity of wind tunnel data and partially due to the large number of variables. The authors are aware of several attempts to systematize double-slotted flap profile drag, specifically one by the Douglas Aircraft Company based on its DC-8, DC-9, and DC-10 jet transports; and one by the Boeing Company (reference 31). However, each of the resulting curves is applicable to double- (or triple-) slotted flaps of a specific type only and cannot be applied with any generality to other flap designs. Hence, until a complete study of the profile drag for multi-segmented flaps can be made, single-slotted flap data is all that can be provided for unblown wing sections.

Pitching Moment: EBF pitching moment comparisons are presented in figure (8.25). The pitching moments are referenced about the quarter mean aerodynamic chord point of the wing. The agreement between experiment and prediction is generally good, both for C_{m_o} and C_{m_α}. As for the IBF pitching moment, discrepancies can in part be attributed to the complex fuselage geometry, fuselage/sting interference, etc.

8.3 STOL Aircraft Employing Mechanical Flap System with Vectored Thrust

An MF/VT system in which a conventional double-slotted mechanical flap system was used in conjunction with the engine exhaust ducted downward by nozzles clear of the flap was employed in the third phase of this test program. The basic MF/VT model tested was identical to the EBF model described in Section 8.2.1, except for the ducting of the engine exhaust. The analysis of this system is similar in many respects to the EBF analysis for the unpowered case plus interferences and jet reaction forces and moments arising from the vectored thrust.

8.3.1 Configuration Description

The basic aircraft configuration is illustrated in figure (8.1). The model is typical of a four engine, high wing, T-tail subsonic STOL transport with a front loading cargo fuselage. Basic wing geometric characteristics are listed in table (8.1), and basic flap characteristics are listed in

table (8.12). Leading edge flap, fuselage, and empennage geometry are identical to those employed in the IBF and EBF tests. Nozzle geometry for the MF/VT is illustrated in figure (8.26). Only engine position "E" has been analyzed here. Tabulated below are the coordinates of the engine exhaust exit centerline.

Table (8.24). MF/VT Engine Position E Coordinates

δ_f (deg)	Engine	$\frac{X_o}{b/2}$	$\frac{Y_o}{b/2}$	$\frac{Z_o}{b/2}$
0	Inbd	0.161	0.30	-0.102
	Otbd	0.280	0.49	-0.089
30	Inbd	0.184	0.30	-0.108
	Otbd	0.320	0.49	-0.094
60	Inbd	0.200	0.30	-0.125
	Otbd	0.349	0.49	-0.109

8.3.2 Geometry Preparation for Computer Analysis

Geometric inputs to the STAMP computer program are nearly identical to those used for the EBF configuration. Identical spanwise and chordwise divisions have been used, but jet sheet inputs have been omitted. Instead, vectored jet inputs must be provided. Symmetry and repeat jet options can be used for the vectored jet input so that only one jet trajectory need be calculated. Jet exit locations are listed in table (8.24), and the jet exit diameter D_o is 0.08 b/2. Two jet cases have been run: $\tau C_{J_e} = 0.94$, $\delta_J = 60^o$ ($\theta_J = 33.57^o$) and $\tau C_{J_e} = 1.96$, $\delta_J = 60^o$ ($\theta_J = 33.45^o$). It should be noted that θ_J differs from δ_J for two reasons: the engines are canted upward 3.5^o and the nozzles have extremely poor turning characteristics. It is difficult to say why the turning angle of the nozzles is so poor while the turning efficiency is so good ($\tau = 0.94$ and 0.98 in these cases). Note that tne jet momentum coefficient per engine is required for the computer program input (i.e., $C_{J_e} = 0.235$ and 0.49).

Fundamental cases for the MF/VT are the same as those used for the EBF except that the last case (jet sheet deflection) is omitted. Composite cases are also the same, except that there is no jet sheet deflection.

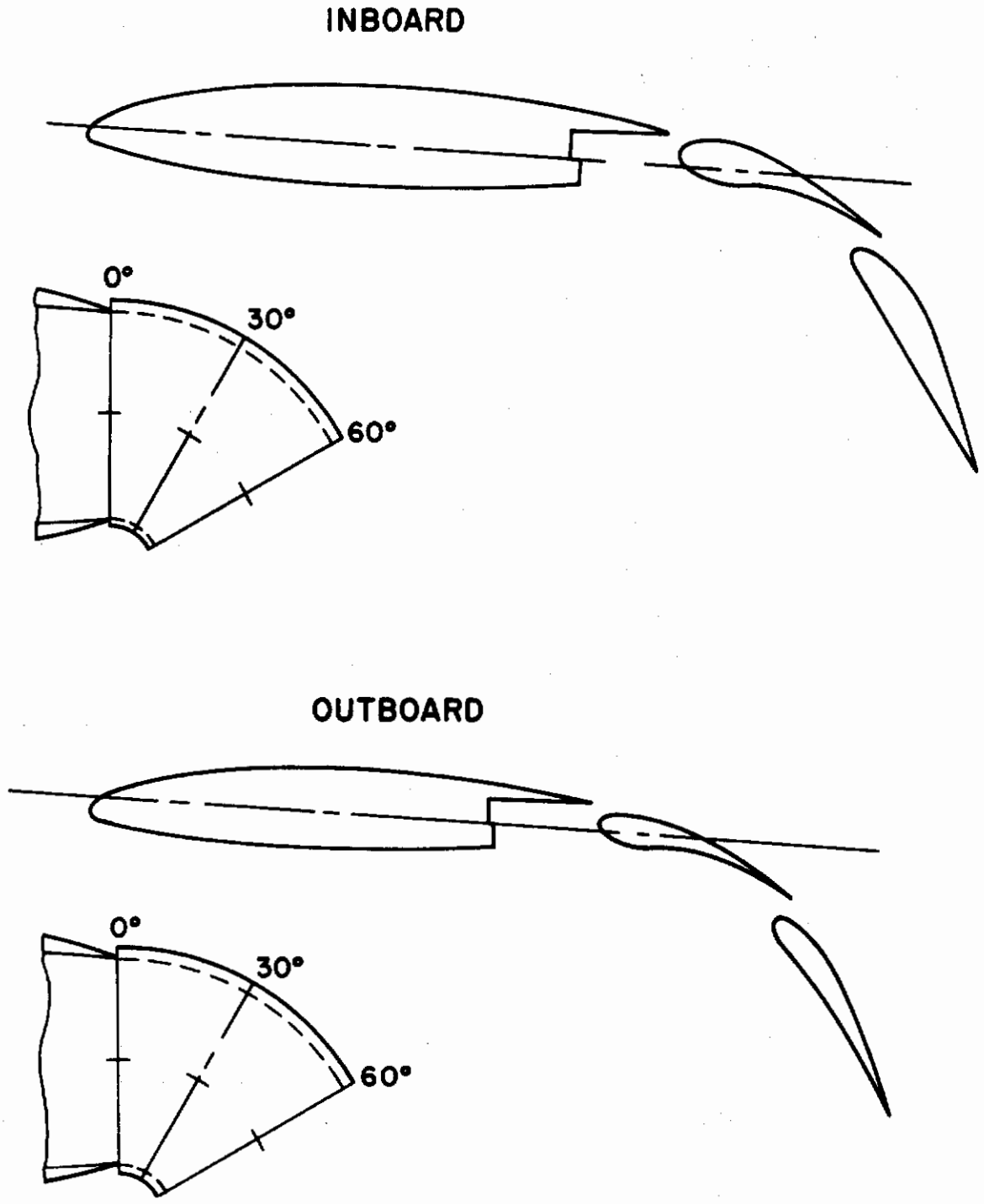

Figure (8.26). MF/VT Wing-Nozzle Geometry (Engine Position "E")

Basic case flags and parameters are again the same as for the EBF, except NCASES = 5 and JETFLG = 2 for the MF/VT. Also, since within the context of the present vectored jet interference techniques the jets do not affect dynamic stability derivatives, IDERIV = 0. It is assumed that MF/VT dynamic stability derivatives are the same as for the EBF with power off. The computer run parameter estimates were 30 minutes of IBM/370 CPU time, 30 minutes I/O time, and 50,000 lines of print.

8.3.3 Interpretation of Computer Data

This section presents the computer generated aerodynamic data for the MF/VT configuration and demonstrates application of the engineering methods presented in this volume to complete the aerodynamic analysis. Since certain portions of this analysis are identical to work already presented for the IBF and EBF configurations, many of the details have been omitted.

The actual STAMP computer analysis for this MF/VT configuration was run on the McDonnell Douglas IBM 370/165 computer system and required 19.2 minutes of CPU time. Application of the engineering methods to these data is presented below. Aerodynamic data for the MF/VT are presented in terms of interferences to show the effects of the jets on the wing. ΔC_L, ΔC_D, and ΔC_m are increments relative to the power off case.

Lift: MF/VT lift curves calculated by the computer program are corrected using the same procedures as for the EBF unpowered case. Since C_L is calculated by STAMP at specific angles of attack (α = 0, 5, 10, 15, 20) for the MF/VT, only the C_{L_o} correction should be used:

$$C_{L_\Gamma}{}_{VT} = \begin{Bmatrix} 0.8538 \\ 0.8110 \\ 0.7732 \end{Bmatrix} C_{L_\Gamma}\Big|_{\substack{STAMP \\ VT}} \quad \text{for } \delta_f = \begin{Bmatrix} 30° \\ 45° \\ 60° \end{Bmatrix}$$

C_{L_J} is calculated directly by the computer program, but to calculate $\Delta C_{L_\Gamma}\big|_{VT}$ it is not necessary to include jet reaction:

$$\Delta C_{L_\Gamma}\Big|_{VT} = C_{L_\Gamma}\Big|_{VT} - C_{L_\Gamma}\Big|_{C_{J_e}=0}$$

$\Delta C_{L_\Gamma}\big|_{VT}$ versus α is plotted in figure (8.27).

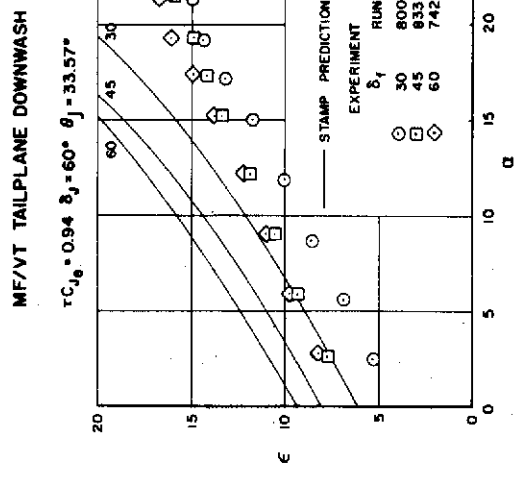

Figure (8.28). MF/VT Tailplane Downwash Comparisons (Test GDLST 612-3)

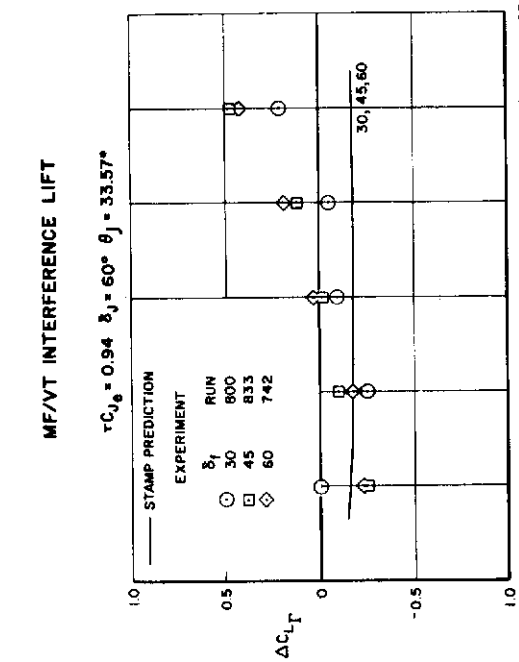

Figure (8.27). MF/VT Lift Comparisons (Test GDLST 612-3)

Mean tailplane downwash is calculated using equation (3.20) and is plotted in figure (8.28).

Drag: MF/VT drag polars are calculated using the same procedure as for the EBF power off case. There the wing profile drag was calculated to be

$$C_{D_o}\Big|_{profile} = \begin{Bmatrix} 0.0629 \\ 0.1367 \\ 0.2597 \end{Bmatrix} @ \quad \delta_f = \begin{Bmatrix} 30° \\ 45° \\ 60° \end{Bmatrix}$$

Ram drag and fuselage drag are unchanged. Wing induced drag is computed using equation (3.27), applying the $C_{D_{i_o}}$ correction only to the values calculated at each angle of attack:

$$C_{D_i}(\alpha)\Big|_{VT} = \left(\frac{C_{L_T}\Big|_{VT}}{C_{L_T}\Big|_{VT}^{STAMP}}\right) C_{D_i}(\alpha)\Big|_{VT}^{STAMP}$$

MF/VT drag polars are then computed by summing induced, profile, ram, and fuselage drag. $\Delta C_D\Big|_{VT}$ is then computed from

$$\Delta C_D\Big|_{VT} = C_D\Big|_{VT} - C_D\Big|_{C_{J_e}=0}$$

The quantity $\Delta C_D\Big|_{VT}$ is plotted in figure (8.29) and includes a jet reaction term $\tau C_{J_e}\,[1-\cos(\theta_o+\alpha)]$, which is labeled in the computer program output as CCDJ.

Pitching Moment: MF/VT pitching moment curves are calculated using the same procedure as for the EBF, power off. The C_{m_o} correction should be applied to C_m calculated by STAMP at each angle of attack:

$$C_{m_T}\Big|_{VT} = \begin{Bmatrix} 0.55 \\ 0.8 \\ 1.0 \end{Bmatrix} C_{m_T}\Big|_{VT}^{STAMP} \quad \text{for } \delta_f = \begin{Bmatrix} 30° \\ 45° \\ 60° \end{Bmatrix}$$

C_{m_J} and C_{m_T} are calculated directly by the computer program. The MF/VT ram drag pitching moment is slightly different than for the EBF because of the different engine position. Calculating C_{m_R} as before,

$$C_{m_R} = 2C_{D_{R_E}}\{-1.015\cos\alpha + 1.346\sin\alpha\}$$

The fuselage contribution to C_m is calculated by the computer program, including interference effects due to the wing and jets. Two corrections to account for afterbody vortex shedding must be made, however, following the same procedure as used earlier.

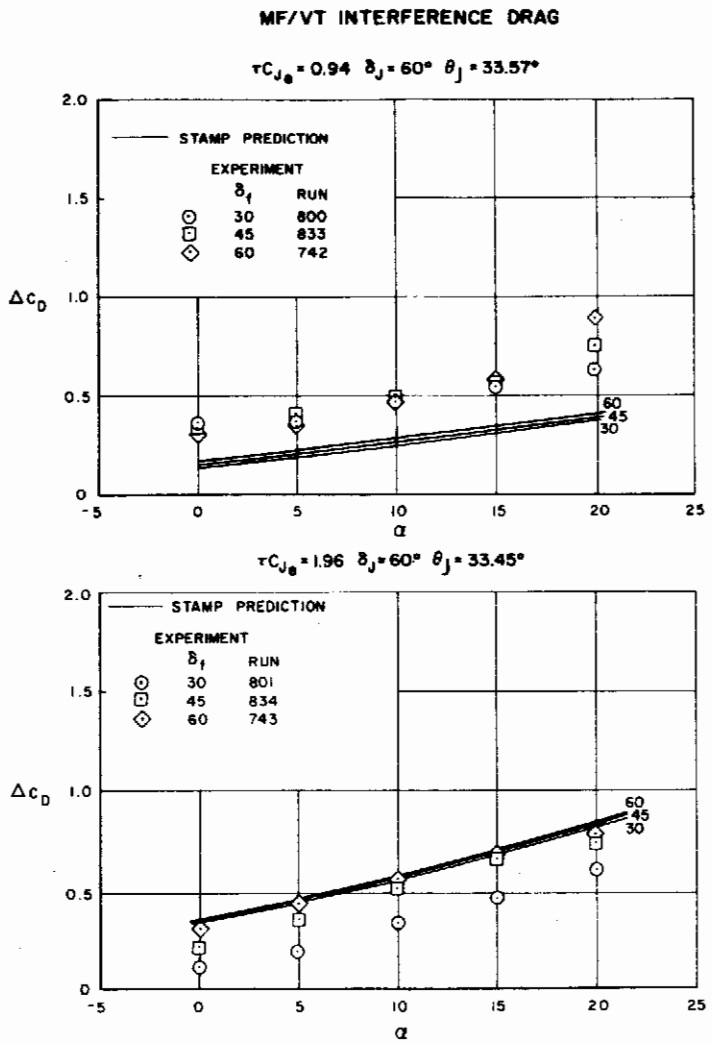

Figure (8.29). MF/VT Drag Comparisons (Test GDLST 612-3)

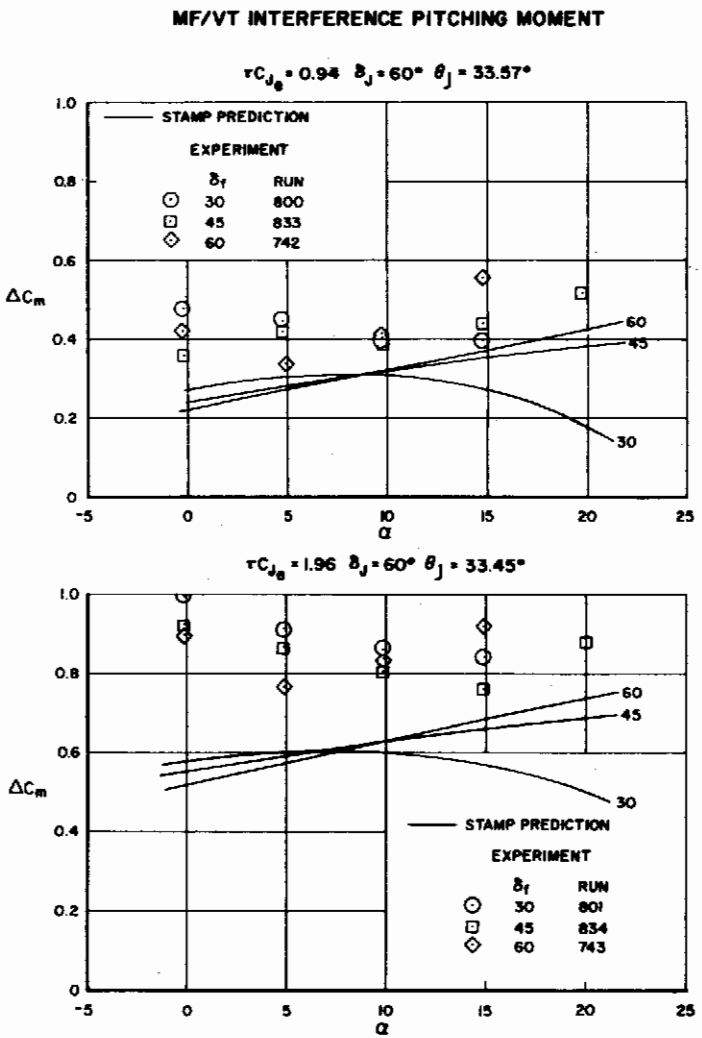

Figure (8.30). MF/VT Pitching Moment Comparisons (Test GDLST 612-3) (Tail Off)

The incremental pitching moment due to vectored thrust interference is calculated by summing $C_{m_T}|_{VT}$, C_{m_R}, and C_{m_F}, and then subtracting from this sum the MF/VT power off pitching moment:

$$\Delta C_m|_{VT} = \left(C_{m_T}|_{VT} + C_{m_R} + C_{m_F}\right) - C_m\Big|_{C_{J_e}=0}$$

$\Delta C_m|_{VT}$ is plotted in figure (8.30) and includes terms for the jet reaction pitching moment.

8.3.4 Comparison with Experiment (MF/VT)

Comparisons between the predictions of the methods developed in this report and wind tunnel test data for the MF/VT configuration are presented in figures (8.27), (8.28), (8.29), and (8.30) for incremental circulation lift due to power effects, tailplane downwash, incremental drag, and incremental pitching moment, respectively. Increments were obtained from experimental data by subtracting power-on aerodynamic data from power-off data. In the following paragraphs these comparisons are discussed to assess the validity of the present prediction techniques and to ascertain where further work is required.

Figures (8.27), (8.29), and (8.30) indicate that vectored thrust interferences are, qualitatively, being predicted reasonably well, although the actual level of the predicted interferences is not good, particularly at large angles of attack. For example, ΔC_{L_T} predictions near $\alpha = 0°$ fall within the scatter of the experimental data, but near $\alpha = 20°$ the predictions do not even show the proper sign of the interference. Drag and pitching moment comparisons indicate similar discrepancies.

The comparisons presented here do not show the level of agreement with experiment as was presented for the simple MF/VT configuration in figure (3.3) of Volume I. Certainly the fact that the STAI MF/VT configuration is considerably more complex than the configuration discussed in Volume I can partially account for the different levels of agreement obtained, but there are other effects which can also be responsible for some of the discrepancies. First is the means by which the power-effects increments have been calculated. This has been done by taking power-on data and subtracting from it power-off

data. However, the power-off data was taken with the engines in place, so the possibility of spillage at the engine inlets exists. Such a spillage can occur because there is a smaller mass flow through the engines with power off than with power on. Such spillage can manifest itself by changes in lift, drag, and pitching moment.

Secondly, wind tunnel wall effects, which have been shown to be acceptably small for the IBF and EBF tests, may be of increased importance for the MF/VT tests due to the highly deflected high velocity round jets. For example, figure 10 of reference 24 shows that a jet of velocity ratio 5·0 deflected 60 degrees will penetrate 5 jet diameters into the flow 5 jet diameters downstream. Since this corresponds approximately to the $C_{J_e} = 2.0$ case tested in the STAI, it indicates that jet impingement can occur less than one wing span downstream of the jet exit. As angle of attack increases, the impingement point would move upstream.

Third, the poor turning characteristics of the nozzles employed in the STAI program, shown in static runs to be 22 degrees less than the nozzle angle ($\theta_J \approx 38°$ for $\delta_J = 60°$), could have some impact on the applicability of the present methodology. For example, internal flow separation within the nozzles may lead to a non-uniform flow at the exit and may change the jet entrainment characteristics from that employed in the prediction methods.

The applicability and adequacy of the present MF/VT methodology to configurations such as that tested in the STAI must also be considered. The present jet interference technique is a "far-field" method able to account for jet interferences on the wing only if the jet does not pass closely to the wing. For the jet locations of the STAI configuration, this restriction will be least satisfied for small jet deflections in conjunction with large flap angles and angles of attack. This can, in part, explain the discrepancies indicated in figures (8.27), (8.29), and (8.30). Another area of concern is the mutual interaction between the jets. The two engines on each wing are closely spaced, so the presence of one jet on the other seemingly would be important. No account for mutual jet interaction is made in the current methodology. A final questionable point concerning the interference prediction techniques is the viscid/inviscid interaction of the jets. The

The model is equipped with a leading edge flap from the fuselage to the outboard pylon with chord extension of one percent local chord and flap-chord ratio at 15 percent. The leading edge flap was deflected 20 degrees. From the outboard pylon to the wing tip, a leading edge slat deflected 19 degrees is used. Slat extension varied from 11 percent local chord inboard to 18 percent outboard, while the slat-chord ratio varies from 15 to 25 percent.

The double-slotted trailing edge flap system is divided into inboard and outboard sections. The inboard section, extending from the fuselage to 50 percent b/2, has a deflection of 20°/0°, which means the forward flap segment is deflected 20 degrees relative to the main wing and the aft flap segment 0 degrees relative to the forward segment. The flap chord extension is 14 percent and the flap-chord ratio is 50 percent. The outboard flap segment, extending from 50 to 75 percent b/2, has a deflection of 20°/20°, flap chord extension of 27.5 percent, and a flap chord ratio of 63 percent. The planform, as input into the STAMP computer program, is illustrated in figure (8.31).

The LB-305D model fuselage is much simpler than that used in the STAI tests, having a circular cross-section, only moderate upsweep, and a conventional forebody. In addition, since the model was strut mounted rather than sting mounted, support interferences with the fuselage should be minimal.

Wind tunnel wall constraints for this test are of considerably less importance than for the STAI tests. For example, $\Delta\alpha$ can be calculated simply, with $\delta = 0.139$ for a square test section, wing area $S = 5.143\ ft^2$, tunnel area $C = 900\ ft^2$, hence

$$\Delta\alpha = \frac{57.3}{1+\frac{2C_J}{\pi AR}}\ \delta\ \frac{S}{C}\ C_L = \begin{Bmatrix} 0.0455\ C_L \\ 0.0417\ C_L \\ 0.0385\ C_L \\ 0.0358\ C_L \end{Bmatrix} \text{ for } C_{J_e} \begin{Bmatrix} 0 \\ 1 \\ 2 \\ 3 \end{Bmatrix}$$

Therefore, allowable maximum values of C_L to meet the $\Delta\alpha \leq 2$ degrees criterion are much larger than required. Similarly, wake and solid blockage for this test are considerably smaller than for the STAI tests. Corrections to account for wall constraints and wake blockage have been applied. Finally,

interference flow field induced on the wing by the vectored jets may sufficiently alter the wing pressure distribution to promote or forestall trailing edge separation. It has been implicitly assumed in the methodology that there are no boundary layer control effects due to vectored jets.

8.4 Other Methods Applications

In addition to the STOL Tactical Aircraft Investigation configurations discussed in detail in the preceding section, various other STOL aircraft configurations have been analyzed using the theoretical and empirical methods developed in this work. Application of the prediction methods to these configurations is part of a continuing effort at the Douglas Aircraft Company to validate and improve STOL aerodynamic prediction techniques. Some of the wind tunnel testing problems and uncertainties and inconsistencies in model geometry associated with the STAI test program are not present in these additional correlations, and hence a more meaningful evaluation of the accuracy of the methods can be obtained.

8.4.1 Douglas Model LB-305D Employing Externally Blown Jet Flap

The Douglas Aircraft Company wind tunnel model LB-305D is a high-wing, four-engine STOL transport model employing an externally blown double-slotted flap high-lift system (reference 32). The six-foot span model was tested in the National Research Council (NRC) of Canada 30 by 30 foot V/STOL wind tunnel. The model, powered by four ejector engines, was mounted on the NRC tandem struts. Basic geometric parameters of this model are listed below:

Table (8.25). LB-305D Geometric Characteristics

Aspect Ratio	7.0
Taper Ratio	0.3
1/4-Chord Sweep	25°
Span (in)	72.0
Area (in^2)	740.59
Dihedral	0°
Chord, root (in)	15.83
tip (in)	4.75
MAC (in)	11.28
Incidence, 11% b/2	2.85°
35% b/2	0.90°
95% b/2	-2.20°

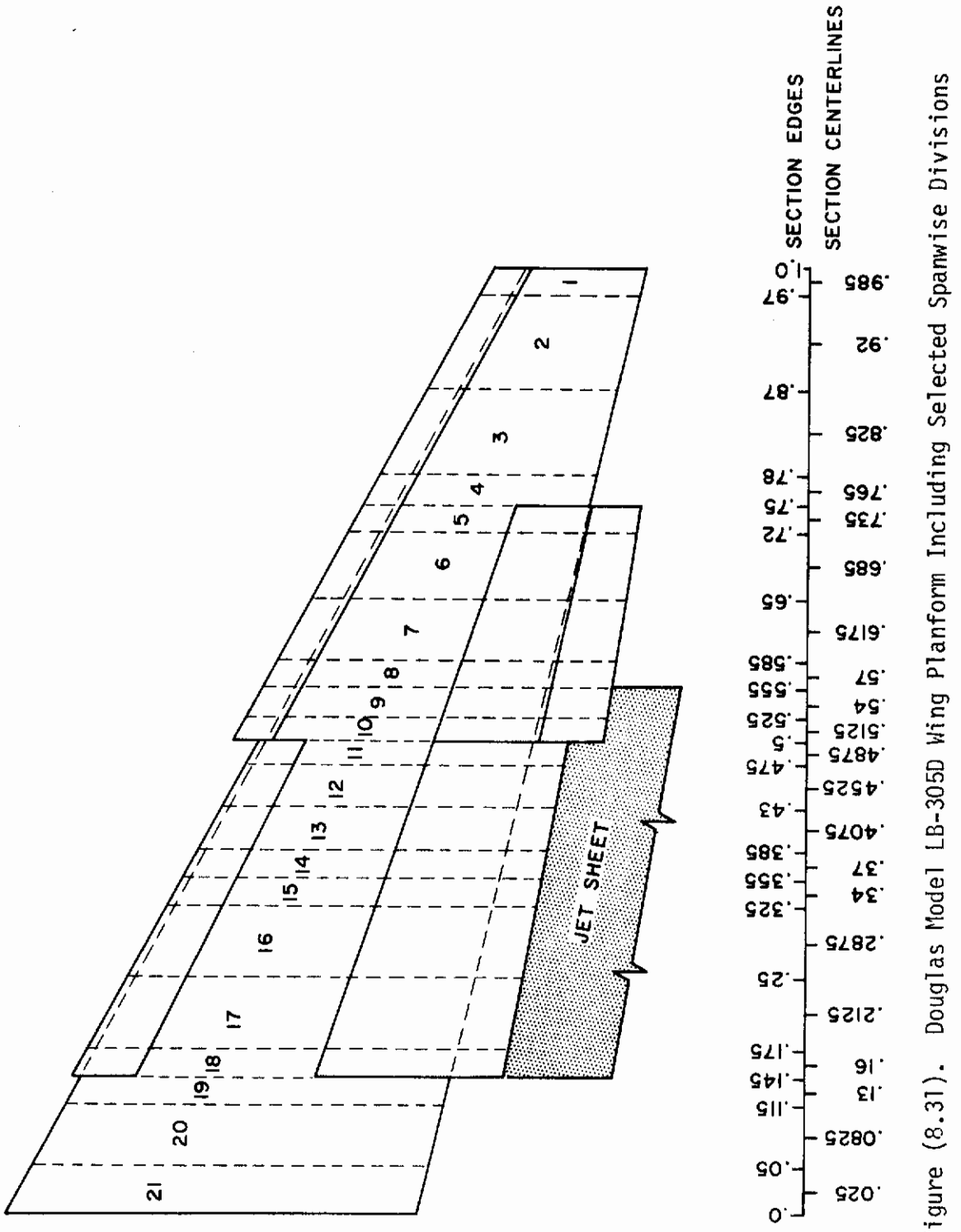

Figure (8.31). Douglas Model LB-305D Wing Planform Including Selected Spanwise Divisions

aerodynamic tares were taken in the LB-305D test program to remove from the test data undesired interferences from the model support system.

Analysis of the STAMP computer data and implementation of engineering methods presented in this volume follow the same procedure as was discussed in detail in Section 8.2.3 for the STAI EBF configuration. Details of these computations are omitted here. Figure (8.32) presents comparisons between experiment and predictions for both unpowered and powered tests. Agreement for lift, drag, and pitching moment is seen to be excellent in all cases. In this presentation thrust rather than drag is plotted. It is the opinion of the authors that this comparison is a more realistic assessment of the capabilities of the STAMP computer program and the associated engineering methods than is the STAI program since the Douglas comparison more adequately treated:

- Wind tunnel interferences
- Geometry definition
- Trailing edge jet momentum (τC_{J_e})

In conclusion, the STAI comparison demonstrates in detail the application of the methods and computer program while the Douglas comparison presents a more realistic assessment of the accuracy of the methods.

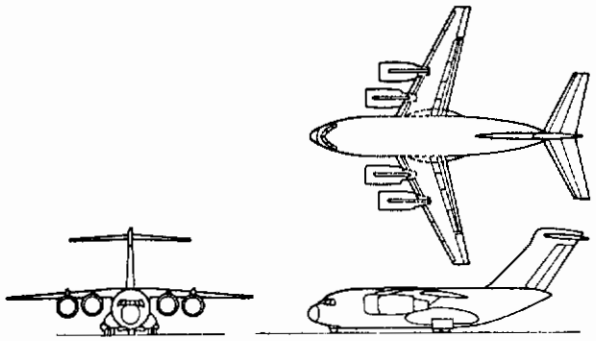

(a) MODEL CONFIGURATION

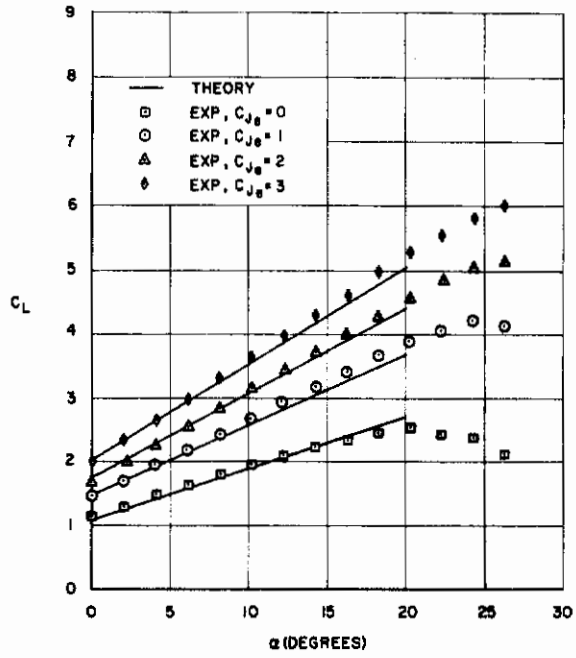

(b) LIFT CURVES

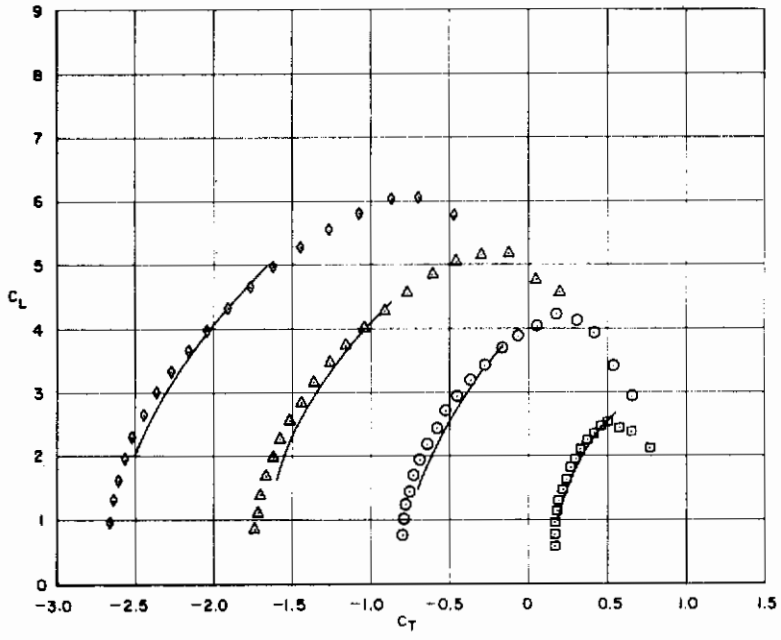

(c) DRAG POLARS

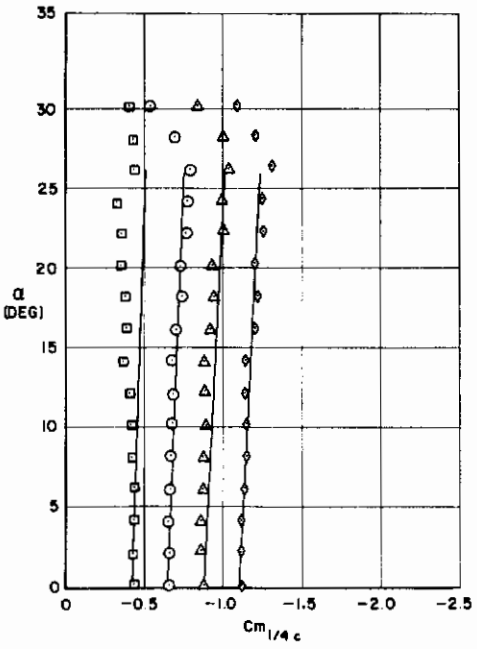

(d) PITCHING MOMENT CURVES

Figure (8.32). Lift, drag, and pitching moment comparisons for Douglas Model LB-305D EBF STOL transport.

9.0 SUMMARY AND CONCLUDING REMARKS

In the three volumes of this report, methods for predicting the aerodynamic and stability and control characteristics of STOL aircraft have been presented. These methods are applicable to STOL aircraft employing mechanical high-lift systems, internally ducted and externally blown jet-flap schemes, and vectored thrust systems. The methods presented herein are largely based on potential flow theory. However, empirical methods are provided to modify and augment the potential flow theory for viscous effects, thickness effects, and phenomena not amenable to theoretical analysis.

Since STOL aerodynamic technology is still a developing one, it was to be expected that our understanding of the complex aerodynamic phenomena associated with each of the high lift systems considered as well as the available experimental data base would be broadened as the result of concurrent and related investigations. Wind tunnel studies conducted as part of the Air Force "STOL Tactical Aircraft Investigation," for example, have provided a major source of experimental data on a significant number of important configuration variables. These data were intended to be used by the authors in the validation and modification of the methodology developed as part of the present program. It was, therefore, unfortunate that, due to a delay in receiving this data, much remains to be accomplished with it. To be more specific, in the limited time available it has only been possible to illustrate with a selected number of examples the implementation of the methodology rather than its validation and subsequent modification through analytical/experimental correlations. Despite these misgivings and the recognized shortcomings of some of the theoretical methods, an improved basic theoretical background for the development and methods for predicting the aerodynamic and stability and control characteristics of STOL aircraft has emerged.

The methodology described in this report is intended for use by design personnel during preliminary design and configuration evaluation activities. It was, therefore, both convenient and desirable to present

this program in a three volume report format which, in general, does not require reference to outside sources in the determination, for a given configuration, of a complete set of aerodynamic and stability and control derivatives and coefficients. The complete theoretical development of the relevant analytical methods for each of the STOL high-lift systems studied were presented in Volume I. The use of the STOL Aerodynamic Methods Computer Program (STAMP) described in Volume II is essential to the implementation of the methodology. STAMP was structured as a computer program package consisting of several major subprograms, each of which is intended to analyze a particular STOL aircraft component (e.g., wing, fuselage, and empennage), plus subprograms developed for the evaluation of the aerodynamic interferences between the various components. Except for the sharing of common geometric data, each of these major subprograms was written so that it can be used independently of the STAMP package. Thus, maximum flexibility to satisfy the needs of various users is provided. In addition, further developments and/or improvements in the program can be readily accomplished. Engineering methods presented in Volume III supplement and/or modify the results obtained from the theoretical methods. Also in Volume III, the implementation of the methodology is illustrated through typical examples, and limited comparisons with experimental data are presented as a preliminary basis for the assessment of the validity of the methods as well as to indicate, in part, those areas where improvements and/or new developments might be desirable. The authors have already stressed the desirability of further analytical/experimental data correlation studies in the preceding paragraph as an important step in improving the accuracy and applicability of the engineering methods. There are also other areas where further research might not only broaden out present-day knowledge in understanding certain phenomena, but might also provide some noticeable improvements in the ability to predict certain aerodynamic parameters. In this context, some recommendations are presented in the following paragraphs.

- The ground effect problem is one of considerable concern. Comparisons presented in Section 8.0 show only qualitative agreement with experiment, power on or off. Other ground effect comparisons for jet-wing configurations also show poor agreement with experiment. As discussed in Section 2.2.6.3 of Volume I, it is believed that these discrepancies are largely a result of the assumptions adopted in the formulation of the mathematical model including the linearization of the boundary conditions. The accurate prediction of aerodynamic characteristics in ground effect must, in the authors' opinion, be based on a method in which a three-dimensional, non-planar, non-linear mathematical model is adopted.

- The aerodynamic influence of ground proximity has been established as being potentially important in relation to STOL aircraft performance, stability, and flying qualities. Wind tunnel investigations conducted either with fixed or moving ground planes have also established that the nature and magnitude of the aerodynamic characteristics in ground proximity tend to be critically sensitive to aircraft geometry, attitude, and ground clearance, together, in the case of jet-flap lift augmentation schemes, with jet disposition and inclination. There is evidence to suggest, however, that the transient situation of STOL aircraft in takeoff and landing may not be adequately predicted by such stationary model experiments. The stationary wind tunnel model with the ground plane parallel to the mainstream can simulate neither the correct model attitude nor the dynamics associated with changing altitude.

- Although predicted derivatives and coefficients are intended for application in the vehicle equations of motion for trimmed flight conditions, an accurate prediction of tailplane downwash at zero angle of attack (i.e., ε_0) is desirable. That improvements in the jet-wing flow field are warranted is apparent from some of the comparisons of experimental and analytical data presented in Section 8.0. Admittedly, the prediction of $\frac{d\varepsilon}{d\alpha}$ is acceptable for stability and control purposes. However, a more realistic representation of the jet-wing vortex wake (e.g., roll-up, jet entrainment, and jet blockage) can be expected to result in an improved prediction both in ε_0 and $\frac{d\varepsilon}{d\alpha}$. Consideration should also be given to fuselage effects on tailplane downwash.

- In view of the importance of the aerodynamic propulsion interactions and interferences associated with the majority of STOL high-lift systems, appropriate theoretical aerodynamic methodology is likely, in the context of CTOL aircraft, to be based on more rigorous mathematical models. Thus, an improved prediction over that obtainable with existing methods is to be expected for CTOL aircraft providing the effects of separation, for example, are not severe. In other words, the methodology developed as part of this program has much broader applications than suggested by the title selected for this report. With this in mind, the author's earlier recommendation for further analytical/experimental data correlation in order to improve the accuracy of the engineering methods including empirical procedures should include available STOL and CTOL test data.

- Because of insufficient experimental data, no conclusive assessment of the validity of the dynamic stability derivative predictions can be made. Some of the basic comparisons presented in Volume I, however, indicate that present methods are adequate for conventional wings, except near stall. No comparisons have yet been made for jet-wing dynamic stability derivatives.

10.0 REFERENCES

1. Goldhammer, M. I, Lopez, M. L., and Shen, C.C.: Methods for Predicting the Aerodynamic and Stability and Control Characteristics of STOL Aircraft. Vol. I: Basic Theoretical Methods. McDonnell Douglas Report No. MDC J5965-01, 1973.
2. Goldhammer, M.I., and Wasson, N.F.: Methods for Predicting the Aerodynamic and Stability and Control Characteristics of STOL Aircraft. Vol. II: STOL Aerodynamic Methods Program. McDonnell Douglas Report No. MDC J5965-02, 1973.
3. USAF Stability and Control Datcom. Air Force Flight Dynamics Laboratory, Flight Control Division, Wright-Patterson Air Force Base, Ohio. October 1960, revised February 1972.
4. Benepe, D.B., Kouri, B.G., and Welsh, J.B.: Aerodynamic Characteristics of Non-Straight-Taper Wings. Air Force Flight Dynamics Laboratory, Research and Technology Division, Air Force Systems Command, Wright-Patterson Air Force Base, Ohio. Report No. AFFDL-TR-66-73, October 1966.
5. Nelson, F.R., Koerner, W., and Trudel, R.G.: Dynamics of the Airframe. Bureau of Aeronautics, Navy Department. Report No. AE-61-4II, September 1952.
6. May, F., and Widdison, Colin,A.: STOL High-Lift Design Study. Vol. I: State-of-the-Art Review of STOL Aerodynamic Technology. Air Force Flight Dynamics Laboratory, Air Force Systems Command, Wright-Patterson Air Force Base, Ohio. Report No. AFFDL-TR-71-26, Vol. I., April 1971.
7. Etkin, B.: Dynamics of Flight-Stability and Control. John Wiley & Sons, Inc., May 1959.
8. Perkins, C.D., and Hage, R.E.: Airplane Performance Stability and Control. John Wiley & Sons, Inc., 1949.
9. Spence, D.A.: Some Simple Results for Two-Dimensional Jet-Flap Airfoils. The Aeronautical Quarterly, November 1958.
10. Kuchemann, D.: A Method for Calculating the Pressure Distribution over Jet-Flapped Wings. RAE R&M 3036, May 1956.
11. Dimmock, N.A.: Some Early Jet-Flap Experiments. The Aeronautical Quarterly, November 1957.
12. Halsey, N.D.: Two-Dimensional Nonlinear Jet-Flap Potential Flow Method. Unpublished work. McDonnell Douglas Corporation proprietary information.

13. Maskell, E.C. and Spence, D.A.: A Theory of the Jet Flap in Three Dimensions. Proc. Roy. Soc., Vol. A251, pp. 407-425, 1959.
14. Wickens, R.H.: Observations of the Vortex Wake of a Lifting Fuselage Similar to Those on Rear-Loading Transport Aircraft. National Research Council of Canada, Aeronautical Report LR-395 (NRC No. 7911), January 1964.
15. Peake, D. J.: Three-Dimensional Flow Separations on Upswept Rear Fuselages. Canadian Aeronautics and Space Journal, Vol. 15, No. 10, December 1969.
16. Lanchester, F.W.: Aerodonetics. A. Constable & Co. Ltd., London, 1908.
17. Bryan, G.H.: Stability in Aviation. MacMillan Co., London, 1911.
18. Advanced STOL Transport (Medium) Study. Douglas Aircraft Company Report No. MDC J5560. Contract No. F33615-72-C-1479.
19. Summary of Low-Speed Wind Tunnel Data on Several Externally Blown Flap STOL Transport Configurations. Douglas Aircraft Company Report No. MDC J5431. Contract No. F33615-72-C-1534.
20. Schollenberger, C.A.: A Three-Dimensional Wing/Jet Interaction Analysis Including Jet Distortion Influences. AIAA Paper 73-655.
21. Pope, A. and Harper, J.J.: Low-Speed Wind Tunnel Testing. John Wiley and Sons, Inc., 1966.
22. Anscombe, A. and Williams, J.: Some Comments on High-Lift Testing in Wind Tunnels with Particular Reference to Jet-Blowing Models. AGARD Report 63, August 1956.
23. Kuhn, R.E. and Naeseth, R.L.: Tunnel-Wall Effects Associated with VTOL-STOL Model Testing. AGARD Report 303, March 1959.
24. Carter, A.W.: Effects of Jet-Exhaust Location on the Longitudinal Aerodynamic Characteristics of a Jet V/STOL Model. NASA TN D-5333, July 1969.
25. Turner, Thomas R.: Ground Influence on a Model Airfoil with a Jet-Augmented Flap as Determined by Two Methods NASA TND-658, February 1961.
26. STOL Tactical Aircraft Investigation. Volume IV. Wind Tunnel Data Analysis. Convair Aerospace Report No. GDCA-DHG73-001. January 1973.
27. Low Speed Wind Tunnel Tests of a Powered 1/20 Scale STOL Tactical Transport Model with Externally and Internally Blown Trailing Edge Flaps, Blown Leading Edge Flaps, and Vectored Thrust Engines, Wing Sweep of 25°, Aspect Ratio of 8.0. Convair Aerospace Report GDLST 612-3. Volumes I, II, III. January 1973.

28. Low Speed Wind Tunnel Tests of a Powered 1/20 Scale STOL Tactical Transport Model in Ground Effect With Externally and Internally Blown Trailing Edge Flaps, Blown Leading Edge Flaps, and Vectored Thrust Engines, Wing Sweep of 25°, Aspect Ratio 8.0. Convair Aerospace Report GDLST 621. Volumes I, II, III. January 1973.
29. Lachmann, G.V.: Boundary Layer and Flow Control. Pergamon Press, 1961.
30. Brown, W.S.: Wind Tunnel Corrections on Ground Effect. British Aeronautical Research Council, R&M 1865, July 1938.
31. STOL Tactical Aircraft Investigation. Aerodynamic Technology: Design Compendium, Vectored Thrust/Mechanical Flaps. AFFDL TR-73-19-Volume II, Part I, May 1973.
32. Summary of Low Speed Wind Tunnel Data on Several Externally Blown Flap STOL Transport Configurations. McDonnell Douglas Report MDC J5431. Submitted to USAF under contract F33615-72-C-1534.

Unclassified
Security Classification

DOCUMENT CONTROL DATA - R & D

(Security classification of title, body of abstract and indexing annotation must be entered when the overall report is classified)

1. ORIGINATING ACTIVITY (Corporate author) McDonnell Douglas Corporation ~~Douglas~~ Douglas Aircraft Company Long Beach, California 90846	2a. REPORT SECURITY CLASSIFICATION Unclassified 2b. GROUP

3. REPORT TITLE

METHODS FOR PREDICTING THE AERODYNAMIC AND STABILITY AND CONTROL CHARACTERISTICS OF STOL AIRCRAFT. VOL. III ENGINEERING METHODS

4. DESCRIPTIVE NOTES (Type of report and inclusive dates)

Final Technical Report

5. AUTHOR(S) (First name, middle initial, last name)

Mark I. Goldhammer
Michael L. Lopez

6. REPORT DATE December, 1973	7a. TOTAL NO. OF PAGES 236	7b. NO. OF REFS 32
8a. CONTRACT OR GRANT NO. F33615-71-C-1861 b. PROJECT NO. 643A c. d.	9a. ORIGINATOR'S REPORT NUMBER(S) MDC J5965-03 9b. OTHER REPORT NO(S) (Any other numbers that may be assigned this report) AFFDL-TR-73-146, Volume III	

10. DISTRIBUTION STATEMENT

Approved for public release; distribution unlimited

11. SUPPLEMENTARY NOTES	12. SPONSORING MILITARY ACTIVITY Air Force Flight Dynamics Laboratory Wright-Patterson Air Force Base Ohio 45433

13. ABSTRACT

This volume describes engineering methods for the prediction of the aerodynamic and stability and control characteristics of STOL aircraft employing internally ducted jet flaps, externally blown jet flaps, and mechanical flap systems with vectored thrust. These methods are intended to be used in conjunction with the theoretical methods and the associated computer program (STOL Aerodynamic Methods Computer Program) discussed in Volumes I and II, respectively. These engineering methods are intended to provide a rational approach for the aerodynamic analysis of complete STOL aircraft configurations and to provide semi-empirical methods to account for those effects not treated by the theoretical methods.

For the three selected powered high-lift systems, a common set of analytical engineering methods has been presented, and these methods have been divided into three major sections:

- o Static Coefficients and Derivatives
- o Dynamic Stability Derivatives
- o Control Derivatives

The methods presented include brief discussions of the importance of each coefficient and derivative and the impact of each term on the overall stability and control characteristics of the aircraft.

Finally, these methods have been applied to configurations representative of each of the powered high-lift concepts, and the results of these analyses have been presented along with available experimental data to indicate the validity and range of applicability of the methods.

DD FORM 1 NOV 68 1473

Unclassified
Security Classification

14. KEY WORDS	LINK A		LINK B		LINK C	
	ROLE	WT	ROLE	WT	ROLE	WT
AERODYNAMICS						
AERODYNAMIC STABILITY AND CONTROL						
AERODYNAMIC FORCES						
AERODYNAMIC MOMENTS						
CONTROL DERIVATIVES						
EMPIRICAL METHODS						
HIGH LIFT SYSTEMS						
JET FLAP						
JET INTERACTION						
SHORT TAKEOFF AND LANDING AIRCRAFT						
STABILITY DERIVATIVES						
VECTORED JETS						

☆U.S.Government Printing Office: 1974 — 657-015/235